INVESTIGATION OF GCAPE QUASI-EQUILIBRIUM IN THE MIDLATITUDES

by Douglas G. Cripe

David A. Randall, Principal Investigator

Colorado State University

DEPARTMENT OF ATMOSPHERIC SCIENCE

PAPER NO. **568**

INVESTIGATION OF GCAPE QUASI-EQUILIBRIUM IN THE MIDLATITUDES

by

Douglas G. Cripe

Research supported by the
National Science Foundation
under Grant number ATM-9214981
and by the U.S. Department of Energy
under Grant number DE-FG02-92ER61363

Department of Atmospheric Science
Colorado State University
Fort Collins, CO

November 1994

Atmospheric Science Paper No. 568

ABSTRACT

INVESTIGATION OF GCAPE QUASI-EQUILIBRIUM IN THE MIDLATITUDES

Lorenz (1955, 1978, 1979) developed the concept of the "moist available energy" (MAE) of the atmosphere. This he defined as the portion of non-kinetic energy (NKE) available for conversion to kinetic energy (KE). Randall and Wang (1992) and Wang and Randall (1994) showed that it is possible to consider the component of the MAE that resides in the vertical structure of the atmosphere as a "generalized convective available potential energy" (GCAPE). Using data from the tropics, they tested the GCAPE quasi-equilibrium hypothesis (Arakawa and Schubert, 1974) which asserts that cumulus convection "consumes" GCAPE as quickly as it is produced by large-scale (non-convective) forcing such that the convectively active atmosphere remains close to a state of conditional neutrality.

The main purpose of this study is to also investigate the GCAPE quasi-equilibrium hypothesis, only this time in a midlatitude setting. This is a tougher test of the hypothesis given the significantly larger temperature and moisture fluctuations resulting in stronger large-scale forcing in the midlatitudes, compared with the tropics

Data recently made available by the Atmospheric Radiation Measurement (ARM) program has been used. This new data comes from radiosonde measurements collected at ARM's Cloud and Radiation Testbed (CART) site located in north-central Oklahoma during Intensive Operation Periods (IOPs) run periodically throughout the year.

Since this is one of the first studies to make extensive use of this data, a further goal was to evaluate the quality of the wind and thermodynamic measurements being produced by the CART site. Additionally, analysis data from the Mesoscale Analysis and Prediction System (MAPS) was used, both as a check on the reasonableness of the ARM data, and also to detect any possible errors in the MAPS model output.

Acknowledgments

First, I would like to especially thank my advisor, Dr. David A. Randall, for his patience, guidance, and for believing in me. I will not forget his example in striving for excellence, and his willingness to give me a chance.

I would also like to thank my committee members: Drs. Wayne Schubert, Michael Montgomery, and Tobin Jones. Dr. Schubert has been an inspiration to me in his clarity of teaching and devotion to his students, always finding a spare moment to help them understand the complexities of atmospheric dynamics. Dr. Montgomery I have only recently become acquainted with, but his comments and questions have been very helpful in the review process. Dr. Jones was enlightening and thought-provoking during my original work in the Department of Foreign Languages, and has been supportive of my change to the Department Atmospheric Science. *Pour cela, un grand merci!*

Thanks are due to the members of my group, especially Cindy Carrick, Don Dazlich, Scott Denning, Ping Ding, Michael Kelly, Junyi Wang, and Kelley Wittmeyer for their help and expertise in matters ranging from computer applications to understanding the atmosphere.

I also wish to express my gratitude to ARM, and to the Experiment Center staff at LLNL, including Ric Cederwall, Marty Leach and John Yio, for all their help and long hours. Also, thanks to the Scientific Computing Division at the National Center for Atmospheric Research for the use of their Cray computer.

I would like to say thanks to my housemates David Hahn and Roger McGowan for their support, and to my good friends Jarrod Goentzel, Jennifer Granata, Dan and Lisa Johnson, Kenneth Shears, Bryce Unruh, and Ned Woodring for the coffee and sympathy.

Finally, a very special thanks goes to my mother, Eliane Recher-Cartier, and to Thomas Recher for their understanding, encouragement and solid confidence in my academic abilities.

This study was supported by grant #ATM9214981 from the National Science Foundation, and by grant #DE-FG02-92ER61363 from the Department of Energy.

Table of Contents

List of Symbols and their Definitions

A	area
c	area-averaged condensation rate
C	specific heat of liquid water
C_p	specific heat of dry air at constant pressure
C_{pw}	specific heat of moist air at constant pressure
C_v	specific heat of dry air at constant volume
D	horizontal divergence
e	vapor pressure
e_s	saturation vapor pressure
E	area-averaged evaporation rate
g	gravity
h	enthalpy per unit mass
h_G	enthalpy per unit mass of given state
h_R	enthalpy per unit mass of reference state
H	total mass-integrated enthalpy
i	internal energy
K	total mass-integrated kinetic energy
l	distance
L	latent heat of condensation
M	total mass
M_d	mass of dry air
$M_{\bar{w}}$	mass of liquid water and water vapor
$\boldsymbol{n}$	outward normal unit vector
N	total number of parcels
O	O'Brien adjustment parameter
p	pressure
p_0	reference pressure
p_d	partial pressure of dry air
p_r	reference state pressure
p_s	saturation pressure
q	water vapor mixing ratio

Q	diabatic heating
Q_R	radiational heating
Q_1	apparent heat source
Q_2	apparent moisture sink
rh	relative humidity
R_d	gas constant for dry air
R_w	gas constant for moist air
s	entropy per unit mass
S	dry static energy
t	time
T	temperature
T_s	saturation temperature
T_v	virtual temperature
u	east-west wind component
v	north-south wind component
V	volume
$\mathbf{V}$	horizontal wind vector
w	water vapor mixing ratio
w_l	liquid water mixing ratio
$\overline{w}$	total parcel water content
x	east-west distance
y	north-south distance
z	vertical distance
α	specific volume
ε	R_d/R_w
κ	Poisson's constant = $\frac{R_d}{C_p}$
Φ	potential energy
ρ	air density
σ	static stability parameter
θ	potential temperature
θ_e	equivalent potential temperature
$\dot{\theta}$	time rate of change of θ
Θ	any scalar variable

ω	vertical (pressure) velocity
ω'	adjusted vertical (pressure) velocity
ω_0	vertical (pressure) velocity at surface
ω_T	vertical (pressure) velocity at top of atmosphere
$\bar{(\ )}$	indicates mean field in Reynolds averaging (with the exception of $\overline{w}$)
$(')$	indicates transient field in Reynolds averaging (with the exception of ω')

List of Acronyms

APE	Available Potential Energy
ARM	Atmospheric Radiation Measurement
CAPE	Convective Available Potential Energy
CART	Cloud and Radiation Testbed
DAE	Dry Available Energy
DOE	Department of Energy
FSL	Forecast Systems Laboratory
GARP	Global Atmospheric Research Project
GATE	GARP Atlantic Tropical Experiment
GCAPE	Generalized Convective Available Potential Energy
GCM	General Circulation Model
GEWEX	Global Energy and Water Cycle Experiment
GMS	General Measurement Strategies
IOP	Intensive Observation Period
KE	Kinetic Energy
LLNL	Lawrence Livermore National Laboratories
MAE	Moist Available Energy
MAPS	Mesoscale Analysis and Prediction System
NKE	Non-Kinetic Energy
NOAA	National Oceanic and Atmospheric Administration
NWS	National Weather Service
PNL	Pacific Northwest Laboratories

RAFS	Regional Analysis and Forecast System
SAO	Surface Aviation Observation
SCM	Single Column Model
SGP	Southern Great Plains
SMOS	Surface Meteorological Observing Station
TRMM	Tropical Rainfall Measuring Mission
USGCRP	United States Global Change Research Program
UTC	Universal Coordinated Time (*Universel Temps Coordonné*)

CHAPTER 1

Introduction

1.1 Scientific Background

Moist convective processes result in the formation of cumulus clouds and thunderstorms, both of which have a strong influence on the atmospheric general circulation. They do so by means of heat, moisture and momentum redistribution, as well as by latent heating and precipitation, and by producing radiatively important stratiform clouds. An example of the importance of moist convection can be seen in one of the more noticeable features of the general circulation, the Hadley Cell. In spite of the fact that the earth continuously receives energy from the sun, the earth-atmosphere system remains in a constant state of energy equilibrium. The contribution that the Hadley Cell makes in maintaining this equilibrium is to redistribute a surplus of energy in the tropics towards higher latitudes, where eventually the excess energy may be radiated back to space. The Hadley Cell accomplishes this energy redistribution by taking warm humid air (with high energy) at low levels in the tropics and exporting it towards the poles at high levels in the form of potential energy. The means by which this energy is carried to high levels in the atmosphere is through the deep convection that takes place in the tropics. In effect, the cumulus towers that are virtually a daily feature of life in the tropics act as pipelines, removing mass near the surface and depositing it high in the atmosphere. This displaced mass is replenished with a return meridional flow of more warm, moist air at low levels, and so the cycle is perpetuated. Of course, the Hadley Cell is not the only feature of the mean meridional circulation, nor is it the only means by which excess energy may be transported poleward, but it does provide a ready illustration of the connection between moist convection and the general circulation of the atmosphere.

Additionally, the deep cumulus convection that occurs in the tropics and summer mid-latitudes accounts for the injection of moisture from the boundary layer to the upper layers of the troposphere, as moist air is detrained from the cumulus towers. This moist detrainment results in the formation of horizontally extensive anvil and cirrus clouds. The anvil clouds contribute up to 40% of the precipitation that falls from the convective systems (Houze and Betts, 1981) whereas the cirrus clouds, which have life-spans on the order of several days, may be dispersed by upper-tropospheric winds up to thousands of kilometers away from their places of origin. Both of these types of clouds, generated by deep convection, may have a substantial impact on the general circulation of the atmosphere in terms of the solar shortwave radiation scattered or reflected back to space and the terrestrial longwave radiation absorbed and re-emitted back to earth.

In order to examine certain aspects of deep, tropical convection and its effects on the general circulation, Randall and Wang (1992) and Wang and Randall (1994) (hereafter referred to as RW92 and WR94, respectively) investigated moist convective processes using data collected in regions of the equatorial Atlantic Ocean. Among other things, they wanted to determine the extent to which moist convection can convert non-kinetic energy into cumulus kinetic energy using the concept of Moist Available Energy as developed by Lorenz, a brief description of which follows.

Lorenz (1955) first introduced the idea of the Available Potential Energy (APE) of a dry atmosphere as the portion of non-kinetic energy (NKE) that is available for conversion to kinetic energy (KE). The basis of his idea was to focus on the enthalpy, which, for an ideal gas, is defined as the product of the temperature and the specific heat of dry air at constant pressure per unit mass, as a useful tool for understanding the framework of any given atmospheric state. Thus, he constructed the notion of the APE of the atmosphere by examining the total enthalpies of any particular state of the atmosphere, known as the "given" state, and some final hypothetical state in which the mass of the atmosphere had been rearranged reversibly and adiabatically. The key characteristic of this final, or "reference" state is that it represents an arrangement in which NKE or enthalpy has been minimized and at the same time KE has been maximized. This can be seen by considering the total energy equation, integrated over the entire atmosphere. In the absence of energy sources or sinks (i.e. considering the atmosphere as an ideal, frictionless fluid that does no work on the Earth's surface, and that no energy crosses either boundary at the Earth's surface or the top of the atmosphere), this may be expressed as

$$\frac{d}{dt}(H+K) = 0, \qquad (1.1)$$

where H is the total mass-integrated enthalpy and K is the total kinetic energy.

The APE, then, is the difference in total enthalpy between the given state and the reference state. In a later paper (1978), Lorenz extended the idea of APE to include moist adiabatic processes as well, and coined the term Moist Available Energy (MAE) to represent the NKE available for conversion to KE. This time, however, the enthalpies of the given and reference states included the effects of latent heat. This modification generally increases the amount of NKE (in the form of MAE) available for conversion. It is this quantity, MAE, that we wish to investigate in this study, along the lines followed by RW92 and WR94. The difference here is that we will be using data from the midlatitudes as opposed to the tropics. The importance of this difference, as will be more fully developed in later chapters, is that we expect to see greater forcing due to large-scale processes (i.e. stronger temperature and moisture advection), which should in turn lead to much larger values of MAE than RW92 and WR94 found with the GATE data. Additionally, the concept of MAE and its application to moist convection will be developed in greater detail in Chapter 2.

1.2 Objectives of this Study

1.2.1 Utilization of New ARM Data Source

As stated above, the main focus of this study is to investigate the MAE of the atmosphere in a midlatitude setting. To achieve this goal a suitable source of data, from a location where moist convection takes place on a fairly regular basis, is required. Thus, an additional objective of this study is to evaluate atmospheric data recently made available from balloon-borne radiosondes, launched at regular intervals, at an observation site in northern Oklahoma. These radiosonde observations form an integral part of a comprehensive suite of instruments gathering atmospheric data under the auspices of the Atmospheric Radiation Measurement project (ARM). ARM is being funded by the United States Department of Energy (DOE) and was created out of the desire on the part of the DOE to improve atmospheric models currently being used for investigating climate change. The radiosonde data sets used in this study come from two observation periods, the first of which was held in January-February 1994 and the second in April 1994.

Therefore, this is a relatively new source of data and it stems from the efforts by ARM to provide comprehensive information about meteorological variables such as temperature, pressure, moisture, and winds at successive levels in an atmospheric column. Further, the goal of ARM is that all of these data be provided at regularly scheduled times throughout the year. A more in-depth background discussion on ARM and the scientific goals it has set out to accomplish through this project, followed up by an explanation of the observation site set-up and radiosonde arrangement, will be given in Chapter 4. Then, the procedures used in processing the raw data to obtain the derived fields used in this study, and conclusions about reliability of the data, will be covered in Chapter 5.

1.2.2 Evaluation of ARM Data by Comparison with MAPS Model Output

Another of the objectives of this study is to compare the results obtained using this new data source provided by ARM with other established data sets produced by models, such as the Forecast System Laboratory's (FSL) Mesoscale Analysis and Prediction System (MAPS). This is done partly in order to ascertain the reasonableness of the data being produced by the ARM project. However, and more importantly, it is hoped this study can also shed some light on the degree to which the MAPS model output may be in error. Indeed, one of the main goals of the ARM project is to test current parameterization schemes included in climate models by comparing the model output with real data. The parameterization process and the testing procedure will be more fully explained in Chapter 4. Then, after a brief discussion of the meteorological conditions during the periods in which the data were collected, the findings of our comparison of the ARM data with the MAPS model output will be discussed in the chapters on results, Chapters 6 and 7. The MAPS data used in this study are diagnostic analyses only; no prognostic output has been included.

1.2.3 *Raison d'Etre*: Test of GCAPE Quasi-Equilibrium in Midlatitudes

As discussed above, Lorenz developed the idea of atmospheric MAE in the course of papers he wrote in 1955 and 1978. In a subsequent paper, Lorenz (1979) outlined a numerical procedure for calculating the MAE of the global atmosphere, in which homogeneous parcels of equal mass are rearranged adiabatically from the given state to find the arrangement yielding the state of minimized enthalpy, or reference state. RW92 and WR94 further developed the idea of MAE and explained how it is possible to distinguish between the component of MAE that resides in the horizontal structure of the atmosphere, and that which resides in the vertical structure. The former type of MAE is available to the long time-scale synoptic motions of the atmosphere, whereas the latter is available for cumulus convection involving time-scales of a few hours. The vertical component they termed the "Generalized Convective Available Potential Energy" (GCAPE). They went on to produce an algorithm, based on the ideas introduced by Lorenz, to actually compute the GCAPE of given soundings from the GARP Atlantic Tropical Experiment (GATE). They wanted to test the hypothesis that cumulus convection "consumes" GCAPE virtually as quickly as it is produced (Arakawa and Schubert 1974; Lord and Arakawa 1980; Soong and Tao 1980; Krueger 1988; Dudhia and Moncreif 1988; Xu 1991), which supports the theory that the convectively active atmosphere usually remains near a state of conditional neutrality (Arakawa and Schubert 1974). To do this, they first determined the GCAPE from a sounding at a particular observation time. Next, they "constructed" a hypothetical sounding, valid several hours later, based on the large-scale horizontal and vertical advective tendencies of temperature and moisture at the time of the original observation. Finally, they computed the GCAPE of the hypothetical sounding, and subtracted from it the GCAPE of the given sounding. Dividing by the time interval, they were able to calculate the GCAPE production rate due to large-scale processes, which they then compared with the observed GCAPE rate of change. What they found is that the rate of GCAPE production by the large-scale tendencies was rather large compared with the observed GCAPE rate of change. This led them to conclude that, indeed, convective processes do consume GCAPE nearly as fast as the large-scale tendencies can produce it and thus the atmosphere stays close to a state of GCAPE quasi-equilibrium.

In this study, we also wish to establish the GCAPE quasi-equilibrium state of the atmosphere. However, as mentioned previously, instead of using tropical data we will be making use of data from the midlatitudes to test this hypothesis. The reason is that we wish to investigate the GCAPE quasi-equilibrium hypothesis in a region of strong moisture and temperature gradients, as opposed to the tropics where these gradients tend to be much weaker. Thus, an area of greater temperature and moisture forcing (through advection, among other things) should prove to be a more rigorous environment for testing the GCAPE quasi-equilibrium hypothesis. A detailed explanation of the GCAPE algorithm used and a survey of results from RW92 and WR94 will be given in Chapter 3, following the discussion on MAE in Chapter 2. Then, the results of our work will be discussed in Chapters 6 and 7, followed by the conclusions in Chapter 8. The reader who wishes to skip directly to the results of this study is therefore directed to turn to these last 3 chapters.

CHAPTER 2

Lorenz's Concept of Moist Available Energy

Even the most casual observer of the atmosphere will note that it is almost constantly in motion on disparate time and space scales; gusts of wind felt one minute are gone the next, cumulus clouds form, move across the sky and dissipate in a matter of hours, and large synoptic-scale weather systems traverse the earth's continents while maintaining their coherence for days at a time. In short, the atmosphere is anything but static. This constant atmospheric movement or circulation needs sources of energy to drive it; this source can ultimately be traced to the sun.

As introduced in Chapter 1, the solar energy received and transformed by the earth-atmosphere system can be divided up into two categories: kinetic energy (KE) and non-kinetic energy (NKE). The motions of the atmosphere, such as extra-tropical cyclones, are the more obvious manifestations of KE. NKE, on the other hand, includes less directly visible forms of energy such as potential and internal energies. Internal energy may be further broken down into thermal energy and the latent energy due to condensation/evaporation, fusion/melting and fusion/sublimation of water between its various phases. Consider the total energy conservation equation for the atmosphere in the absence of heating and friction:

$$\frac{\partial}{\partial t}(C_p T + Lq + K) = -\nabla \bullet [V(C_p T + Lq + K + \Phi)] - \frac{\partial}{\partial p}[\omega(C_p T + Lq + K + \Phi)] \tag{2.1}$$

According to this equation, the time rate of change of the sum of the KE and NKE per unit mass is due to spatial redistributions of enthalpy $h = C_p T + Lq$ and potential energy Φ. Then, integrating (2.1) over the mass of the entire atmosphere, the transport terms drop out and we are left with

$$\frac{d}{dt}\int_M (C_p T + Lq + K)\, dM = 0, \tag{2.2}$$

where we see that the sum of the enthalpy and kinetic energy is conserved.

Since the earth absorbs solar radiation non-uniformly (more at the equator and less at the poles), a temperature imbalance is created on a global scale creating a store of NKE which is subsequently converted to KE as the atmosphere attempts to reach thermal equilibrium. As alluded to briefly in the Introduction, Lorenz (1977) discussed this conversion of NKE into KE by adiabatic reversible processes, and identified Available Potential Energy (APE) as the portion of NKE that is available for this conversion. We will now summarize his proposal as to how one would go about estimating the APE of a given atmosphere.

If the mass of the atmosphere is conceived of as being divided up into many parcels of equal mass, which can be rearranged under reversible, adiabatic conditions, then, among the many possible states the atmosphere could occupy, there would be one state in which the NKE is minimized, and the KE maximized. This is evident if we rewrite the mass-integrated total enthalpy H, or

$$H \equiv \int_M h dM, \tag{2.3}$$

and kinetic energy relation in (2.2) as

$$\frac{d}{dt}(H+K) = 0. \tag{2.4}$$

Note that (2.4) is identical with (1.1). The state in which H has been minimized Lorenz calls as the "reference state," in contrast to the original disposition of the atmosphere which he terms the "given state." Then, in a nutshell, the APE is the amount by which the total enthalpy of the given state exceeds that of the reference state, because this difference represents the portion of NKE that can be altered adiabatically and reversibly by redistributing the atmospheric mass on a global scale. In other words, the APE is the portion of NKE (or enthalpy) that is available for conversion to KE through reversible, adiabatic processes.

Lorenz (1955) originally considered only a dry atmosphere in his formulation of the concept of APE, such that enthalpy was defined as

$$h_{DRY} = C_p T. \tag{2.5}$$

He subsequently (1978) extended the notion of APE to include the effects of latent heating as we have done here in (2.1), since an adiabatic process may be either dry or moist. Hence APE is considered to be synonymous with Dry Available Energy (DAE), whereas the more general version of APE with the effects of latent heating included is referred to as Moist Available Energy (MAE). The MAE, then, is defined as the difference between the total enthalpy of the given state and that of the reference state for air containing moisture.

It is quite convenient to speak hypothetically of "rearranging" at will the mass of the atmosphere, but what does this really mean? When we talk about the reversible, adiabatic rearrangement of a given atmospheric state to reach the reference state (with minimized H), it is helpful to first introduce the concept of air parcels, each of which has equal mass. These will be the "bricks" we will use in reconstructing the atmosphere under controlled conditions. There are three prerequisites that this concept of a parcel must satisfy (Brown, 1991):

1) It must contain a sufficient number of molecules to define the meteorological variables pressure, temperature, etc.

2) It must be small enough so that its meteorological variables may be considered as spatially homogeneous. Thus we may talk in terms of the parcel's unique temperature, pressure, density, mixing ratio, velocity, etc.

3) It must be separate and distinguishable from other parcels for short periods of time.

Furthermore, to the extent that all parcels from one state may be transformed into another state via thermodynamically reversible and adiabatic processes, those two states may be considered as equivalent.

Now we turn to the manner in which the rearrangement is allowed to be carried out. In terms of a skew-T chart, "reversible and adiabatic" means that a parcel is displaced dry-adiabatically along its potential temperature line until it reaches saturation, at which point it then moves moist-adiabatically along its equivalent potential temperature line. Another way of thinking about a reversible adiabatic process is that the entropy of a parcel is not changed but conserved as it moves from one state to another. Thus, for example, none of a parcel's water vapor that would condense upon reaching the level of saturation should be allowed to precipitate out, as this would irreversibly change the parcel's entropy. The goal, then, is to compare equivalent states resulting from the rearrangement of the mass of the atmosphere by varying the distribution of the parcels in order to find the state in which the total enthalpy has been minimized. All of this is carried out under the constraint of strictly conserving the parcel's entropy.

Thus far, we have been speaking in terms of the reference state being the state in which H has been minimized. Another way of looking at the reference state is from the perspective of maximized KE. If it is indeed to be the state in which KE has reached a maximum, then as Lorenz (1978) pointed out, the reference state must be characterized by three attributes:

1) Surfaces of constant pressure must be horizontal. Otherwise, the presence of a horizontal pressure gradient force would result in a state where the atmospheric mass is subject to horizontal accelerations, leading us to conclude that KE had not been maximized.

2) Similarly, the reference state must be in hydrostatic equilibrium. For if this were not the case, then the vertical pressure gradient force would again result in accelerations, this time in the vertical, and, again, KE had obviously not been maximized in the proposed reference state. The implication of this requirement (hydrostatic equilibrium) is that the specific volume α must be everywhere horizontally stratified. In other words, *hydrostatic equilibrium* means that the upwards-directed pressure gradient force per unit mass acting on an air parcel at a particular height is exactly balanced by the downwards-directed force of gravity per unit mass acting on the same parcel. As a parcel travels upwards in a state of hydrostatic equilibrium, the pressure from the surrounding environment it encounters will decrease monotonically with height since the amount of mass above it is decreasing. This decrease in pressure will cause the parcel to expand in volume as it seeks to maintain pressure equilibrium with its environment. Thus, just as the pressure is horizontally stratified under conditions of hydrostatic equilibrium, so is the specific volume α. This in turn means that every function of α and p must be likewise horizontally uniform, including the temperature and virtual temperature. The importance of this fact, that the virtual temperature must be horizontally stratified in the reference state, will be seen by the key role that it plays in the numerical procedure for determining the proper ordering of the individual air parcels in the reference state (discussed below).

3) The reference state must be statically stable. In other words, potential temperature and equivalent potential temperature must be monotonically increasing with height in sub-saturated and saturated layers of the atmosphere, respectively. Otherwise, regions of statically unstable air would experience vertical motions (convection) if any type

of triggering mechanism were imposed, and once more, KE would be less than maximized in the proposed state of the system.

From the above, we have argued that in the reference state surfaces of constant pressure must be horizontal (so to insure KE has been maximized) and also the pressure must be horizontally stratified (hydrostatic equilibrium requirement). Additionally, the reference state must be statically stable. Thus, a consequence of these reference state attributes is that the pressure will be uniform along isentropic surfaces in the reference state, and vice-versa. This in turn implies that isobars and isentropes must not only be horizontally stratified, but also parallel to each other. If the given state is dry statically stable, then the average pressure on an isentropic surface will be the same in the reference state as in the given state, since only adiabatic processes are allowed (i.e. $\dot{\theta} = 0$, which means no mass is allowed to cross an isentropic surface). Therefore, to the extent that pressure varies along isentropic surfaces in the given statically stable state (or that potential temperature varies along isobars), it may be concluded that APE resides in the horizontal structure of the atmosphere. In going from the given state to the reference state, the vertical arrangement of the isentropes is left intact; only the mass between the isentropes is allowed to be redistributed so that the resultant pressure will be uniform along the isentropes in the reference state. On the other hand, if the given state is dry statically unstable, then a vertical rearrangement of the isentropes is needed to go from the given state (in which potential temperature decreases with height in some portion of the atmosphere) to the reference state (where potential temperature monotonically increases with height). From this, it can then be concluded that a certain portion of the APE resides in the vertical structure of the atmosphere as well.

To borrow an illustration from RW92, suppose we have a very simple, dry atmospheric system that contains just two parcels of mass, one residing at pressure p_1 and the other at p_2, with $p_1 > p_2$. To make the arrangement unstable, let us further suppose that the potential temperature associated with the lower parcel at p_1 is higher than the potential temperature associated with the upper parcel at p_2, or $\theta_1 > \theta_2$. Then, using Poisson's equation, we may state the enthalpy per unit mass of the kth parcel as

$$h_k = C_p \theta_k \left(\frac{p_k}{p_0}\right)^{\kappa}. \tag{2.6}$$

Now, if we create a new state in which we exchange the position of the two parcels so that the parcel with potential temperature θ_1 occupies the position of the former parcel at p_2 and vice-versa, the change in total enthalpy per unit mass associated with going from the given to the new state may be expressed as

$$\begin{aligned} h_2 - h_1 &= C_p \theta_1 \left[\left(\frac{p_2}{p_0}\right)^{\kappa} - \left(\frac{p_1}{p_0}\right)^{\kappa}\right] + C_p \theta_2 \left[\left(\frac{p_1}{p_0}\right)^{\kappa} - \left(\frac{p_2}{p_0}\right)^{\kappa}\right] \\ &= C_p (\theta_1 - \theta_2) \left[\left(\frac{p_2}{p_0}\right)^{\kappa} - \left(\frac{p_1}{p_0}\right)^{\kappa}\right] \end{aligned} \tag{2.7}$$

In (2.7), we are merely computing the change in enthalpy each parcel experiences in the exchange (subtracting the enthalpy of the given state from that of the new state) and then summing up the enthalpy changes. It turns out that $h_2 - h_1$ is negative, implying that the total enthalpy of the new state is less than that of the given state. Thus, we can surmise that the new state is indeed the reference state since the total enthalpy per unit mass has been minimized by the transaction, and the APE of this system is in fact given by (2.7).

Thus far, we have used a dry atmosphere to illustrate the existence of APE (DAE) when going from the given state to the reference state. Lorenz (1978, 1979) pointed out that the APE of a given dry atmosphere cannot be greater than the MAE of the same atmosphere containing moisture. As an example, consider an idealized, horizontally homogeneous atmosphere that is statically stable. Such an atmosphere could nevertheless be conditionally unstable. Under these circumstances, the DAE would be zero due to the statically stable structure of the atmosphere, but the MAE would be positive because of the conditional instability.

Now, extending this example to the real atmosphere, which is inhomogeneous and contains areas of conditional instability, it becomes possible to conceptualize the global MAE as really being composed of two components; that part which lies in the horizontal structure of the atmosphere, and that which occupies the vertical. As RW92 have pointed out, the MAE residing in the horizontal structure of the atmosphere is released through mechanisms that operate on longer, synoptic time-scales, such as baroclinic instability, and is not available to short time-scale mechanisms such as cumulus convection. In contrast, RW92 have found, using GATE data, that the vertical component of MAE tends to be consumed by cumulus convection almost as rapidly as it is produced, so that the atmosphere stays close to a state of conditional neutrality at all times. Therefore, the point of making a distinction between these two components is that it allows us to study them individually since they operate on such different time scales. In keeping with RW92, the local vertical component of the MAE will be referred to in this paper as the Generalized Convective Available Potential Energy (GCAPE) to distinguish it from Lorenz's definition of global MAE.

CHAPTER 3

GCAPE

3.1 GCAPE Algorithm

Now that the concept of global MAE has been explained, our goal is to actually calculate the vertical component of the MAE residing in a given atmospheric column, i.e. the GCAPE, from a series of soundings. In order to do this, we need some sort of computerized algorithm that can take large numbers of observed pressure, temperature and moisture data representing parcels from these soundings and rearrange them to reach the reference state. Additionally, we would like to investigate the rate of GCAPE production by large-scale processes, and compare that with the observed GCAPE tendency, and for this we need to know quantities such as the horizontal and vertical advective tendencies of temperature and moisture. In this chapter, the background of the GCAPE algorithm and its subsequent translation to a numerical procedure as developed by RW92 will be elaborated. Following this, Chapter 4 will focus on the source of data we will use for calculating the GCAPE of our system, and then Chapter 5 will be devoted to a detailed explanation of how we go about deriving divergences and advective tendencies from the observational data.

Section 3.1 GCAPE Algorithm

In his initial paper developing the concept of MAE, Lorenz (1978) presented a graphical procedure by which the MAE might be calculated. He also introduced some ideas as to how a numerical procedure might be invented to calculate the MAE with more ease, speed and accuracy. A subsequent paper (1979) outlined more fully how a numerical procedure could be constructed. In essence, the algorithm must somehow be able to take a representative global state of the atmosphere that has been divided up into layers of equal mass (i.e. equal pressure levels), determine the total enthalpy of the arrangement, and then test every possible permutation of the layers (parcels) in the search for the combination that would yield the lowest total enthalpy. As stated before, this process must be carried out adiabatically, conserving the parcel's entropy by keeping its total water content constant, and be able to determine the parcel's final pressure level and virtual temperature in the reference state. Therefore, we need a way to determine the parcel's virtual temperature, entropy and enthalpy at every step of the process.

Randall and Wang (1991) developed such a numerical process to calculate the GCAPE of an atmospheric column. The procedure is based on Lorenz' suggested outline, although slight modifications were made. The steps of the algorithm may be outlined as follows:

1) Divide up a sounding into layers of equal mass (parcels), with the assumptions that the parcels are horizontally homogeneous, and that they contain a unit mass of dry air, w units of water vapor and $\overline{w} - w$ units of liquid water, with $\overline{w}$ being the total water content of the parcel which is held strictly constant.

2) Determine the entropy per unit mass of all parcels and the total enthalpy of the column in the given state.

3) Find the saturation temperature and pressure of each parcel using an iteration procedure, in which the parcel's initial entropy value, conserved throughout the parcel's displacement, is used to converge on a saturation temperature.

4) Move the parcels to a new pressure level. Based on whether or not a particular parcel is saturated at the new pressure level, find its new temperature at that level. If the parcel is unsaturated, the new temperature calculation is straightforward, based on the conservation of the parcel's potential temperature. On the other hand, if the parcel is saturated, an iteration procedure must again be implemented.

5) Determine which parcel should occupy the highest position in the column. This choice is made by identifying the parcel that has the highest virtual temperature amongst all the parcels brought to the uppermost level. Similarly, the parcel with the highest virtual temperature amongst all parcels at the lowest level in the column is identified. Then, the total enthalpy of the column is calculated separately, with each of these parcels in the topmost position and all other parcels shifted down one position. The arrangement that minimizes the total enthalpy of the column is retained, with the appropriate parcel of the two candidates in the highest position. Then whole procedure is repeated to find which parcel should occupy the next highest position, and so on until all the levels have been filled. Once accomplished, this new ordering of the parcels constitutes the reference state in which the total enthalpy of the column has been minimized.

6) Subtract the total enthalpy per unit mass of the reference state from that of the given state to find the amount of GCAPE in the system.

Now we will explain the entire procedure in more detail. Randall and Wang (1992) found that, in order for the numerical procedure to be able to detect GCAPE in a given sounding, the sounding must be divided up into at least 40 layers of equal mass, corresponding to parcels residing at 40 equally spaced pressure levels. This is because in convective situations, the cumulus mass flux has been estimated to be 200-300 mb per day (Yanai et al. 1973; Cheng 1989), which means that approximately 200-300 mb of boundary-layer mass may be transported vertically per day by cumulus towers to the tropopause (with a corresponding amount of subsident mass in the surrounding environment replacing that which is removed by the towers). However, it has been shown (Soong and Tao 1980; Dudhia and Moncrieff 1987; Krueger 1988) in experiments with cloud models that convection can deplete the conditional instability present in a real sounding in a matter of hours, provided, of course, that there is no mechanism operating which would act to maintain the instability. If we assume, then, that conditional instability is released on the order of, say, 2 hours, this would mean that only 1/12 of the 200-300 mb, or roughly 16-25 mb of mass, could conceivably be transported to the tropopause before exhausting the local supply of MAE. Considering that the troposphere is approximately 800 mb deep, it is therefore necessary to divide it up into about 40 parcels, each of which would be 20 mb thick. In this study, for the January-February 1994 data set, a column of air between 950 and 250 mb was divided up into 50 parcels, each of which was a little over 14 mb thick. The column of air for the April 1994 data was chosen to be between 950 and 175 mb, which was again divided up into 50 parcels approximately 16 mb in thickness.

The lowest pressure level was chosen to be 950 mb as this was the lowest level for which there was reliable data from all of the radiosondes. The upper limits of 250 mb and 175 mb were chosen as these represented the average location of the tropopause, based on the temperature readings from the radiosondes, for the January-February 1994 and April 1994 data sets, respectively. Finally, since one of the data sets we used was obtained in the middle of winter, our reason for choosing smaller parcels reflects the fact that convective activity in the Southern Great Plains is not, typically, as vigorous in the winter as it would be in the spring or summer. As a consequence, even less mass can ascend to the tropopause before the local supply of MAE is depleted.

In a moist atmosphere, the thermodynamic state of a parcel may be determined from the equation of state if we know three things about it: for example, its pressure p, its specific volume α and its relative humidity. Or, another choice of variables would be the parcel's pressure, its total water mixing ratio $\overline{w}$ and temperature T. Using this latter set of variables, Lorenz (1979) derived an expression for the calculation of the entropy s of a parcel, which may be obtained from a form of the First Law of Thermodynamics

$$Tds = di + pd\alpha. \quad \textbf{(3.1)}$$

Noting that $di = C_v dT$, we see that

$$Tds = C_v dT + pd\alpha = C_p dT - \frac{R_d T}{p} dp. \quad \textbf{(3.2)}$$

Then dividing (3.2) by T and integrating yields

$$s = C_p \ln T - R_d \ln p + Const. \tag{3.3}$$

Finally, if we include the presence of water vapor and liquid water in (3.3), the expression Lorenz uses, valid for any total mixing ratio is

$$(1+\overline{w})\,s = (C_p + \overline{w}C_{pw})\ln T - R_d \ln(p-e) - \overline{w}R_w \ln e - (\overline{w}-w)\frac{L}{T} + Const \tag{3.4}$$

in which the enthalpy of the dry air is summed with that of $\overline{w}$ units of water vapor and then the excess latent heating associated with the conversion of $\overline{w}-w$ units of vapor to liquid is subtracted off.

The expression for the enthalpy h of each (dry) parcel may be expressed as

$$h = i + p\alpha = C_v T + p\alpha + Const = C_p T + Const. \tag{3.5}$$

Again, including the presence of moisture in vapor or liquid phase, a form of (3.5) that is valid for any total mixing ratio is given by

$$(1+\overline{w})\,h = (C_p + \overline{w}C_{pw})\,T + (\overline{w}-w)\,L + Const. \tag{3.6}$$

Here, the specific heats at constant pressure of dry and moist air, C_p and C_{pw} respectively, are assumed to remain constant as are, of course, the gas constants for dry and moist air, R_d and R_w. Also, for our purposes the constant term is assumed to be zero. The importance of (3.4) and (3.6) is that they are valid for both unsaturated and saturated conditions. Thus, in the former case, the water vapor mixing ratio (w) would be identical with the total water mixing ratio $(\overline{w})$ of the parcel, while in the latter case,

$\overline{w}$ represents the total mixing ratio for both liquid water and water vapor. The total enthalpy per unit mass of the column is then found simply by summing up the enthalpies of the individual parcels and dividing by the total number N of parcels in the column, or

$$h_{tot} = \frac{1}{N}\sum_{k=1}^{N} h(k)\,. \tag{3.7}$$

Once the entropy of each parcel has been established in the given state, as well as the total enthalpy per unit mass, it is necessary to determine the condensation temperature and pressure of each parcel. Different procedures are used, based on whether or not it is saturated, to determine the parcel's new temperature when it is displaced to a new pressure level. Using an integrated form of the Clausius-Clapeyron equation

$$R_w \ln e_s(T) = -(C - C_{pw})\ln T - \frac{L(T)}{T} + R_w \ln e_0, \tag{3.8}$$

and an expression for the latent heat of condensation

$$L(T) = -(C - C_{pw})\,T + L_0, \tag{3.9}$$

an alternate version of (3.4), suitable for finding the temperature of the parcel at the point of saturation (but without condensation having yet taken place), may be expressed as

$$\begin{aligned}(1+\overline{w})\,s = {} & [C_p + \varepsilon(C - C_{pw}) + \overline{w}C]\ln T + (\varepsilon + \overline{w})\frac{L_0}{T} \\ & - R_d \ln\left(\frac{\varepsilon}{\overline{w}}\right) - (\varepsilon + \overline{w})\,[C - C_{pw} + R_w \ln e_0]\end{aligned}, \tag{3.10}$$

where we have made use of the fact that at saturation $e = e_s$ and $w = \overline{w}$. The constants e_0 and L_0 may be determined from (3.8) and (3.9) using the known values of $L(T)$ and e_s for a particular value of T (the algorithm employed here uses $L(T)$ and e_s for $T = 0^{\circ}C$). In (3.10), C is the specific heat of liquid water at constant pressure, and $\varepsilon = \frac{R_d}{R_w}$. Taking the derivative of (3.10) with respect to temperature yields

$$(1+\overline{w})\frac{\partial s}{\partial T} = \frac{[C_p + \varepsilon(C - C_{pw}) + \overline{w}C]}{T} - (\varepsilon + \overline{w})\frac{L_0}{T^2}, \tag{3.11}$$

which we need in the iteration of (3.10) to find the saturation temperature T_s. The saturation temperature is found by making successive approximations according to

$$T_{s,k+1} = T_{s,k} + \frac{(s - s_k)}{\left(\frac{\partial s}{\partial T}\right)_k}, \tag{3.12}$$

where s is the parcel's entropy calculated from (3.4), s_k is the parcel's entropy determined from the kth iteration of (3.10), and $\left(\frac{\partial s}{\partial T}\right)_k$ is given by the kth iteration of (3.11). To "get the ball rolling," the parcel's temperature in the given state is used as the initial guess in (3.10) and (3.11). The new values of s_k and $\left(\frac{\partial s}{\partial T}\right)_k$ are then used in (3.12) to determine a new T_s, and the whole process is then repeated. The iteration stops when the numerator in (3.12) converges within some predetermined criterion. Once T_s has been satisfactorily determined, the saturation pressure may be obtained from

$$p_s = \frac{e_s}{\overline{w}}(\varepsilon + \overline{w}) = e_s\left(\frac{\varepsilon}{\overline{w}} + 1\right). \tag{3.13}$$

Now that the parcel's T_s and p_s have been determined, we are ready to start rearranging the parcels in the column to determine which one should occupy the topmost level at pressure p_a. Each parcel will be brought adiabatically to level p_a, and its new temperature T_{fa} and virtual temperature T_{va} determined there. Then, each parcel will be brought down adiabatically to the lowest pressure level in the column p_b, and its new temperature T_{fb} and virtual temperature T_{vb} likewise computed at this level. Finally, the parcel with the highest T_{va} and the one with the highest T_{fb} will be reserved as possible candidates for the uppermost level, to be determined by a test for the arrangement which yields the lowest enthalpy per unit mass for the entire column. The reason for taking this approach using virtual temperatures is that in the reference state, as we have argued, the arrangement of the parcels should be one that is statically stable. Thus, if a parcel, residing at its reference pressure p_r, is saturated in the reference state, it should have a greater equivalent potential temperature θ_e than all other parcels with reference pressure p_r' where $p_r < p_r'$. Consequently, this parcel will have the greatest virtual temperature when moved adiabatically to the top pressure level p_a in the column in comparison to all other parcels similarly placed at p_a. On the other hand, if the parcel at reference pressure p_r is unsaturated, it should possess the highest potential temperature θ of all parcels with reference pressure p_r', such that it will have the highest virtual temperature when brought down adiabatically to the lowest level at pressure p_b in the column when compared with all other parcels at p_b.

Before we can find the virtual temperature of the parcels, however, we must first determine the actual temperature each parcel will eventually acquire when moved adiabatically to a new pressure level. Obviously, this temperature depends on whether the parcel follows a dry or a moist adiabat; hence the need to first determined the parcel's saturation temperature and pressure. If a parcel is displaced to a pressure that is *below* its saturation pressure $(p_f > p_s)$, then it will be unsaturated and its temperature can easily be found following a dry adiabat to p_f, since the parcel conserves the potential temperature it has at the saturation point. The temperature may be found from

$$T_f = T_s\left(\frac{p_f}{p_s}\right)^{\kappa}, \tag{3.14}$$

where Poisson's constant $\kappa = \dfrac{R_d + wR_w}{C_p + wC_p}$ takes into account the masses of both dry and moist air in the parcel.

However, if it is the case that the new pressure level to which the parcel is moved is *above* the saturation pressure $(p_f < p_s)$, the parcel will be saturated and its new temperature must be found by iteration of (3.4) in a similar fashion to the procedure used to find T_s from (3.10). Taking the derivative of (3.4) with respect to T, we find

$$(1+\overline{w})\frac{\partial s}{\partial T} = \frac{(C_p + \overline{w}C - w(C - C_{pw}))}{T} + \frac{w(\varepsilon + w)L^2}{RT^3}. \tag{3.15}$$

Once again, the initial guess for T_f is the temperature of the parcel in the given state, and then successive corrections are made to T_f according to

$$T_{f,k+1} = T_{f,k} + \frac{s - s_k}{\left(\frac{\partial s}{\partial T}\right)_k}, \tag{3.16}$$

using k iterations of (3.4) and (3.15) to obtain s_k and $\left(\frac{\partial s}{\partial T}\right)_k$, respectively, until a predetermined convergence criterion for $s - s_k$ has been reached.

Once a satisfactory value of T_f has been found it is straightforward to determine the virtual temperature T_v of a parcel at both levels p_a and p_b. To derive an equation for T_v that is valid for any mixing ratio (including liquid water), we start with the definition of specific volume

$$\alpha \equiv \frac{V}{M}, \tag{3.17}$$

where we see that it is defined as the volume per unit mass. Because the presence of liquid water does not alter a parcel's temperature or pressure, the total specific volume of a parcel containing both dry and moist air may be expressed as

$$\alpha = \frac{V}{M_d + M_{\overline{w}}}, \tag{3.18}$$

where, as before, $\overline{w}$ indicates the presence of liquid water and water vapor. Dividing both numerator and denominator in (3.18) by the mass of dry air (M_d), and keeping in mind that the mixing ratio is defined as the mass of water divided by the mass of dry air in a parcel, we see that

$$\begin{aligned}\alpha &= \frac{\alpha_d}{1+\overline{\overline{w}}} = \frac{R_d T}{p_d}\left(\frac{1}{1+\overline{\overline{w}}}\right) = \frac{R_d T}{p}\left(1+\frac{e}{p_d}\right)\left(\frac{1}{1+\overline{\overline{w}}}\right) \\ &= \frac{R_d T}{p}\left(1+\frac{e}{p-e}\right)\left(\frac{1}{1+\overline{\overline{w}}}\right) = \frac{R_d T}{p}\left(1+\frac{w}{\varepsilon}\right)\left(\frac{1}{1+\overline{\overline{w}}}\right)\end{aligned}, \tag{3.19}$$

where the partial pressure of dry air $p_d = p - e$. Then,

$$p\alpha = R_d T_v, \tag{3.20}$$

with the virtual temperature of a parcel under all saturation conditions is given by

$$T_v = T\left(1 + \frac{w}{\varepsilon}\right)\left(\frac{1}{1 + \bar{\bar{w}}}\right). \tag{3.21}$$

What (3.21) means is that, since a parcel of air containing moisture is more buoyant at a particular temperature and pressure than a parcel of purely dry air at the same temperature and pressure, the virtual temperature is the temperature to which the dry parcel would have to be heated in order to attain the same density as the moist parcel at the same pressure. Thus, the virtual temperature gives an indication of the buoyancy of all parcels at any particular pressure. Once the appropriate parcel has been placed at the highest level in the column, all remaining parcels are then moved down by one level and the entire process is repeated to determine which parcel should reside at the next highest level, and so on until all the levels have been filled. An intermediate stage in this process is illustrated in Fig. 3.1 where a parcel originating at a lower tropospheric level in the given state is moved to a higher level in the reference state.

Previously, it was mentioned that the parcels with the highest T_{va} and the highest T_{vb} were reserved as candidates for the topmost position in the column. The key to understanding which of the two parcels with virtual temperatures, T_{va} or T_{vb} should be selected may be shown by considering (3.1), rewritten as

$$di = Tds - pd\alpha, \tag{3.22}$$

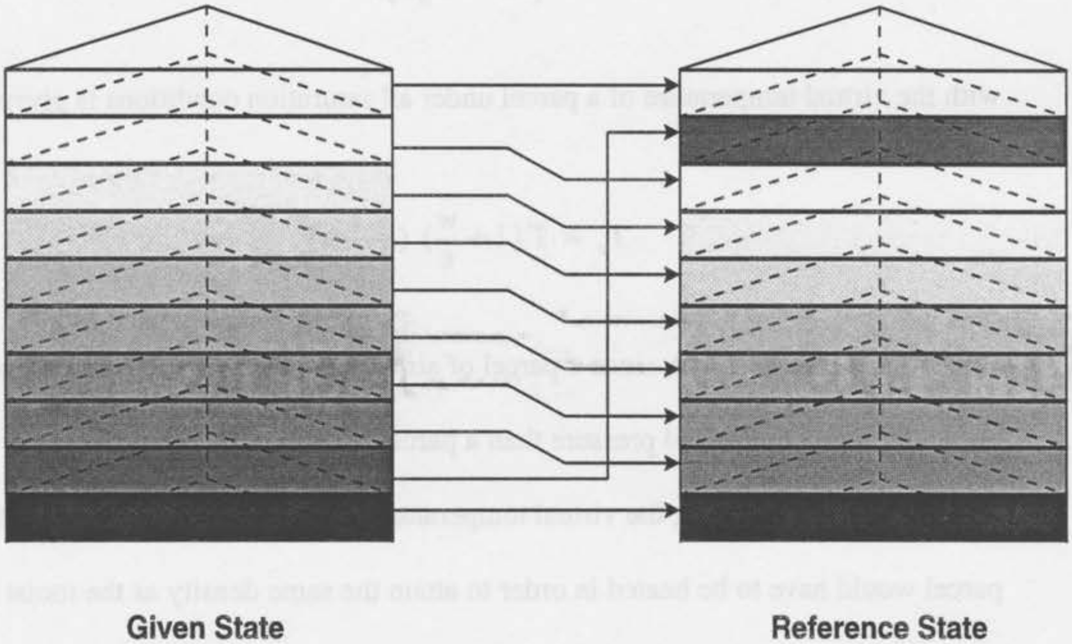

FIGURE 3.1: In an intermediate step, a parcel is moved from the lower troposphere in the given state to the upper troposphere in the reference state to obtain an arrangement in which the total column enthalpy has been minimized. All intervening parcels are shifted down one level to compensate.

which is again a form of the First Law of Thermodynamics. Differentiating (3.5),

$$di = dh - (\alpha dp + p d\alpha) , \tag{3.23}$$

we see that (3.22) becomes

$$dh = Tds + \alpha dp . \tag{3.24}$$

If the atmosphere is subject to adiabatic processes only, (3.24) may be further expressed as

$$dh = R_d T_v \frac{dp}{p} . \tag{3.25}$$

Now, consider a simple two-parcel system with a given state where parcels 1 and 2 are residing at pressure levels p_a and $p_a + \Delta p$ respectively, Δp being some small pressure increment (see Fig. 3.2). If these two parcels are swapped adiabatically to result in a new

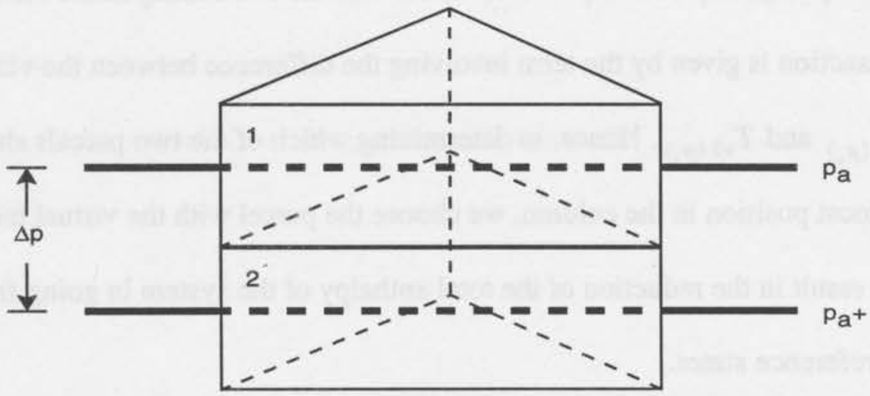

FIGURE 3.2: Simple two-parcel system, with parcel 1 residing at pressure level p_a and parcel 2 residing at pressure level $p_a + \Delta p$, a small increment Δp below parcel 1 in the given state.

atmospheric state, the enthalpy change experienced by parcel 1 as given by (3.25) is

$$\Delta h = h_{1\,(p_a + \Delta p)} - h_{1\,(p_a)} \cong R_d T_{v1\,(p_a)} \frac{[\,(p_a + \Delta p) - p_a]}{p_a}, \tag{3.26}$$

where we have assumed that $T_{v1\,(p_a)} \cong T_{v1\,(p_a + \Delta p)}$ since Δp is small. Similarly, the enthalpy change experienced by parcel 2 is

$$\Delta h = h_{2\,(p_a)} - h_{2\,(p_a + \Delta p)} \cong R_d T_{v2\,(p_a)} \frac{[p_a - (p_a + \Delta p)\,]}{p_a}. \tag{3.27}$$

Then the total enthalpy change in the system is given by summing up (3.26) and (3.27)

$$\begin{aligned} \Delta h_{tot} &= [h_{1\,(p_a + \Delta p)} - h_{1\,(p_a)}] - [\,(h_{2\,(p_a + \Delta p)} - h_{2\,(p_a)}\,)\,] \\ &\cong \frac{R_d}{p_a} [\,(p_a + \Delta p) - p_a]\,[T_{v1\,(p_a)} - T_{v2\,(p_a)}] \end{aligned} \tag{3.28}$$

If the sign of (3.28) turns out to be negative, the implication is that the total enthalpy of the system in the new state is less than that of the given state and thus the new state is in fact the reference state. Since the pressure difference on the right side of the approximate equality in (3.28) will be positive, we see that the controlling factor for the sign of the transaction is given by the term involving the difference between the virtual temperatures $T_{v1\,(p_a)}$ and $T_{v2\,(p_a)}$. Hence, in determining which of the two parcels should occupy the topmost position in the column, we choose the parcel with the virtual temperature that will result in the reduction of the total enthalpy of the system in going from the given to the reference states.

Lorenz (1979) originally suggested that the way to find out which parcel in fact belongs at the highest level is by first placing one parcel there while putting the other at the lowest level, and then calculating the combined enthalpy of the two parcels. Next, reverse the ordering of the parcels and again calculate the enthalpy of the two parcels. The arrangement that produced the lowest enthalpy would then be the correct choice. However, RW92 found that this algorithm needed slight modification as it sometimes produced erroneous results. The procedure they followed instead is to move the parcel with the highest T_{va} to the top of the column, shift all remaining parcels down one level and compute the enthalpy per unit mass for the *entire* column. Then do the same thing, only placing the parcel with the highest T_{vb} at the topmost level. The arrangement that leads to the lowest enthalpy of the *total* system is subsequently selected, and then the entire process is repeated to fill up all remaining levels. It can be seen that this procedure leads to intermediate states where the total enthalpy is kept constant or decreased until the final reference state is reached.

Finally, once the reference state has been found the GCAPE of a particular sounding may be expressed (in units of energy per unit mass) as

$$GCAPE = \frac{1}{N}\sum_{k=1}^{N} [h_G(k) - h_R(k)] , \qquad \textbf{(3.29)}$$

where $h_G(i)$ and $h_R(i)$ are the enthalpies of the ith parcel in the given and reference states, respectively. Fig. 3.3 shows a schematic diagram of the fortran GCAPE computer program used in this study, with Fig. 3.4 - Fig. 3.6 showing more detailed outlines of the subroutines used in the main GCAPE program. In all of these figures, the program or subroutine that is the focal point of the diagram is shown by a black-bordered box on a white background, and the data needed as initial input to the featured program or subroutine is displayed inside a large arrow on a white background. The flow of logic is shown by black arrows leading from one section of the program to the next. Subroutines called by the main program (or main subroutine) are shown in shaded boxes, with the required input data indicated by the arrows leading from the main program (or subroutine) to the shaded box. Similarly, data output by the subroutines are shown on the arrow leading from the shaded boxes back to the main program (or subroutine). Portions of the program that carry out tests or comparisons are indicated by parallelograms, and decisions are indicated by diamond boxes. Final output from the program or subroutine is displayed inside a circle. Note that even though the main program (or subroutine) being featured may have been broken up into two or more parts in the diagrams, this is purely for diagrammatic convenience and should not be interpreted to mean there are different programs being represented. Thus, for example, in Fig. 3.3 the fact that there are two boxes

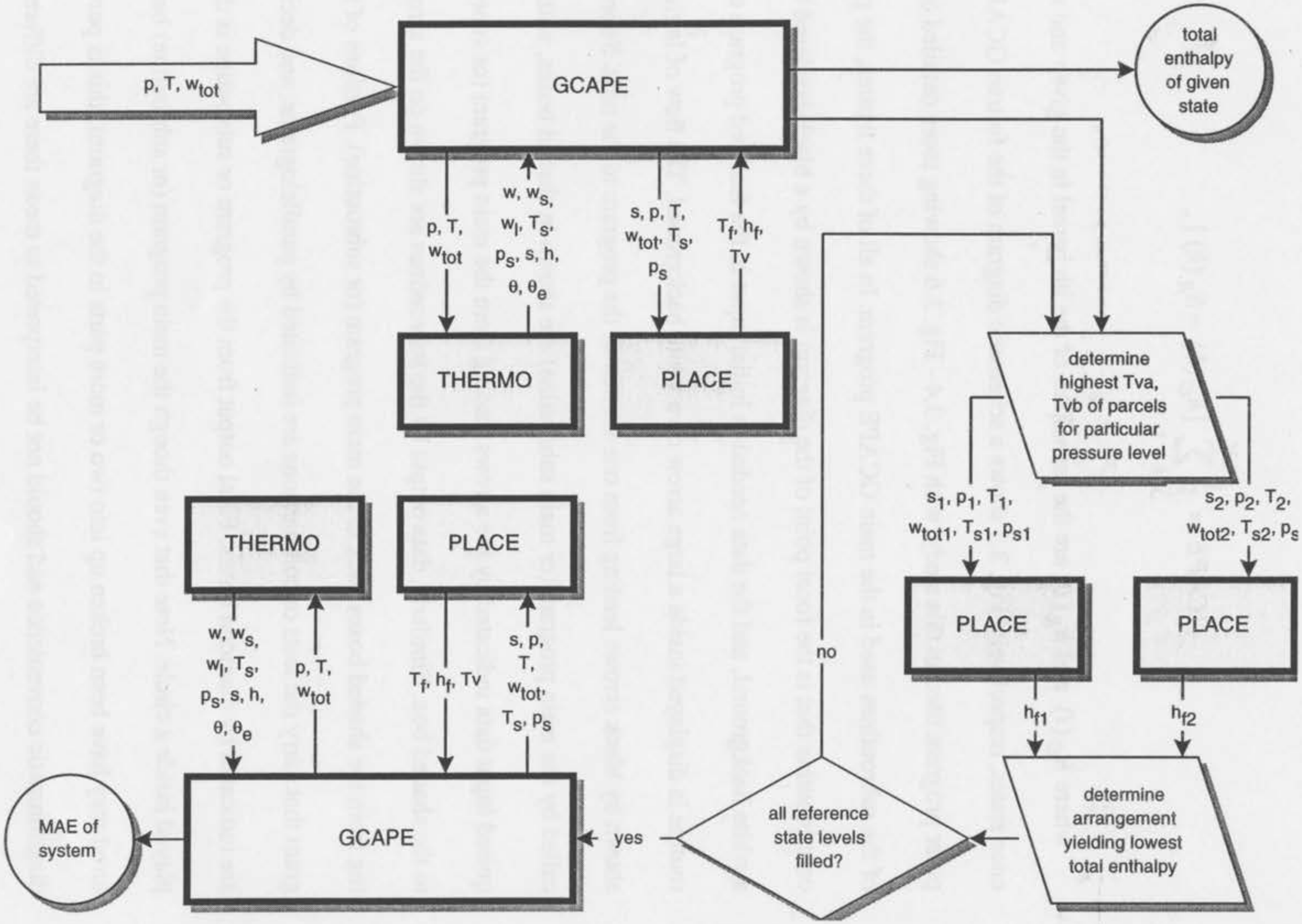

FIGURE 3.3: Schematic outline of program **gcape**: input pressure p, temperature T, total mixing ratio w_{tot}; find the moist available energy of the atmospheric column.

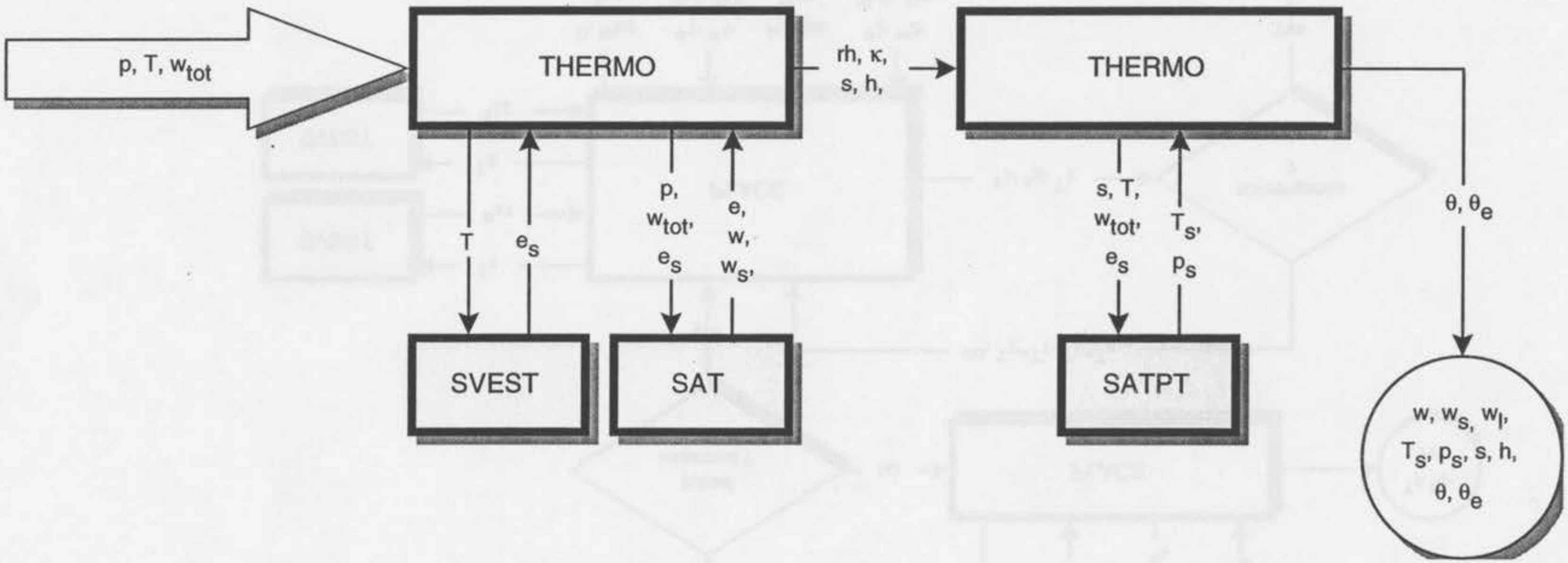

FIGURE 3.4: Outline of subroutine **thermo**: input pressure p, temperature T and total mixing ratio w_{tot}; find relative humidity rh, Poisson's constant for moist air κ, water vapor mixing ratio w, saturation mixing ratio w_s, liquid water mixing ratio w_l, saturation temperature T_s and pressure p_s, entropy s, enthalpy h, potential temperature θ and equivalent potential temperature θ_e for all parcels.

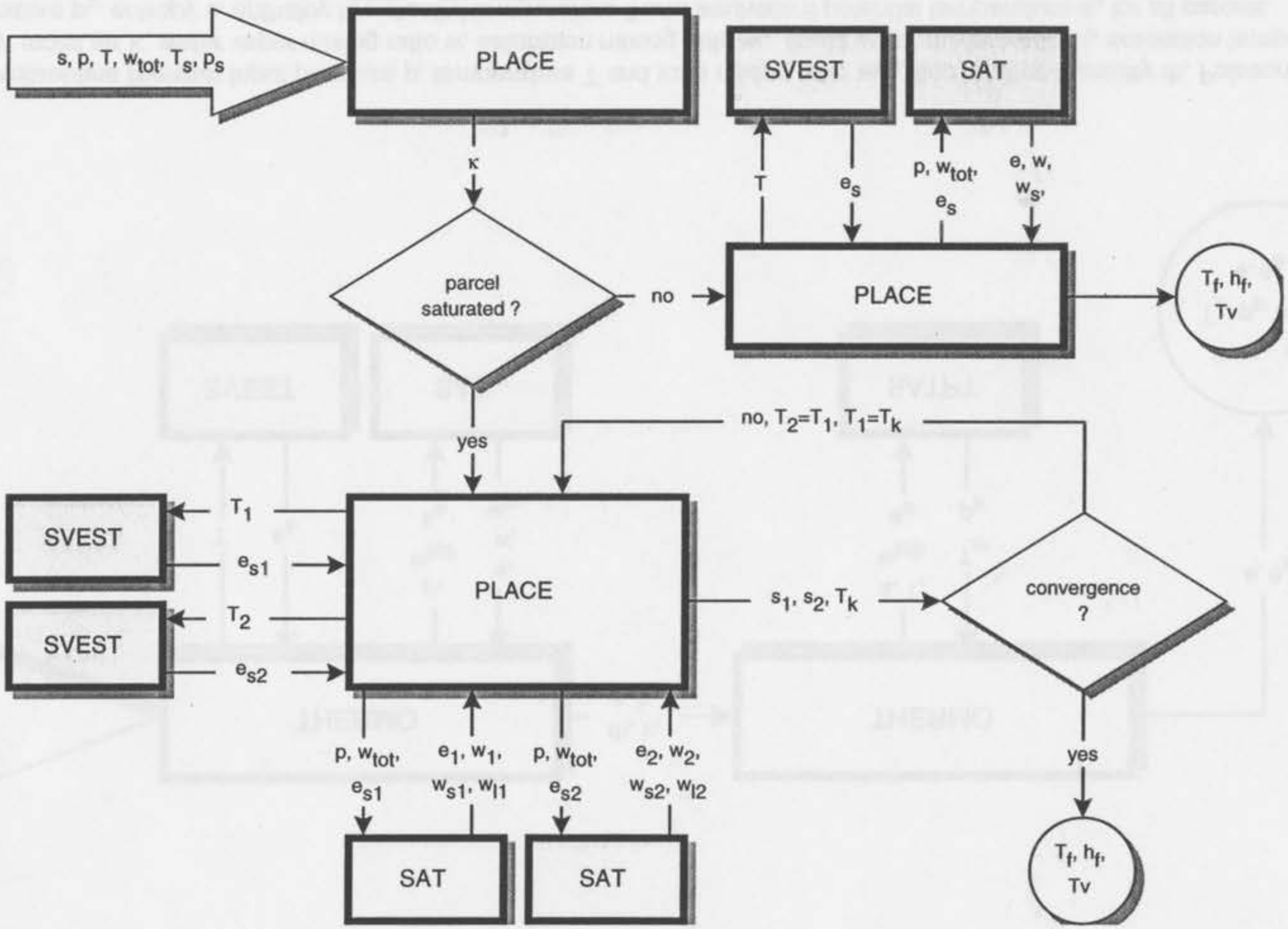

FIGURE 3.5: Outline of subroutine **place**: input entropy s, pressure p, temperature T, total mixing ratio w_{tot}, saturation temperature T_s and pressure p_s; find Poisson's constant for moist air κ, temperature T_f, enthalpy h_f and virtual temperature T_v of a parcel as it is placed at all possible pressure levels.

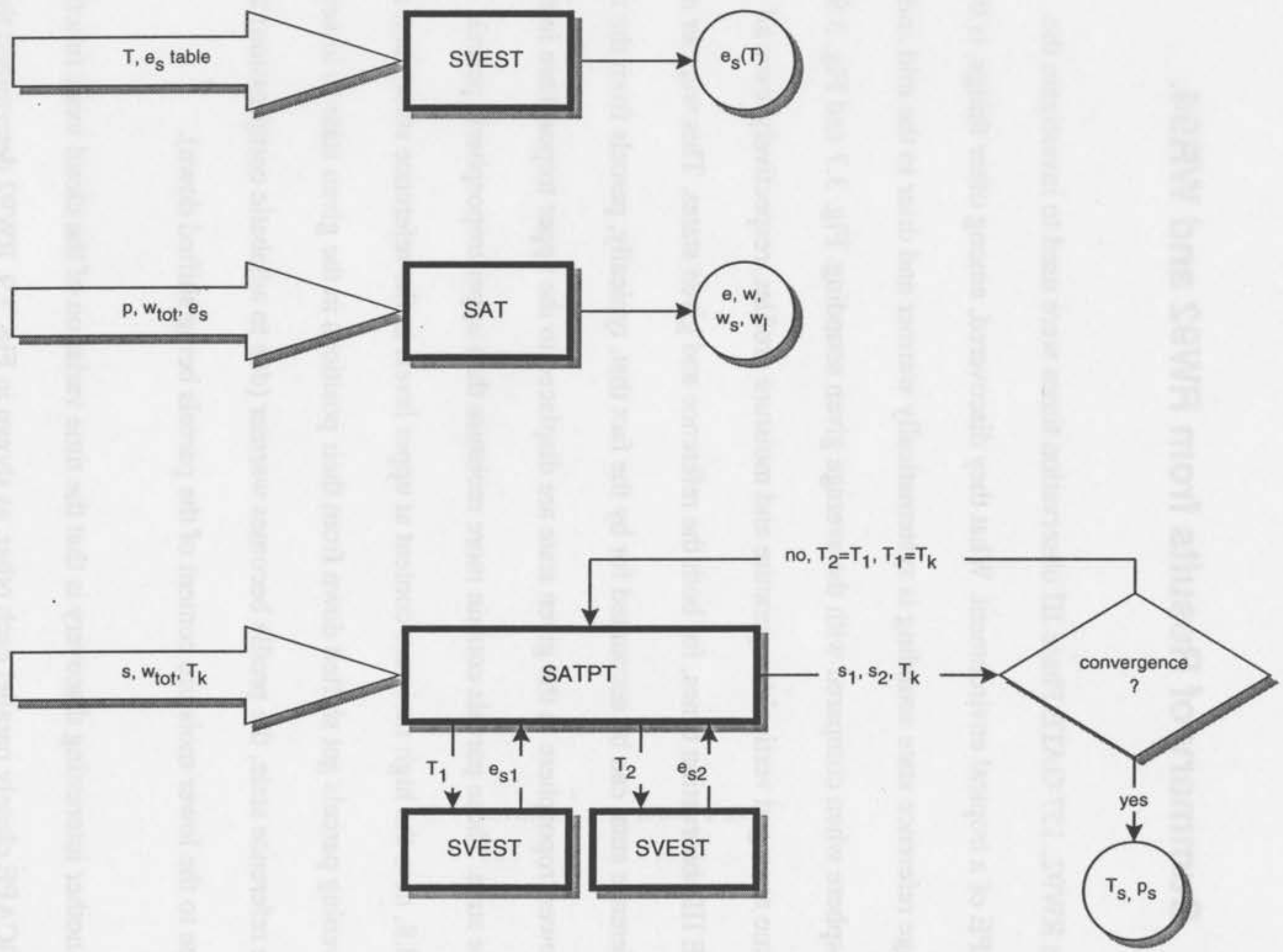

FIGURE 3.6: Subroutine **svest**: input temperature T, and table of saturation vapor pressures e_s; find e_s that corresponds to given T. Subroutine **sat**: input array of pressure levels p, total mixing ratio w_{tot}, and saturation vapor pressure e_s for all parcels; find vapor pressure e, water vapor mixing ratio w, saturation water vapor mixing ratio w_s, and liquid water/ice mixing ratio w_l for all parcels. Subroutine **satpt**: input entropy s, total mixing ratio w_{tot}, and the temperature of the kth iteration T_k; find saturation temperature T_s and pressure p_s for each parcel (temperature of ice used as initial guess).

labelled GCAPE does not mean there are two separate GCAPE programs; in actuality, they are one and the same.

3.2 Summary of Results from RW92 and WR94.

In RW92, 157 GATE Phase III observation times were used to investigate the GCAPE of a tropical environment. What they discovered, among other things, is that the average reference state sounding is systematically warmer and drier in the mid and lower troposphere when compared with the average given sounding. Fig. 3.7 and Fig. 3.8 show the time averaged vertical temperature and moisture profiles, respectively, over all 157 GATE III observation times, for both the reference and given states. This warmer and drier reference state can be accounted for by the fact that, typically, parcels from the mid and lower troposphere in the given state are displaced to the upper troposphere in the reference state. These parcels contain more moisture than upper tropospheric parcels (in Fig. 3.8, note the high moisture content at upper levels in the reference state), and as all intervening parcels get shifted down from their positions in the given state to lower levels in the reference state, the profile becomes warmer (due to adiabatic compression) and drier (due to the lower moisture content of the parcels being shifted down).

Another interesting discovery is that the time variation of the cloud work function and GCAPE closely parallel each other, as shown in Fig. 3.9. RW92 determined the GCAPE using 37 and 100 parcels, and the cloud work function for the case of no entrainment (Arakawa and Schubert 1974) using a single parcel. In the absence of entrainment, the cloud work function may be considered as equivalent with the Convective Available

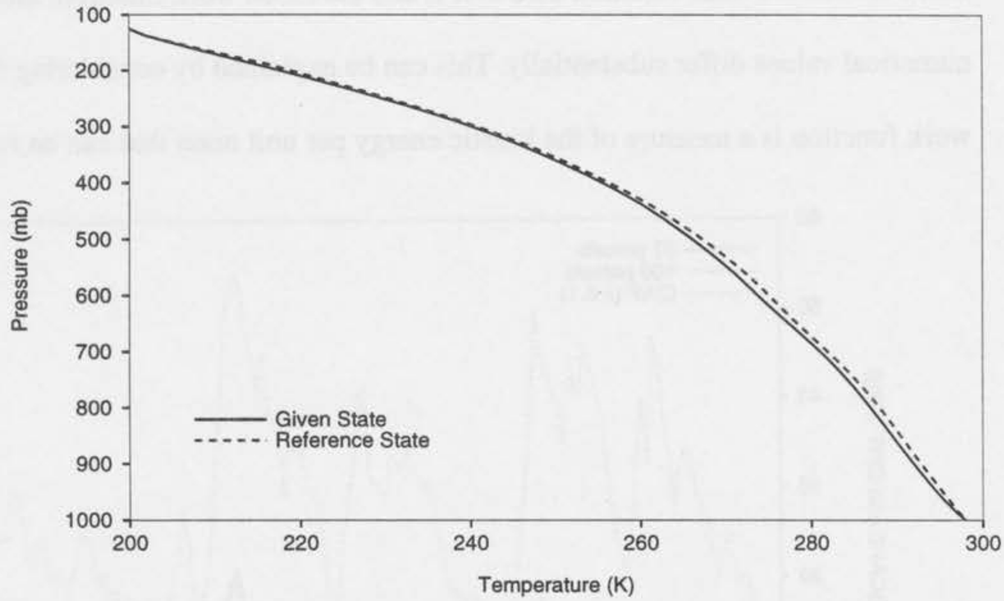

FIGURE 3.7: From RW92: Time averaged temperature profile over all 157 GATE III observation times for both the given and reference states.

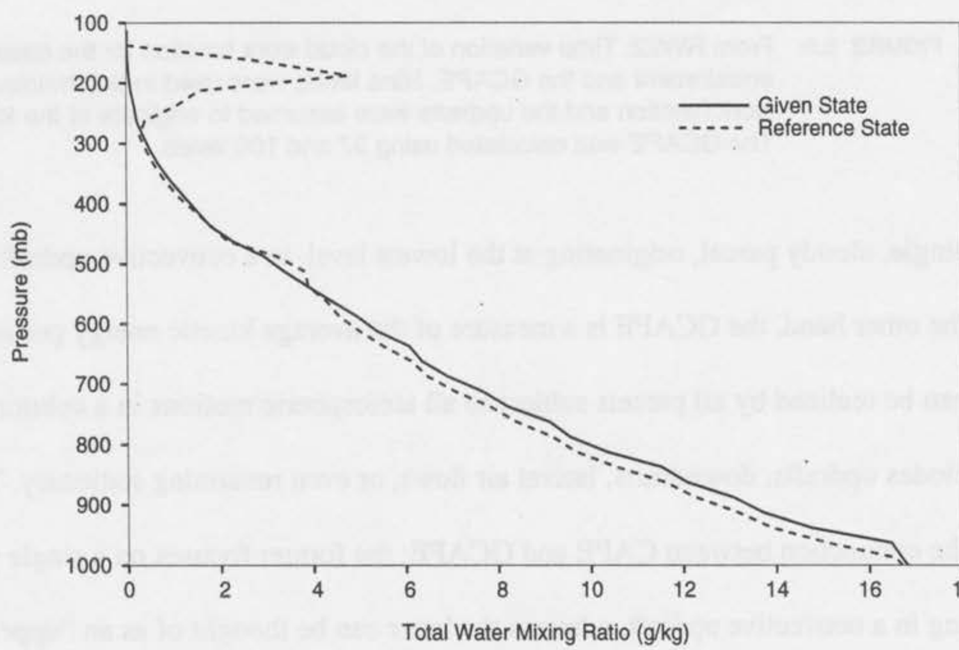

FIGURE 3.8: From RW92: Time averaged total water mixing ratio profile over all 157 GATE III observation times for both the given and reference states.

Potential Energy (CAPE). As can be seen from Fig. 3.9, there is a strong positive correlation between the time variation of GCAPE and the cloud work function, although their numerical values differ substantially. This can be explained by considering that the cloud work function is a measure of the kinetic energy per unit mass that can be realized by a

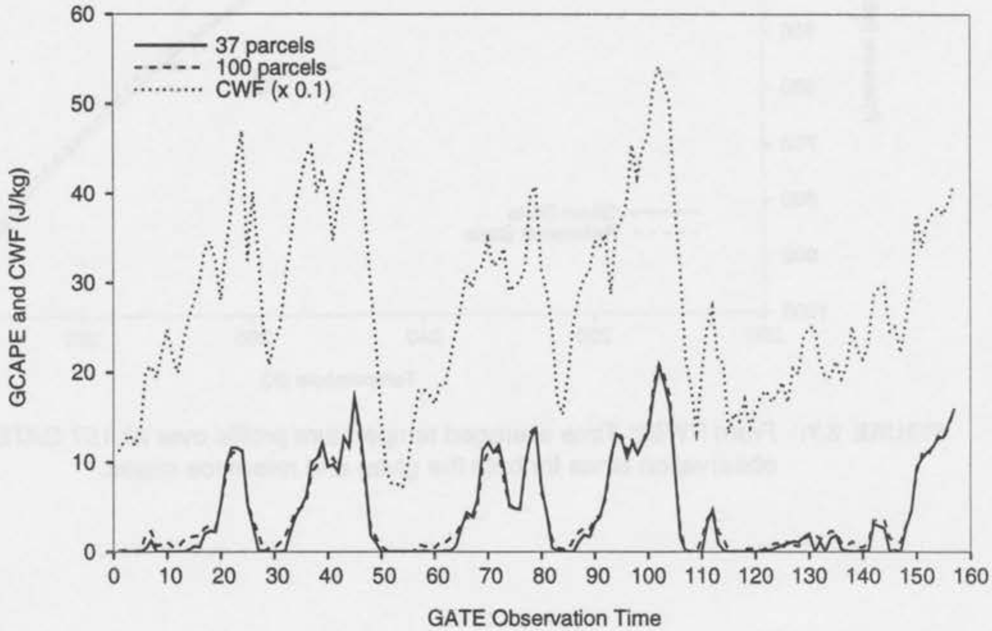

FIGURE 3.9: From RW92: Time variation of the cloud work function for the case of no entrainment and the GCAPE. Nine levels were used in determining the cloud work function and the updrafts were assumed to originate at the lowest level. The GCAPE was calculated using 37 and 100 levels.

single, cloudy parcel, originating at the lowest level, in a convective updraft alone. On the other hand, the GCAPE is a measure of the average kinetic energy per unit mass that can be realized by all parcels subject to all atmospheric motions in a column, which includes updrafts, downdrafts, lateral air flows, or even remaining stationary. This, then, is the connection between CAPE and GCAPE; the former focuses on a single parcel moving in a convective updraft, whereas the latter can be thought of as an "upper limit" on the amount of kinetic energy that could in theory be realized since it is a more realistic appraisal of the kinetic energy per unit mass averaged over all air parcels, taking into account a larger spectrum of air movement. The important point here is that both the CAPE and GCAPE show positive correlation, which means the relatively new GCAPE procedure for detecting MAE responds with the same sensitivity to atmospheric instability as does the more established CAPE method.

In WR94, where the same set of GATE Phase III data were used, an important discovery made was that the time variation of GCAPE from the observed soundings had a correlation coefficient of -.043 when compared with the observed precipitation rate as shown in Fig. 3.10. This finding implies that, using precipitation as an indicator of convective

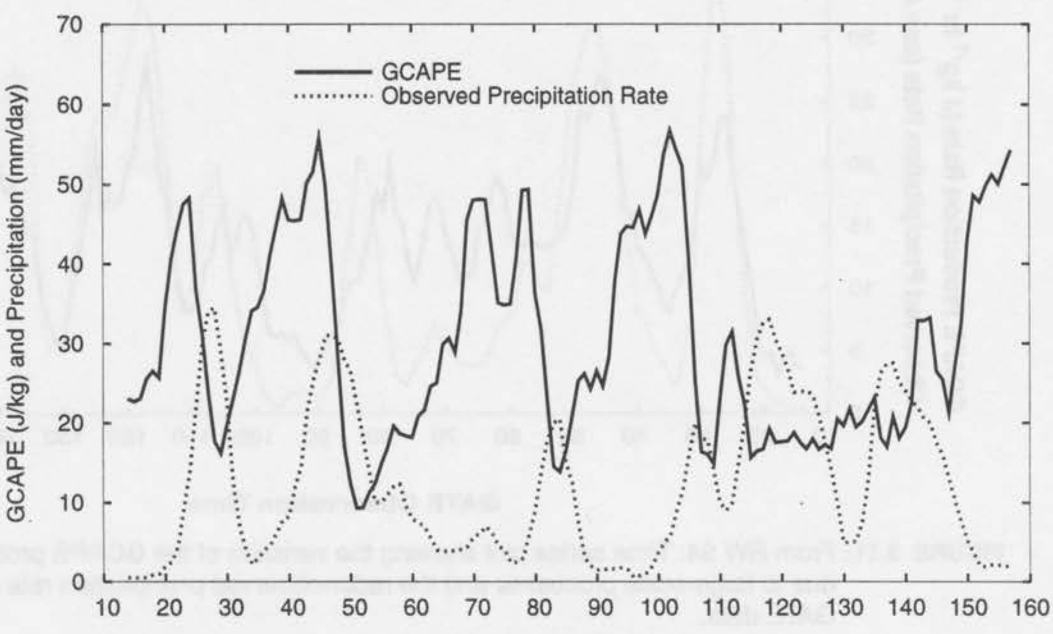

FIGURE 3.10: From WR94: Time series plot comparing the variation in the observed GCAPE with the radar-observed precipitation rate, using GATE data.

activity levels, there doesn't appear to be any evidence of increased convection as the degree of convective instability increases. On the contrary, the convective activity level seems to be somewhat inversely proportional to the amount of convective instability. WR94 interpret this finding as an indication that the actual amount of convective instability is strongly affected by the rate at which cumulus convection depletes the supply of GCAPE.

Next, they again examined the observed precipitation rate, this time comparing it with the rate of GCAPE production by large-scale processes (using the procedures outlined above) and found the correlation coefficient to be positive and rather high (0.79) as Fig. 3.11 shows. The implication here is rather straightforward, and that is cumulus con-

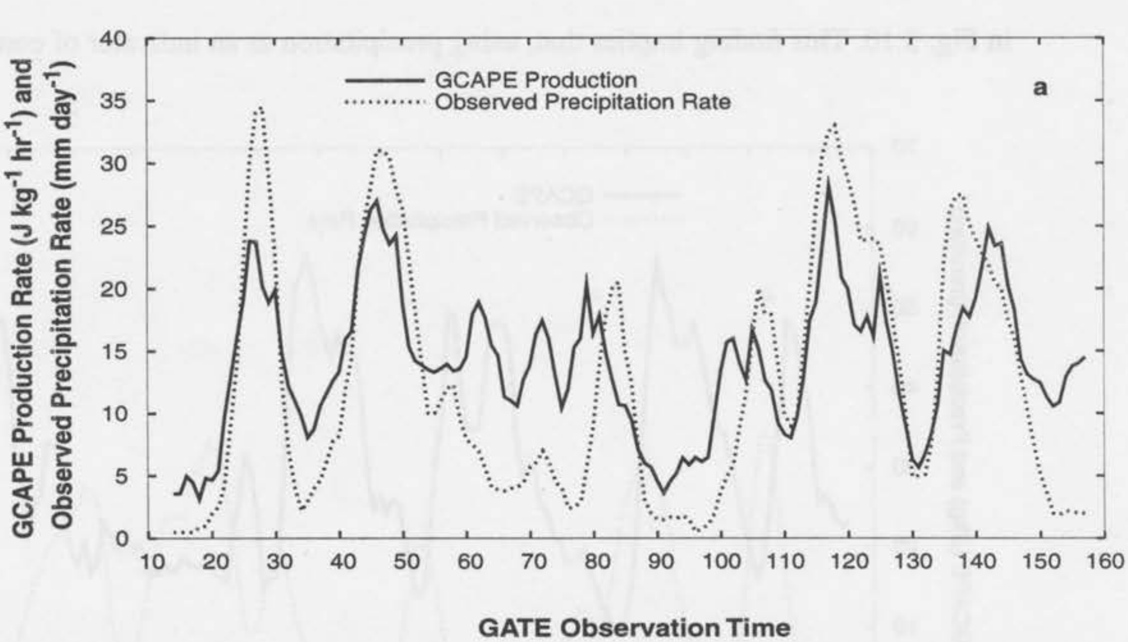

FIGURE 3.11: From RW 94: Time series plot showing the variation of the GCAPE production rate due to large-scale processes and the radar-observed precipitation rate using GATE data.

vection levels are a direct result of (and lag slightly behind) the rate at which GCAPE is being produced by large-scale processes. The difference between this finding and that of the preceding paragraph is that the rate of GCAPE production by large-scale processes is a good indicator of the expected level of convective activity (detectable by precipitation rates), whereas the mere presence of GCAPE itself at any given moment does not necessarily mean the atmosphere is highly convectively unstable as cumulus convection could be rapidly consuming the GCAPE at that time.

The last result from WR94 that bears discussion in connection with this study is the comparison of the observed GCAPE time rate of change with the rate of GCAPE production by large-scale tendencies. Each of the points in Fig. 3.12 represents one observation time. What is apparent from this figure is that the observed GCAPE time rate of change

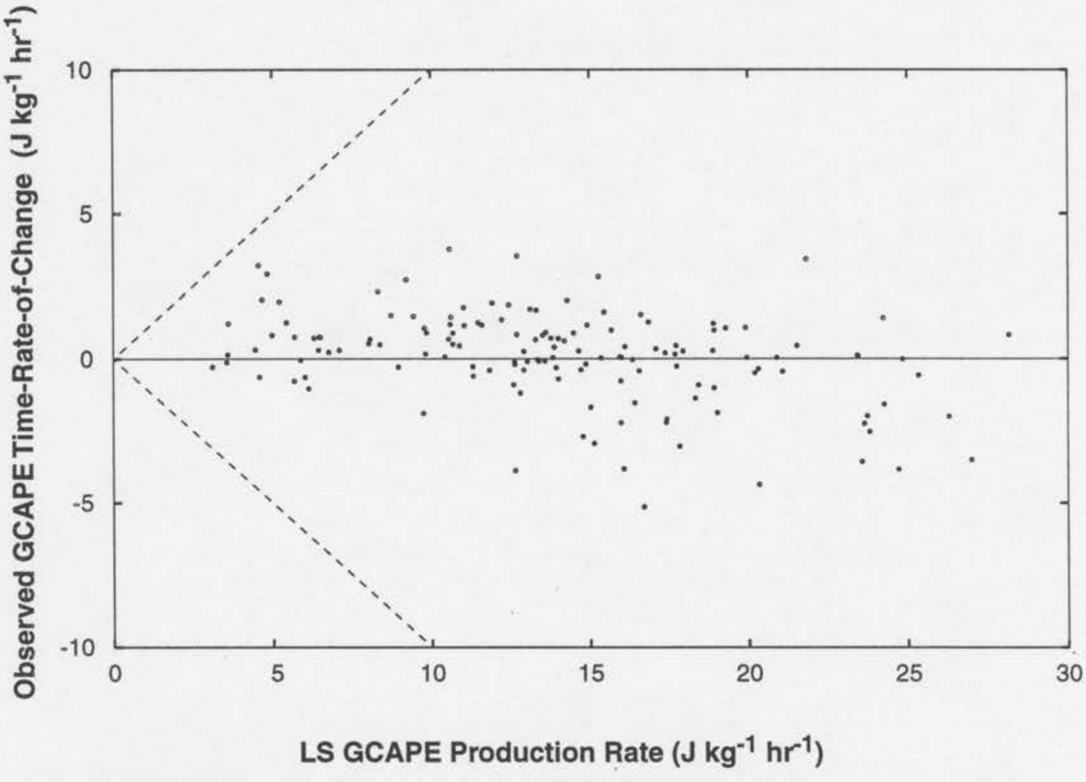

FIGURE 3.12: From WR94: Scatter plot comparing the time rate of change of the observed GCAPE (ordinate) with the GCAPE rate of production by large-scale processes (abscissa). Each of the points represents one GATE observation time.

was consistently much smaller than the rate of GCAPE production by large-scale processes. The implication, then, is that the GCAPE of the atmospheric column is indeed consumed by cumulus convection as fast as nonconvective processes can produce it. This important finding can explain why the atmosphere never strays very far from a state of convective neutrality (represented by the reference state) as suggested by Arakawa and Schubert (1974). This is the hypothesis we will be examining using data from the midlatitudes.

CHAPTER 4

The Atmospheric Radiation Measurement Program

4.1 What is ARM?

Having discussed the GCAPE algorithm and its previous applications in some detail, we now turn our attention to the source of data we will be using to calculate the GCAPE of an atmospheric column. The data has been provided by the Atmospheric Radiation Measurement (ARM) program and an explanation of what ARM is, the motivation for its existence, and the kinds of data that is being collected by ARM is in order.

Climate studies make use of what are known as General Circulation Models (GCMs) in an attempt to understand the processes that influence the earth's climate and, consequently, to evaluate the possible impact of human activity on our climate in the future. One of the major atmospheric science issues of today is the global warming question, and the role that clouds may play in controlling the earth's climate. If indeed the earth's surface temperature does rise over the next few decades, a result of an enhanced greenhouse effect due to the increase of greenhouse gases such as CO_2, then one line of reasoning asserts that the higher surface temperatures will lead to an increase in evaporation from the earth's oceans. Increased evaporation means sending more water vapor into the atmosphere, which might in turn lead to an increase in cloudiness. Now, if this increased evaporation leads to the formation of more low-level clouds, such as stratocumulus, this would tend to favor a decrease in surface temperatures as stratocumulus have a high albedo and thus reflect more solar radiation back to space than do other types of clouds. On the other hand, if the increase in atmospheric moisture leads to the formation of upper-level clouds, such as cirrus, then this would tend to increase surface heating since cirrus clouds are great absorbers of infrared radiation, but are mostly transparent to shortwave radiation. Normal amounts of solar radiation would thus continue to reach the earth's surface while there would simultaneously be an increase in infrared emitted by the cirrus back down to the surface. So, either a negative or positive cloud feedback could result depending on whether stratocumulus or cirrus clouds, respectively, end up being produced in greater amounts.

Since the nature of GCMs is such that they have a limited resolution (i.e. limited number of gridpoints) at which the state of the atmosphere is represented, a way must be found to include factors, such as clouds and radiation, that often occur on scales too small to be "seen" by the GCM and yet play major roles in influencing the earth's climate. Capturing and incorporating the effects of subgrid-scale atmospheric phenomena in terms of resolved variables is called parameterization. Stokes and Schwartz (1994) point out there are many approaches to parameterization which may be thought of as falling along a continuum, from a purely empirical approach on the one end to a theoretical one on the other. Using the former approach, one would empirically parameterize certain phenomena by based on a curve-fit to observed data. Then the parameterizations would be subjected to testing by comparing the output from the model into which they had been incorporated with observational data. In contrast, the theoretical approach involves a prior understanding of the physics behind the particular atmospheric phenomena to be described, deriving a suitable simple model depicting the physics, and then similarly testing this model as a parameterization by comparison of the model output with observed data.

There are, however, drawbacks to both these approaches. The large number of types of situations requiring parameterization make the empirical approach difficult to implement, while the physical approach can be hampered by an incomplete understanding of the processes involved. Despite the potential shortcomings of the physical parameterization process, it is this approach that is being used with increasing frequency as a means of representing certain atmospheric phenomena in GCMs.

In the quest to improve the performance and credibility of the models being used to study and predict climate change, two important, basic atmospheric processes are the focus of current parameterization efforts: 1) atmospheric radiative transfer; and 2) the mechanisms involved in cloud formation, duration and dissipation, as well as the capacity to predict the types of clouds that will be formed with their corresponding radiative properties. It is essential that these processes be accurately depicted in GCMs because of the critical role that they play in the earth's radiation budget (Ramanathan et al. 1989), as well as the possibility that cloud properties may change as the climate changes. Therefore, a thorough understanding of atmospheric radiation and its interaction with cloud processes is of utmost importance.

Whatever the choice of parameterization schemes, the evaluation of the parameterization by comparison with observational data plays a crucial role in the testing phase, as alluded to above. Thus, the ARM program has the development and testing of radiation and cloud parameterizations as its overall goal, in an effort to improve on the understanding of processes that affect atmospheric radiation and the description of these processes in climate models. This goal is to be accomplished by the direct comparison of model calculations with a comprehensive set of field observations, obtained under a wide variety of meteorological conditions. The program is supported by the U.S. Department of Energy (DOE) and is an outgrowth of the United states Global Change Research Program (USGCRP; CEES 1990). Accordingly, ARM has been designed to meet the needs of scientific inquiry into areas of major concern, such as the role of clouds, identified by the USGCRP in its objective of understanding climate and hydrological systems.

The main objectives of ARM as outlined by Stokes and Schwartz may be broken down into two areas of activity:

1) Relating observed radiative fluxes in the atmosphere to the atmospheric temperature, composition and surface radiative properties. Composition here specifically includes the presence of water vapor and clouds, while the radiative fluxes are to be spectrally resolved and observed as a function of time and space.

2) Developing and testing parameterizations that describe atmospheric water vapor and clouds, as well as the surface properties affecting atmospheric radiation. This testing is to be carried out through the comparison of relevant prognostic variables from the model with real atmospheric data.

The ultimate objective is the incorporation of these parameterizations into GCMs. It is thus that ARM intends to meet the objective established by the DOE to improve GCMs and provide reliable simulations of regional and long-term climate change in response to increasing greenhouse gases.

There are many ways to parameterize atmospheric processes such as radiative transfer and cloud life-cycles, and, as has been stated, one of the goals of ARM is to sift through these parameterizations to evaluate their effectiveness at describing these processes and suitability for use in a GCM. Thus, a reliable source of meteorological data, obtained under a wide variety of atmospheric conditions, is an important part of this operation. This data would be used in several capacities; to supply input for initialization of the models, to serve as a check for the output of the models in predictive mode, and also to provide forcing for the models. Furthermore, the data should be approximately representative of the areal extent covered by a GCM grid cell, which is typically on the order of 200 km on a side. Finally, it was decided that this observational data should be made available on a continual basis, over the span of several years, while staying within labor and financial constraints. To meet each of these facets of the ARM program, it was decided the labor should be divided up into two spheres of activity. Thus, the branch of ARM responsible for carrying out the research phase of the project is the Science Team. Their duties encompass the actual process of development and testing of models and parameterizations, as well as instrument development and testing. On the other hand, the Cloud and Radiation Testbed (CART) personnel oversee the set-up and maintenance of the instruments at the observation site, collect and process the raw data, and check to see that the experimental requirements of the members of the Science Team were being met. An explanation of the CART site setup will now be given.

The function of a CART site is to provide the source of field data necessary to meet the goals of the Science Team. As previously mentioned, these goals essentially encompass

1) Describing the radiative energy flux profile of the atmosphere (under clear sky and cloudy conditions).

2) Understanding the processes governing the flux profile.

3) Parameterizing these governing processes for use in GCMs.

Therefore, an empirical data set is required for initializing and running the models, and then comparing the model results to observed data. This data set needs to include both longwave and shortwave radiation fluxes; turbulent fluxes of heat, moisture and momentum; the distribution of radiatively significant particulates, aerosols and gases; cloud types, composition and distribution; a complete thermodynamic description of the air mass; surface fluxes of heat and moisture; and finally any processes (such as precipitation/evaporation or generation of cloud condensation nuclei) that might have an impact on these variables. Additionally, an efficient ingest and archival system for the data streams is needed for distribution of ARM data to the scientific community. An analysis of the Science Team needs, which is referred to as General Measurement Strategies (GMS), was drawn up to specifically address these issues, and has served as a guide for designing and selecting the appropriate CART site.

With the objective of studying radiation transfer in the atmosphere and atmospheric processes that influence it, the choice of a CART site was to be made in light of several radiation-influencing factors, such as latitude/longitude, altitude, terrain/surface, cloud frequency/type, precipitation, temperature and humidity. Once several potential sites had been identified, three additional criteria were established in the GMS to help narrow down the pool of CART site candidates. The first of these criteria was that the site should exhibit a great temporal variability in terms of weather conditions. Second, ideally the CART site would experience as much atmospheric variation as possible while remaining logistically accessible; i.e. the region would be capable of supplying the roads, power, communications and living accommodations necessary to keep such a site functioning. At the same time, the CART site should be located far enough away from urban areas so that it would not be negatively influenced by urban-generated factors such as air pollution or the heat-island effect. Lastly, if at all possible, it should be situated in proximity to other agencies or projects similarly involved in atmospheric measurements so that constructive interaction might take place.

Although the ARM project calls for the eventual installation of three CART sites at diverse locations around the globe, geographically and climatologically speaking, there is currently only one CART site in operation, and it is located near the town of Lamont in northeastern Oklahoma. This is the site that has served as the source of data for the present study. The Southern Great Plains (SGP) region of the United States was chosen for this prototype CART site since it meets many of the requirements outlined above. Due to its interior location, it has a continental-type climate and thus meets the criterion of high seasonal ranges in temperature, humidity, and precipitation. Additionally, it is well suited for the purposes of this study since the SGP region experiences deep and vigorous convection in the spring and summer seasons. Further, the terrain is spatially homogeneous which reduces complexities introduced by discontinuities such as mountains and coastlines in model testing. It is not far from urban areas, yet far enough to be relatively undisturbed by the problems associated with them. Finally, there are several on-going projects which offer the possibility of beneficial collaboration in the region: 1) the National Oceanic and Atmospheric Administration (NOAA) is currently in the process of installing a dense network of wind profilers in this area, called the Wind Profiler Demonstration Network, which could be quite advantageous for several ARM experiments, 2) the Global Energy and Water Cycle Experiment (GEWEX) is undertaking a project in the area, and 3) the Tropical Rainfall Measuring Mission (TRMM) has a satellite orbiting over the SGP site which is expected to provide important information concerning relevant physical and radiative variables, 4) the new generation of doppler radar operating sites, installed by the National Weather Service (NWS).

The CART site itself consists of a central facility, an auxiliary station network, an extended observation network, and boundary facilities as shown in Fig. 4.1. The observations at the central facility aim to construct as detailed a characterization of the atmospheric column above the facility as possible. Consequently, more data is collected at the central facility than elsewhere on the CART site, with instruments installed there taking measurements of upwelling and downwelling radiation, cloud fractional coverage, cloud-base altitude, liquid water path, local surface reflectance, temperature and emissivity. Additionally, radiosondes provide atmospheric temperature, humidity, wind speed and direction above the central facility.

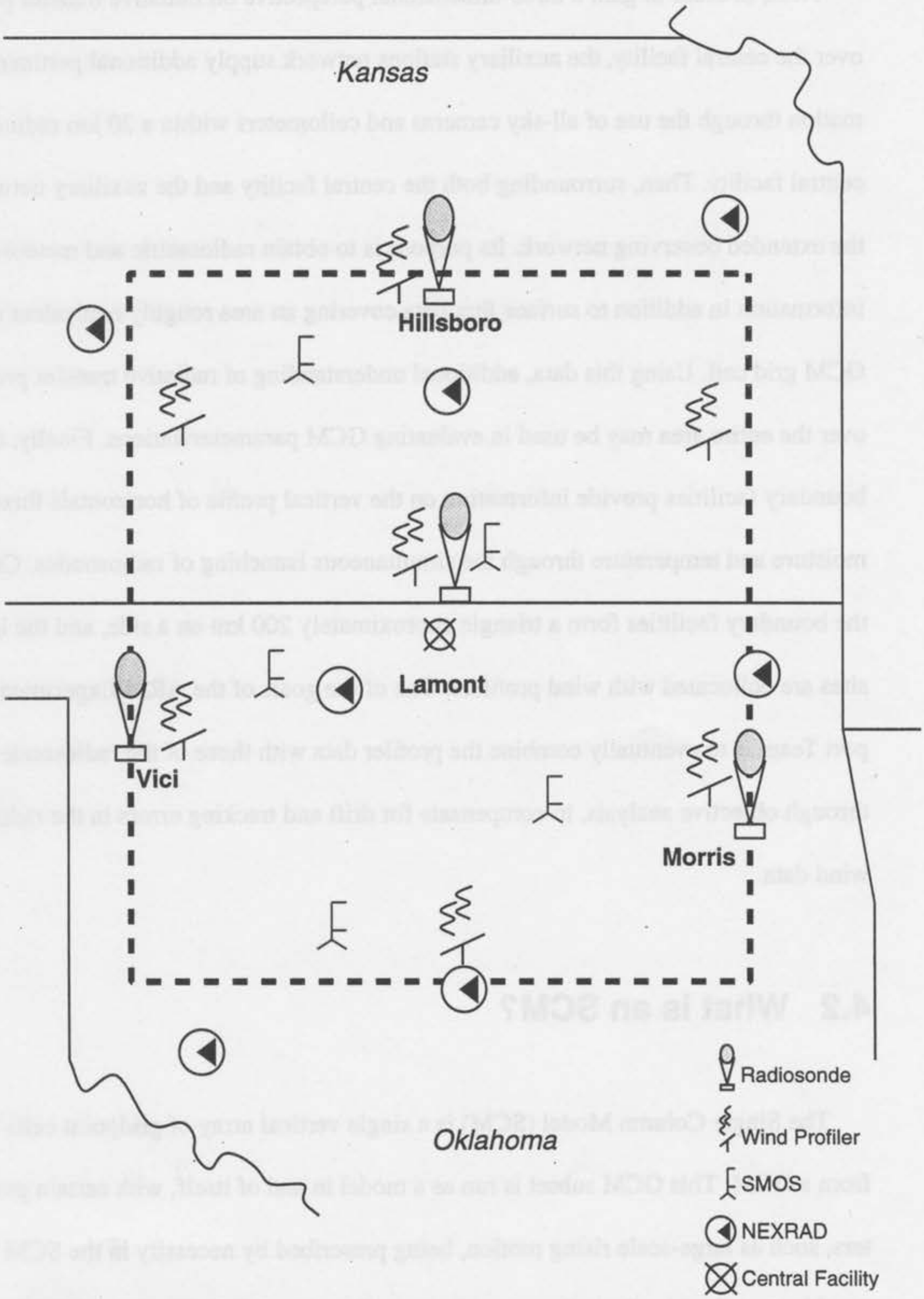

FIGURE 4.1: Diagram showing the layout of the SGP CART site, composed of the Central Facility, extended observing network and boundary facilities. Also shown are the locations of NEXRAD, the new generation of doppler radar being installed by the NWS.

Next, in order to gain a three-dimensional perspective on radiative transfer processes over the central facility, the auxiliary stations network supply additional pertinent information through the use of all-sky cameras and ceilometers within a 20 km radius of the central facility. Then, surrounding both the central facility and the auxiliary network is the extended observing network. Its purpose is to obtain radiometric and meteorological information in addition to surface flux data covering an area roughly equivalent to a GCM grid cell. Using this data, additional understanding of radiative transfer processes over the entire area may be used in evaluating GCM parameterizations. Finally, the boundary facilities provide information on the vertical profile of horizontals fluxes of moisture and temperature through the simultaneous launching of radiosondes. Currently, the boundary facilities form a triangle approximately 200 km on a side, and the launch sites are collocated with wind profilers. One of the goals of the ARM Experiment Support Team is to eventually combine the profiler data with those of the radiosondes through objective analysis, to compensate for drift and tracking errors in the radiosonde wind data.

4.2 What is an SCM?

The Single Column Model (SCM) is a single vertical array of gridpoint cells taken from a GCM. This GCM subset is run as a model in and of itself, with certain parameters, such as large-scale rising motion, being prescribed by necessity in the SCM (this would naturally arise from the governing equations in a full 3-dimensional GCM). However, it is this very feature makes the SCM a convenient vehicle for testing a particular parameterization scheme. This is because certain atmospheric processes can be studied in an SCM which would otherwise be difficult or impossible to isolate in the 3-dimensional GCM. Randall et al. (1991) investigated in the observed diurnal precipitation oscillation over certain oceanic regions, and made use of prescribed vertical motion fields in an SCMs to reach their conclusion.

In addition to the prescribed boundary conditions mentioned above, the types of data needed as input for an SCM also include initial values of the prognostic variables within the cell, such as temperature, humidity, wind velocity, cloud fraction, planetary boundary layer depth, radiation field, precipitation and soil moisture. Other boundary conditions besides large-scale vertical motion are thermodynamic variables at the lateral boundaries, surface emittance and reflectance at the lower boundary, and the top of the atmosphere solar flux. The connection with the CART site is now evident: it supplies the necessary data for the boundary and initial conditions to run an SCM, and for parameterization evaluation by comparison with the actual state of the atmosphere through tracking the evolution in time of the model's prognostic variables. Further, since the midlatitude atmospheric data we needed for this study is the same type of data needed to operate an SCM, it seemed reasonable to use the data supplied by the SGP CART site.

4.3 What is an IOP?

Under normal operations, the ARM observational strategy calls for continuous atmospheric observational data to be provided by the CART site. In addition, supplemental data is to be provided during time spans of limited duration known as Intensive Observation Periods (IOPs). Examples of the kinds of data that are provided on a continuous basis would be upwelling and downwelling solar and terrestrial radiation; column-integrated precipitable water vapor and liquid water path; brightness temperature; cloud cover, type, and elevation; sensible and latent heat flux at the surface, plus surface temperature, pressure, precipitation, soil moisture, wind speed and direction. Much of these data are provided by remote sensors at the central facility as well as the extended/auxiliary/boundary network locations. However, the supplemental data will be furnished by observations that are too expensive to be implemented continuously and/or require additional personnel to be performed (such as frequent radiosonde launches). These observations will instead be conducted periodically throughout the year during IOPs according to a schedule agreed upon by the Science Team.

The purpose of an IOP is two-fold: 1) IOPs will be used to calibrate and verify the validity of data gathered by the remote sensing instruments, and 2) they will provide additional data needed by the Science Team to perform certain experiments or to test more detailed models of atmospheric processes. The needs of this study fall into the latter category as we wish to examine large-scale advective forcing in an atmospheric column to establish GCAPE quasi-equilibrium. This necessitates wind and thermodynamic information throughout all levels in the column (from the boundary facilities as well as the central site) at frequent and regularly-spaced intervals. Consequently, we have made use of data gathered during the IOP conducted in January-February 1994 and April-May 1994, in which radiosondes were launched at the central and boundary facilities every three hours for the three-week duration of the IOP instead of the normal mode launch schedule (once per day) carried out at the central facility.

4.4 How does this Study fit into ARM?

Since one of the goals of the ARM Science Team is to provide the science community with a source of reliable, accurate atmospheric data from the CART site for research and experimentation, it is crucial that the data collected during the IOPs be subjected to scrutiny and testing before dissemination. This study fits into the ARM project by virtue of the fact that it is one of the first studies to make extensive use of the new data being made available by the SGP CART site. Although our main goal is to investigate the GCAPE equilibrium hypothesis in midlatitudes, a by-product of this endeavor is that the SCM IOP data is being used, and consequently inspected for accuracy and reliability. Additionally, our work relates to atmospheric convection which is an essential agent in cloud formation processes and the vertical redistribution of water vapor. Thus, important components of convection, such as vertical velocity, have been computed as a part of this study. These components are also needed to run an SCM and it is our intention to carry this out as a future project.

In a sense, then, this study dovetails in with the testing phase of the IOP data. Foremost in this testing phase is checking on the proper functioning of the data collecting instruments while simultaneously assuring that the data is being ingested correctly. The CART site itself is responsible for carrying out these checks, and our study is not directly involved at this stage. Where it does begin to have a bearing is at the next stage, when the data reaches the ARM Experiment Support Team. As related above, I personally visited the Lawrence Livermore National Laboratories, where the January-February 1994 SCM IOP data was being processed. Initially, simply consulting weather maps and NWS observations for the time in question served as a means of checking on the plausibility of the raw data. Then, once the data had been satisfactorily collected and given an spot check, there was the whole phase of data processing in which the derived fields were produced. The check on this phase entailed a verification of the algorithms employed and the mathematics used to construct them. Again, some knowledge of what the atmosphere was doing at the time of the data collection served as a plausibility check. It was also important to have some idea of what reasonable values would be expected for such derived variables as divergences and advective tendencies, given the observed meteorological conditions. Once these issues were addressed to everyone's satisfaction, it was then possible to proceed with the investigative portion of this study.

As an aside, not only was the proper functioning of the algorithms and equipment to be confirmed, but also our analysis of the data produced by the SGP CART site raised questions as to whether or not the current arrangement of wind profilers and balloon soundings, as presented below, is capable of furnishing the needed data. Indeed, considerable concern was voiced at the 1994 ARM Science Team Meeting held in Charleston, SC, regarding the fact that only three balloon sounding facilities were located on the perimeter of the CART site during both the June 1993 and January-February 1994 IOPs. At a special breakout session during the conference, devoted solely to the deroulement of the IOPs, it was pointed out that the ARM plan had originally called for six balloon sites to be collocated with the wind profilers, but due to budget constraints this number was cut down to three. Given that these three sites were situated approximately 200 km from each other, one issue that this sparsity of data collection sites raised was that of spatial aliasing. In other words, the data was being sampled at points too widely spaced to adequately identify mesoscale and microscale events; one good downdraft at a particular site could seriously skew divergences and other values with the current triangular arrangement of sounding locations. The point was made that increasing the number of sounding sites from three to four on the perimeter would greatly improve the quality of the raw data in terms. It was decided that four radiosondes would be deployed around the perimeter of the CART site as soon as logistically feasible for subsequent IOPs, although there was not enough time to accomplish this in time for the April-May 1994 SCM IOP.

To sum up, in terms of the ARM program, the intention of this study was to examine the raw data so that any instrumentation malfunctions at the CART site might be detected and rectified, and any potential errors in the algorithms used by the ARM Experiment Support Team for calculating the derived fields identified and resolved before the data was made available on a general basis. In addition, through the derivation of certain quantities such as vertical velocity, and heat and moisture budgets, it is hoped that this study may shed some light on the usefulness of the raw data collected by the CART site, and on a more general level, ascertain to what degree the goals of the ARM SCM IOP project are being met.

CHAPTER 5

SCM IOP Data

5.1 New Data Source

We are now ready to examine some actual data obtained from ARM during an IOP and observe how it is put to use. As previously stated, not only do we need pressure, temperature and moisture from a sounding to evaluate the GCAPE, we also need to know the horizontal and vertical temperature and moisture advective tendencies if we wish to investigate the production rate of GCAPE due to large-scale processes. Consequently, these advective tendencies require knowledge of the horizontal and vertical wind fields. In addition, as long as the advective tendencies are being calculated, it is instructive to use them for evaluating what is referred to as the apparent heat source Q_1 and moisture sink Q_2. These quantities tell us about atmospheric heat and moisture budgets, which will provide some insight into the convective nature of the atmospheric column at the time of the observation. For example, Q_1 gives information concerning the atmospheric heat source in terms of latent heating, radiational heating and the vertical transport of sensible heat. Now, these terms are difficult to measure directly, but it is possible to calculate them instead by using terms that involve horizontal and vertical temperature advection as will be explained in more detail below. Therefore, we will begin with an explanation of how the new SCM IOP data is collected and processed. Then the algorithms used in the actual calculation of vertical motion and advective tendencies will be outlined. Finally, to wrap up the chapter, a short detour will elucidate some of the problems encountered in the data collection and processing.

5.1.1 Ingest of Raw Data

During the 21 January-11 February 1994 SCM IOP, atmospheric soundings were taken approximately every three hours by balloon-borne radiosondes. The radiosondes released at each of the perimeter sites were set to measure and record the temperature, pressure and relative humidity of the atmosphere every two seconds during their ascent. In the lower troposphere, the balloon ascent rate was about 5 m s^{-1} (Bluestein, 1992), so that in the 2 seconds between measurements the radiosondes travel a vertical distance of approximately 10 m. This distance corresponds to a measurement taken about every millibar of pressure traversed in the lower troposphere. The ascent rate slowly decreases, however, with increasing height as a balloon loses buoyancy, such that in mid-tropospheric levels the sondes rose at about 2.5 m s^{-1}, slowing to 1-2 m s^{-1} as they passed through the tropopause. These ascent rates would correspond to data being recorded at roughly 0.5 mb increments in the mid-troposphere, decreasing to 0.1 mb in the tropopause region. Thus, for a typical launch, a radiosonde would make on the order of 2500 measurements as it travelled from the surface to tropopause and beyond.

The u- and v- wind components, on the other hand, cannot measured directly by the sondes, but were instead calculated from the azimuth angle, elevation angle, and slant range of the balloon relative to the launch site as recorded by the balloon tracking system. These data were then converted to wind direction and speed, in addition to the individual wind components, by the National Weather Service's Vaisala software in the micro-computers at each of the launch sites where the data were being ingested. The latitude and longitude of the balloon's position were subsequently derived based on the u- and v- wind components.

5.1.2 Processing of Raw Data

5.1.2.1 Layer Averages and Slab Averages

The intent of the ARM Science Team was to make this data available to the scientific community as an empirical basis for research, and it was decided that all data derived from the SCM IOP should be evaluated along isobaric surfaces. Thus, the column of air formed by the radiosonde triangle was divided up into layers of equal pressure, with 1050 mb and 150 mb being the maximum and minimum pressure levels respectively. In actuality, these levels represent the midpoint average pressure of a "slab" of air 25 mb thick. Given that the radiosondes each produced a data stream of over 2,000 measurements per launch, it was convenient to first determine a "layer" average for quantities such as temperature, relative humidity and u- and v- wind components at each of the sonde positions during the ascent. These layer averages were comprised of data recorded by the sondes in a range of +/- 12.5 mb from a particular slab-average pressure level. Thus, for example, if we are considering the slab of air whose average midpoint pressure is 900 mb, a layer average would be calculated at the center and vertices of the triangle from the data ranging between 912.5 mb and 887.5 mb recorded at each of the four sonde positions. Taking temperature as the variable of interest, the four-layer averages at the 900 mb level would include of all the temperature measurements between 912.5 mb and 887.5 mb averaged together (about three values based on the ascent rate in the lower troposphere as explained above). Next, these four-temperature layer averages would themselves be averaged together to form a single "slab-averaged" temperature, corresponding to the midpoint pressure of 900 mb in a 25 mb thick slab of air (see Fig. 5.1).

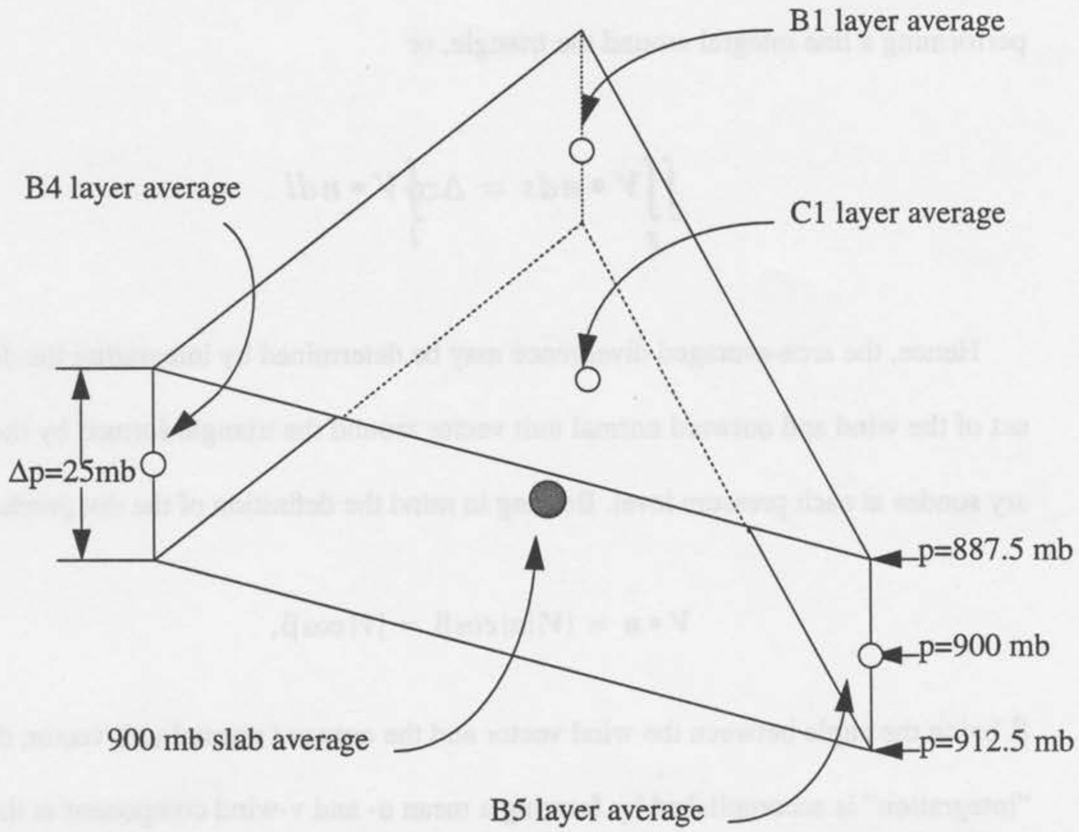

FIGURE 5.1: Location of each of the four layer averages and corresponding slab-average for a given pressure level.

5.1.2.2 Divergence

Having determined the layer-averaged u- and v-wind components, the divergences on isobaric surfaces at each level of the column may readily be calculated. First, making use of the divergence theorem, the area-averaged divergence integrated over the volume of an air parcel may be expressed as the area-averaged dot product of the total wind with the outward normal unit vector $\boldsymbol{n}$, integrated over the surface bounding the parcel. If the surface we are dealing with is only 2-dimensional, as is the case with the triangular arrangement of slab-averaged wind values, then the divergences may be calculated by performing a line integral around the triangle, or

$$\iint_s \boldsymbol{V} \bullet \boldsymbol{n} ds = \Delta z \oint_l \boldsymbol{V} \bullet \boldsymbol{n} dl \ . \qquad (5.1)$$

Hence, the area-averaged divergence may be determined by integrating the dot product of the wind and outward normal unit vector around the triangle formed by the boundary sondes at each pressure level. Bearing in mind the definition of the dot product

$$\boldsymbol{V} \bullet \boldsymbol{n} = |\boldsymbol{V}||\boldsymbol{n}|\cos\beta = |\boldsymbol{V}|\cos\beta, \qquad (5.2)$$

β being the angle between the wind vector and the outward normal unit vector, the "integration" is accomplished by forming a mean u- and v-wind component at the midpoint of each triangle leg, multiplying this mean by the cosine of angle β at that point, multiplying the product by the length of the leg Δl, and then summing up the resultant values of the three legs (see Fig. 5.2). Since we know the latitude and longitude of each of the sondes at all levels, the angle β may be determined by using simple geometry.

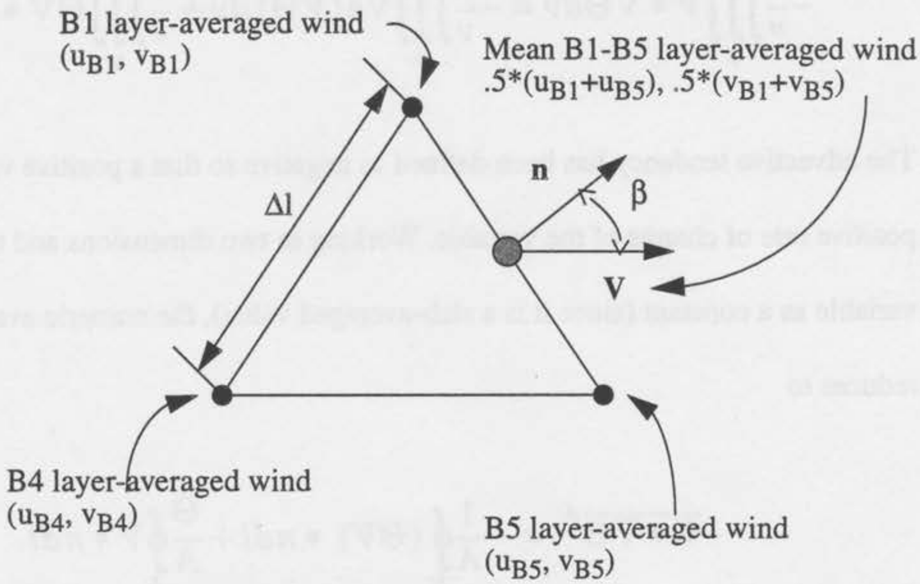

FIGURE 5.2: The dot product of total wind and outward normal unit vector, calculated at the midpoint of the leg joining sondes B1 and B5. This product, multiplied by the length of the leg Δl, is also obtained for the other two legs, then the three quantities are summed up and divided by the area of the triangle as a means of evaluating the line integral of the volume-averaged divergence.

5.1.2.3 Advective Tendencies

Once the divergence has been calculated for each pressure level, the advective tendencies of water vapor mixing ratio and temperature may subsequently be derived. Using the vector identity

$$\nabla \bullet (V\Theta) = V \bullet \nabla\Theta + \Theta\nabla \bullet V, \tag{5.3}$$

we see that the flux-divergence of any scalar variable Θ, such as temperature or water vapor mixing ratio, is equal to the advection of the variable plus the variable times the divergence. Then, the volume-averaged advective tendency of any scalar quantity may be expressed as

$$-\frac{1}{v}\iiint\limits_{v} V \bullet \nabla\Theta dv = -\frac{1}{v}\iiint\limits_{v} \nabla\bullet(V\Theta)\, dv + \frac{1}{v}\iiint\limits_{v} \Theta\nabla \bullet V dv. \tag{5.4}$$

The advective tendency has been defined as negative so that a positive value indicates a positive rate of change of the variable. Working in two dimensions and treating the scalar variable as a constant (since it is a slab-averaged value), the numeric evaluation of (5.4) reduces to

$$-\overline{V \bullet \nabla\Theta}^{A} = -\frac{1}{A}\oint_{l} (\Theta V) \bullet \boldsymbol{n} dl + \frac{\Theta}{A}\oint_{l} V \bullet \boldsymbol{n} dl. \tag{5.5}$$

The first term on the right-hand side of (5.5) is evaluated by determining a layer-averaged flux at each of the sonde positions. This flux would simply be the layer-averaged temperature or water vapor mixing ratio multiplied by the layer-averaged wind components. Then, a mean flux value for each of the legs is calculated from these layer-averages. This value is in turn multiplied by the outward normal unit vector at the leg midpoint, analogous to the procedure outline above for the divergence calculation. Finally, this product is multiplied by the length of the leg and then the three values of the three legs are summed up to form the integrated flux over the surface. The second term is simply the divergence as obtained in (5.1) above, multiplied by the slab-average of the scalar quantity in question (see Fig. 5.3).

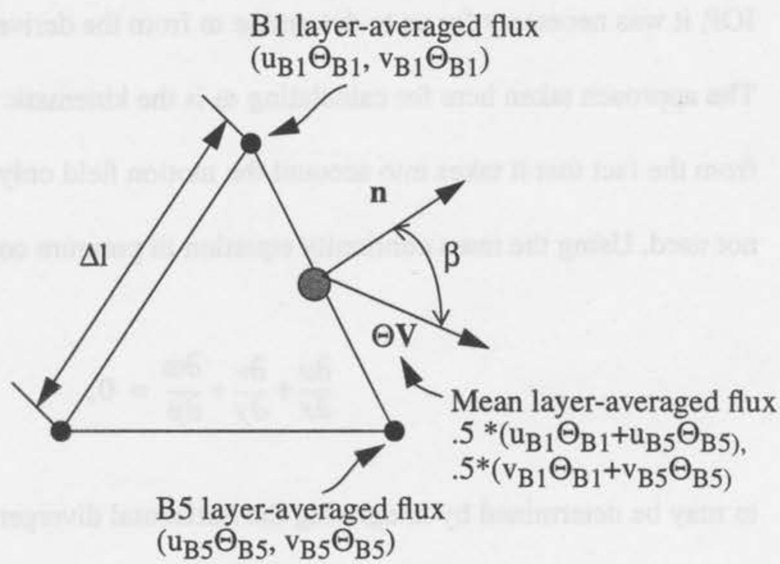

FIGURE 5.3: A mean layer-averaged flux of either temperature or water vapor mixing ratio is computed at the midpoint of each leg. Then, the dot product is taken with the outward normal unit vector and the result is multiplied by the length of the leg Δl. This procedure is repeated for each leg, the three quantities summed up and the result divided by the area of the triangle to compute the volume-averaged line integral of the scalar flux.

5.2 Algorithms

5.2.1 Vertical Velocity

The principal objective of this study as stated in Chapter 1 is a test of the GCAPE quasi-equilibrium state of the atmosphere. In order to do this, we need not only the horizontal advective tendencies for temperature and moisture, but also the vertical advection of these quantities. In addition, we will be investigating the heat and moisture budgets of the atmospheric volume contained in the SCM (discussed below) which also involves vertically advected heat and moisture. For these reasons, we need the vertical velocity ω.

However, since ω was not included as part of the derived data products from the SCM IOP, it was necessary for us to determine ω from the derived divergences in the column. The approach taken here for calculating ω is the kinematic method, which gets its name from the fact that it takes into account the motion field only; the dynamical equations are not used. Using the mass continuity equation in pressure coordinates

$$\frac{\partial u}{\partial x} + \frac{\partial v}{\partial y} + \frac{\partial \omega}{\partial p} = 0, \qquad (5.6)$$

ω may be determined by integrating the horizontal divergence

$$D = \frac{\partial u}{\partial x} + \frac{\partial v}{\partial y} = \nabla_p \bullet V, \qquad (5.7)$$

with respect to pressure between any two desired pressure levels

$$\int_p^{p+\Delta p} \frac{\partial \omega}{\partial p} dp = -\int_p^{p+\Delta p} D dp, \qquad (5.8)$$

so that

$$\omega_{(p)} = \omega_{(p+\Delta p)} + D\Delta p. \qquad (5.9)$$

Since the divergences for the SCM IOP were calculated using slab averages of the u- and v-wind components as explained above, it is important to note that ω is actually calculated at the interface between slab layers. In other words, the grid in the vertical is staggered, with all field variables except ω corresponding to the midpoint pressure of each slab layer (see Fig. 5.4). Note also that in the integration, the limit $p + \Delta p$ refers to some level *below* level p since pressure increases downwards.

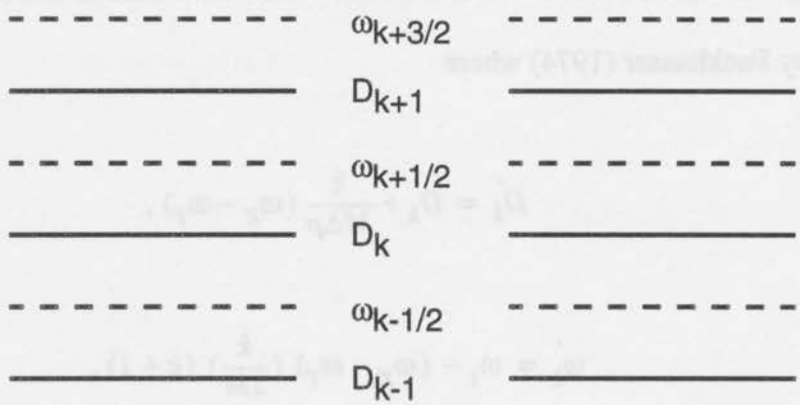

FIGURE 5.4: Structure of staggered grid, showing vertical space relation of ω to the slab-averaged divergences from which it has been derived.

5.2.1.1 O'Brien Adjustment Scheme

Obviously, the measurement of the divergence for each slab layer must be accurate if it is to be of any use as a basis for calculating vertical velocity, and even though there are often problems in obtaining such measurements from balloon soundings, even in a qualitative manner (Bluestein, 1992), it is nevertheless possible to reach reasonable results from radiosonde data (i.e. Thompson et al., 1979, using GATE data; Gallus and Johnson, 1991, using PRESTORM data). The principal sources of error in this regard, not counting instrument bias, can be traced to the strong winds aloft and deterioration in the wind values reported by the balloons with increasing height throughout the sounding (Fankhauser, 1974). Assuming that this error is minimal at the surface while increasing linearly with height, O'Brien (1970) suggests an adjustment scheme in which the initial (surface) and final (top of column) values of ω are independently chosen, and then a correction made to the divergences (D') as a function of height. A new value of the vertical velocity (ω') is subsequently derived based on these corrections. The equations for determining this adjustment take several forms, but the ones used in this study were those used by Fankhauser (1974) where

$$D_k' = D_k + \frac{k}{M\Delta p}(\omega_K - \omega_T), \tag{5.10}$$

$$\omega_k' = \omega_k - (\omega_K - \omega_T)\left(\frac{k}{2M}\right)(k+1), \tag{5.11}$$

with

$$M = \sum_{k=1}^{K} k = \frac{1}{2}K(K+1). \tag{5.12}$$

Here, K represents the total number of layers, ω_K is the value of ω as calculated by the sum of divergences before any adjustments, and ω_T is the boundary condition set on ω at the top of the column.

In this study, both ω_0 and ω_T were set to zero. As an academic exercise, if we suppose that the amount of heating in the upper troposphere is very small or negligible, the latter condition $(\omega_T = 0)$ may be independently established by application of the adiabatic method to determine ω near the tropopause. Considering the adiabatic form of thermodynamic equation

$$C_p\frac{dT}{dt} - \alpha\omega = 0, \tag{5.13}$$

we may derive an expression for ω by expanding the total derivative and rearranging the terms to find

$$\frac{\partial T}{\partial t} + V \bullet \nabla T + \omega \left(\frac{\partial T}{\partial p} - \frac{\alpha}{C_p} \right) = 0, \tag{5.14}$$

or

$$\omega = \frac{\frac{\partial T}{\partial t} + V \bullet \nabla T}{\left(\frac{\alpha}{C_p} - \frac{\partial T}{\partial p} \right)}. \tag{5.15}$$

Using the ideal gas law

$$p\alpha = RT, \tag{5.16}$$

along with Poisson's equation for potential temperature

$$\theta = T \left(\frac{p_0}{p} \right)^{\kappa}, \tag{5.17}$$

the denominator in (5.15) may be rewritten as

$$\frac{\alpha}{C_p} - \frac{\partial T}{\partial p} = \frac{RT}{pC_p} - \frac{\partial}{\partial p}\left[\theta \left(\frac{p}{p_0} \right)^{\kappa} \right] = \frac{RT}{pC_p} - \left[\left(\frac{p}{p_0} \right)^{\kappa} \frac{\partial \theta}{\partial p} + \theta \frac{\partial}{\partial p} \left(\frac{p}{p_0} \right)^{\kappa} \right] = -\frac{T}{\theta} \frac{\partial \theta}{\partial p}, \tag{5.18}$$

so that (5.15) becomes

$$\omega = \frac{\frac{\partial T}{\partial t} + V \bullet \nabla T - \frac{Q_R}{C_p}}{-\frac{T}{\theta}\frac{\partial \theta}{\partial p}}. \tag{5.19}$$

Here T is the temperature, t the time, p the pressure, R the gas constant, p_0 the standard pressure (usually taken to be 1000 mb), and $\kappa = \frac{R}{C_p}$. The quantity in the denominator of (5.19) is known as the static stability parameter

$$\sigma = -\frac{T}{\theta}\frac{\partial \theta}{\partial p}, \tag{5.20}$$

so that in regions of high static stability such as the tropopause region where $\frac{\partial \theta}{\partial p}$ is large, we would expect ω to be small. Indeed, when calculated using this method, ω was found to be on the order of 1 μb s^{-1}or less for most of the observation times in the tropopause region as can be seen in Fig. 5.5. Therefore choosing ω_T to be zero at the

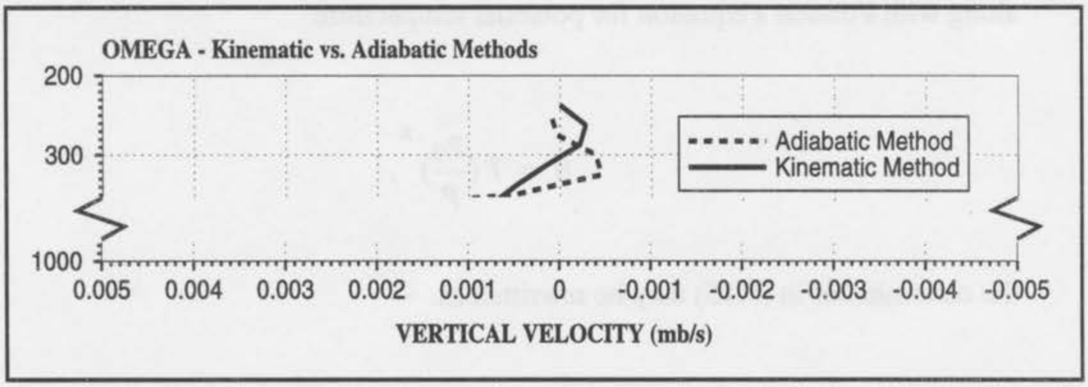

FIGURE 5.5: Two profiles of ω derived from SCM IOP data gathered on 30 January 1994, averaged to 19:30 UTC. Note that the adiabatically-derived profile (dashed line) naturally goes to zero in the tropopause region around 225 mb, whereas the kinematically-derived profile is required to go to zero.

tropopause, which was taken to be situated at around 225 mb based on the temperature profile and reversal in sign of $\frac{\partial T}{\partial p}$, appears to be a reasonable choice.

The former condition $(\omega_0 = 0)$ was chosen based on the idea that the O'Brien correction scheme is applicable only if ω_0 is small compared with ω at mid-tropospheric levels. For most synoptic weather situations, this would indeed be the case. However, it is useful to illustrate circumstances where the validity of setting $\omega_0 = 0$ would be questionable. Considering the lower boundary condition that no mass cross the earth's surface, the vertical velocity at the surface is

$$\omega_s = \frac{\partial p_s}{\partial t} + V_s \bullet \nabla p_s. \tag{5.21}$$

We see that ω at the surface is entirely due to the local time rate of change of surface pressure and the work done by the pressure gradient at the surface. Estimating a worst-case scenario, the requirement for the classification of an intensifying surface low pressure system as a "bomb" is a 12 mb deepening in 24 hours. If we imagine that the surface pressure gradient would be on the order of 10 mb per 200 km with a straight westerly wind blowing at 50 km per hour, using (5.21) we would end up with a value for ω at the surface on the order of 10^{-4} mb s^{-1}, which is roughly an order of magnitude less than expected values of ω at mid-tropospheric levels on a quiet day as can be seen in Fig. 5.5. Thus our condition that $\omega_0 = 0$ appears justified under most circumstances.

Fig. 5.6 illustrates the application of the linear O'Brien adjustment scheme. The value of ω' is essentially the same as the original estimate of ω near the ground, while the adjustments to ω' take increasing effect as the calculations work towards the lowest pressure levels (in keeping with the assumption that the divergences are subject to increasing error with height), eventually bringing ω' to the chosen boundary condition ω_T as required.

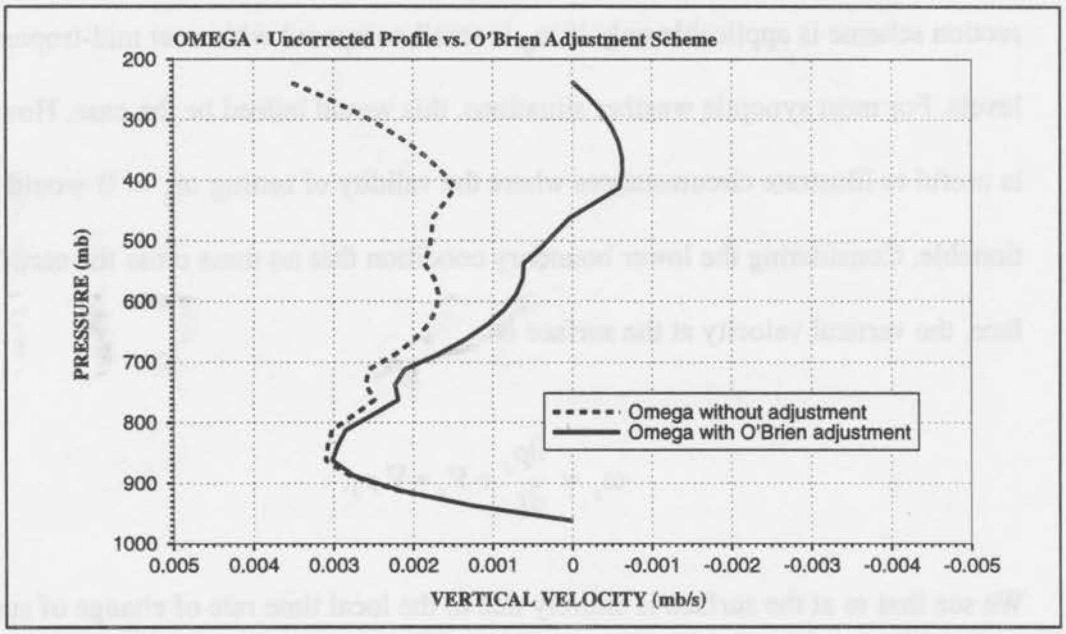

FIGURE 5.6: Example of ω profiles without the O'Brien adjustment (dashed line) and with the adjustment (solid line). The data used in this example are from the IOP 19 UTC observation on 30 January 1994. Note that positive values indicate

5.2.2 Apparent Heat Source (Q_1)

A further objective of using the SCM IOP data in this study is to determine the heat and moisture budgets as diagnostics for each day of the ten-day duration of the IOP. The motivation behind calculating these budgets is two-fold: First, in combination with precipitation and cloud data, they can provide an independent check on the accuracy of the data being collected by the SCM IOP instruments. Second, assuming the proper functioning of the instruments is not in question, these budgets will also give an indication of whether or not it is reasonable to expect that meaningful data can be collected from the profiler/balloon-borne sounding system as it is currently set up. Thus, in light of the meteorological conditions during the period, it should be possible to verify the heat and moisture budgets as calculated from these data.

The apparent heat source, Q_1, for an air parcel (in which properties such as temperature and water vapor can be considered to be homogeneous) may be derived from the first law of thermodynamics (Yanai et al, 1973; Cotton and Anthes, 1989; Gallus and Johnson, 1991)

$$C_v dT + p d\alpha = Q dt, \tag{5.22}$$

where C_v is the specific heat of air at constant volume and Qdt is the diabatic heating term.

As an aside, this relationship describes the conservation of energy of an air parcel, in that any heating (Qdt>0) produces an increase in the internal energy of the parcel ($C_v dT$>0), as well as work on the surrounding environment by the expanding parcel ($pd\alpha$>0). Alternatively, cooling (Qdt<0) will bring about a decrease in the parcel's internal energy ($C_v dT$<0) and allow the environment to do work on the shrinking air parcel ($pd\alpha$<0). In the absence of heating ($Qdt = 0$, we can also see why a parcel that is lifted adiabatically must expand as its internal energy decreases in order to satisfy (5.22). Dividing (5.22) by dt and making use of the ideal gas law, (5.22) can be written

$$C_p \frac{dT}{dt} - \alpha\omega = Q \tag{5.23}$$

where the specific heat of air at constant pressure $C_p = R + C_v$.

With V representing the horizontal wind vector and ∇_p the gradient operator along constant pressure surfaces, the material derivative in (5.23) may be expanded as

$$\frac{d}{dt} = \frac{\partial}{\partial t} + V \bullet \nabla_p + \omega\frac{\partial}{\partial p}, \tag{5.24}$$

so that (5.23), combined with the continuity equation, becomes

$$\frac{\partial T}{\partial t} + \nabla_p \bullet (VT) + \frac{\partial}{\partial p}(\omega T) - \frac{\alpha\omega}{C_p} = \frac{Q}{C_p} \quad . \tag{5.25}$$

If the diabatic heating term Q is broken up into terms distinguishing latent heating from radiative heating, the left side of (5.25) can be expanded as

$$\frac{\partial T}{\partial t} + \nabla_p \bullet (VT) + \frac{\partial}{\partial p}(\omega T) - \frac{\alpha\omega}{C_p} = \frac{L}{C_p}(c-e) + \frac{Q_R}{C_p}, \tag{5.26}$$

where L is the latent heat of condensation, Q_R the average radiative heating rate, and c and e represent the condensation and evaporation rates respectively.

Thus far, we have only been concerned with these properties as they relate to a particular air parcel. However, if we wish to apply this equation to the volume of an atmospheric column, it is convenient to decompose each variable into a mean component $(\bar{x})$ and a component deviating from the mean (x'). Using Reynolds averaging (in which the horizontal mean is denoted by an overbar), (5.26) can be written

$$\frac{\partial \bar{T}}{\partial t} + \nabla_p \bullet \bar{V}\bar{T} + \frac{\partial}{\partial p}[\bar{\omega}\bar{T}] - \frac{\bar{\alpha}\bar{\omega}}{C_p} = \frac{L}{C_p}(\bar{c}-\bar{e}) + \frac{\bar{Q}_R}{C_p} - \nabla \bullet \overline{V'T'} - \frac{\partial}{\partial p}[\overline{\omega' T'}] + \frac{\overline{\alpha'\omega'}}{C_p}. \tag{5.27}$$

We neglect the horizontal eddy flux term ($\nabla \bullet \overline{V'T'}$) since, in most cases, it is very small in comparison to vertical eddy flux terms for large scale tendencies (Cotton and Anthes, 1989). This assumption obviously depends on averaging length and would therefore not be as valid for studies of squall lines for example, where horizontal eddy flux convergences might be rather large in an area of limited areal extent (Gallus and Johnson, 1991).

If we focus on the last term on the left-hand side of equation (5.27) we see that

$$-\frac{1}{C_p}(\bar{\alpha}\bar{\omega}) = -\frac{1}{C_p}(\bar{\alpha}\frac{d\bar{p}}{dt}) = -\frac{1}{C_p}(\bar{\alpha}\frac{\partial\bar{p}}{\partial z}\frac{d\bar{z}}{dt}) = \frac{1}{C_p}(g\frac{d\bar{z}}{dt}) = \frac{1}{C_p}(\frac{d\bar{\Phi}}{dt}), \qquad (5.28)$$

using the definition of ω

$$\omega = \frac{dp}{dt}, \qquad (5.29)$$

and the hydrostatic relation

$$\frac{\partial p}{\partial z} = -\frac{g}{\alpha}, \qquad (5.30)$$

where g is the earth's gravitational attraction and z the height above sea level. Now, substituting (5.28) into (5.27), we arrive at the usual form of the definition for Q_1

$$Q_1 \equiv C_p\frac{d\bar{T}}{dt} + \frac{d\bar{\Phi}}{dt} = \frac{d}{dt}[C_p\bar{T} + \bar{\Phi}] = \frac{d\bar{s}}{dt}, \qquad (5.31)$$

which is cast in terms of dry static energy

$$s = C_p T + gz, \tag{5.32}$$

with geopotential $\Phi = gz$.

If we expand the right-hand side of (5.31) and include the terms on the right-hand side of (5.27), we find

$$Q_1 \equiv \frac{\partial \bar{s}}{\partial t} + \nabla \bullet \bar{V}\bar{s} + \frac{\partial}{\partial p}[\bar{\omega}\bar{s}] = L(c-e) + Q_R - \frac{\partial}{\partial p}[\overline{\omega' s'}] \tag{5.33}$$

What equation (5.33) says is that the apparent heat source is due to latent heating, radiational heating, and the vertical eddy transport of sensible heat. As previously mentioned, it is practically impossible to measure these terms directly, especially the vertical eddy transport. This is because of the spatial scales involved when trying to sample updrafts and downdrafts. In the boundary layer these turbulent eddies tend to have similar dimensions in their horizontal and vertical extent. Thus, it is feasible to sample them, for example, by use of aircraft flying through the boundary layer. However, in larger cumulus clouds, updrafts and downdrafts account for a very small fraction of the total air movement and as such are difficult to sample with any degree of accuracy. The only alternative, therefore, is to calculate these terms using the expressions to the immediate right of Q_1 in (5.33), involving the local time rate of change of dry static energy, as well as both the horizontal and vertical divergences of dry static energy flux.

An algorithm for the calculation of Q_1 will now be explained in detail. If we make use of the fact that mass is conserved, or

$$\nabla_p \bullet V + \frac{\partial \omega}{\partial p} = 0, \tag{5.34}$$

then it is convenient to write (5.27) or (5.31) in advective form

$$Q_1 = C_p\left[\frac{\partial \overline{T}}{\partial t} + \overline{V} \bullet \nabla_p \overline{T} + \overline{\omega}\frac{\partial \overline{T}}{\partial p}\right] - \overline{\alpha\omega}. \tag{5.35}$$

Taking the first term on the left-hand side of (5.35), a finite-difference approximation for the local time rate of change of temperature is

$$\frac{\Delta T}{\Delta t} \tag{5.36}$$

in which Δt is taken to be three hours and ΔT is the change in the slab-average temperature. Since the data for each day were provided at three-hour intervals starting at 00 UTC and ending at 21 UTC, all terms involving differentiation with respect to time were calculated at the midpoint between observation times so that a centered time-differencing scheme, which is second-order accurate, could be employed. In other words, all derivatives with respect to time were defined as

$$\left.\frac{\Delta T}{\Delta t}\right|_{n+\frac{1}{2}} = \frac{T^{n+1} - T^n}{\Delta t} \tag{5.37}$$

so that, for example, a total of seven values would be calculated from eight observations times for one day, or a total of 15 values would be calculated from 16 observations for two consecutive days, and so on (see Fig. 5.7).

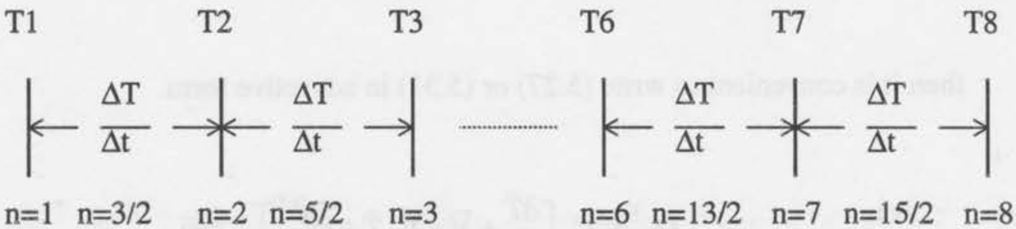

FIGURE 5.7: Position of temperature derivative with respect to time, using the second-order accurate centered time-differencing scheme.

Next, we consider the horizontal advection of temperature in (5.35). In finite difference form, this may be approximated as

$$\bar{V} \bullet \nabla_p \bar{T} \cong u \frac{\Delta T}{\Delta x} + v \frac{\Delta T}{\Delta y}. \tag{5.38}$$

However, the alternate approach, based on divergences, that the ARM Support Team took for calculating the advective tendency has been explained above in section 5.1.2.3. Since the advective tendencies were calculated to be valid at each observation time, it was necessary to obtain an average value between observation times to be consistent with the centered time-differencing scheme which evaluates $\frac{\partial T}{\partial t}$ at time level $n + \frac{1}{2}$. Thus, the advective temperature tendency has been averaged between time intervals according to the scheme

$$V \bullet \nabla T\Big|_{n+\frac{1}{2}} = \frac{1}{2}\left(V \bullet \nabla T|_n + V \bullet \nabla T|_{n+1}\right). \tag{5.39}$$

Similarly, a finite-difference form for the vertical advection of temperature is

$$\omega\frac{\Delta T}{\Delta p}. \tag{5.40}$$

Now, a problem arises, as alluded to earlier, in that ω represents the vertical velocity at the interfaces between layers for which the divergences have been provided. Thus, not only must an average across time intervals be constructed for each derivative, but also ω must be spatially averaged in the vertical to correspond to the slab midpoint pressure level at which the temperature derivative is being evaluated. This was carried out using the following finite-difference approximation

$$\begin{aligned}\omega\Big|_{k+1}^{n+\frac{1}{2}} = {} & \frac{1}{4}\left[\left(\omega^{n}_{k+\frac{3}{2}}\right)\frac{(T^{n}_{k+2}-T^{n}_{k+1})}{\Delta p}+\left(\omega^{n+1}_{k+\frac{3}{2}}\right)\frac{(T^{n+1}_{k+2}-T^{n+1}_{k+1})}{\Delta p}\right]+ \\ & \frac{1}{4}\left[\left(\omega^{n}_{k+\frac{1}{2}}\right)\frac{(T^{n}_{k+1}-T^{n}_{k})}{\Delta p}+\left(\omega^{n+1}_{k+\frac{1}{2}}\right)\frac{(T^{n+1}_{k+1}-T^{n+1}_{k})}{\Delta p}\right]\end{aligned} \tag{5.41}$$

Essentially, the temperature derivatives were initially calculated at the current pressure level where ω is defined, and then averaged across the time interval. This procedure was repeated for the level immediately below the current one, a layer also corresponding to a value of ω. Then, the two mean-time quantities were themselves averaged together so that the final answer corresponded to a layer for which the temperature is defined (see Fig. 5.8). For the lowest level of vertical advection of temperature, the second term in (5.41) was treated as zero, since ω is forced to be zero at the surface. Similarly, at the top of the column, the first term in (5.41) was set to zero, because ω is forced to be zero at the tropopause.

Finally, the $-\frac{\alpha\omega}{C_p}$ term in (5.27) needs to be considered. Rewriting this term using

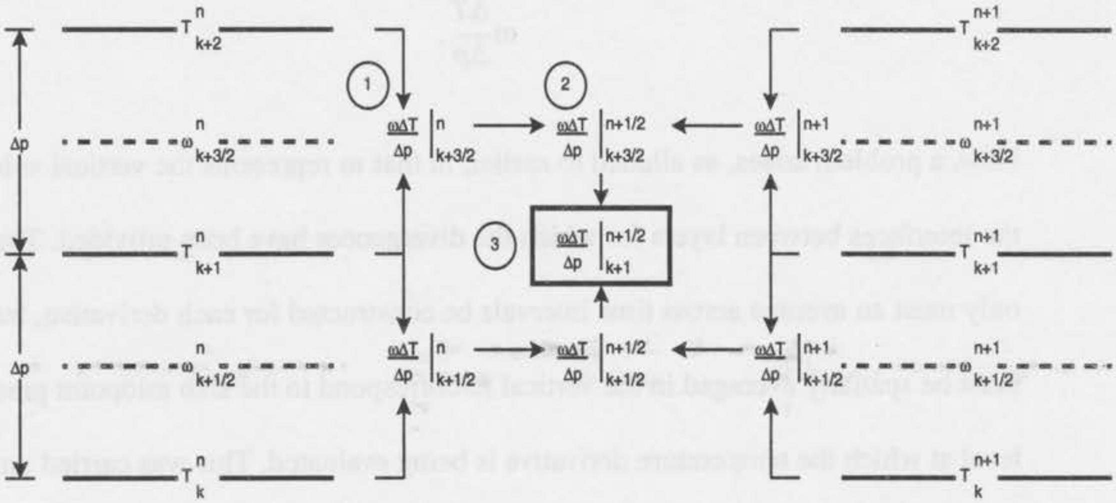

FIGURE 5.8: Complex evaluation of vertical advection: derivative is first calculated to correspond with ω level (1), then advective term is averaged across time interval (2) before being averaged spatially (3).

the ideal gas law yields

$$-\frac{RT\omega}{pC_p}. \tag{5.42}$$

In this particular case, the temperature for a given layer must be averaged across the time interval, while the pressure does not, obviously, since the same constant pressure surfaces are being used at all time intervals for the derived quantities. However, ω is a bit more complicated as it must be averaged in both time and space, as it was before in the vertical advection term. Thus we used

$$-\frac{RT\omega}{pC_p} \cong -\frac{R}{C_p}\left(\frac{1}{p_k^n}\right)\left[\frac{1}{2}\left(T_k^n + T_k^{n+1}\right)\right]\left[\frac{1}{4}\left(\omega^n_{k+\frac{1}{2}} + \omega^{n+1}_{k+\frac{1}{2}} + \omega^n_{k-\frac{1}{2}} + \omega^{n+1}_{k-\frac{1}{2}}\right)\right]. \tag{5.43}$$

in the computations for the adiabatic term involved in evaluation of Q_1. Time series plots of the apparent heat source will be shown and discussed below in the chapters on results.

5.2.3 Apparent Moisture Sink (Q_2)

The second of the moisture budget diagnostics, the apparent moisture sink, can be useful as a way of identifying regions of evaporation and condensation. In the case of evaporation, water undergoes a phase change from liquid to vapor and we would expect negative values of Q_2 (a negative moisture sink) near the earth's surface in response to solar heating after a period of rain or heavy dew. On the other hand, positive values of Q_2 would indicate that condensation is taking place, as in areas of cloud formation.

In order to derive an expression for the apparent moisture sink, we consider the equation for the time rate of change of the water vapor mixing ratio in an air parcel

$$\frac{dq}{dt} = -(c-e)\,, \tag{5.44}$$

where c and e are the area-averaged condensation and evaporation rates respectively. If we apply Reynolds averaging as before and expand the total derivative, we obtain

$$\frac{\partial\bar{q}}{\partial t} + \nabla_p \bullet (\bar{V}\bar{q}) + \frac{\partial}{\partial p}(\bar{\omega}\bar{q}) = -(\bar{c}-\bar{e}) - \nabla_p \bullet (\overline{V'q'}) - \frac{\partial}{\partial p}(\overline{\omega'q'})\,. \tag{5.45}$$

From this equation we see that large scale horizontal and vertical moisture flux-divergences, as well as the area-averaged condensation rate and eddy flux-divergences, bring about changes in the mixing ratio. Assuming as before that the horizontal moisture eddy flux-divergence is small compared with the vertical eddy flux-divergence and multiplying both sides of (5.45) by $\frac{L}{C_p}$, a definition of Q_2 is

$$Q_2 \equiv -\frac{L}{C_p}\left[\frac{\partial \bar{q}}{\partial t} + \nabla_p \bullet (\bar{V}\bar{q}) + \frac{\partial}{\partial p}(\bar{\omega}\bar{q})\right] = \frac{L}{C_p}\left[(\bar{c} - \bar{E}) - \frac{\partial}{\partial p}(\overline{\omega' q'})\right]. \tag{5.46}$$

The above definition states that the apparent moisture sink at a particular level in the column is due to the area-averaged condensation and vertical eddy flux of moisture. As was the case with Q_1, these terms are difficult to measure directly. Instead, we may use the expression to the immediate right of Q_2 in (5.46) since the large-scale terms involving the local time rate of change and flux-divergence of water vapor mixing ratio are more readily accessible.

The algorithm for calculating Q_2 closely parallels that outlined above for Q_1. As before, we take into account mass continuity and write the advective form of (5.46)

$$Q_2 = -\frac{L}{C_p}\left[\frac{\partial \bar{q}}{\partial t} + \bar{V} \bullet \nabla_p \bar{q} + \bar{\omega}\frac{\partial \bar{q}}{\partial p}\right], \tag{5.47}$$

which is computed using finite-difference approximations. Each of the terms in (5.47) were evaluated entirely analogously to equations (5.37), (5.39) and (5.40), only substituting the slab-average water vapor mixing ratio q for temperature T.

5.3 Problems With Data Analysis

When the 21 January-11 February 1994 SCM IOP data first began to be processed by the Experiment Support Team at the Lawrence Livermore National Laboratories (LLNL), it became apparent that there were some problems with the algorithms they were using for calculating the derived fields. For example, in some instances, the advective tendencies of moisture and temperature were overestimated by about an order of magnitude. In other cases, bogus data from the radiosondes that somehow managed to escape detection by quality checks at the ingest site were incorporated into the derived products, instead of being flagged as missing. Working together with the data processing team at LLNL, we located several errors in the algorithms and the actual computer code, and rewrote the offending portions to correct for these problems.

CHAPTER 6

January-February 1994 IOP Results

The first set of data from the SGP CART site we examined was obtained during the 3-week mid-winter period beginning 21 January 1994 and ending 11 February 1994. There was a lot of missing data during the first few days, associated with typical start-up bugs and problems regarding interference between the radiosondes' transmissions and the frequencies being used by the wind profilers, among other things. This meant that the actual chunk of usable data suitable for our purposes began on 29 January and extended through 10 February, giving us 10 contiguous days of reasonably good data, several gaps notwithstanding. Before discussing the results of the January-February IOP, it is instructive to review the day-by-day meteorological conditions during this period so that we have some guideline to go by in evaluating the data. This information was obtained from Michael Splitt of the CART Site Scientist Team.

6.1 Meteorological Conditions.

Saturday, 29 January 1994

A high pressure system moved southward into the Central Plains, pushing a cool front through the CART site. At the surface, winds were initially from the north and then shifted to become east-northeast over the area. Cloudiness increased from the north during the course of the day. Upper-level disturbances began to move into the southern portion of the CART site and mid-level humidity increased in the southwestern portion. A few flurries were reported in the extreme west and southwest sections.

Sunday, 30 January 1994

The high pressure system continued to move into the CART site and easterly surface winds continued. Significant snows occurred to the west of the CART site in association with strong upslope flow and the continued influence of upper-level disturbances moving across the southern portions of the site. Southwestern sections of the CART site received from 1 to 3 inches of snow.

Monday, 31 January 1994

Surface high pressure was centered over the CART site while skies cleared and cool conditions prevailed. Daytime maximum temperatures remained below freezing over most of the CART site.

Tuesday, 1 February 1994

The surface high pressure over the CART site continued to move south into Texas. A low pressure system developed over the Dakotas and moved southeastward. An associated cold front swept through the CART site and strong westerly surface winds became more northwesterly as the front passed. Some very light precipitation occurred over areas of the site at the time of frontal passage. A broad upper-level trough remained over the area while northwesterly winds aloft strengthened. Clouds increased over the CART site as the frontal system passed by, but then clearing occurred late in the day in the north.

Wednesday, 2 February 1994

Mainly clear skies prevailed and west to southwest downslope winds brought warm and dry weather to the site. Maximum temperatures ranged from 4-6°C in the north to 10-12°C in the south. Late in the day, another cold front moved into the northern CART zone. The upper level trough pushed slightly to the east during the day.

Thursday, 3 February 1994

The cold front that had moved into the CART site from the north began to stall over northern Oklahoma. Winds to the north of the front were from the southeast to northeast, while southerly winds dominated south of the front. Cloudiness increased, especially to the north. Another low pressure system formed in the Texas Panhandle late in the day and pushed into the southwestern edge of the CART site near the end of the day. No precipitation, however, was associated with this system.

Friday, 4 February 1994

The cold front passed through Oklahoma overnight and by morning it was positioned along the red river. Light northerly winds dominated the CART site for the day. Skies were generally fair with patches of high clouds. Strong westerly winds existed aloft over the site while the upper-level trough dominated the eastern half of the country.

Saturday, 5 February 1994

High pressure at the surface extended from Oklahoma to Illinois. A low pressure system centered over the Dakotas in the morning moved quickly eastward. Winds at the surface became southerly over most of the CART site and skies remained generally clear.

Sunday, 6 February 1994

An area of low pressure in the northern plains moved into Wisconsin by morning. A trailing arctic cold front moved southward into Nebraska during the morning and continued on into the northern portions of the CART site by late in the day. Most of the site experienced southerly winds and fair skies throughout the day, but clouds increased to the north with the onset of the arctic front.

Monday, 7 February 1994

The arctic front pushed quickly into Oklahoma. A strong temperature gradient existed over the CART site during the day with temperatures below -12°C in the north and from 15-20°C in the south. The arctic front's movement southward slowed during the day and it eventually moved south of the CART site overnight. Cloudy conditions prevailed over the area in conjunction with the passage of the front.

Tuesday, 8 February 1994

The arctic front continued to move slowly southward while precipitation began to breakout over the site. Light snow occurred mainly in Kansas while light freezing rain fell over Oklahoma. An upper-level storm system over Southern California moved towards the east while out ahead of the system upper-level winds became more southwesterly and helped pull moisture over the CART site, mainly in the south. Bitterly cold air became entrenched over Kansas while skies began to clear in the extreme north late in the day.

Wednesday, 9 February 1994

Low temperatures in the morning were less than -12°C over most of the site with near -17 to -20°C temperatures in the north. The arctic front continued to move to the south and pushed into central Texas and southeastern Arkansas. High pressure situated over South Dakota was moving to the east. The skies over the CART site cleared in the north, but over the south there was still significant cloudiness. Northwest winds continued at the surface, but became southerly over the northwest part of the site during the day. Freezing precipitation occurred early in the day in the extreme southern areas and moved out of the site later on. The upper-level storm system in the west moved eastward to south of New Mexico with a trough extending northeast to the CART site.

Thursday, 10 February 1994

The arctic low pressure system moved quickly eastward to over the Great Lakes by morning with a surface high pressure ridge extending southwestward into Oklahoma. Mainly clear skies occurred over the site except in the south where cloudy conditions early in the day gradually diminished. South of the surface ridge axis in the extreme southeast portion of the CART site winds were out of the north, while in the northwest sector of the site winds were southerly. The upper-level storm system moved into central Texas, well to the south of the CART site.

6.2 SCM IOP Data Compared with MAPS Model Output.

The results of the radiosonde data collected at the SGP CART site during the January-February 1994 IOP and MAPS data corresponding to the same time period are shown in Fig. 6.1 - Fig. 6.8. These are time series plots of temperature, water vapor mixing ratio, u- and v- wind components, divergence, vertical pressure velocity (ω), and temperature and water vapor mixing ratio tendencies due to horizontal advection. Also, the apparent heat source Q_1 and moisture sink Q_2 are presented in time series plots Fig. 6.9 - Fig. 6.10. This is followed by discussions (and related plots, Fig. 6.11 - Fig. 6.17) pertaining to 13-day temporal averages, standard deviations and the correlation as a function of pressure. For all plots, the temporal span covers the period commencing at 00 UTC on 29 January 1994 and terminating at 21 UTC on 10 February 1994.

Any missing data was flagged for both radiosonde and MAPS data sets, and the way in which missing data was taken into account will be discussed further below. The field variables of temperature, water vapor mixing ratio, and u- and v-wind components may be considered as "raw" data, having only undergone a minimum amount of processing to check for outliers and be consolidated into layer and slab averages. On the other hand, the field variables of divergence, vertical pressure velocity, and temperature and water vapor mixing ratio advective tendencies have been derived from the raw data by processing at the LLNL experiment support center as detailed in Chapter 5.

According to Marty Leach at LLNL (personal communication), the coordinates used in defining the CART site during the processing of the MAPS data is from 34.25 - 38.5 degrees north latitude, and from 95.25 - 99.5 degrees west longitude. The coordinates at launch time of the radiosondes are 38.35 °N, -97.25 °E for B1; 36.07 °N, -99.22 °E for B4; and 35.8 °N, -95.78 °E for B5. This means the area covered by the radiosondes is approximately 39,810 square kilometers, while that covered by the MAPS data sets is approximately 179,767 square kilometers. Thus, the areal coverage of the MAPS data set is roughly 4.5 times that of the radiosonde triangle. This difference in coverage is important as it may have a bearing on the results of the comparison of the MAPS and radiosonde data sets in 2 ways:

1) The much smaller sampling area covered by the radiosondes, along with the fact that this area is sampled at only 4 locations, should result in larger standard deviations and noisier profiles in the radiosonde data set when compared to the much larger and more densely sampled MAPS data. Since the gridpoints in the MAPS model are not only denser but also more evenly spaced, sharp differences in any of the field variables would tend to be averaged out over the MAPS domain, whereas the radiosondes presumably miss much atmospheric information over the area they sample.

2) Related to the above difference in sampling size and number of gridpoints, the MAPS data assimilation process takes into account atmospheric processes that are occurring outside the limited scope of the CART site boundaries; i.e. all of North America is

included in the data assimilation cycle (as will be explained below). On the other hand, the radiosondes report data only from their specific locations, and are "unaware" of any atmospheric processes going on elsewhere. Consequently, the additional outside information incorporated into the MAPS analyses could influence atmospheric signals resolved by the model over the CART domain in several ways, such as artificial smoothing from the statistics used to modify the entire background field over North America, or the increased chance that errors have been introduced somewhere along the line considering the greater number of sources used as data input for the MAPS model.

The operational version of the MAPS model (Benjamin et al. 1991; Benjamin, Smith et al. 1991; Miller and Benjamin 1992; Bleck and Benjamin 1993) has a mesh size of 60 km, uses a hybrid isentropic-sigma vertical coordinate system, and operates on a 3-hour intermittent data assimilation cycle. This data assimilation cycle consists of data ingest, objective quality control of the observations, objective analysis, and finally a 3-hour prognosis using a primitive equation forecast model. Each forecast subsequently becomes the background field for the next analysis. In case of any malfunctions, gridded forecast data from the NGM are interpolated to isentropic coordinates and used as the background field. Additionally, the NGM forecast data are used twice every 24 hours to provide boundary conditions.

Data ingested into the model come from a variety of sources: radiosondes, commercial aircraft reports, wind profilers and surface aviation observations (SAOs). All data is incorporated at the time of analysis, with the exception of aircraft data which is accepted within a window of 1.5 hours before and after the analysis time. Then the data are subjected to a series of quality control checks before passing to the objective analysis phase. A multivariate optimal interpolation scheme is used, in which the Montgomery potential and the horizontal wind components and are analyzed, so as to provide a degree of balance between the mass and wind fields. Next, the dynamic equations are solved on a regular grid superimposed on a polar stereographic projection, covering the contiguous United States between approximately 20° and 55°N. There are five prognostic equations in the primitive equation model: one for each of the two horizontal velocity components, one for mass continuity, and one each for potential temperature and moisture. Finally, verification is accomplished by comparison with the NGM 12-hour forecast as a standard of reference. The 3-hour assimilation cycle and analyses of the Regional Analysis and Forecast System (RAFS) is also used.

The radiosonde data were collected at the SGP CART site in northeast Oklahoma from the IOP held during the dates mentioned above. The data were immediately subject to "nominal" processing at the CART ingest site, which included checks for outliers and spurious ascent rates (e.g. when the balloon started to descend after reaching the upper troposphere) among other things. The data were then transferred to the Experiment Support Centers at LLNL and PNL where the thousands of data points from each radiosonde were processed to provide layer and slab averages for the triangular column formed by the radiosondes. Once the layer- and slab- temperature, water vapor mixing ratio, u- and v- wind component averages were produced, further processing produced the derived fields of divergence, vertical pressure velocity, and temperature and water vapor mixing ratio tendencies due to horizontal advection.

Finally, all plots have been drawn up using Spyglass Transform, Improv and NXY-Plot software, and both the processed radiosonde data and the MAPS model output initialized with the SCM IOP data are presented.

6.2.1 Qualitative Comparison

In most cases, blank areas in the time series plots indicates that data was missing for specific observations times and atmospheric levels. However, there are some subtleties involved with missing data and the way it is represented that should be pointed out. First, as mentioned above regarding the radiosonde data, many hundreds of data points from each radiosonde were averaged together to obtain the individual radiosonde layer-averages initially, which in turn were averaged together to arrive at the slab-average for a particular 25 mb "chunk" of the vertical atmospheric column, as discussed in Chapter 5. For variables such as temperature, water vapor mixing ratio, or wind components, what this means is that one or several data points from a particular sonde (or sondes) could be missing at any given observation time, and yet a slab-average could still be constructed from data furnished by the remaining functioning sonde(s). Therefore, any blank areas on the time series plots for these variables implies *none* of the radiosondes provided usable data at that particular moment in space and time. Regarding the MAPS data, on the other hand, the interpretation of blank areas is straightforward, and that is there simply was no data furnished for these particular variables at the time and level in question.

In the interest of trying to use as much of the radiosonde and MAPS data as possible, linear interpolation was selectively used to reconstruct gaps in the slab-averages for temperature, water vapor mixing ratio, and wind components. By selective, we mean that for a given observation time, if ten or fewer consecutive slab-averages were missing, a linear interpolation scheme was employed to fill in the gap (see Appendix A). Beyond this, any soundings missing more than ten consecutive slab-averages were left alone. Originally, linear interpolation had been used indiscriminately to replace all missing data, but this approach was found to lead to some rather obviously erroneous results.

Although the slab-averages for both wind components could be calculated as long as at least one of the four radiosondes provided usable data, the calculation of the divergence requires the three radiosonde layer-averages at the vertices of the triangle, as explained above in Chapter 5. Therefore, if even one of the layer-averages for the B1, B4 or B5 radiosondes was missing, then the divergence could not be calculated for that particular time and level. At first, an alternative triangle configuration involving the central C1 radiosonde was considered as a way of calculating the divergence in case data from one of the vertex radiosondes were missing. However, after comparing the results of divergences calculated both ways for instances when data from all four radiosondes were present, it was decided that this approach would not work as there was virtually no correlation between the two methods. Thus, a blank in the time series plot of divergence indicates at least one of the radiosonde layer averages was missing. As for the divergences based on MAPS gridded wind data, they were derived using a completely different algorithm at LLNL.

As explained in Chapter 5, the vertical pressure velocity was determined using the kinematic method. Thus, any missing divergences in the atmospheric column have serious implications for the computation of omega since, at any particular level, it involves the summation of divergences up to that point. Once again linear interpolation was used to reconstruct gaps in which divergences were missing at ten or fewer pressure levels for a given observation time. Consequently, based on the number of missing divergences, omega was either calculated for the entire column (and in some instances based on interpolated divergence values) or not at all, and this is reflected by the way the blanks appear in the vertical pressure velocity time series plots.

Regarding the temperature and water vapor mixing ratio tendencies due to horizontal advection, any missing ingredients will have an impact on their derivation. Slab-averaged temperatures and water vapor mixing ratios are necessary, obviously, in the derivation, yet these are least likely to be missing for the reasons stated above. At the same time, divergences are also needed in the calculations and missing divergences are much more common problem. In any event, the tendencies could not be computed if either the slab-averaged quantities or the divergence (or both) were missing.

Finally, Q_1 and Q_2 are the most sensitive to usable data, since any missing slab-averages of temperature or water vapor mixing ratio, and vertical pressure velocity (and all that entails) will prevent them from being calculated. Similar to the tendencies due to horizontal advection, the presence or absence of omega (based on divergence) at a given level is a deciding factor as to whether or not Q_1 and Q_2 was able to be computed. Even more important, however, is to bear in mind that Q_1 and Q_2 involve the computation of the time rates of change of temperature and water vapor mixing ratio, respectively. As such, all data from two adjacent observation times must be present for Q_1 and Q_2 to be computed at a given level in the atmosphere since the time derivative is evaluated at the midpoint between the observation times, as explained in Chapter 5. Unfortunately, there are several major gaps in the time series plots for Q_1 and Q_2 due to the amount of missing data.

Temperature

One feature that is consistently striking in all plots is the somewhat "noisier" appearance of any given variable profile from the radiosondes compared to MAPS, and this is certainly apparent in the time series plots of temperatures (Fig. 6.1) for both data sets. As discussed above, the smoother appearance of the MAPS data would presumably be due to factors such as the larger and more frequently sampled domain from which the MAPS data has been collected, and also artificial smoothing in the model. Especially apparent are spiked anomalies in the radiosonde data around observation numbers 64 and 75. This was due to radiosondes apparently malfunctioning and reporting temperatures as high as 40°C in the lower troposphere, which was tempered somewhat by the slab-averaging process. Aside from these anomalies, both data sets appear to show a good deal of agreement and have captured the main synoptic features accurately. In particular, the arrival of the cold front on 29-30 January (observations 8-16) and subsequent cooling of surface temperatures is evident on both plots, although the radiosonde plot shows a more rapid drop in temperatures with the passage of the front. The next frontal passage during the day on 1 February (observations 32-40) is depicted well on the radiosonde plot, and the warm-up that followed due to the "downslope" winds on 2 February (observations 35-40) can be seen on both plots. Diurnal heating and cooling is noticeable on the radio-

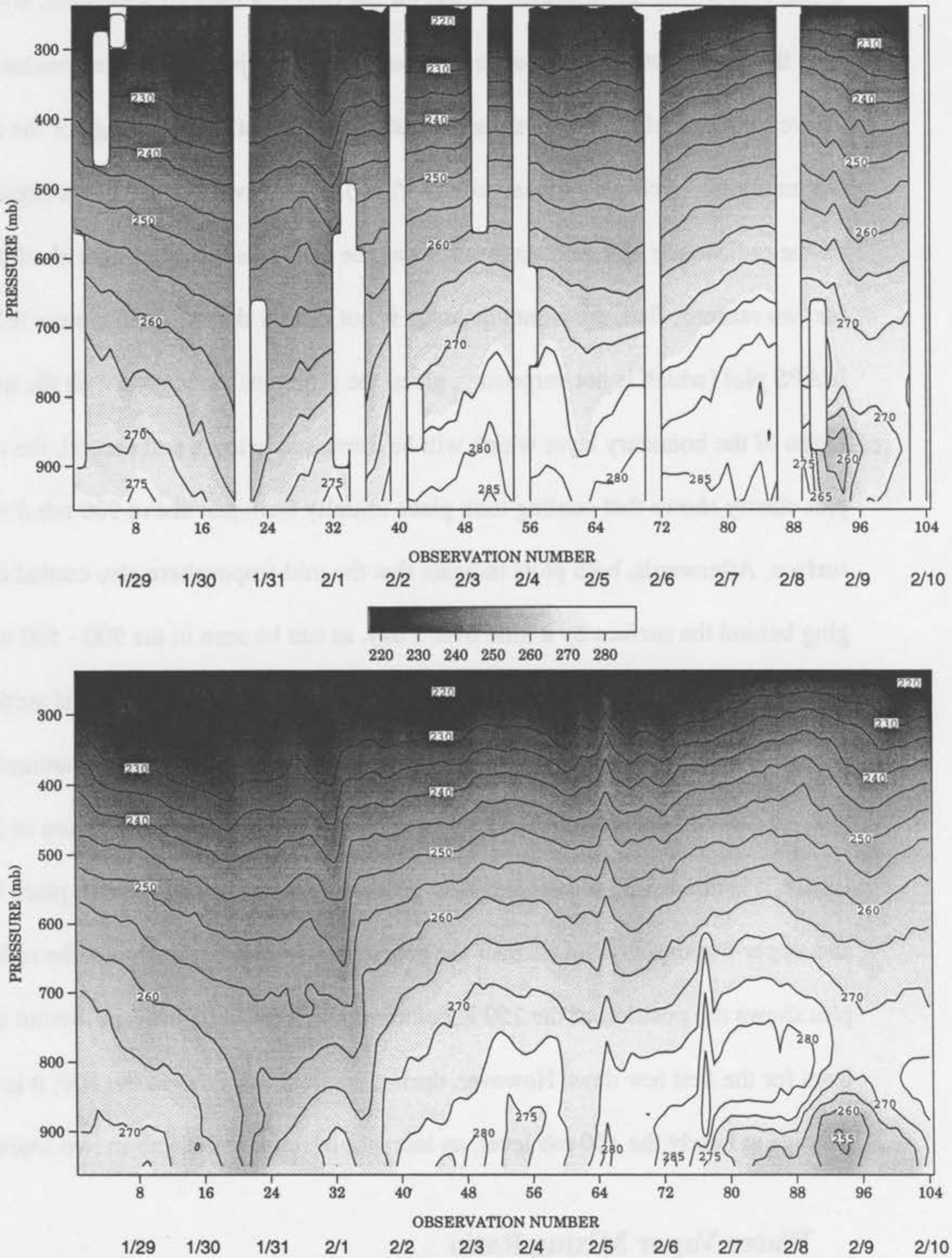

FIGURE 6.1: 13-day time series plots of temperature from MAPS model output (upper) and radiosonde data (lower), starting at 00 UTC on 29 January 1994 through 21 UTC on 10 February 1994. Contours are in K, and numbers on the abscissa represent multiples of 8 observations spaced 3 hours apart (8 observations per day), with dates below.

sonde plot during the quiescent period for the next few days (observations 40-56), and then the next frontal passage occurring on 4 February (just before observation 56) shows up well on both plots. The next major feature of interest is the passage of the arctic front, beginning on 7 February (observations 75-80). The arrival of the front is depicted well on the radiosonde plot, and apparently was the leading edge of a rather shallow air mass for two reasons: first, the frontal passage is not clearly defined in the lower levels of the MAPS plot (which is not surprising, given the problems associated with the model's resolution of the boundary layer which will be discussed below), and second, the radiosonde plot clearly shows that cooling took place initially from just above 900 mb down to the surface. Afterwards, both plots indicate that the mid-troposphere also cooled down, lagging behind the surface by a little over a day, as can be seen in the 900 - 500 mb region from 8-9 February (observations 85-94). The coldest temperatures of this arctic outbreak near the surface were below 255 K as suggested by the radiosonde plot around 925 mb at observation 94, whereas the MAPS plot indicates a larger cold pool region of 260 K. Lastly, it is interesting to note the slow general warming trend that took place in the mid- and upper-tropospheric levels over the course of the IOP. For example, the radiosonde plot shows the position of the 250 K contour to be located on average around the 550 mb level for the first few days. However, during the final few days of the IOP, it is located on average at nearly the 450 mb level, an increase of roughly 100 mb in two weeks.

Water Vapor Mixing Ratio

Again, the overall appearance of the radiosonde plot (Fig. 6.2) is noisier than that of the MAPS data. However, the plots are similar in the general patterns they capture. In the

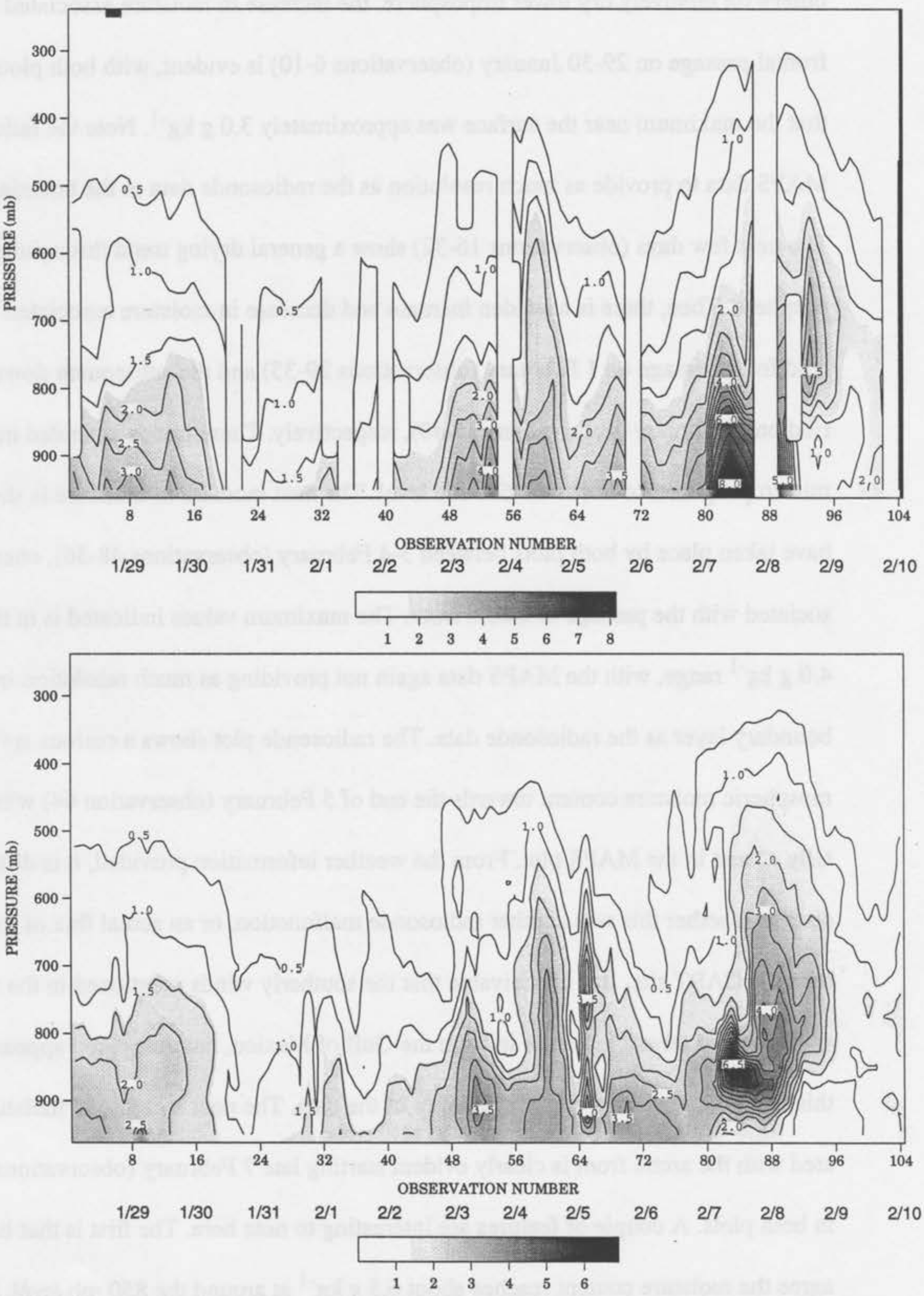

FIGURE 6.2: 13-day time series plots of water vapor mixing ratio from MAPS model (upper) and radiosonde (lower) data, starting at 00 UTC on 29 January 1994 through 21 UTC on 10 February 1994. Contours are in g kg^{-1}, and numbers on the abscissa represent multiples of 8 observations spaced 3 hours apart (8 observations per day), with dates below.

otherwise relatively dry lower troposphere, the increase in moisture associated with the frontal passage on 29-30 January (observations 6-10) is evident, with both plots agreeing that the maximum near the surface was approximately 3.0 g kg^{-1}. Note the failure of the MAPS data to provide as much resolution as the radiosonde data in the boundary layer. The next few days (observations 16-32) show a general drying trend throughout the troposphere. Then, there is a sudden increase and decrease in moisture associated with the cold front passage on 1 February (observations 29-35) and the subsequent downslope period on 2 February (observations 35-40), respectively. These trends extended into the mid-troposphere, to about the 600 mb level. The next increase in moisture is shown to have taken place by both plots between 3-4 February (observations 48-56), once more associated with the passage of a cold front. The maximum values indicated is in the 3.5 - 4.0 g kg^{-1} range, with the MAPS data again not providing as much resolution in the boundary layer as the radiosonde data. The radiosonde plot shows a curious spike in atmospheric moisture content towards the end of 5 February (observation 64) which is totally absent in the MAPS plot. From the weather information provided, it is difficult to discern whether this was another radiosonde malfunction, or an actual flux of moisture over the CART site. It is conceivable that the southerly winds mentioned in the weather summary did advect moisture in from the Gulf of Mexico, but the spiked appearance of this feature casts doubt on the reliability of the data. The next increase in moisture associated with the arctic front is clearly evident starting late 7 February (observations 78-88) in both plots. A couple of features are interesting to note here. The first is that both plots agree the moisture content reaches about 6.5 g kg^{-1} at around the 850 mb level. For the radiosonde plot, this represents a maximum, with the lowest atmospheric levels from this point down to the surface being considerably drier. The MAPS plot, on the other hand, maintains this amount of moisture (and even increases it) all the way to the surface. Once again, it appears we have an example of the problems associated with the model's treatment of the boundary layer. The other item of interest is the "double-pronged" nature of the moisture extending up into the mid-troposphere, which can be seen in both plots. For example, following the 2.0 g kg^{-1} contour in the MAPS plot, it reaches just over the 700 mb level at observation 83, before sinking back down and then rising again to 550 mb at observation 86. Similarly, the radiosonde plot shows the 2.0 g kg^{-1} contour going up to 750 mb at observation 83, sinking a bit and then rising up to the 550 mb level at observation 86. Finally, considering both plots from a general perspective, a remarkable feature stands out, and that is there appear to be three strong "waves" of moisture during this two-week period. The first one occurs from the beginning to observation 16, the second from observation 48 to 64, and the third from roughly observation 80 through to the end. Each successive wave contains more moisture throughout its depth and reaches higher into the troposphere. This periodicity suggests the frequency with which perturbations cross the winter mid-latitudes along the jet stream, and the increase in moisture of each wave could be associated with the slow warming of the atmosphere seen in the temperature plots as the mid-latitudes receive increasing amounts of solar radiation going from winter into spring.

U-Wind Component

Overall, the MAPS and radiosonde time series plots (Fig. 6.3) show very much the same the features, with one noticeable exception: the MAPS plot shows constant wind

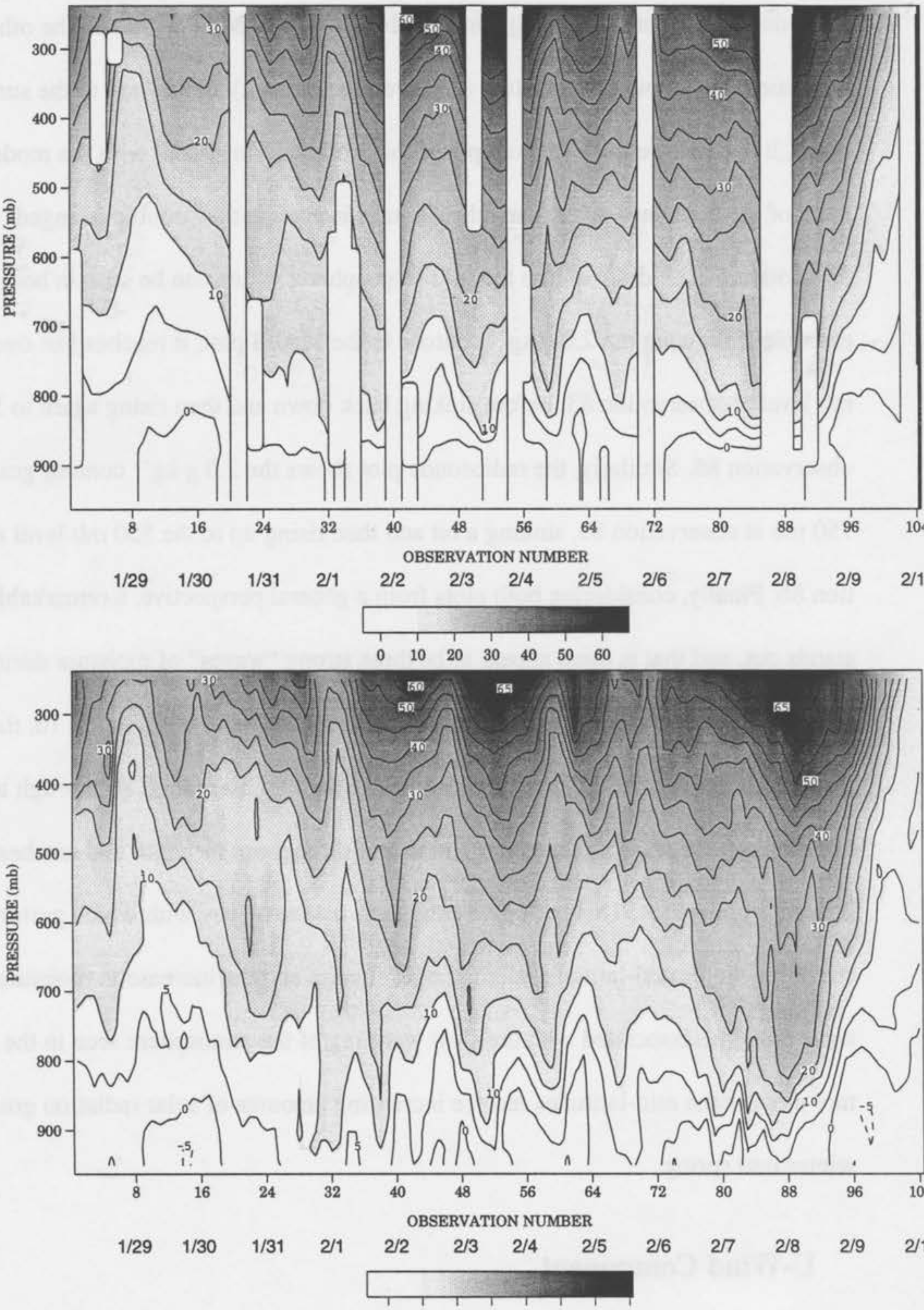

FIGURE 6.3: 13-day time series plots of u-wind component from MAPS model (upper) and radiosonde (lower) data, starting at 00 UTC on 29 January 1994 through 21 UTC on 10 February 1994. Contours are in m s^{-1} (dashed contours represent negative values), and numbers on the abscissa represent multiples of 8 observations spaced 3 hours apart (8 observations per day), with dates below.

values from about 875 - 900 mb down to the surface, corresponding to the boundary layer region. The data set from MAPS has practically identical wind values at each of the lowest levels of the atmosphere, and this consistently at every observation. Apparently, this has something to do with the background field used in the initialization process of MAPS, according to John Yio at LLNL (personal communication). The data are not shown to be missing, but rather carry the same wind value down to the surface from the last valid entry around 875 - 900 mb. In any case, above 875 mb the two plots are very similar. The strong westerly component of the jet stream is nicely depicted above 400 mb from observations 48 - 64, from 80 - 96 and, to a lesser extent, from the beginning to observation 8. These periods coincide with the three waves noted in the water vapor mixing ratio plots. The easterly surface winds mentioned in the weather summary on 30 January (observation 8-16) may be discerned on the radiosonde plot, but unfortunately are not resolved by the plot of MAPS data. The increasing westerly component to the downslope winds on 2 February (observations 32-40) and then the strong westerly winds aloft mentioned in the weather summary for 4 February (observations 48-56) are evident in both plots throughout the depth of the troposphere. An easterly component to the wind near the surface on the last day (observations 96-104) after the passage of the arctic front appears in the radiosonde plot, but is only hinted at in the MAPS plot.

V-Wind Component

As with the u-wind component, there is a great deal of similarity between the radiosonde and the MAPS time series plots (Fig. 6.4), aside from the boundary layer. Three periods of strong, upper-level southerly wind components, corresponding to the passage

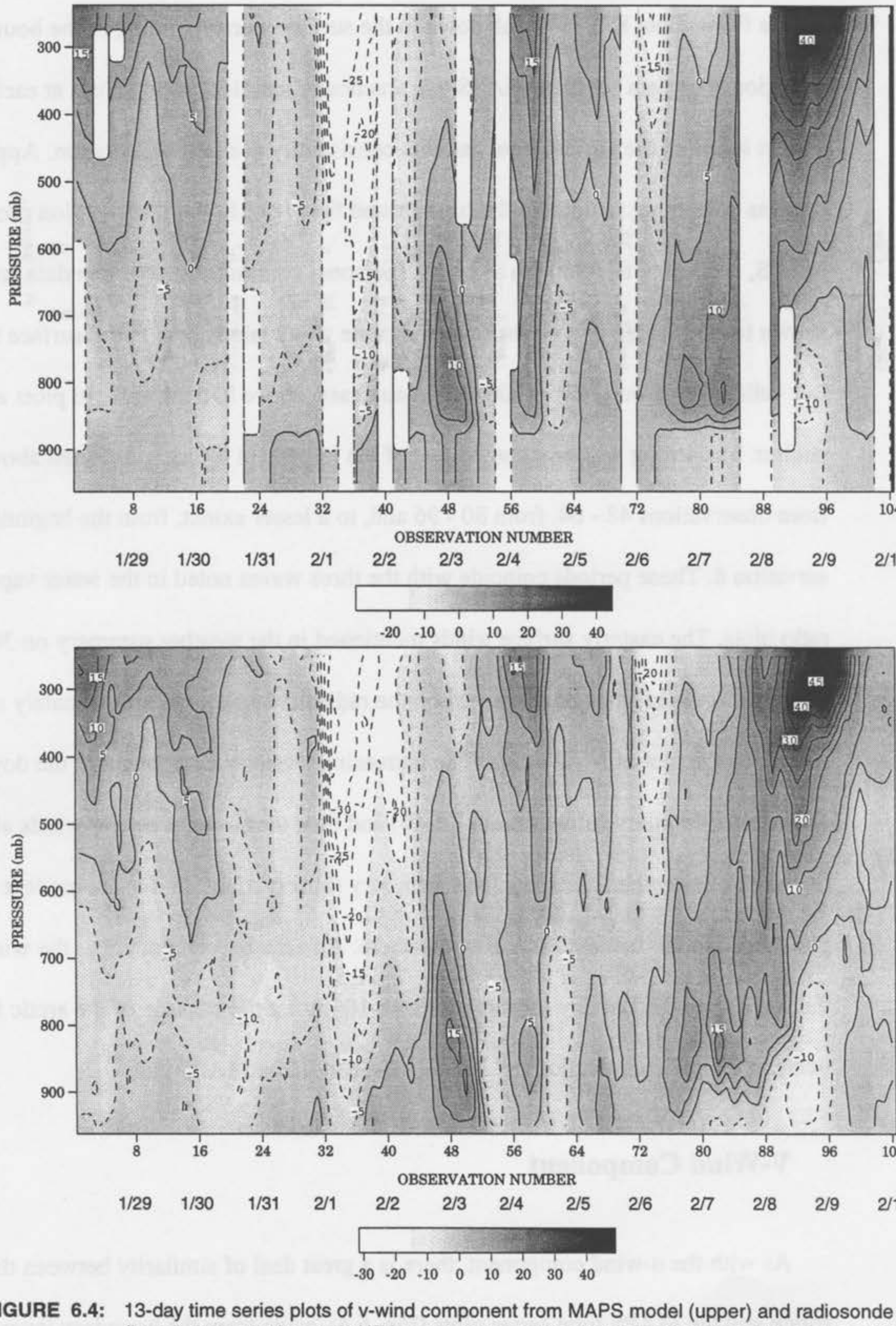

FIGURE 6.4: 13-day time series plots of v-wind component from MAPS model (upper) and radiosonde (lower) data, starting at 00 UTC on 29 January 1994 through 21 UTC on 10 February 1994. Contours are in m s^{-1} (dashed contours represent negative values), and numbers on the abscissa represent multiples of 8 observations spaced 3 hours apart (8 observations per day), with dates below.

of the three waves mentioned before, are noticeable from the beginning to observation 8, from observations 48 - 64, and from observations 80 - 96. A main difference, however, from the u-wind component plots, is that there tends to be more of a dual nature to the v-wind component. Each of the strong southerly component periods alternates with an often equally strong northerly component period. This northerly component takes on a local maximum of roughly 30 m s^{-1} at about 400 mb just after observation 32 in both plots. Another local northerly maximum of around 15 m s^{-1} can be seen between 400 - 300 mb at observation 72 in both plots. The largest value, however, is the strong southerly component of over 40 m s^{-1} right at 300 mb for observation 96 in both plots. An interesting feature in the lower troposphere that is captured by the v-wind component time series plot is the windshift that accompanies the passage of a cold front. This is especially evident on 4 February (observations 48-56) and 7 February (observations 72-80) in the radiosonde plot, and to a lesser extent in the MAPS plot. In both cases, the v-wind component can be seen to shift fairly abruptly from a southerly to a northerly direction, which is typical of the classic frontal passage in the northern hemisphere.

Divergence

The time series plots of the MAPS and radiosonde divergence fields (Fig. 6.5) are a bit difficult to interpret due to the strength of the noise and missing data. The time-average and correlation plots that follow in the next section provide a more precise evaluation of the extent to which these divergence fields agree. A few features do stand out here, however, and those are the regions of relatively strong divergence in both plots around 550 mb between observations 32-35, and around 500-475 mb between observations 96-

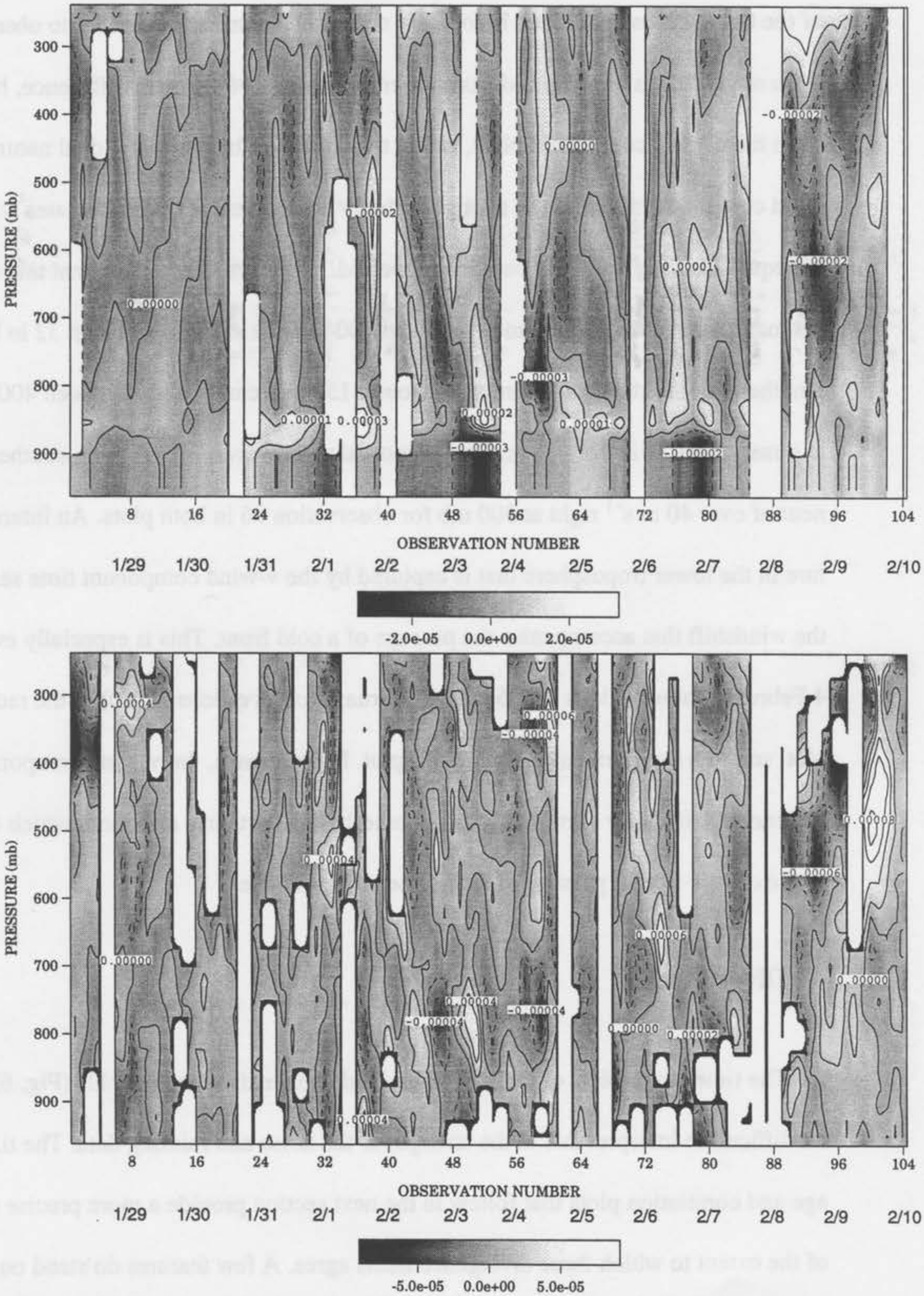

FIGURE 6.5: 13-day time series plots of wind divergence from MAPS model (upper) and radiosonde (lower) data, starting at 00 UTC on 29 January 1994 through 21 UTC on 10 February 1994. Contours are in m $s^{-1}m^{-1}$ (dashed contours represent negative values), and numbers on the abscissa represent multiples of 8 observations spaced 3 hours apart (8 observations per day), with dates below.

104. These would presumably be associated with the upper-level troughs mentioned in the weather summary on 1 February and 10 February, respectively. Another zone of positive divergence can be discerned between observations 48-56 in both plots, throughout almost the entire depth of the troposphere. The stronger values near the surface would probably be due to the subsident air mass following the passage of the cold front on 3 February (observations 45-50), since the weather summary mentions that skies were generally fair the following day. Other areas of surface divergence in the radiosonde plot (unfortunately not resolved in the MAPS plot) can be seen between observations 8-16, corresponding to the surface high pressure mentioned in the summary on 30 January, and between observation times 35-40 during the period of downslope winds on 2 February. Areas of convergence can be seen on both plots between observations 56-64 from 800 - 750 mb, and again around observation 92 between 600-500 mb.

Vertical (pressure) Velocity

Several of the interesting synoptic features during this IOP are corroborated by the time series MAPS and radiosonde plots for vertical motion (Fig. 6.6). As before, the radiosonde plot reveals more detail and shows generally stronger atmospheric motions than does the MAPS plot. An example of this difference is clearly seen in the upward wind velocity associated with the first frontal passage between observations 6-10 (late 29 January). Whereas this upward motion is quite clearly depicted throughout the entire troposphere in the radiosonde plot, with a maximum velocity of -20 mb hr^{-1} occurring between 625-525 mb at observation 8, the MAPS plot only hints at this occurrence. This vagueness may be due to the lack of important boundary layer wind information in the

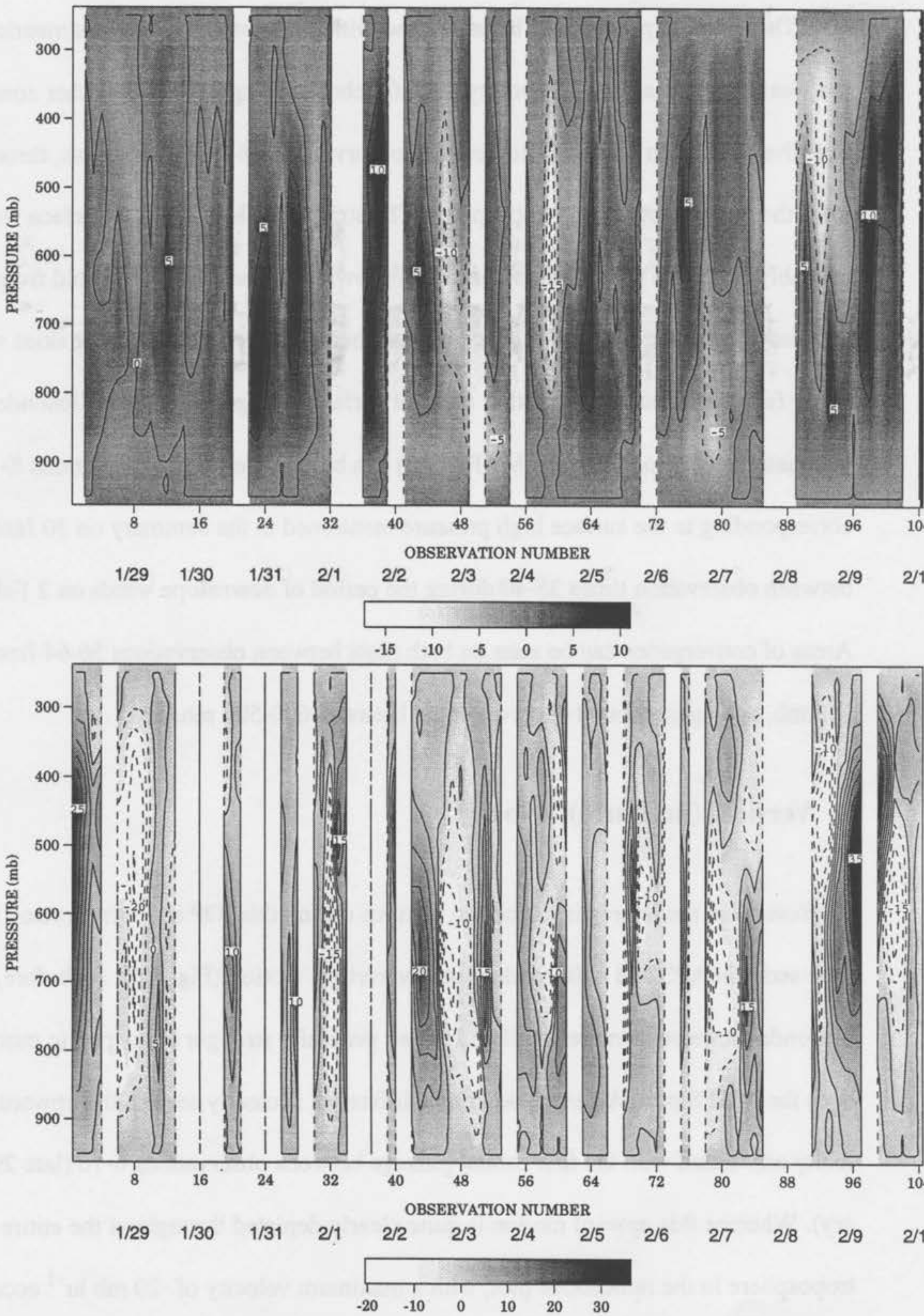

FIGURE 6.6: 13-day time series plots of vertical pressure velocity from MAPS model (upper) and radiosonde (lower) data, starting at 00 UTC on 29 January 1994 through 21 UTC on 10 February 1994. Contours are in mb hr^{-1} (dashed contours represent negative values), and numbers on the abscissa represent multiples of 8 observations spaced 3 hours apart (8 observations per day), with dates below.

MAPS model. Other periods of rising motion can be seen in both plots between observation times 45-50 and 58-62. The former extends from near 900 mb all the way to the top of the troposphere, corresponding to the cold front on 3 February, whereas the latter is centered between 800-500 mb, relative to the upper level trough on 4-5 February. Additionally, the radiosonde plot shows the two cold fronts that went over the CART site around observation times 32 and 40, as explained in the weather summary for 1-2 February, while the intervening downslope period is not shown due to data problems. The downslope wind is, however, visible on the MAPS plot where a maximum downward velocity of over 10 mb hr^{-1} is centered at the 500 mb level. Curiously, the relatively strong upward motion associated with the passage of the arctic front on 7-8 February (observation times 75-80) is virtually absent in the MAPS plot, again probably the victim of poor boundary layer resolution. Finally, post frontal passage mid-tropospheric downward motion can be clearly seen on both plots on 9-10 February (observations 96-104). The MAPS plot shows a maximum downward velocity of over 10 mb hr^{-1} between 500-700 mb, while the radiosonde plot indicates a stronger downward velocity of over 30 mb hr^{-1} in the same region.

Temperature Tendency due to Horizontal Advection

Once again, the radiosonde time series plot reveals considerably more detail than does the MAPS plot (Fig. 6.7), especially in the boundary layer. For example, the low-level cold air advection associated with the passage of the cold front on 29 January (observations 6-10) shows up rather well from the surface up to 875 mb on the radiosonde plot, whereas the MAPS plot does not capture this event. The same thing happens with

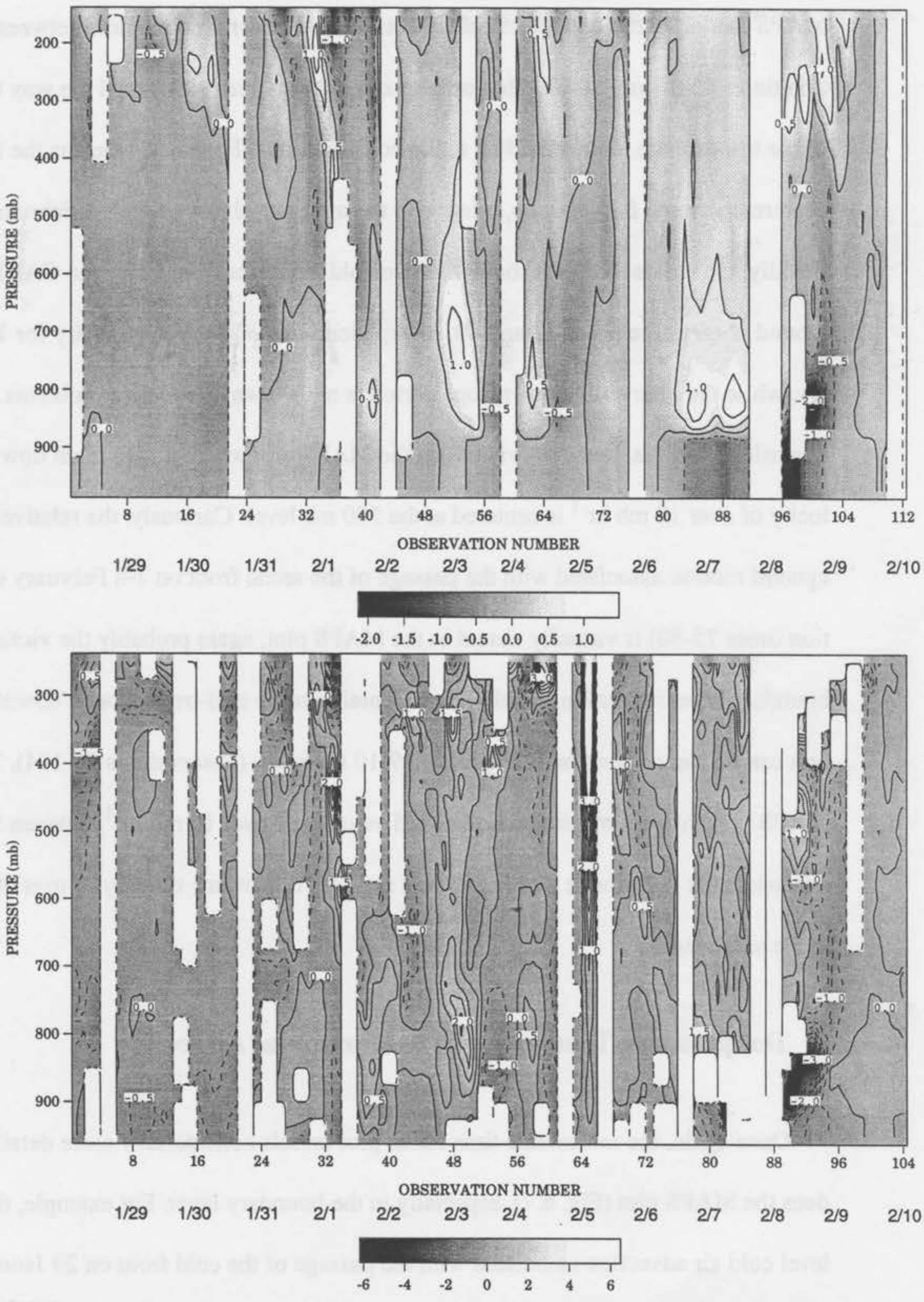

FIGURE 6.7: 13-day time series plots of horizontal temperature advective tendency from MAPS model (upper) and radiosonde (lower) data, starting at 00 UTC on 29 January 1994 through 21 UTC on 10 February 1994. Contours are in K hr^{-1} (dashed contours represent negative values), and numbers on the abscissa represent multiples of 8 observations spaced 3 hours apart (8 observations per day), with dates below.

the passage of the cold front on 4 February (observations 52-56), where the radiosonde plot shows the cold air advection extending from the surface to nearly 700 mb and the cooling reaching a maximum of -1 K hr^{-1} around 850 mb. By contrast, this cooling is only hinted at in the MAPS plot. On the other hand, the warming event due to the downslope winds on 2 February (observations 34-38) was captured by both data sets in spite of large sections of missing data. What is interesting to note is that the warm air advection appears to have taken place first in the upper atmosphere, and then each underlying level in turn experienced the warming down to the surface over the span of about 24 hours. The radiosonde plot shows that maximum warming took place between 400 -500 mb, reaching a peak of about 2 K hr^{-1}. Both plots also indicate warm air advection took place (observations 48-52) in the lower troposphere prior to the cold front passage on 4 February, from the surface to just about 600 mb, reaching a maximum of about 2 K hr^{-1}. Presumably this could be explained by the southerly winds reported in the weather summary ahead of the front. The strong warm air advection that appeared to take place at observation 64 (5 February) in the radiosonde plot is nowhere to be found in the MAPS plot. This is because it is associated with the anomalous spike in temperatures indicated by the radiosonde data set at this observation time, seen in Fig. 6.2 above. The temperature tendency due to horizontal advection based on radiosonde data is missing at the observation time corresponding to the second temperature spike in Fig. 6.2 (observation 75), so we do not see a similar region of strong warming in Fig. 6.7 at this observation. Unfortunately, there is a lot of missing data surrounding the arrival of the arctic front during the day on 7 February (ending at observation 80). We can, however, see that cooling did indeed take place during and after the frontal passage, and the MAPS plot indicates that the cooling rate was in excess of $-2\ K\ hr^{-1}$ from about 800-850 mb. Contrary to the downslope event on 2 February, both the radiosonde and MAPS plots indicate that cold air advection took place initially in the lowest levels of the troposphere, and then progressed to higher and higher levels over the span of nearly 2 days, reaching as high as 400 mb in Fig. 6.7 and even higher in Fig. 6.7. At the same time the cold air advection was reaching the highest levels, the lowest levels were beginning to cool at a slower rate. The overall picture, then, is of a cold air mass that was shallow initially at its southern flank yet fairly deep at its northern edge. As it moved over the CART site, the lower levels in contact with the earth were modified to a certain extent, such that the air mass was warmed slightly in these regions while the upper portions remained unaffected.

Water Vapor Mixing Ratio Tendency due to Horizontal Advection

In general, the values of the water vapor mixing ratio tendency due to horizontal advection are very small, which is to be expected considering the time of year. Positive values associated with the frontal passage and period of precipitation that followed on 1 February (observations 28-32) can be clearly seen on the radiosonde time series plot (Fig. 6.8), extending from the surface only as high as about 850 mb. Since this shallow flux of moisture is situated in the boundary layer, it is no surprise that the MAPS plot does not pick up this feature. Both data set indicate a small influx of moisture at the time of the next frontal passage on 3-4 February (observations 48-52). However, this is followed very quickly by the advection of drier air, which would be in agreement with the observation that clouds, but no precipitation was associated with this particular system. As before, the levels experiencing moistening were mainly confined to the boundary lay-

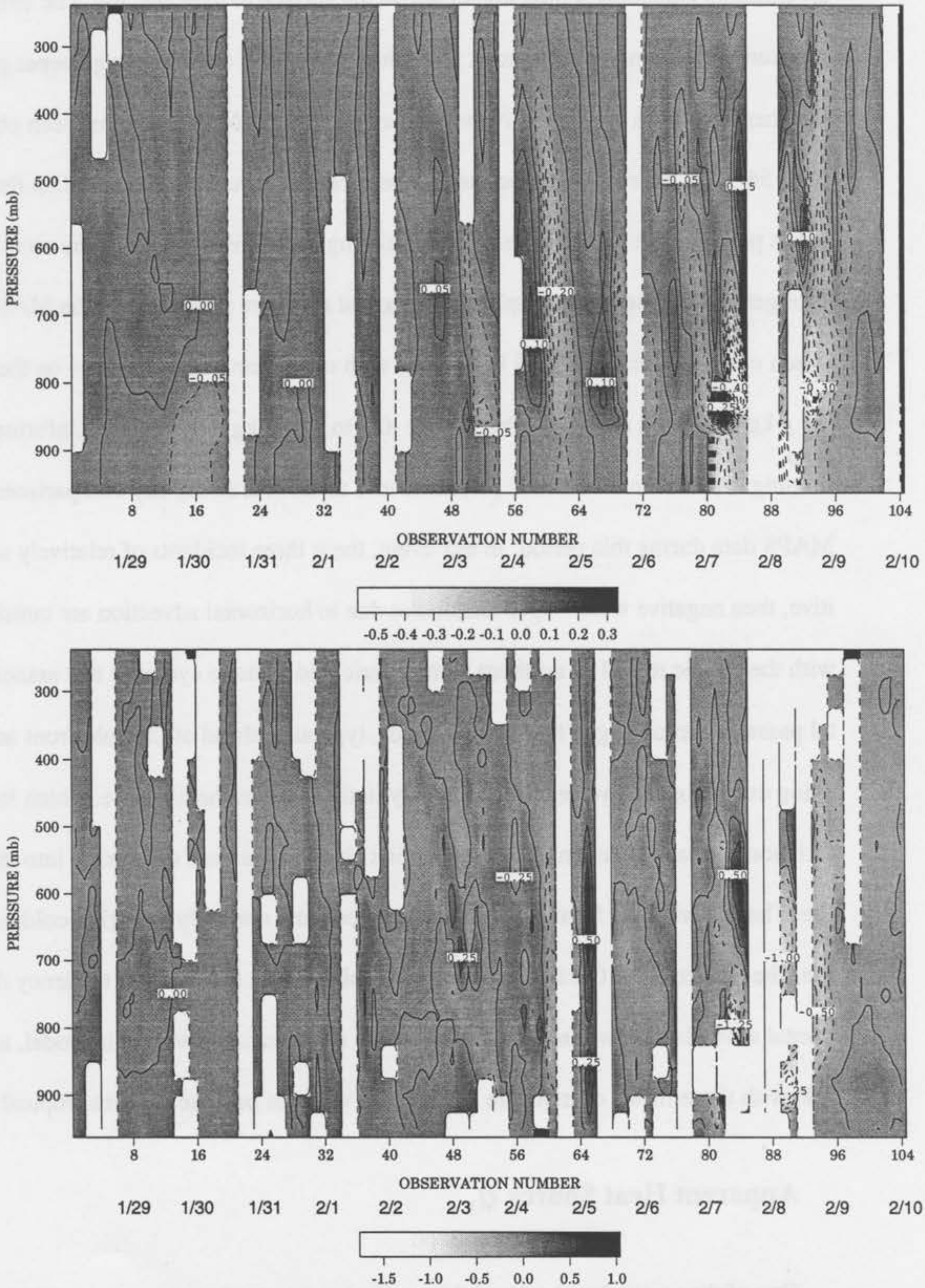

FIGURE 6.8: 13-day time series plots of horizontal water vapor mixing ratio advective tendency from MAPS model (upper) and radiosonde (lower) data, starting at 00 UTC on 29 January 1994 through 21 UTC on 10 February 1994. Contours are in g kg^{-1} hr^{-1} (dashed contours represent negative values), and numbers on the abscissa represent multiples of 8 observations spaced 3 hours apart (8 observations per day), with dates below.

er, although extending a little higher above the surface to over 800 mb. The strongest moisture advection, however, took place during a period of alternating deeper positive, then negative, then again positive values, evident on the MAPS plot between observations 56-72 (4-6 February). The same pattern can be somewhat discerned on the radiosonde plot, despite the large amounts of missing data. This is followed by an even stronger positive/negative couplet of horizontal moisture advection on the MAPS plot between observations 80-96 (7-9 February), with maximum positive values on the order of 0.3 g kg^{-1} hr^{-1} and negative values in the -0.3 to -0.4 g kg^{-1} hr^{-1} range. Unfortunately, missing data on the radiosonde plot precludes us from drawing any comparisons with the MAPS data during this period. In any event, these three incidents of relatively strong positive, then negative water vapor tendencies due to horizontal advection are consistent with the classic model of northern hemispheric mid-latitude cyclones and associated frontal passage. According to this model, winds, typically, ahead of the cold front accompanying extra-tropical cyclones are southerly in the northern hemisphere, which in Oklahoma means advecting warm and moist air from the Gulf of Mexico into the CART site. Then, behind the front the wind shifts to become northerly, bringing colder, drier air over the site from the Great High Plains. The sign of the temperature tendency due to horizontal advection shown in the above plots are also consistent with this model, and coincide with these fluxes of moisture as expected with the passage of extra-tropical cyclones.

Apparent Heat Source Q_1

One of the major drawbacks of this particular data set for our purposes was the absence of significant convective activity. This lack of convection is not surprising, given that the time period is late in the mid-latitude northern hemisphere winter. Solar insolation, although increasing, is not yet to the point where significant warming at the earth's surface has taken place. Moreover, as we have seen in the time series plots for water vapor mixing ratio, the lower troposphere in general is not yet terribly moist, with maximum values only around 6.5-7.0 g kg^{-1}. Thus, the two main ingredients for deep convection, heat and moisture, are lacking. As a consequence, we would expect the time series plot of Q_1 to be relatively quiet, and indeed a look at the time series plot for Q_1 from the MAPS and radiosonde data (Fig. 6.9) shows this to be the case, with a few exceptions. Moreover, as explained above, the fact that *all* data must be present from adjacent observation times in order for Q_1 (and Q_2) to be computed accounts for the large number of gaps evident in the time series plots.

In general, Q_1 is an indication of the diabatic heating (or cooling) effects due to convective processes where condensation (or evaporation) is taking place. Additionally, changes in temperature related to convection can come about through vertical eddy fluxes of heat, as discussed in Chapter 5. Therefore, we mainly expect to see positive values of Q_1 (warming) under two conditions: 1) where clouds are being formed as water changes phase from vapor to liquid, giving off latent heat in the process, and 2) in the upper troposphere where heating would most likely be associated with compensating subsidence in the environment surrounding cumulus clouds. Conversely, we expect that Q_1 will be negative (cooling) in regions where evaporation/sublimation is occurring. This would be the case, for example, where precipitation is falling through sub-saturated air below a cloud base. Additionally, upper tropospheric cooling could be associated with the evaporation of detrained cloud water transported by updrafts.

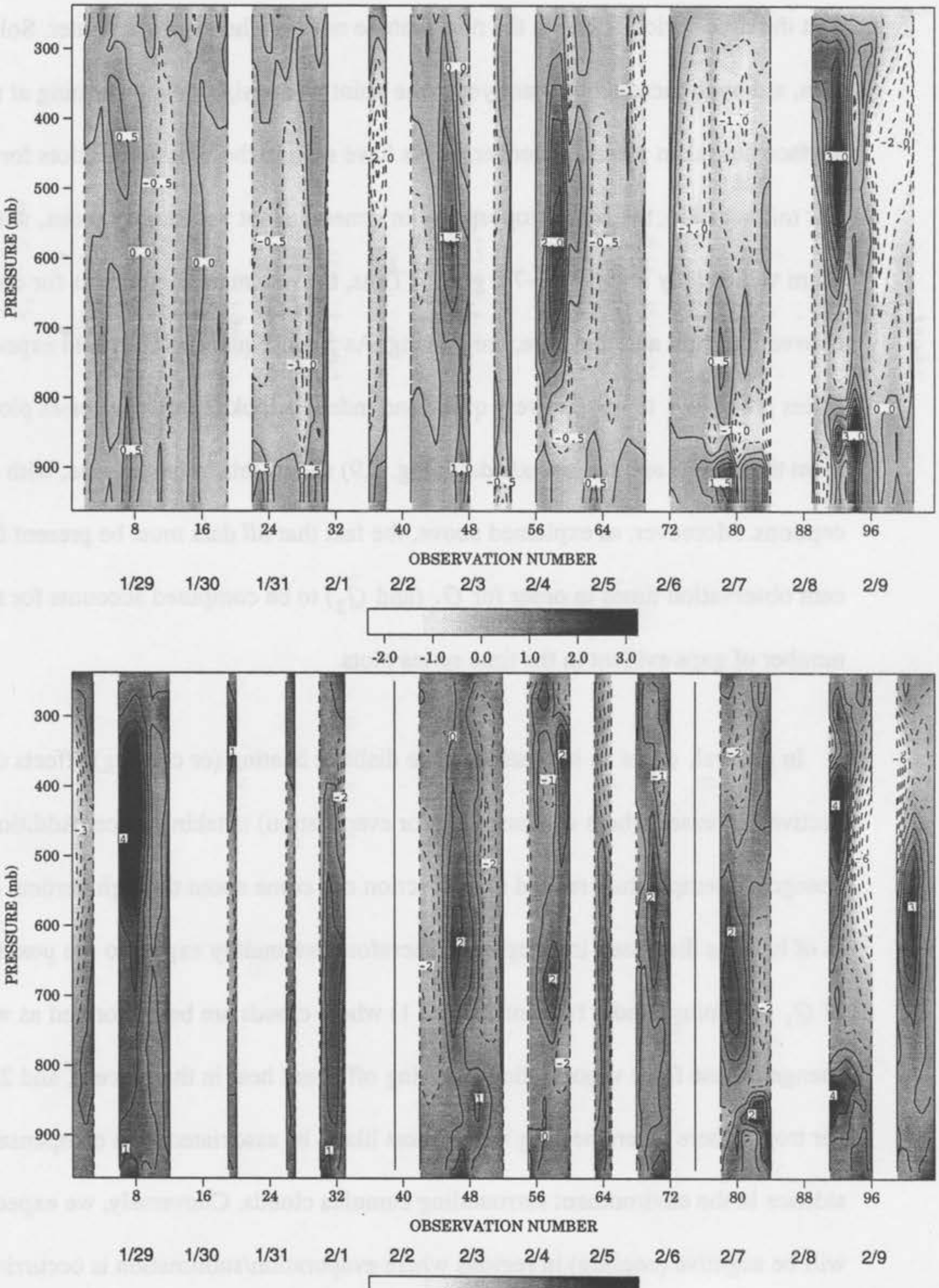

FIGURE 6.9: 13-day time series plots of the apparent heat source from MAPS model (upper) and radiosonde (lower) data, starting at 00 UTC on 29 January 1994 through 21 UTC on 10 February 1994. Contours are in K hr^{-1} (dashed contours represent negative values), and numbers on the abscissa represent multiples of 8 observations spaced 3 hours apart (8 observations per day), with dates below.

Looking at Fig. 6.9, the radiosonde plot reveals a region of relatively strong warming between observations 6-12 (during the days of 29-30 January) from the lower troposphere up to about 275 mb, reaching a maximum of over 4 K hr^{-1} in the 550 - 350 mb range. This warming event coincides with the passage of the cold front mentioned in the weather summary and is therefore probably associated with any weak convective activity leading to cloud formation. The MAPS plot also shows warming throughout the depth of the troposphere during this interval, although the magnitude of the warming, 0.5 K hr^{-1} between 500 - 350 mb, is quite a bit less than that indicated by the radiosonde plot. A few hours later, an area of negative Q_1, extending from about 850 -300 mb, is evident in the MAPS plot. This could be due to evaporation of clouds in drier air above the low-level upslope reported on 30 January in the weather summary. Unfortunately, this negative tendency does not show up in the radiosonde time series plot due to missing data, so it is difficult to verify that the cooling really did take place. Both the radiosonde and MAPS plots indicate that two other regions of relatively strong warming occurred in the mid- to upper-troposphere, the first being located between observation 45 - 50 (2-3 February), and the second between observations 56-60 (4-5 February). During both of these events, the weather summary indicates that there was a significant amount of cloudiness in conjunction with the passage of a slow-moving cold front, and the positive values of Q_1 confirm this observation. In these instances, the location and magnitude of maximum warming are comparable between the two data sets, with the MAPS plot showing over 1.5 K hr^{-1} and 2.0 K hr^{-1} centered at about 575 mb for the two intervals respectively, while the radiosonde plot shows over 2.0 K hr^{-1} for both intervals, centered near 650 mb and 675 mb, respectively. Interestingly, during the second interval (observations 56-60), there is a small zone of negative Q_1 indicated in both plots in the lower troposphere, below and lagging slightly behind the regions of positive Q_1. Since the weather summary states that no precipitation was detected with the passage of this particular front, these negative values could indicate that precipitation may have actually been occurring below the cloud bases, only to be totally evaporated as it fell through drier air near the surface.

Another period of significant trends in the apparent heat source is in relation to the passage of the arctic front. Both plots show a region of positive Q_1 in the lower troposphere at the onset of the arctic front, between observations 75-85 (7-8 February), while cooling took place simultaneously in the upper troposphere. The advent of low-level cloudiness accompanying the arrival of the front could explain the positive values of the apparent heat source in the low- to mid-troposphere. On the other hand, the cooling in the upper-troposphere might be associated with the evaporation of cirrus and high level altostratus. In both instances, the heating and cooling rates are shown to be greater in magnitude for the radiosonde than for the MAPS data, with the former reaching heating rates of over 2.0 K hr^{-1} at 850 mb and 750-550 mb, compared with 0.5 -1.5 K hr^{-1} between 900 - 700 mb for the latter. Similarly, the cooling rates reached a maximum of -2.0 K hr^{-1} centered at 350 mb for the radiosonde data, compared with roughly half that intensity for the MAPS data between 450 - 350 mb. A second period of relatively strong warming in the upper-troposphere is shown in both plots centered around observation 90 (8-9 February), with a secondary zone of warming in the lower troposphere. Sandwiched in-between is an area of negative Q_1. During this time, the weather summary indicates that there continued to be considerable cloudiness over the CART site, and that precipitation eventually broke out. A possible scenario that would tie together this pattern of heating in the upper-troposphere, cooling in the mid-troposphere, and heating again in the lower-troposphere would be a feeder-seeder process. Upper-level clouds could have formed, eventually leading to precipitation in the form of ice crystals considering the temperature at that altitude. Evaporation may then have taken place as the crystals fell through drier air in the mid-troposphere, resulting in the cooling shown. Those crystals that survived could have subsequently served as nucleating sites, promoting cloud formation and growth in the lower troposphere. This might explain not only the warming that took place between 900 - 800 mb, but also the slight lag in time behind the upper-tropospheric warming. What is interesting to note is that both the MAPS and radiosonde plots are fairly close in agreement as to the magnitude of the heating and cooling rates that took place during this period.

One final feature on the MAPS plot that is of interest is the two stronger regions of negative Q_1 in the mid- and upper-troposphere. The first is shown to have occurred between observations 36 - 38 (2 February), reaching a peak value of -2 K hr^{-1} at around 450 mb. This cooling is possibly explained by cirrus and other lower clouds being evaporated in the dry downslope winds reported on that particular day. Unfortunately, missing data in the radiosonde plot prevents a second perspective on this episode. A second mid- to upper-tropospheric cooling event is indicated by both plots to have taken place during the last day shown. This coincides with the period of high pressure and clearing skies indicated in the weather summary. Thus, the cooling shown is again possibly due to the evaporation of clouds in subsident atmospheric motions, implied by the presence of the high pressure ridge. In both cases, evaporation of cloud liquid water had to be the dominating effect to counteract any warming due to adiabatic compression in the subsident flow, and thus result in the net cooling displayed.

As discussed, the maximum warming rates observed during the January-February 1994 IOP were on the order of 4 K hr^{-1}, while the strongest cooling rates were over -6 K hr^{-1}. This is more or less comparable to the results obtained by Gallus and Johnson (1991) where maximum warming and cooling rates of over 13 K hr^{-1} and -6 K hr^{-1}, respectively, were noted during the life cycle of the Oklahoma squall line they analyzed. The fact that they found stronger maximum heating rates is further evidence of the lack of strong convective activity during the January-February IOP used here. By way of contrast, the largest values of Q_1 shown by Cotton and Anthes (1989) for diagnostic studies performed on data from the tropics are on the order of +/- 5-10 K day^{-1}, which is considerably less than the computed rates we have seen for the midlatitudes. We anticipate that the apparent heat source computed for the April 1994 will show even larger warming rates due to the more vigorous convection typical for that time of year in the Southern Great Plains.

Apparent Moisture Sink Q_2

The time series plot of the apparent moisture sink derived from the radiosonde and MAPS data sets (Fig. 6.10) provides an indication of areas where water vapor is decreasing (or increasing), depending on whether condensation (or evaporation) is the dominant process at a given level in the atmosphere. We would expect these processes to be enhanced in proportion to the level of any convective activity. Therefore, positive values of

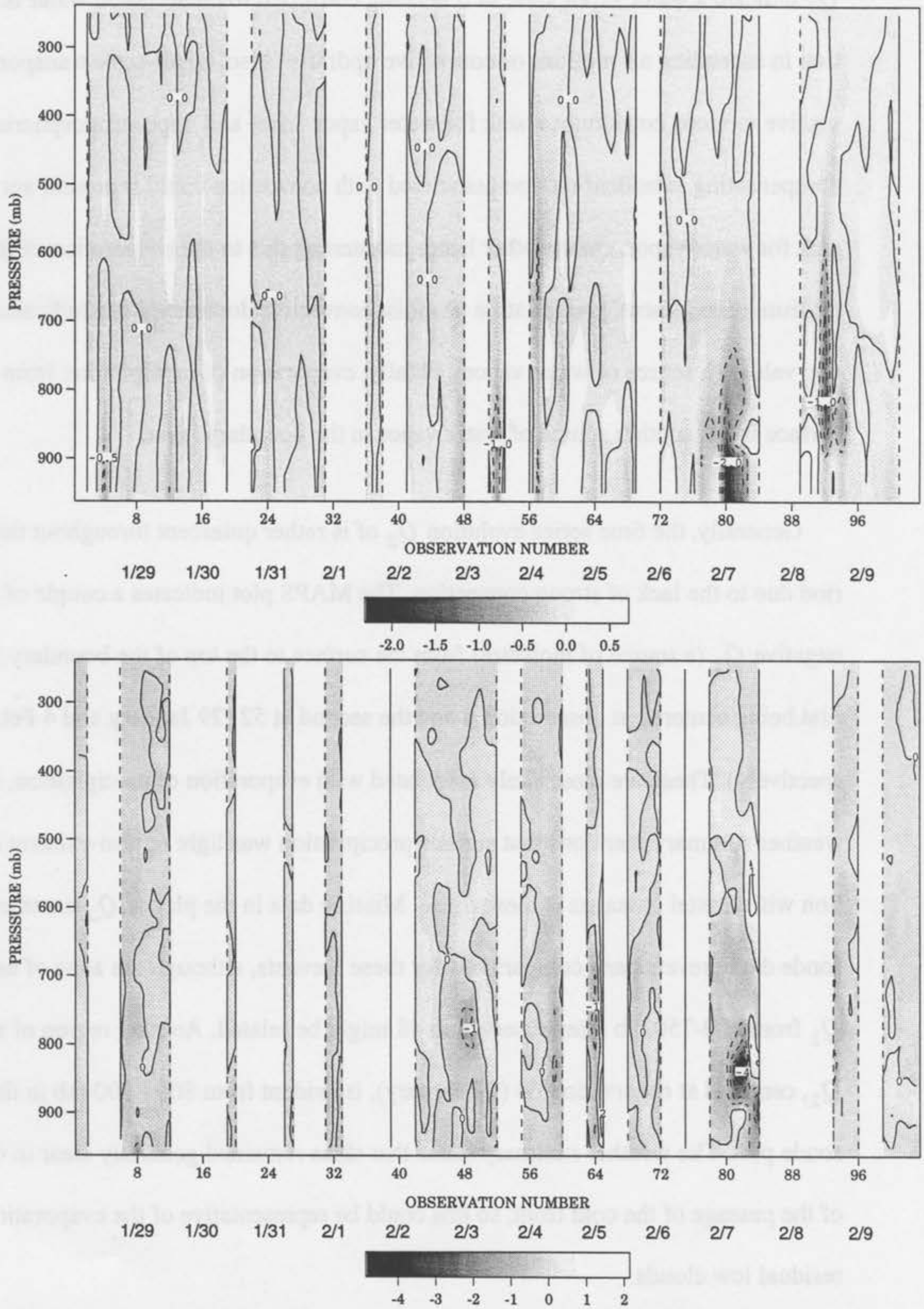

FIGURE 6.10: 13-day time series plots of the apparent moisture sink from MAPS model (upper) and radiosonde (lower) data, starting at 00 UTC on 29 January 1994 through 21 UTC on 10 February 1994. Contours are in K hr^{-1} (dashed contours represent negative values), and numbers on the abscissa represent multiples of 8 observations spaced 3 hours apart (8 observations per day), with dates below.

Q_2 indicate a water vapor sink, as it is being converted to cloud liquid water or precipitation in ascending air motions or convective updrafts. Also, small-scale transport by convective motions constitutes a sink for water vapor. Mid- and upper-tropospheric drying in compensating subsident motion associated with convection could represent yet another a sink for water vapor. On the other hand, moistening due to the evaporation of liquid water from detrainment, precipitation or moist convective downdrafts are indicated by negative values (a source of water vapor). Finally, evaporation of precipitation from the surface is yet another source of water vapor in the boundary layer.

Generally, the time series evolution Q_2 of is rather quiescent throughout the entire period due to the lack of strong convection. The MAPS plot indicates a couple of zones of negative Q_2 (a source of moisture) from the surface to the top of the boundary layer, the first being centered at observation 4 and the second at 52 (29 January and 4 February, respectively). These are most likely associated with evaporation of precipitation, as the weather summary mentions that surface precipitation was light or non-existent in connection with frontal passages at these times. Missing data in the plot of Q_2 based on radiosonde data prevents any comparisons for these 2 events, although the zone of negative Q_2 from 800-750 mb after observation 48 might be related. Another region of negative Q_2, centered at observation 64 (5 February), is evident from 800 - 700 mb in the radiosonde plot. The weather summary states that skies remained generally clear in the wake of the passage of the cold front, so this could be representative of the evaporation of any residual low clouds.

As in the time series plot of Q_1, the area of most significant changes in Q_2 takes place towards the end of the IOP in relation to the passage of the arctic front. Unfortunately, due to missing data, we are unable to analyze a good portion of this episode. Nevertheless, the MAPS plot shows a region of positive Q_2 from observations 72 - 75 (7 February), reaching from the surface up to almost 800 mb. This could be due to the formation of low clouds as the front advanced over the CART site. The radiosonde plot also shows some low-level warming between observations78-82, as well as mid-tropospheric warming from about 700 mb to the tropopause, with the highest positive value of the entire period being over 1 K hr^{-1}, centered at 600 mb. Again, it is reasonable to associate these zones of positive Q_2 with regions of deeper cloud formation. Next, both radiosonde and MAPS plots agree that fairly strong negative values of Q_2 occurred, extending from the surface up beyond the 800 mb level, indicative of a substantial source of water vapor. This coincides with the outbreak of precipitation recorded in the weather summary and could consequently be another example of lower-level moistening through evaporation of precipitation. The MAPS chart puts the maximum moistening rate at over -2 K hr^{-1} while the radiosonde plot shows it was over -4 K hr^{-1}. Finally, the MAPS plot shows that a zone of weak drying occurred from observation 88 to about observation 90, starting at the surface and extending up to nearly 700 mb, and that moistening took over through observation 94, between approximately 850 - 600 mb. This could be the result of cloud formation and subsequent evaporation in subsiding air associated with the high pressure and clearing skies reported in the weather summary on this date.

We have seen that the maximum rates of Q_2 for the January-February 1994 IOP range from approximately -4 K hr^{-1} to over 1 K hr^{-1}. Again, comparing these with the values obtained by Gallus and Johnson (1991), they reported maximum sink rates of over

8 K hr^{-1}, while the highest source rates were approximately -6 K hr^{-1} for the Oklahoma squall line. On the other hand, Cotton and Anthes (1989) show maximum sink rates of about 10 K day^{-1} and maximum source rates of nearly -5 K day^{-1} for results from tropical studies. As before, we anticipate Q_2 values closer in magnitude to those found by Gallus and Johnson, using data from the more convectively active April 1994 IOP.

6.2.2 Statistical Comparison

Given the magnitude of the missing data problem, the following statistical discussions are based on observations yielding usable data. Thus the temporal averages, standard deviations and correlation were calculated based only on those observation times and pressure levels for which reasonable data was actually present in both the MAPS and radiosonde data sets.

Temperature

The time-averages plotted in Fig. 6.11 show that both the radiosonde and MAPS temperatures are virtually identical from the tropopause down to about 830 mb, below which point the MAPS averages are consistently higher than those of the radiosondes all the way down to the surface. This discrepancy is clearly shown in the correlation plot, where the strongly positive coefficient of approximately 0.98 at all levels above 830 mb abruptly drops down to 0.7 at 950 mb. As opposed to the previous variables, the standard deviations of the MAPS and radiosonde data are quite similar throughout the troposphere, with the radiosonde deviations being slightly greater between 850 - 700 mb, and again between 450 -350 mb. On the other hand, the MAPS data exhibit slightly larger devia-

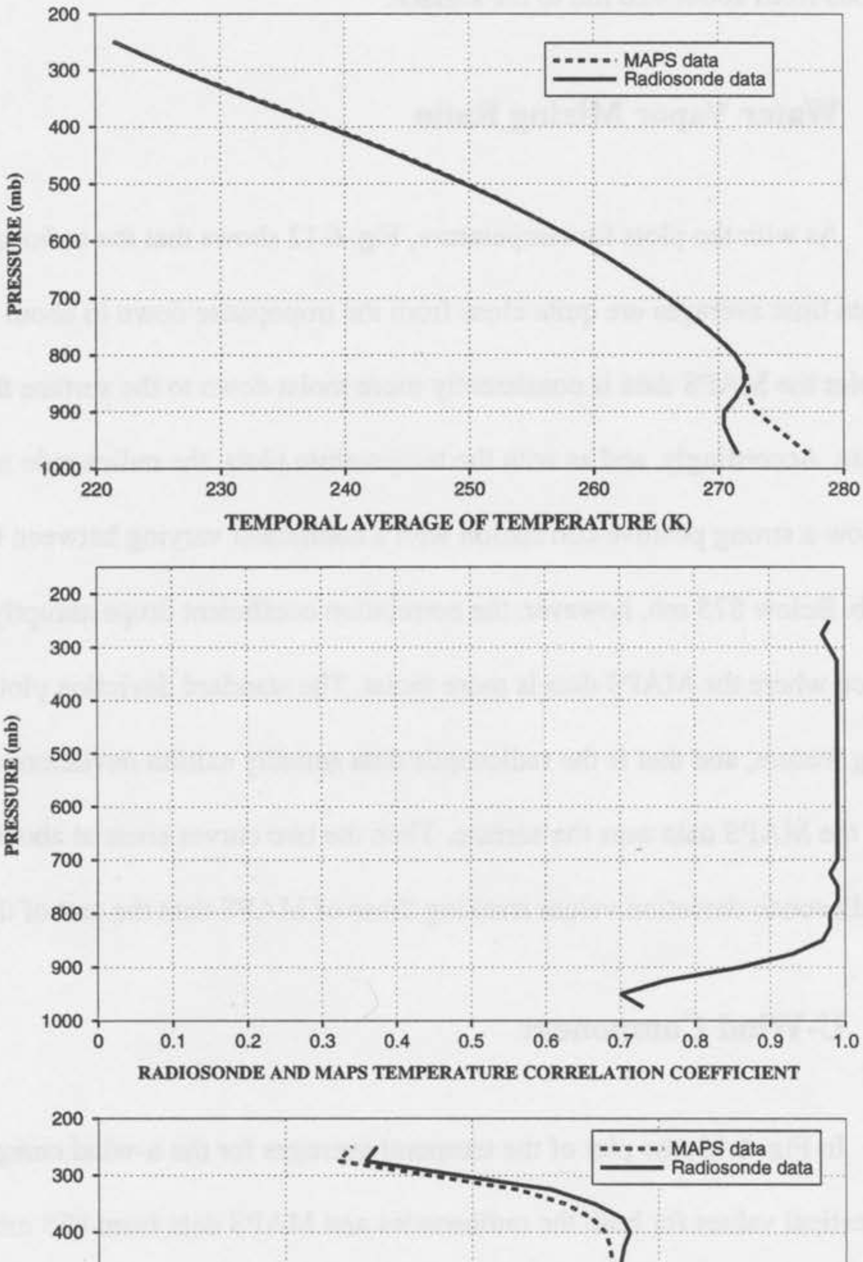

FIGURE 6.11: Temperature temporal averages, correlation and standard deviations of January-February 1994 IOP MAPS and Radiosonde data.

tions from about 920 mb to the surface.

Water Vapor Mixing Ratio

As with the plots for temperature, Fig. 6.12 shows that the radiosonde and MAPS data time averages are quite close from the tropopause down to about 875 mb, at which point the MAPS data is consistently more moist down to the surface than the radiosonde data. Accordingly, and as with the temperature plots, the radiosonde and MAPS data show a strong positive correlation with a coefficient varying between 0.8 - 0.9 above 875 mb. Below 875 mb, however, the correlation coefficient drops abruptly to 0.3 in the region where the MAPS data is more moist. The standard deviation plot shows an interesting feature, and that is the radiosonde data actually exhibit deviations about half as large as the MAPS data near the surface. Then the two curves cross at about 875 mb with the radiosonde deviation values tracking those of MAPS data the rest of the way up.

U-Wind Component

In Fig. 6.13, the plot of the temporal averages for the u-wind component show nearly identical values for both the radiosondes and MAPS data from 875 mb to the tropopause, which is once again similar to the plot for temperature in Fig. 6.11. Below 875 mb, however, the MAPS curve looks rather suspicious and it should since this is in the boundary layer region where resolution for the model is problematic. The correlation coefficient shows a high degree of agreement above 875 mb, and then drops significantly below 875 mb where the MAPS data is questionable (although it does regain some near the surface). The standard deviations are similar for both the radiosonde and MAPS data, with

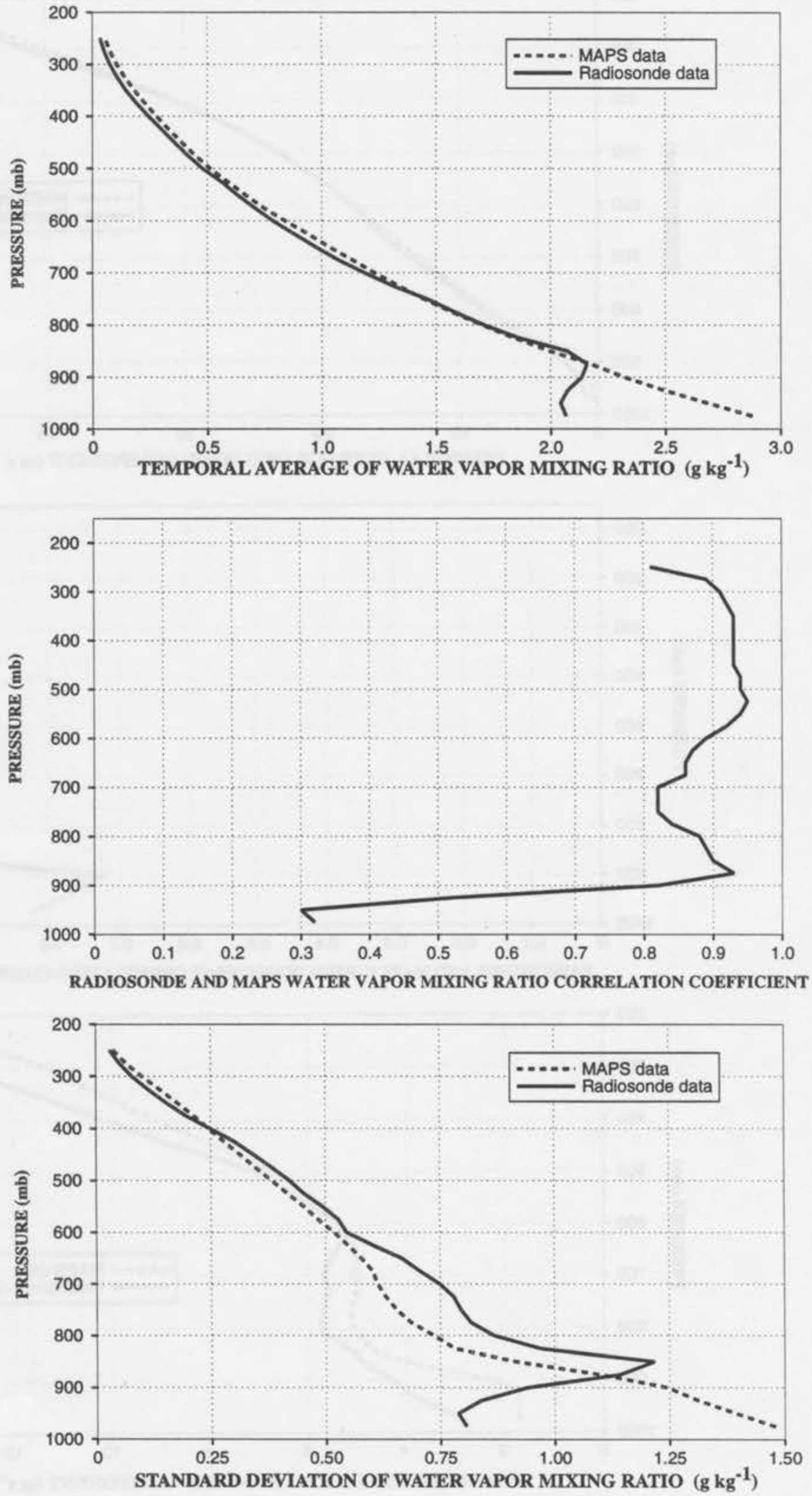

FIGURE 6.12: Water vapor mixing ratio temporal averages, correlation and standard deviations of January-February 1994 IOP MAPS and Radiosonde data.

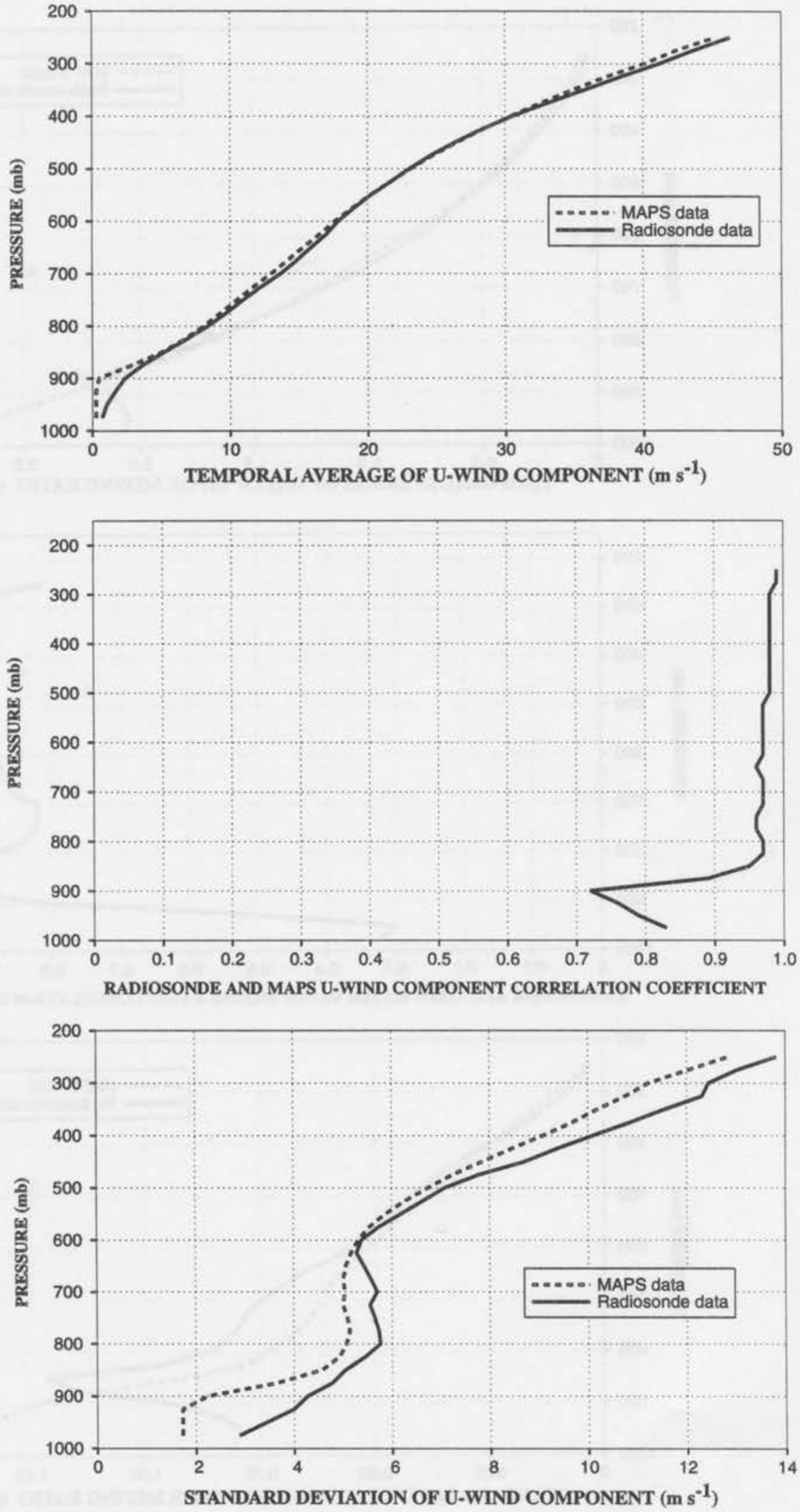

FIGURE 6.13: U-wind component temporal averages, correlation and standard deviations of January-February 1994 IOP MAPS and Radiosonde data.

the radiosonde values once again being slightly larger. What is interesting to observe for both the radiosonde and MAPS data is the steady increase in standard deviation values from the surface to about 800 mb, followed by an interval from 800 - 600 mb of relative constancy, and then a monotonic almost linear increase above 600 mb. This latter increase in standard deviation magnitude might be expected given the influence of the strong prevailing westerlies in winter. However, perhaps the increase in deviations could also be in part explained by the deterioration in radiosonde tracking capabilities and subsequent telemetry degradation with height. The fact that MAPS uses aircraft reports and wind profiler information in addition to radiosonde transmissions in its data assimilation cycle might account for the fact that its data experience consistently smaller deviations than the radiosonde data alone. Note the constant standard deviation value in the lowest levels for the MAPS data.

V-Wind Component

The findings for the v-wind component shown in Fig. 6.14 are practically the same as for the u-wind component, with a few notable exceptions. In the lower half of the troposphere, the average values for the radiosonde data are more strongly negative than those of the MAPS data; conversely, above 500 mb, the MAPS data tends to average higher values than those of the radiosonde data. The same problem of constant wind values below 900 mb is again evident in the MAPS averages. As with the u-wind component, the v-wind component temporal correlation is strongly positive above 875 mb, and then drops off nearly as sharply below this point before regaining a bit near the surface. And, was seen with the u-wind component plot, it is interesting to again note the increase in stan-

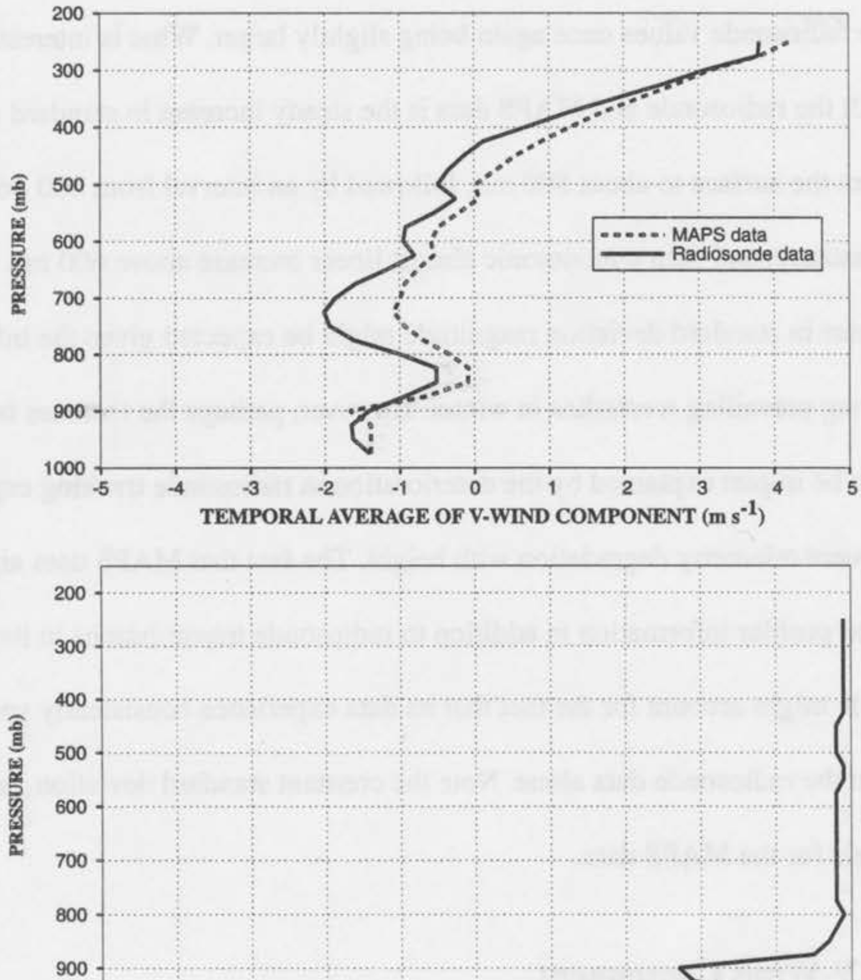

FIGURE 6.14: V-wind component temporal averages, correlation and standard deviations of January-February 1994 IOP MAPS and Radiosonde data.

dard deviations for both the MAPS and radiosonde data from the surface up to around 750 mb (except for the constant MAPS data deviation up to 900 mb), the interval of relatively constant or even decrease in standard deviations between 850 - 625 mb, and then the nearly linear, monotonic increase above 625 mb. This time, the standard deviations are even stronger than was the case for the u-wind component, which perhaps makes sense in light of the fact that the winter time v-wind component would not be as consistent as the u-wind component in terms of direction and strength. Additionally, the monotonic increase in standard deviations with height again suggests a deterioration in radiosonde data quality.

Divergence

Fig. 6.15 shows that the average values for the radiosonde divergences in general follow the sign of the MAPS values. The exceptions to this are in the region between roughly 450 - 575 mb, and from 900 mb to the surface. Additionally, the radiosonde averages tend to be larger than those of MAPS throughout the depth of the troposphere, except in the 825- 900 mb area. The correlation between the radiosonde and MAPS data shows a coefficient ranging back and forth from about 0.1 to 0.6. The zigzag nature of the correlation suggests some type of computational mode problem in the radiosonde processing (also evident in the time-average plot, top panel, of Fig. 6.15). The standard deviations are quite revealing in that the radiosonde data show a standard deviation nearly twice that of the MAPS data throughout the entire troposphere. Moreover, the standard deviations remain relatively constant for the MAPS data above 850 mb, whereas the radiosonde data show a greater degree of variability. This would suggest that the data collected by

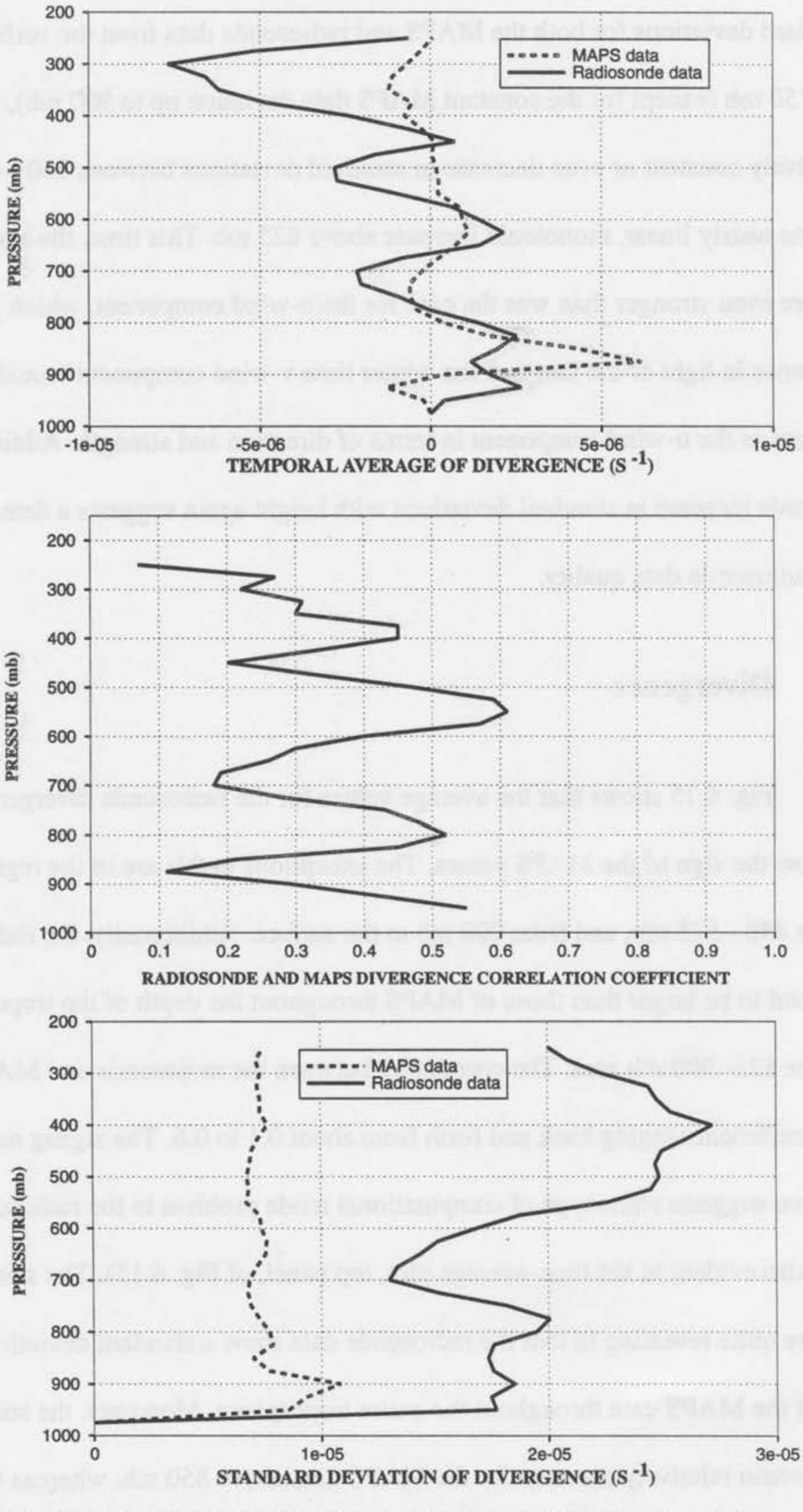

FIGURE 6.15: Divergence temporal averages, correlation and standard deviations of January-February 1994 IOP MAPS and Radiosonde data.

the radiosondes is considerably noisier than the model output from MAPS. On the other hand, this could be a result of artificial smoothing by the MAPS analysis scheme, or the fact that the domain covered by the radiosondes is so much smaller than that covered by the MAPS data.

Vertical Pressure Velocity

The vertical pressure velocity temporal averages of the radiosonde and MAPS data shown in Fig. 6.16 indicate a fair degree of similarity both in sign and magnitude, apart from the 400 - 700 mb region and from 900 mb to the surface. In the former interval, the radiosonde data show much larger average values than do the MAPS data, whereas in the latter region the converse is true. These differences are reflected in the correlation coefficient which reaches a maximum of just over 0.4 from between 900 - 700 mb, and then falls off in the same regions noted above, reaching a minimum of under 0.2 at around 550 mb. A look at the standard deviations shows that the sonde data again exhibits a standard deviation at least twice that of the MAPS data throughout the depth of the troposphere. This is explained by the large standard deviation values noted for the radiosonde divergences since these divergences have been used to calculate the vertical pressure velocity by the kinematic method.

Temperature Tendency due to Horizontal Advection

At first glance, the temporal averages in of the MAPS and radiosonde data in Fig. 6.17 appear to show a fair degree of similarity overall. Both averages are nearly equal in sign and magnitude from the surface up to about 500 mb, at which point there is a small

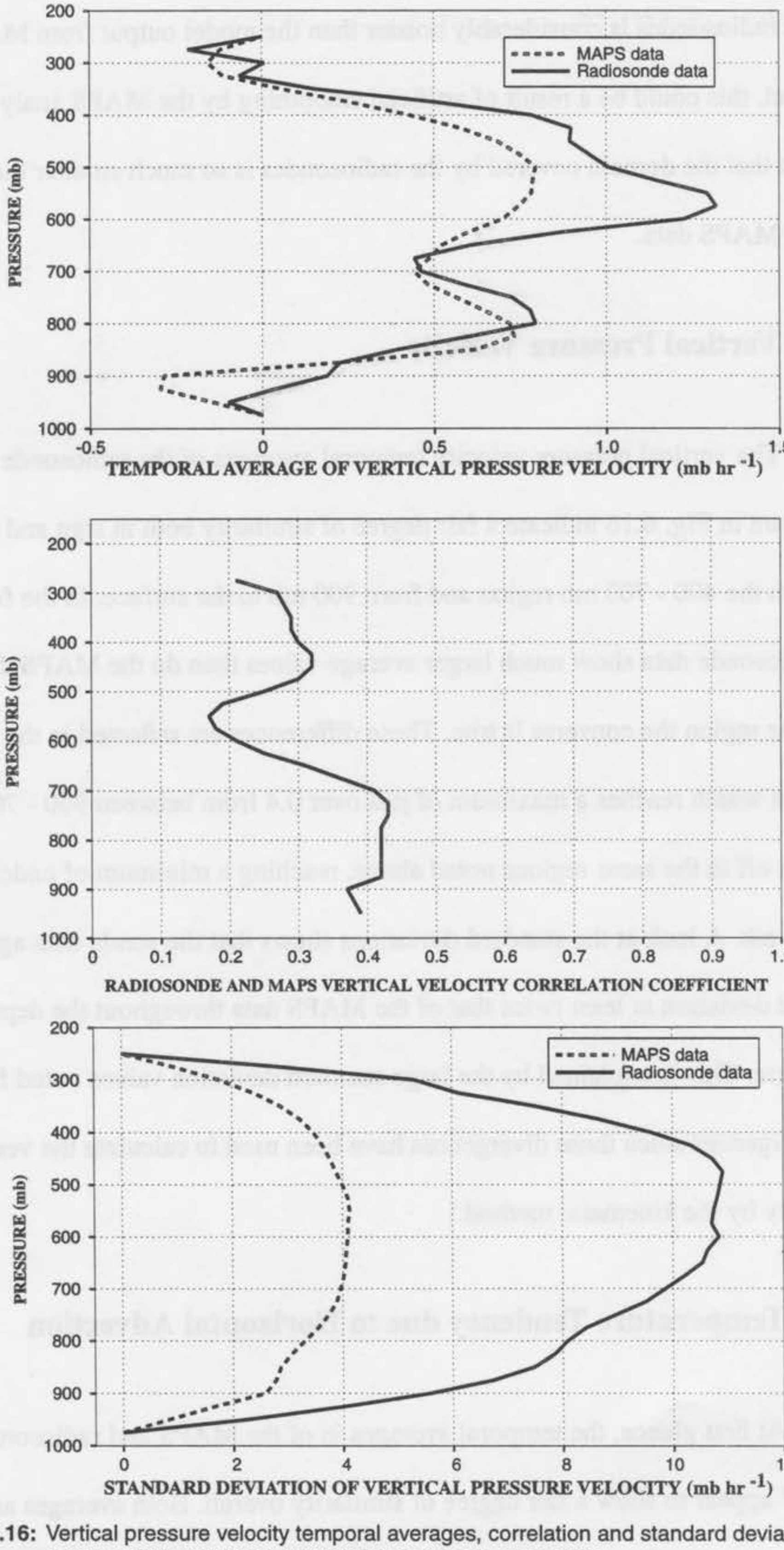

FIGURE 6.16: Vertical pressure velocity temporal averages, correlation and standard deviations of January-February 1994 IOP MAPS and Radiosonde data.

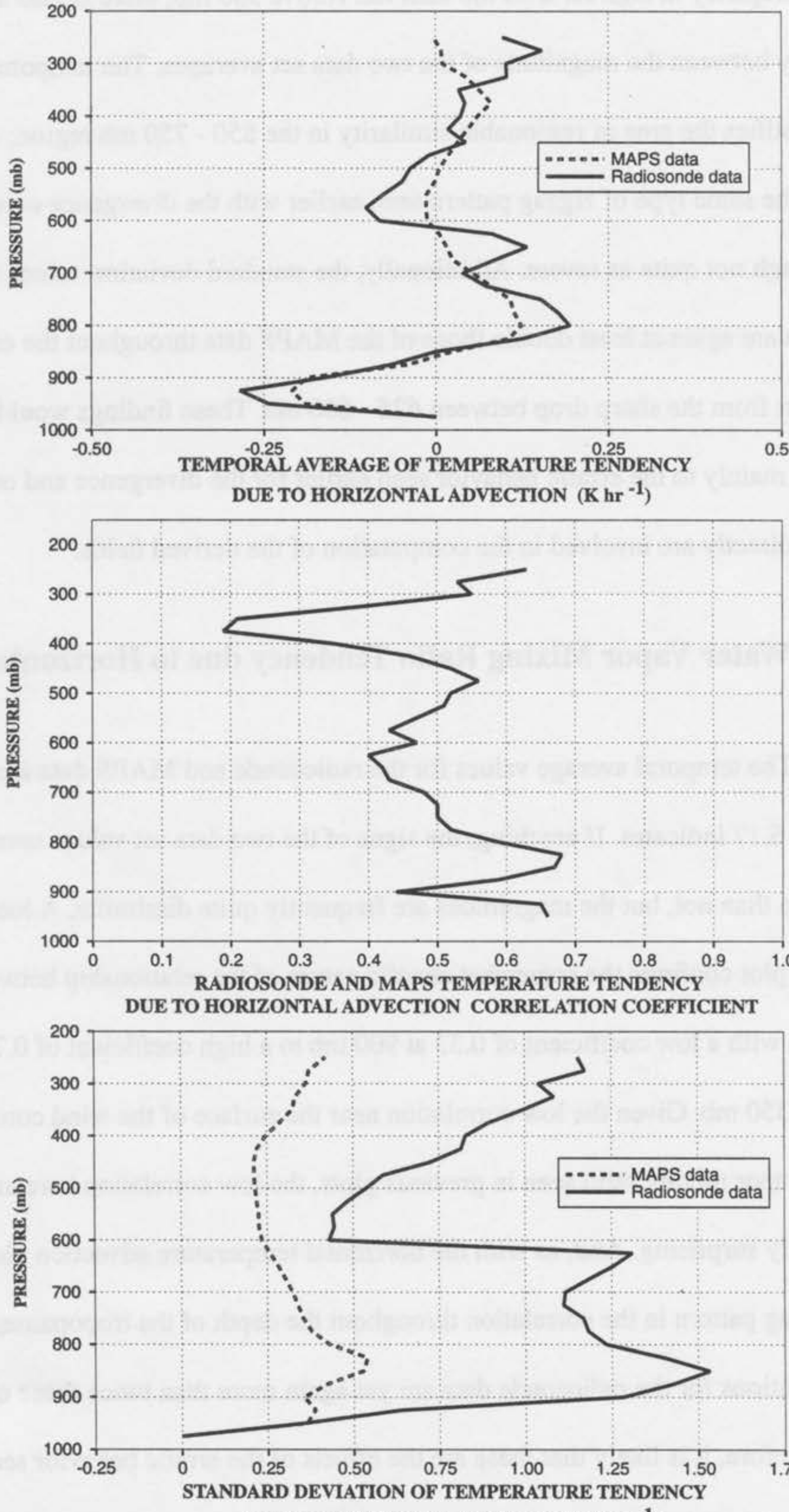

FIGURE 6.17: Temperature tendency due to horizontal advection temporal averages, correlation and standard deviations of January-February 1994 IOP MAPS and Radiosonde data.

discrepancy in sign for a 50 mb interval. Above 350 mb, there is also a widening discrepancy between the magnitude of the two data set averages. The temporal correlation plot identifies the area of reasonable similarity in the 850 - 750 mb region; otherwise it exhibits the same type of zigzag pattern seen earlier with the divergence correlation plot, though not quite as severe. Additionally, the standard deviation values of the radiosonde data are again at least double those of the MAPS data throughout the entire troposphere, apart from the sharp drop between 625 - 600 mb. These findings would presumably be due mainly to the erratic behavior seen earlier for the divergence and omega since these are directly are involved in the computation of the derived fields.

Water Vapor Mixing Ratio Tendency due to Horizontal Advection

The temporal average values for the radiosonde and MAPS data are quite erratic as Fig. 6.17 indicates. If anything, the signs of the two data set values seems to agree more often than not, but the magnitudes are frequently quite dissimilar. A look at the correlation plot confirms the somewhat chaotic nature of the relationship between the two data sets, with a low coefficient of 0.33 at 900 mb to a high coefficient of 0.7 at both 825 mb and 350 mb. Given the low correlation near the surface of the wind components and water vapor mixing ratio seen in previous plots, the low correlation here around 900 mb is hardly surprising. And, as with the horizontal temperature advection plot, we a similar zigzag pattern in the correlation throughout the depth of the tropopause, and the standard deviations for the radiosonde data are yet again more than twice those of the MAPS data. As before, it is likely that these are the effects of the erratic behavior seen earlier with divergence and vertical pressure velocity used in the derivation of the horizontal water va-

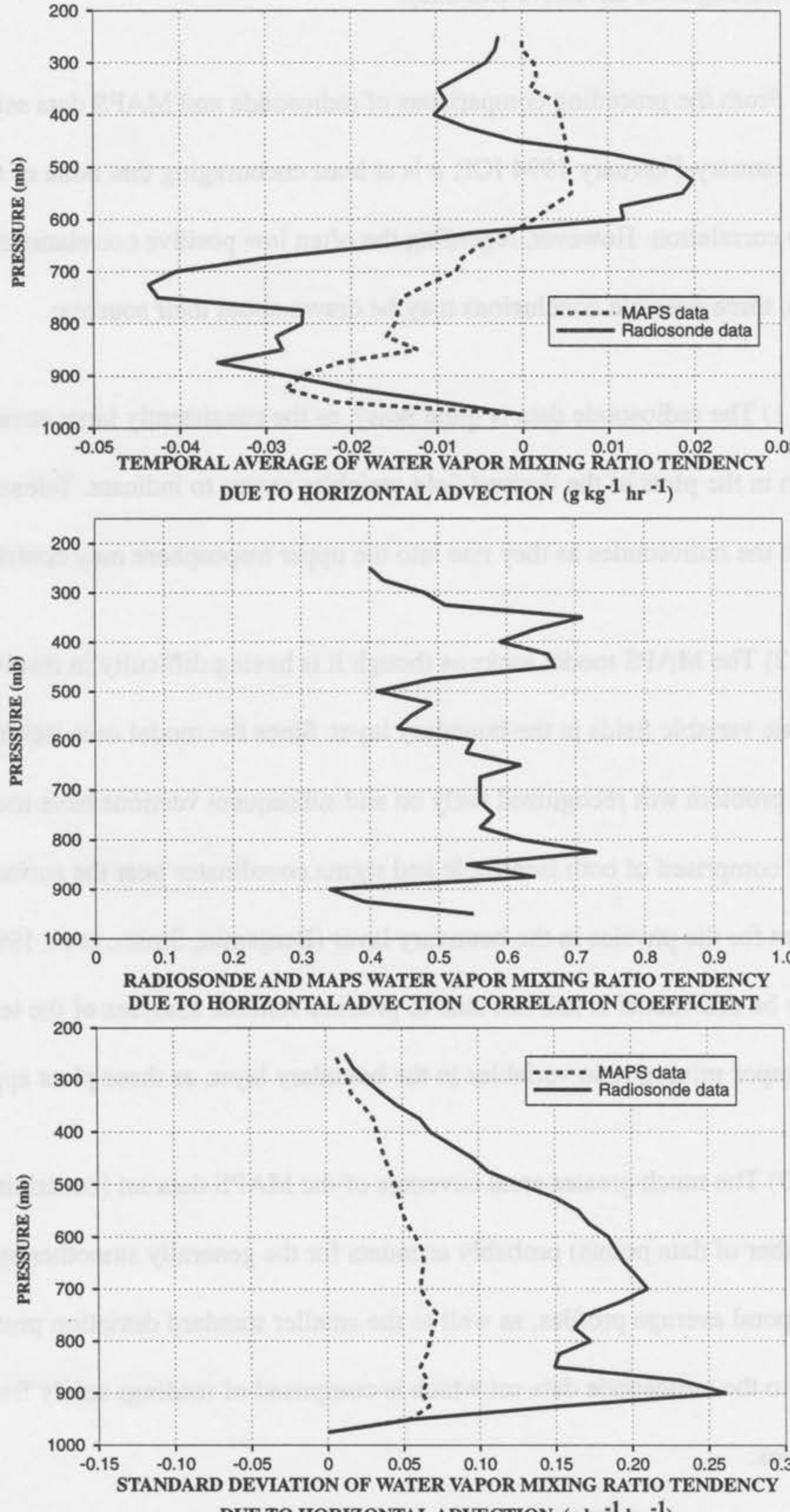

FIGURE 6.18: Water vapor mixing ratio tendency due to horizontal advection temporal averages, correlation and standard deviations of January-February 1994 IOP MAPS and Radiosonde data

por mixing ratio advective tendency.

From the preceding comparisons of radiosonde and MAPS data sets gathered during the January-February 1994 IOP, it is at least encouraging that none of the data show negative correlation. However, regarding the often low positive correlations between the data sets, three possible conclusions may be drawn about their sources:

1) The radiosonde data is quite noisy, as the consistently large standard deviations seen in the plots of the derived field variables seems to indicate. Telemetry problems with the radiosondes as they rise into the upper troposphere may contribute to the noise.

2) The MAPS model looks as though it is having difficulty in resolving the thermodynamic variable fields in the boundary layer. Since the model uses isentropic coordinates, this problem was recognized early on and subsequent versions have included a hybrid grid comprised of both isentropic and sigma coordinates near the surface to better account for the physics in the boundary layer (Benjamin, Smith, et al. 1991). However, it may be that model is still not able to produce reliable analyses of the temperature and water vapor mixing ratio variables in the boundary layer, as these plots appear to indicate.

3) The much greater areal coverage of the MAPS data set (containing a much larger number of data points) probably accounts for the generally smoother appearance of the temporal average profiles, as well as the smaller standard deviation profiles, in comparison to the radiosonde data set which is comprised of readings solely from the 4 radiosondes.

6.3 Moist Available Energy Calculations

RW 92 and WR94 found that the GCAPE is highly correlated with conventional measures of instability. Thus, any increases in temperature in the lower troposphere, or decreases in the upper troposphere, will result in higher amounts of GCAPE, as will increasing the low-level moisture either through advection or surface evaporation fluxes. Additionally, WR94 noted that the effects of large-scale vertical motion on temperature and moisture can have a significant impact on the rate of GCAPE production, in some instances causing the GCAPE to rise dramatically over the span of just a few hours. In this study, we perform the same types of analyses as did WR94: we will examine the actual time rate of change of the GCAPE for each 3-hourly observation interval (to the extent possible), and then compare this with the time rate of change of GCAPE production due to non-convective processes. As explained in Chapter 1, the computation of the GCAPE production rate is performed by constructing a hypothetical sounding based on large-scale processes acting over a time interval Δt (which, in this study, is 3 hours since the observations are made available every 3 hours), which is subsequently used as input into the GCAPE program. These large-scale, non-convective processes include the advection of temperature and moisture, as well as the effects of adiabatic heating (cooling) as air parcels descend (ascend). However, some major differences between this study and WR94 are that we are not taking into account heating or cooling due to radiative effects, nor are we explicitly taking into account surface evaporation or surface sensible heat fluxes. These are omitted here for simplicity.

Given the lack of vigorous convective activity during the winter IOP examined in this chapter, we would not expect to see large values of the actual GCAPE. The large-scale forcing will still be a contributing factor in the hypothetical amount of GCAPE produced, however, and this is quite evident in the 13-day time series plot from the MAPS and radiosonde (Fig. 6.19) data sets for these variables. The MAPS plot shows very little or no GCAPE was detected at any of the observation times throughout the entire period. The highest value computed was 0.3 J kg^{-1} at observation 55. By contrast, the predicted GCAPE from the hypothetical sounding was considerably larger at several observation times, the most notable being a value of 115.7 J kg^{-1} at observation 59. At observations 92 and 93, the hypothetical GCAPE reached 28.2 J kg^{-1} and 23.1 J kg^{-1}, respectively.

The high amount of predicted GCAPE at observation 59 (4-5 January) is difficult to explain, especially since there was no convective activity observed during this time according to the weather summary. However, a look at the large-scale forcing terms at this time shows that there was an interesting combination of events taking place. Both the MAPS and radiosonde plots for horizontal divergence (Fig. 6.5) indicate a zone of low-level convergence at that time in the lower troposphere, with values of over -3×10^{-5} s^{-1} and -4×10^{-5} s^{-1}, respectively. Accordingly, the time-series plot of vertical pressure velocity (Fig. 6.6) shows upward motion at observation 58 of over -15 mb hr^{-1} for the MAPS data, and -10 mb hr^{-1} for the radiosonde data. Additionally, the time series plots of temperature (Fig. 6.7) and moisture tendency (Fig. 6.8) due to horizontal advection indicate weak low-level warming and moistening at observation 58, with the MAPS plot reaching a maximum value of about 0.5 K hr^{-1} at 800 mb and 0.1 g kg^{-1} hr^{-1} at 750 mb respectively, while the radiosonde plot also shows over 0.5 K hr^{-1} at around 800 mb and

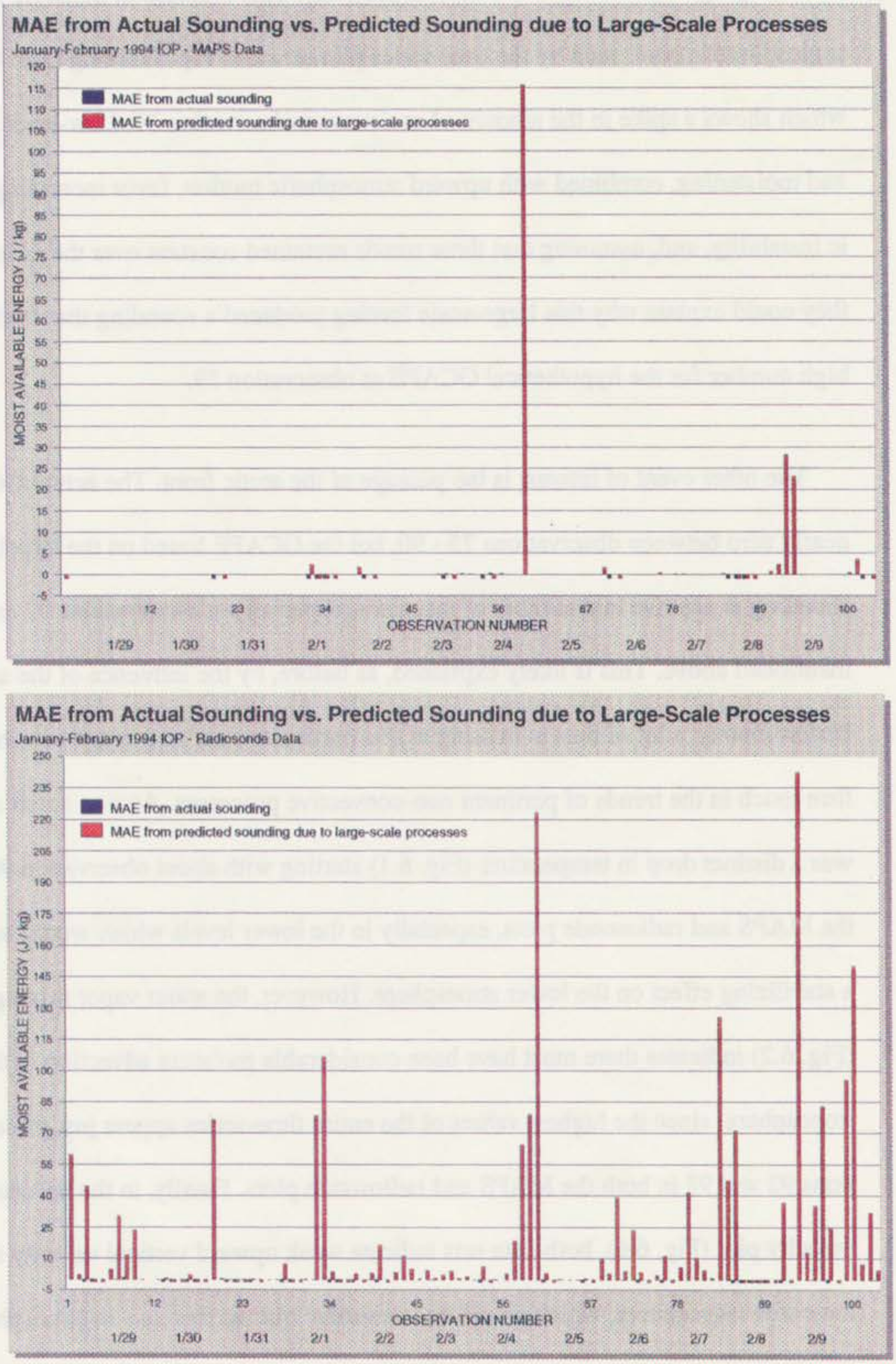

FIGURE 6.19: 13-day time-series plot of the moist available energy (GCAPE) from MAPS (upper) and radiosonde (lower) data, starting at 00 UTC on 29 January 1994 through 21 UTC on 10 February 1994. Units are J kg^{-1}, and numbers on the abscissa represent multiples of observations, with dates below. Negative values indicate data missing for that observation.

over 0.3 g kg^{-1} hr^{-1} at about 775 mb, respectively. This increase in moisture in the lower troposphere is confirmed by the time series plot of water vapor mixing ratio (Fig. 6.2), which shows a spike in the amount of moisture at observation 59. Low-level warming and moistening, combined with upward atmospheric motion, favor increasing atmospheric instability, and, assuming that these trends remained constant over the span of 3 hours, they could explain why this large-scale forcing produced a sounding that lead to such a high number for the hypothetical GCAPE at observation 59.

The other event of interest is the passage of the arctic front. The actual GCAPE is nearly zero between observations 75 - 90, but the GCAPE based on the hypothetical sounding is positive in a number of instances, especially at observations 92 and 93 as mentioned above. This is likely explained, as before, by the influence of the arctic front. Unfortunately, a lot of data is missing at this particular time so it is not possible to confirm much in the trends of pertinent non-convective processes. As was noted above, there was a distinct drop in temperature (Fig. 6.1) starting with about observation 90 in both the MAPS and radiosonde plots, especially in the lower levels which would tend to have a stabilizing effect on the lower atmosphere. However, the water vapor mixing ratio plot (Fig. 6.2) indicates there must have been considerable moisture advection in the lower troposphere, since the highest values of the entire time-series appear just prior to observations 92 and 93 in both the MAPS and radiosonde plots. Finally, in the vertical pressure velocity plot (Fig. 6.6), both data sets indicate weak upward vertical velocity throughout the entire troposphere, which would be consistent with an increase in atmospheric instability.

The plot of the actual GCAPE versus the predicted GCAPE from large-scale processes based on the radiosonde data is similar to the one using MAPS data (Fig. 6.19) in a couple of ways. First, the amount of GCAPE from the actual sounding at each observation was very small or zero. The largest value computed by the GCAPE program was 0.86 J kg^{-1} for the sounding taken at observation 8 (29 January), during the time of the first frontal passage recorded in the weather summary. Second, there are two areas of maximum GCAPE from the hypothetical soundings due to large-scale processes, that coincide with the two similar areas of maximums noted in the MAPS plot. The predicted GCAPE for observations 59 and 60 are 78.8 J kg^{-1} and 223.5 J kg^{-1}, respectively (compared with 115.7 J kg^{-1} at observation 59 for the MAPS data), while the highest predicted amount for the period was 242.4 kg^{-1} at observation 93 during the passage of the arctic system (compared with 23.1 kg^{-1} at observation 93 for the MAPS data). However, a major difference between the results based on the radiosonde data set and those from the MAPS data set is in the frequency and magnitude of the GCAPE computed from the hypothetical soundings. The predicted GCAPE is positive for a total of 73 observations, the highest amount computed being 242.2 J kg^{-1} as we have already seen. In contrast, the predicted GCAPE was positive for a total of 22 observations for the MAPS data set, with the largest value being 115.7 J kg^{-1}. These results are not surprising, considering the greater detail of atmospheric thermodynamic and wind variables provided by the radiosondes, evident in the radiosonde time series plots compared with those of the MAPS analyses (Fig. 6.1-Fig. 6.8). This is especially true in the boundary layer where any large fluxes of moisture and temperature appear to be either poorly represented or altogether missed by the MAPS model. Moreover, the majority of these non-zero events in the radiosonde data tend to be grouped near the episodes of frontal passage and associated precipitation as described in the weather summary, which are, naturally, periods when horizontal moisture and temperature fluxes are significant. These low-level fluxes can be important contributors to the production of GCAPE. The fact that the positive GCAPE production rate is a great deal weaker and less frequent in the MAPS data set compared with that in the radiosonde data is further evidence that much atmospheric information, particularly in the lower troposphere, is not being resolved properly or adequately by the MAPS model analyses.

On the other hand, the large positive GCAPE forcing depicted by the radiosonde data may be in fact due to poor sampling of the thermodynamic and wind variables, leading to temperature and moisture horizontal advective tendencies that do not accurately reflect the non-convective processes at work in the atmosphere at a given time. Yet another possible explanation for this difference is that, as mentioned previously, the areal coverage of the radiosondes is 4.5 times smaller than that of the MAPS analyses and as result, the large-scale forcing may actually be much stronger when considered locally, over the smaller domain.

We now turn our attention to the question of GCAPE quasi-equilibrium. The scatter plots of the time rate of change of the observed GCAPE versus that of the GCAPE production by large-scale processes are shown for the MAPS model data and for the radiosonde data in Fig. 6.20. The observed GCAPE and large-scale GCAPE production changes with time were computed by evaluating the respective GCAPE at a given observation, subtracting from it the observed GCAPE at the previous observation, and divid-

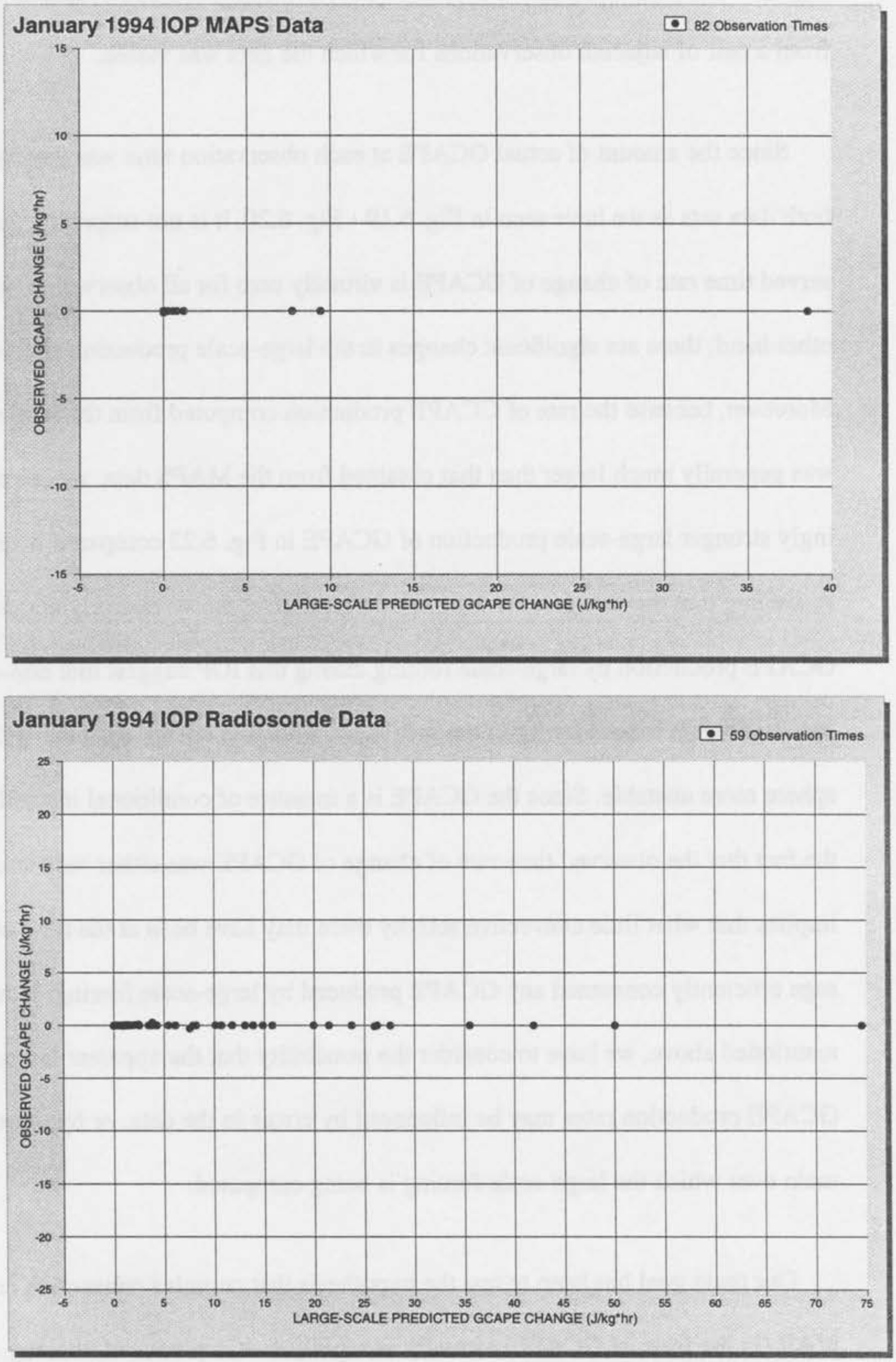

FIGURE 6.20: Scatter plot comparing the time rate of change of the observed GCAPE (ordinate) with the GCAPE rate of production by large-scale processes (abscissa) from MAPS (upper) and radiosonde (lower) data. Each of the points represents the GCAPE calculations corresponding to a pair of temporally adjacent observation times.

ing by the time interval between the observations. Each data point represents the results from a pair of adjacent observations for which the data was viable.

Since the amount of actual GCAPE at each observation time was very nearly zero for both data sets as we have seen in Fig. 6.19 - Fig. 6.20, it is not surprising that the observed time rate of change of GCAPE is virtually zero for all observation pairs. On the other hand, there are significant changes in the large-scale production rate of GCAPE. Moreover, because the rate of GCAPE production computed from the radiosonde data was generally much larger than that obtained from the MAPS data, we see correspondingly stronger large-scale production of GCAPE in Fig. 6.22 compared with Fig. 6.21. Assuming that the data are, for the most part, reliable, these relatively high values of GCAPE production by large-scale forcing during this IOP suggest that non-convective processes were indeed trying to produce moist available energy by making the atmosphere more unstable. Since the GCAPE is a measure of conditional instability (RW92), the fact that the observed time rate of change of GCAPE was either very small or zero implies that what little convective activity there may have been at the time of frontal passage efficiently consumed any GCAPE produced by large-scale forcing. However, as mentioned above, we have to consider the possibility that the apparent large-scale GCAPE production rates may be influenced by errors in the data, or by the size of the domain over which the large-scale forcing is being computed.

Our main goal has been to test the hypothesis that cumulus convection consumes MAE (in the form of GCAPE) virtually as rapidly as it is produced, thereby establishing GCAPE quasi-equilibrium in a midlatitude setting. Since significant convective activity was lacking during this January-February 1994 IOP, these data sets are not entirely suitable for testing this hypothesis. They have, however, been useful in that we are already seeing the kinds of results we expected to see with midlatitude data, namely higher magnitudes of Q_1 and Q_2, and a greater GCAPE production rate due to large-scale forcing. As an example, from the MAPS and radiosonde data sets, we have obtained a maximum value of 38.6 J kg^{-1} hr^{-1} and 74.5 J kg^{-1} hr^{-1}, respectively. This contrasts with a maximum value obtained by WR94 of less than 30 J kg^{-1} hr^{-1} using GATE data (Fig. 3.12). This latter result was anticipated because of the stronger large-scale forcing found in midlatitudes compared to the tropics. Moreover, the January-February data set did provide the opportunity to develop and refine the software necessary to carry out the quasi-GCAPE equilibrium investigation, in anticipation of a more favorable IOP data set scheduled for collection in April 1994 at the SGP CART site. The results from this latter IOP form the subject of the next chapter.

CHAPTER 7

April 1994 IOP Results

7.1 Meteorological Conditions.

As before, a synopsis of the meteorological conditions will begin the discussion of the results from the April 1994 IOP. The information for this IOP, which ran for the three week period starting 11 April 1994 and ending 1 May 1994, was again provided by Mike Splitt of the CART Site Scientist Team.

Monday, 11 April 1994

A strong upper-level trough centered over Colorado moved eastward into Kansas during the day. A front was situated along the southern border of the CART site while an area of low pressure at the surface strengthened over southern Oklahoma and moved north-northeastward. Showers and thunderstorms associated with this storm system continued from the previous day (Sunday) and lasted into the early evening hours. Precipitation totals from these storms amounted to over an inch in many locations across the CART site. Gusty northwesterly winds overtook the whole site as the surface low strengthened and moved into northeast Kansas while the front began to head southeastward. High temperatures were generally in the 10-15°C range north, to near 21°C in the extreme southeast.

Tuesday, 12 April 1994

The upper-level trough and surface low pressure system moved out of Kansas into Iowa during the day and continued to deepen. Low clouds occurred mainly over the northeast half of the CART site with some light rain and light snow reported. Surface winds remained brisk out of the west to northwest, and gradually diminished during the evening hours. Maximum temperatures ranged from 12-14°C north to around 20°C south.

Wednesday, 13 April 1994

Another surface low pressure center developed to the west of the CART site. At the surface winds became strong and southwesterly, while upper-level winds were westerly. Following a cool morning in which temperatures were near freezing in the north, dramatic warming occurred with highs reaching into the 27-30°C range, as thin cirrus clouds moved in from the west and covered portions of the site. A cold front in the northern plains moved southward and approached the northern regions of the CART site late in the day.

Thursday, 14 April1994

The surface low pressure area moved in from the west and strengthened significantly over northern Kansas as an upper-level trough quickly traversed the CART site. Early in the day, a dry-line stretched down the middle of the site with dry westerly winds dominating the western portion while moist southeasterly winds occurred in the eastern portions. The cold front continued southward from the northern plains into central Kansas overnight. Scattered showers and thunderstorms developed along the dry-line and cold front in the evening with the strongest storms over southeastern Kansas and northeastern Oklahoma. Temperatures continued to be warm with high temperatures around 28-30°C north to near 32°C in the southwest.

Friday, 15 April 1994

The strong surface cyclone that developed over the CART site Thursday quickly moved into the Great Lakes region. Meanwhile, high pressure pushed into the site late in the day. The cold front moved into southern Oklahoma overnight and continued southeastward out of the site as the day progressed. Temperatures were significantly cooler with highs only in the 17-20°C range. Winds shifted to the north with maximum gusts reaching 13 m s^{-1}. Showers and thunderstorms in the extreme eastern sections diminished as they departed from the site early in the morning. Scattered mid- to low-level clouds associated with the showers moved out of the CART site as well.

Saturday, 16 April 1994

The upper-level flow continued to be dominated by a ridge in the western U.S. and a trough in the East, leaving northwesterly winds over the site. A broad region of high pressure at the surface extended from Texas to Colorado. Clear and dry conditions prevailed over the Site with light west to Southwest winds and mild temperatures.

Sunday, 17 April 1994

The upper-air pattern remained unchanged with the CART site still under northwesterly flow. The surface high pressure center moved to the southeast of the site while a surface trough developed over western Kansas. Warm and dry conditions with light southerly winds occurred as high temperatures reached above 26°C.

Monday, 18 April 1994

The upper level flow continued to be dominated by a ridge in the western U.S. and a polar vortex over Hudson's Bay in Canada, while the CART site was receiving light northwesterly flow aloft. A surface trough was located over extreme western Kansas and associated mid- and high-level clouds were reported, mainly in the west. Surface winds were from the south-southwest, bringing warm and dry conditions. High temperatures reached near 32°C in the north and 26-28°C in the south. Low-level moisture began to increase in the southeast. High pressure to the north pushed a cold front southward towards the site by day's end.

Tuesday, 19 April 1994

The cold front continued to move southward to the Kansas-Oklahoma border by mid-morning, but then stalled in northern Oklahoma for the remainder of the day. High temperatures cooled down substantially to the 21-23°C range in the north behind the front, while ahead of it they reached above 28°C south. Northeasterly winds prevailed over

Kansas and southerly winds dominated Oklahoma. A few scattered high clouds were reported over the CART site.

Wednesday, 20 April 1994

An upper level ridge still dominated the western states and a trough in the northeast persisted, while the jet stream remained north of the CART site. The cold front pushed further south overnight. However, due to increasing southerly surface winds site-wide as the day progressed, it changed into a warm front and began to retreat northeastward. Low level moisture increased and a few showers were scattered throughout the Kansas portion of the site early in the day. A few showers developed in the extreme south and southeastern zones late in the day as well. More significant showers and thunderstorms occurred along the warm front to the north of the site after the front had pushed up as far as the Kansas-Nebraska border. Maximum temperatures were around 27-30°C, and scattered to broken low-, mid-, and high-level clouds were reported across the CART site.

Thursday, 21 April 1994

A thunderstorm complex moved into the eastern regions of the Kansas portion of the CART site as the frontal boundary reversed itself again and pushed back southward into northern sections of the site. A strong surface high pressure system in south-central Canada advanced towards the Great Lakes. Early morning fog over the southern half of the site quickly dissipated by noon. Then, strong to severe thunderstorms developed along the frontal boundary in the vicinity of the Kansas-Oklahoma border by mid-day and continued into the evening. The thunderstorms, which were confined to mainly the central portions of the site, finally weakened late in the evening as the frontal boundary continued to slip southward.

Friday, 22 April 1994

The upper-level flow pattern began to shift eastward across the U.S. as significant disturbances moved into the western states. High pressure was centered over Lake Michigan early in the day while the frontal boundary moved to the Texas-Oklahoma border. Light showers persisted along the front early in the day and a few showers developed in late afternoon in the extreme southeast. Easterly surface winds dominated the CART site for the day. Behind and to the north of the frontal zone, significant low clouds encompassed most of the site then dissipated during the day, mainly in the south and west. High temperatures cooled to around 20°C in the north and ranged from 24-26°C in the south.

Saturday, 23 April 1994

Surface high pressure moved into mid-Atlantic States while low pressure moved into the northern plains and then continued quickly eastward. The frontal zone dissipated as surface winds became south to southeasterly over the CART site. Low- to mid- level clouds were present mainly in the western part of the site. Maximum temperatures warmed to near 27°C across the site.

Sunday, 24 April 1994

A significant upper-level trough developed in the western U.S. and an associated surface low moved into eastern Colorado by the end of the day, then became stationary.

Strong southwesterly upper-level wind flow moved across the CART site, while at the surface strong southerly winds brought increasing low-level moisture, resulting in dewpoints near 15°C and above over most of the site. Afternoon high temperatures reached the 26-30°C range. A few showers and thunderstorms developed over the southern sections mid-day and dissipated in the evening.

Monday, 25 April 1994

Significant cyclogenesis occurred as the surface low pressure system strengthened and moved northeastward into Nebraska. A significant outbreak of severe weather developed ahead of a dry-line which extended south from the low, separating air with dewpoints around 20°C to the east from that having dewpoints lower than -12°C to the west. Thunderstorms developed by mid-morning to the southwest of the CART site and quickly moved into the western sections. Thunderstorms moved eastward, then exited the site by late evening. The dry-line moved into the central portions of the site during the day. High temperatures reached near 27°C in western sections and 21-23°C to the east.

Tuesday, 26 April 1994

The surface cyclone continued moving northeastward and headed into Minnesota. The dry-line continued to push eastward through the CART site. A cold front advanced in from the north, quickly moved southward and finally merged with the dry-line in the evening. Strong northerly winds and significantly cooler air followed frontal passage. Strong to severe thunderstorms redeveloped along the dry-line in the afternoon and affected the southeastern third of the site. Although skies were mainly clear in the northern portions of the site, there was significant cloudiness to the south in the vicinity of the thunderstorms. Maximum temperatures ranged from 20-23°C north to 28-31°C south.

Wednesday, 27 April 1994

The strong cyclone continued to move northeast into Canada while the CART site remained under the influence of southwesterly flow at the upper-levels as a large-scale upper level trough developed further in the West. The cold front moved to just south of the site overnight and became stationary. Significant low cloudiness engulfed the entire site due to surface winds which continued out of the north. Strong to severe showers and thunderstorms developed by early morning and affected all parts of the site throughout the day. Significant precipitation totals occurred, with several reports of amounts in excess of 2 inches across the site. Freezing early morning temperatures were reported in the northwest and high temperatures there only reached near 4°C, while in the extreme southeast they reached into the 15-17°C range.

Thursday, 28 April 1994

A low pressure area formed at the surface along the frontal boundary in southeastern Oklahoma overnight and moved northeastward as it intensified into Iowa by late afternoon. Significant low cloudiness and cool conditions continued site-wide, with periods of showers and rain mainly before evening. Surface winds were predominantly out of the northwest. Maximum temperatures reached the 12-14°C range north and 17-20°C range south.

Friday, 29 April 1994

The upper-level trough began to move eastward into the plains and another round of showers and thunderstorms affected the CART site, with the heaviest activity being in the southern portion. The frontal boundary edged further south into central Texas and southern Arkansas. Low-level winds were northeasterly and significant low-level cloudiness continued. Precipitation totals of greater than 1 inch were common over Oklahoma. Low temperatures reached freezing in the northwest and highs were in the 4-8°C range across the site.

To summarize, the days on which significant convection took place (i.e. days on which strong/severe thunderstorms were observed, or precipitation amounts were in excess of 1 inch at on the CART domain) during the IOP were: 11, 20-21, 25-27, and 29 April. These would, naturally, be the days on which we expect to see the largest amounts of GCAPE in this period.

7.2 SCM IOP Data Compared with MAPS Model Output.

As stated previously, one of the main difficulties for our purposes with this data set was that the radiosondes were operated in research mode as opposed to nominal mode. Since data collected in research mode is entirely raw in form, the data processing performed at LLNL and PNL was rendered more complicated as the laboratories attempted to imitate the initial quality-control normally executed in nominal mode at the CART ingest site. Additionally, missing data from the radiosondes was an even bigger problem during the April 1994 IOP, for a variety of reasons. Nevertheless, enough data was salvageable to carry out a test of the GCAPE quasi-equilibrium hypothesis. All comments made in Chapter 6 regarding the nature of missing data in connection with each of the fields examined applies equally here.

7.2.1 Qualitative Comparison

Temperature

The generally noisier appearance of the radiosonde time series plot versus that of the MAPS plot (Fig. 7.1) is as apparent during the April 1994 IOP as it was during the January-February 1994 IOP. The passages of cold fronts may be seen rather distinctly in both the MAPS and radiosonde plots at observation times 8-16, 32-40, 88-96 and 128-136 (during the days of 12, 15, 22, and 27 April, respectively). The temperature gradients associated with the cold fronts on 15 and 27 April appear to be especially strong, which is in agreement with the synoptic analyses of the weather summary. Interestingly, the details of the temperature structure of the atmosphere below 700 mb following the strong frontal passage on 27 April are absent in the MAPS plot, but are quite plain to see in the radiosonde plot. The freezing temperatures reported on 27 April in the weather summary are confirmed by the 280 K contour in the radiosonde plot which disappears just prior to, and reappears just after, this date. Here we have another example of the finer resolution that can be made available by the radiosondes, an advantage over the MAPS analyses and the smoothing processes involved in the model. It is also interesting to note that the

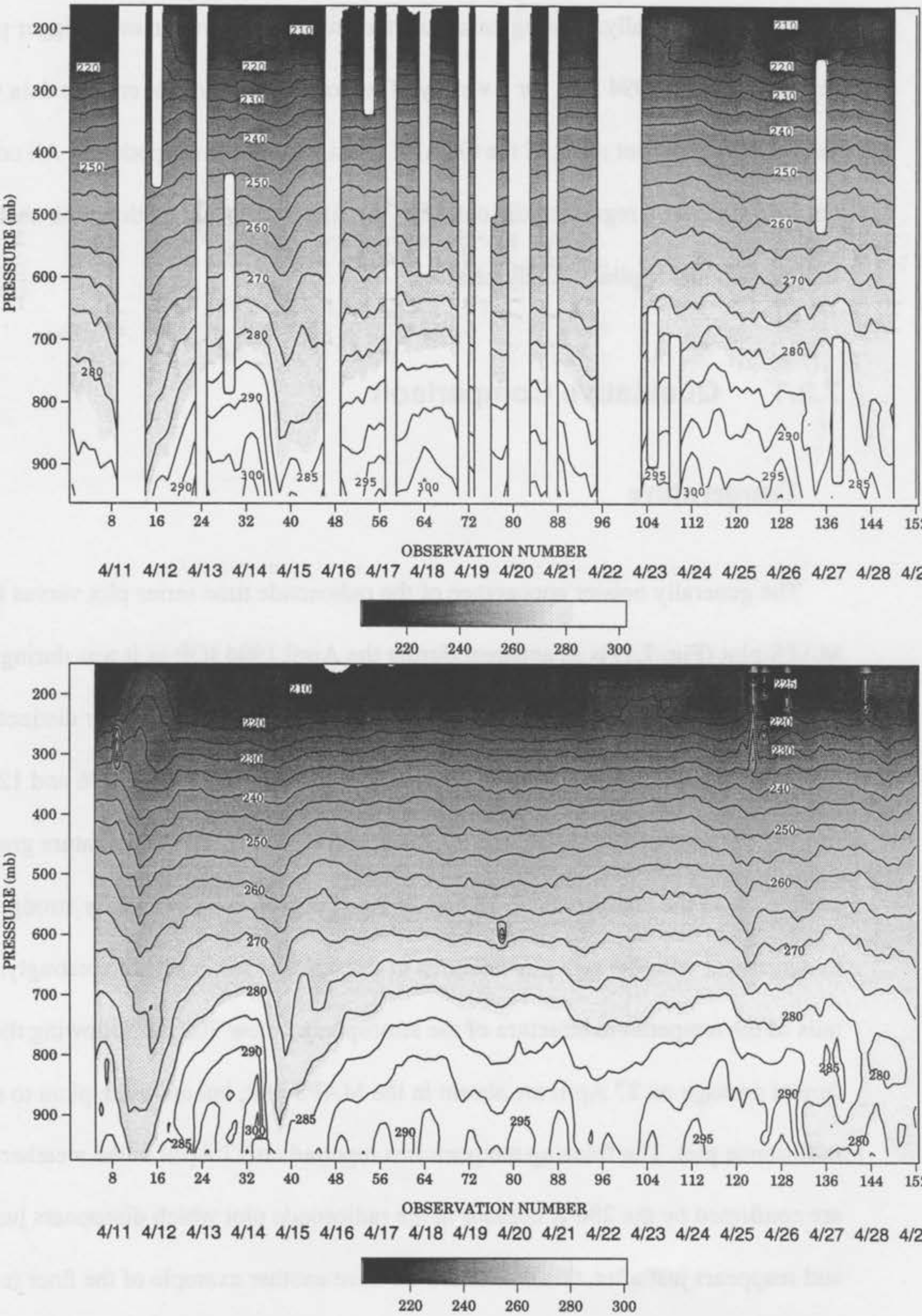

FIGURE 7.1: 19-day time series plots of temperature from MAPS model output (upper) and radiosonde data (lower), starting at 00 UTC on 11 April 1994 through 21 UTC on 29 April 1994. Contours are in K, and numbers on the abscissa represent multiples of 8 observations spaced 3 hours apart (8 observations per day), with dates below.

diurnal cycle of surface warming and cooling shows up clearly in the radiosonde plot, and to a lesser extent the MAPS plot, a phenomenon that was not as discernible in the data from the January-February 1994 IOP. A few areas of anomalous spikes in the temperature readings from the radiosondes are evident: at about 300 mb on 11 April (observation 8), at 600 mb on 20 April (observation 78), from 325 mb to the tropopause on 26 April (observations 124-126) and finally from about 225 mb to the tropopause on 27 and 28 April (observations 129 and 144, respectively). The cause of these radiosondes malfunctions has not been determined.

Water Vapor Mixing Ratio

As with the winter IOP, the time series plot of the water vapor mixing ratio (Fig. 7.2) shows that the overall features depicted by the MAPS and radiosonde data are quite similar. At the same time, we see a fairly dramatic example in this plot of the finer resolution afforded by the radiosondes, in that the contours reveal much more detail than do those of the MAPS plot. Nevertheless, there is another problem with anomalous radiosonde data, and this can be seen at 300 mb on observation 120 (25 April). What is remarkable about these plots in general, compared to their winter counterparts, is that they illustrate the large increase in water vapor that has occurred throughout the troposphere in the intervening months. We can see evidence of this especially in the boundary layer, where a maximum of 14 g kg^{-1} is reached in both the radiosonde and MAPS plots during the day of 25 April (observations 112-120). This is roughly twice the highest amounts seen near the ground in the January-February 1994 IOP plots for water vapor mixing ratio. Also, we see that the contour of 1 g kg^{-1} is often situated between 600 - 500 mb in both the

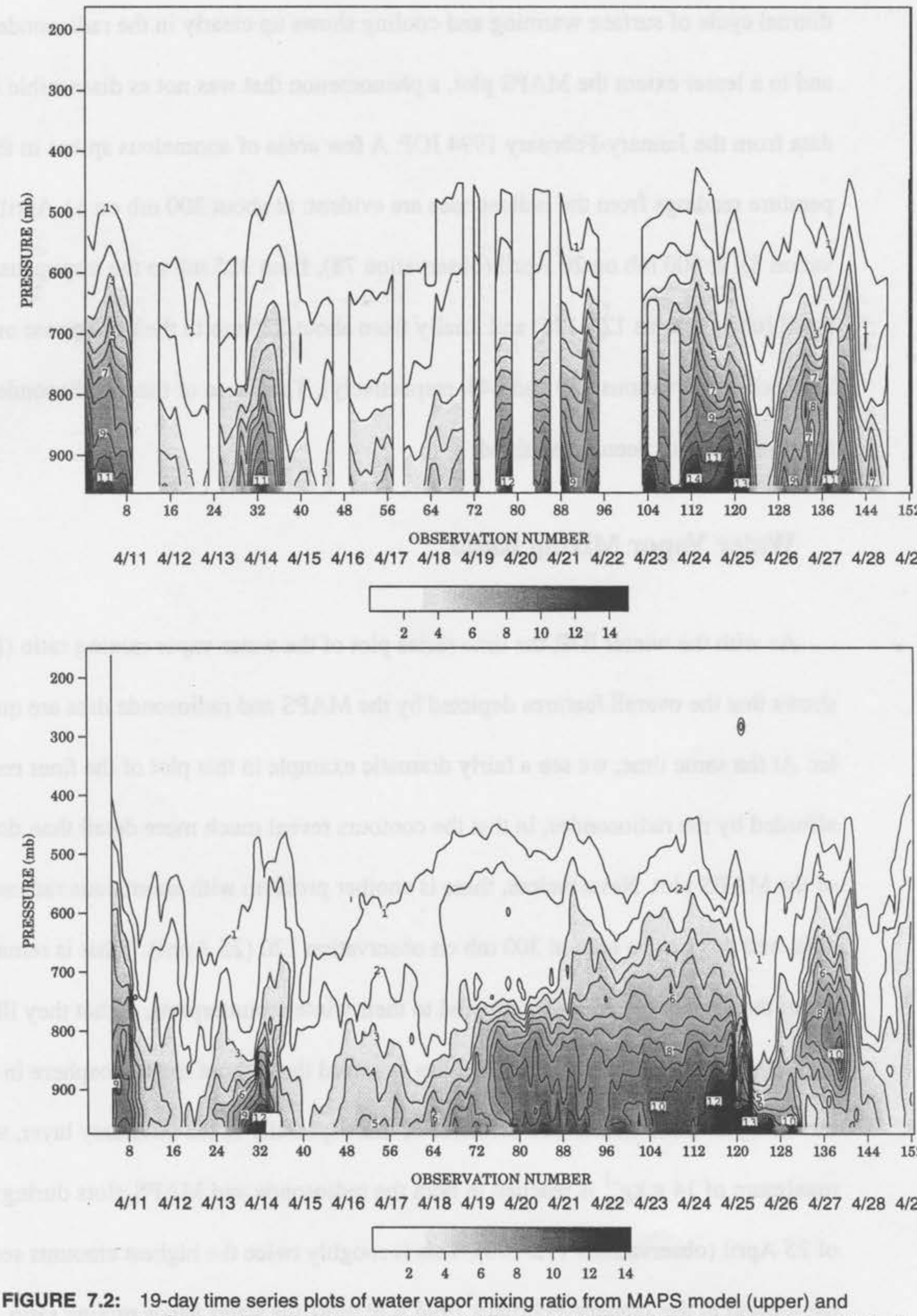

FIGURE 7.2: 19-day time series plots of water vapor mixing ratio from MAPS model (upper) and radiosonde (lower) data, starting at 00 UTC on 11 April 1994 through 21 UTC on 29 April 1994. Contours are in g kg^{-1}, and numbers on the abscissa represent multiples of 8 observations spaced 3 hours apart (8 observations per day), with dates below.

MAPS and radiosondes plots whereas this contour was often located between 700 - 600 mb in the winter IOP. Several interesting events bear mentioning. The increase in low-level moisture that took place during the day of 20 April according to the weather summary (in association with a warm front) is evident on both MAPS and radiosonde plots just before observation 80. Similarly, the increase of water vapor brought on by persistent strong southerly winds mentioned in the weather summary on 24 April (observations 105 - 110) are easily spotted on both plots. On the other hand, the arrival of the dry line mentioned in the weather summary shows up clearly on 26 April (observations 122-126), where the mixing ratio drops from over 13 g kg^{-1} to less that 5 g kg^{-1} in a matter of hours.

U-Wind Component

A prominent feature of the u-wind component field in the April 1994 IOP plots (Fig. 7.3) is the overall decrease in intensity of the component in the upper troposphere, compared with the January-February 1994 IOP. Where we saw speeds in excess of 65 m s^{-1} above 300 mb in the winter IOP, we now find maximum velocities of only 40-45 m s^{-1} at that level in the spring IOP. This should not be surprising, considering the weakening of the jet stream that occurs during this time of the year, along with a general retreat towards higher latitudes. Additionally, the radiosonde plot reveals more extensive regions of negative (east to west) u-wind values than was the case with the winter IOP (due to the boundary layer problem, this does not show up on the MAPS plot). The quiescent stretch of weather, dominated mainly by an upper level ridge and high pressure at the surface, is confirmed in both plots by the relatively small component velocities throughout the troposphere from observations 48-96 (16 - 22 April). The strongest velocities ob-

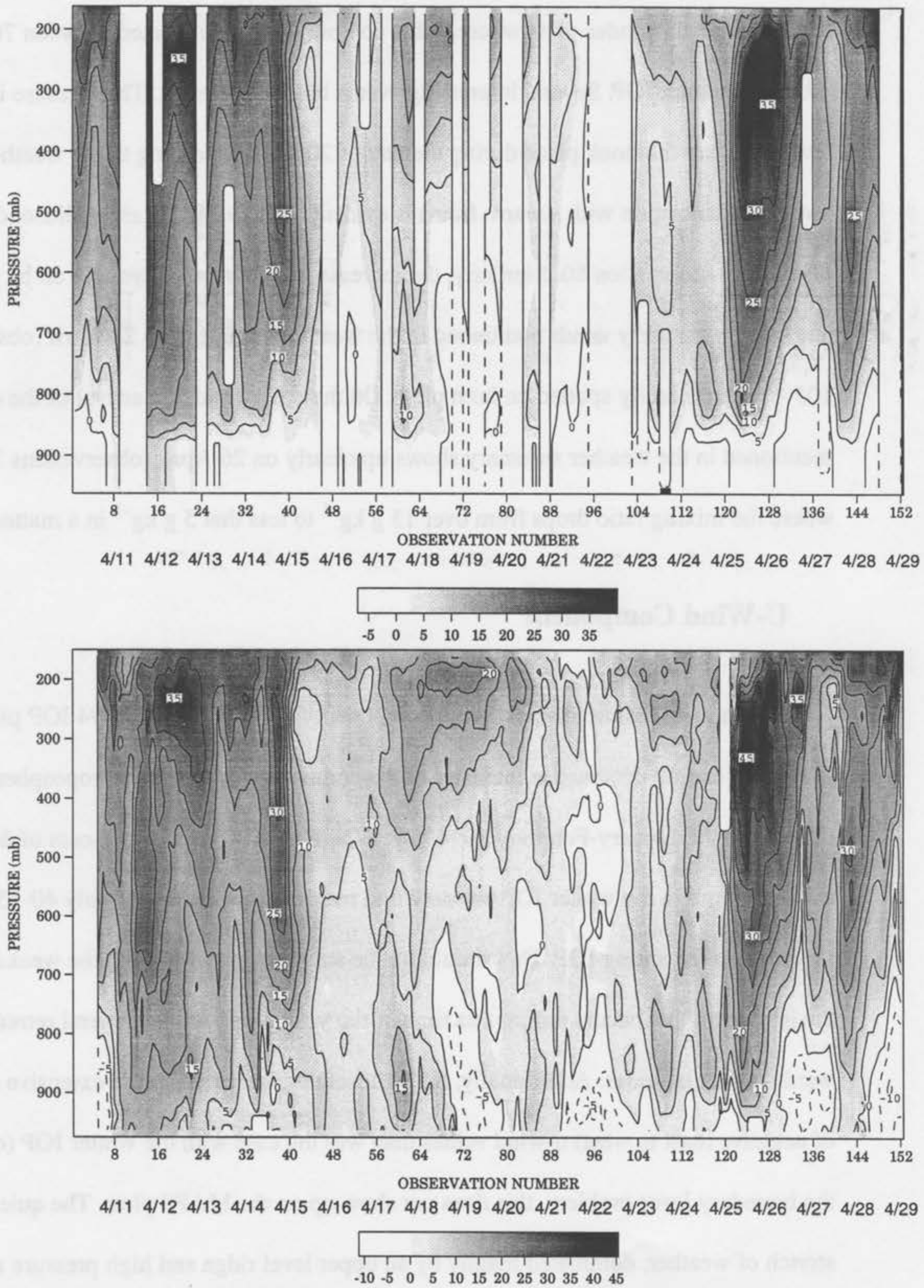

FIGURE 7.3: 19-day time series plots of u-wind component from MAPS model (upper) and radiosonde (lower) data, starting at 00 UTC on 11 April 1994 through 21 UTC on 29 April 1994. Contours are in m s^{-1} (dashed contours represent negative values), and numbers on the abscissa represent multiples of 8 observations spaced 3 hours apart (8 observations per day), with dates below.

served in the upper troposphere are only around 20 m s^{-1} (observations 64-74), which is scarcely stronger than those observed near the surface in the vicinity of observations 58-62. This interval of calm is framed on both sides by more vigorous velocities associated with, and slightly preceding, the main frontal passages on 12, 15, and 27 April. These periods of stronger winds are obviously associated with intrusions of the jet stream and the disturbances that go along with it.

V-Wind Component

Contrary to the u-wind component trend seen above, the tim series plot of the v-wind component (Fig. 7.4) shows an overall increase in intensity during the April 1994 IOP, when compared with the January-February 1994 IOP. Upper-tropospheric values on several occasions are in the 35-45 m s^{-1} range, whereas the highest values seen in the winter IOP were typically on the order of 15 m s^{-1} (although there was one instance where 45 m s^{-1} was noted at the time of the arctic front). Not only are the magnitudes higher, but they are also more extensive throughout the troposphere compared to the winter IOP, extending from their maximums in the upper-troposphere down to the mid- and lower-tropospheric levels. This strengthening of the positive v-wind component through the depth of the troposphere helps account for the doubling of the amount of water vapor in the atmosphere seen above, as a stronger southerly wind component would tend to advect deeper moisture from the Gulf of Mexico into the region. The same period of relative calm in the center of the April 1994 IOP, seen in the u-wind component time series plot, is also discernible here. Likewise, this calm interval is surrounded by stronger component velocities associated with the main frontal passages. The shift in component direction due to

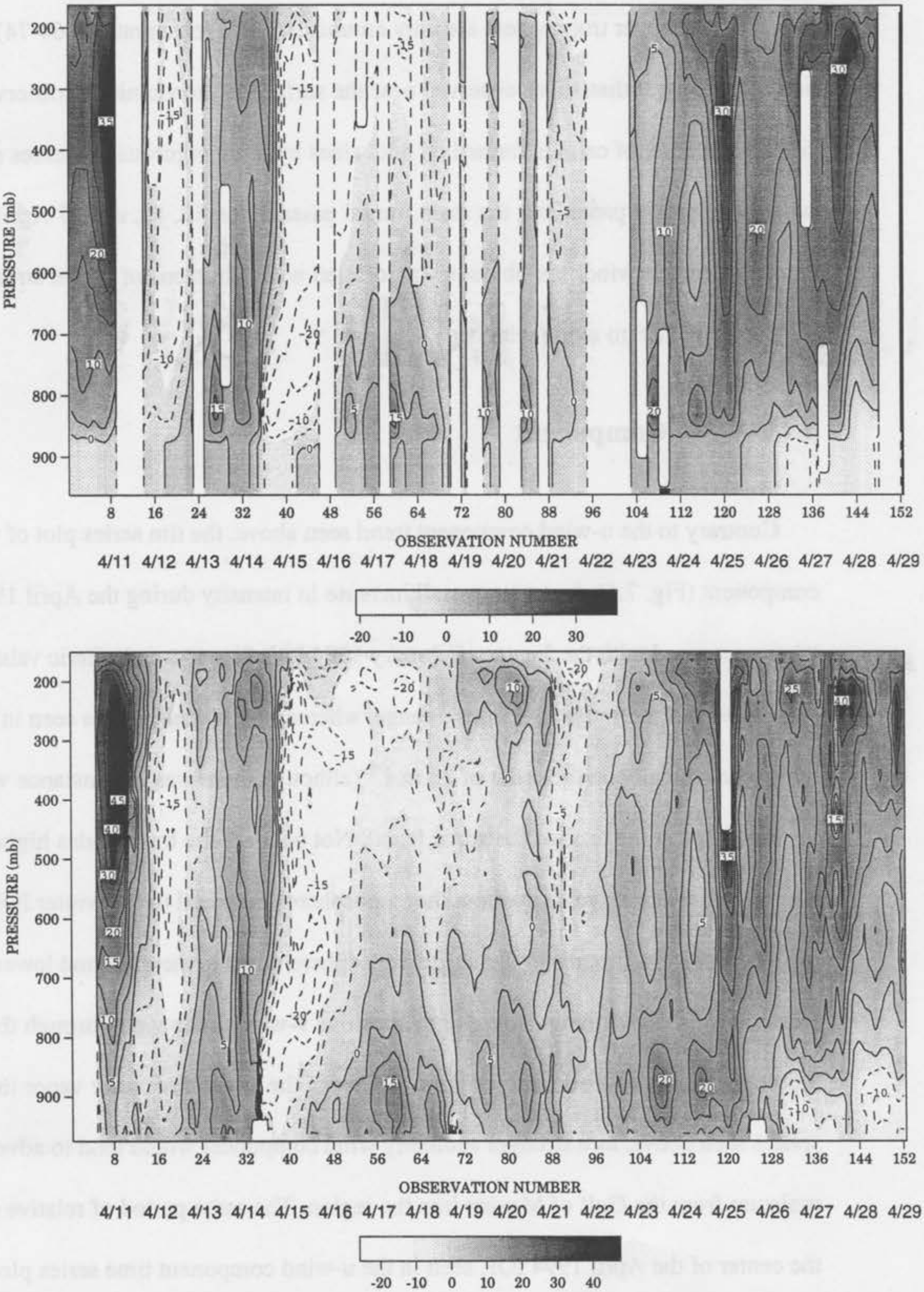

FIGURE 7.4: 19-day time series plots of v-wind component from MAPS model (upper) and radiosonde (lower) data, starting at 00 UTC on 11 April 1994 through 21 UTC on 29 April 1994. Contours are in m s^{-1} (dashed contours represent negative values), and numbers on the abscissa represent multiples of 8 observations spaced 3 hours apart (8 observations per day), with dates below.

frontal passages is especially evident at the time of the first two events, from observations 8-16 and 32-40 (12 and 15 April, respectively). Prior to the arrival of the front, the component is strongly positive (blowing from south to north). After the frontal passage, the component is negative (blowing from north to south), which would be expected in the northern hemisphere as clockwise circulation around a surface high pressure area moves over the region. This windshift is also evident at the surface with the last frontal passage mentioned in the weather summary on 27 April, although it does not extend up through the mid- and upper-troposphere. This may be due to the strength of the upper-level trough and its relative slowness to move east. As with the u-wind component time series plot, there quite a bit of agreement between the MAPS and radiosonde v-wind component time series plots, aside from the boundary layer problems, which is encouraging.

Divergence

Unfortunately, the extent of missing data from the radiosondes here is even more apparent than was the case with the winter IOP as the time series divergence chart for the April 1994 IOP (Fig. 7.5) reveals. However, the MAPS plot does capture some interesting features. At the time of observations 1-8, 32-40, 112-116, 120-124, and 132-140 (during 11, 14-15, 24, 25-26, and 27-28 April), the MAPS data indicates that there was low-level and mid-level convergence taking place (negative values) while upper-level divergence (positive values) occurred at roughly the same time. This would be consistent with the significant thunderstorm activity reported in the weather summaries corresponding to these times, in that low-level wind convergence (along with moisture convergence) is a primary mechanism for triggering thunderstorm development. The divergence aloft is a

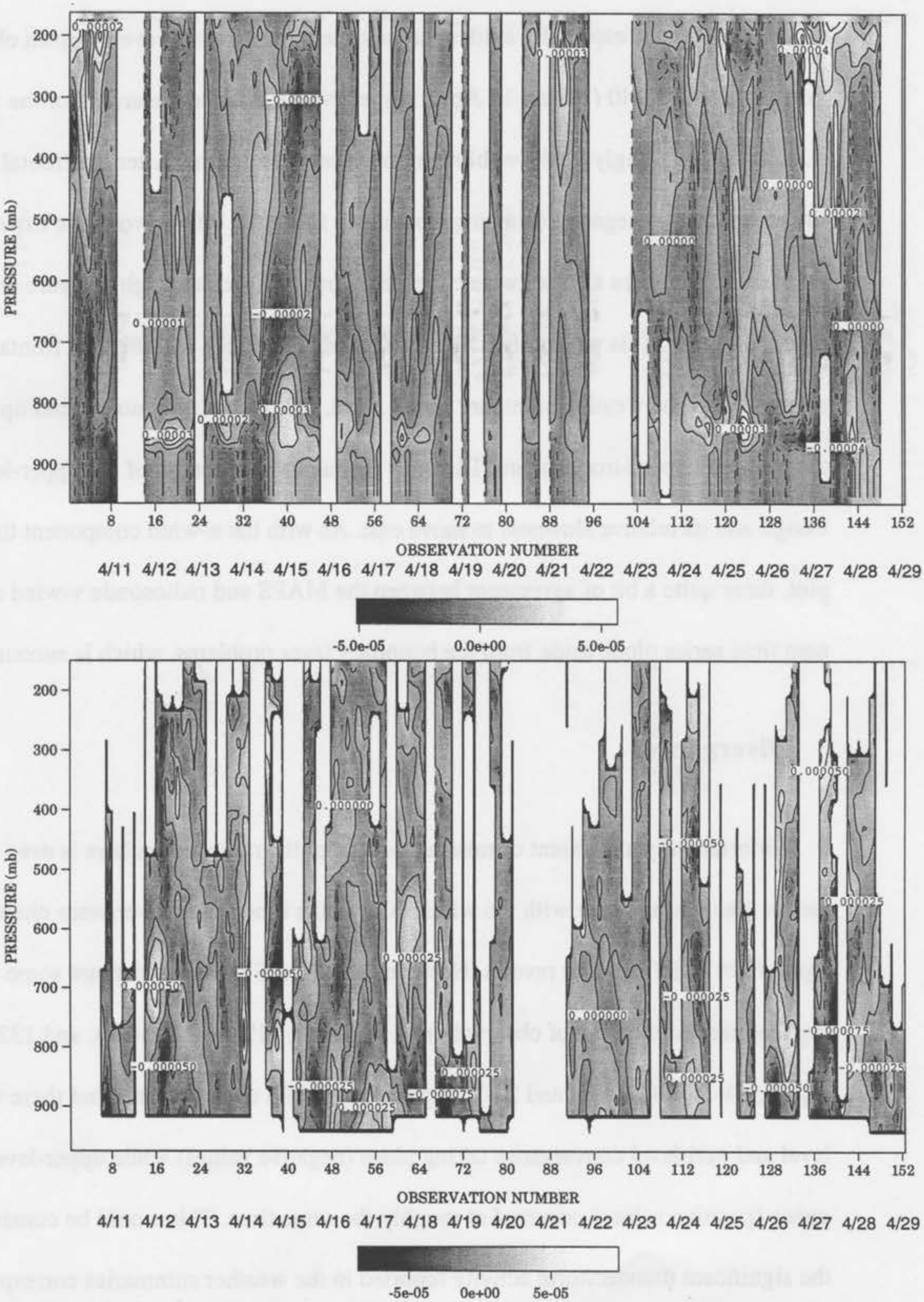

FIGURE 7.5: 19-day time series plots of wind divergence from MAPS model (upper) and radiosonde (lower) data, starting at 00 UTC on 11 April 1994 through 21 UTC on 29 April 1994. Contours are in m $s^{-1}m^{-1}$ (dashed contours represent negative values), and numbers on the abscissa represent multiples of 8 observations spaced 3 hours apart (8 observations per day), with dates below.

result of the detrainment of atmospheric mass brought up by updrafts in the thunderstorm as the cumulonimbus reaches the tropopause and cannot develop any higher. On the other hand, the quiescent period of weather in the center of the IOP, stretching from observations 48-96, is virtually free of any regions of strong convergence. The divergence field is either flat or positive through the depth of the troposphere, which is not conducive to thunderstorm activity.

Vertical (pressure) Velocity

The time series plot of vertical pressure velocity (Fig. 7.6) confirms the existence of vigorous upward vertical motion, attributable to strong convection, in several instances. This is especially true of the MAPS plot since there is so much missing information in the radiosonde data set. We see stronger upward velocities here compared with the values calculated for the winter IOP. Additionally, the magnitudes of the upward velocities tend to be higher in the radiosonde plot compared with the MAPS plot, whereas the magnitudes of the downward velocities are more similar between the two data sets. The MAPS plot shows 2 instances of where the upward velocity was on the order of -30 mb hr^{-1}, and the radiosonde plot indicates that on at least one of these occasions the upward velocity was over -40 mb hr^{-1}. This contrasts with the strongest upward velocities noted in the January-February 1994 IOP of about -20 mb hr^{-1}. These instances in the April 1994 IOP of vigorous upward velocity coincide directly with some of the more severe thunderstorm activity noted in the weather summary. More precisely, on 11 April (observations 1-8), strong thunderstorms with significant rain were observed and the MAPS plot shows that the vertical pressure velocity was virtually upward throughout the entire

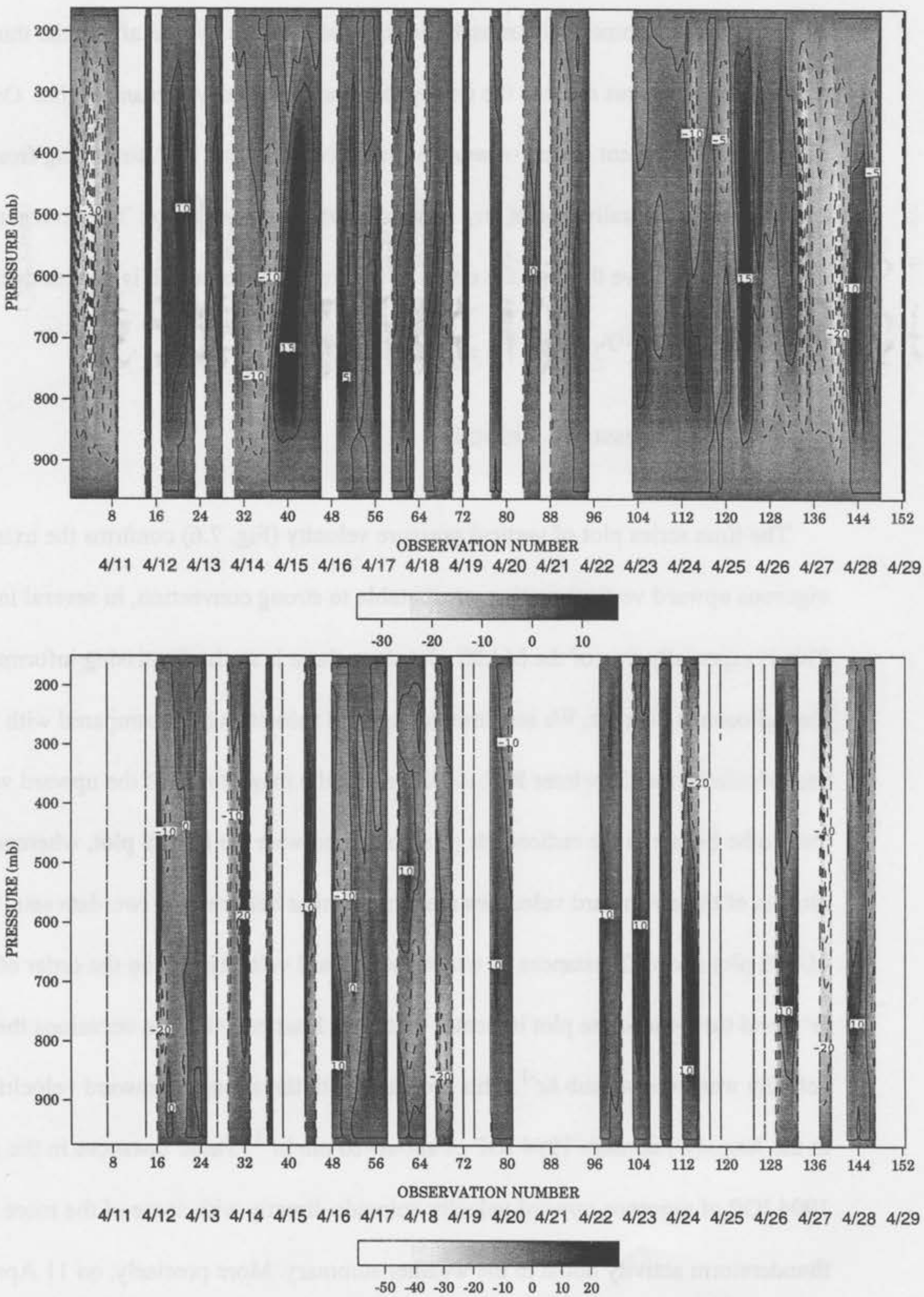

FIGURE 7.6: 19-day time series plots of vertical pressure velocity from MAPS model (upper) and radiosonde (lower) data, starting at 00 UTC on 11 April 1994 through 21 UTC on 29 April 1994. Contours are in mb hr^{-1} (dashed contours represent negative values), and numbers on the abscissa represent multiples of 8 observations spaced 3 hours apart (8 observations per day), with dates below.

troposphere on that day, reaching a maximum of over 30 mb hr^{-1} at around 500 mb. Next, we see upward velocities for a good portion of the troposphere on 14-15 April (observations 32-40). Though not as strong as the 11 April event, there were still several thunderstorms with rain observed on this occasion. Immediately following the upward velocities, we see downward motion starting with observation 40 as the upper ridge and surface high pressure moved over the area. Generally, from this observation through observation 112, the plot indicates that subsident air motions were predominant, although a few pockets of upward motion can be seen in the radiosonde plot. Also, the MAPS plot shows there was a period of deep, upward motion associated with the thunderstorms and rain that broke out on 22 April (observations 88-96), as noted in the weather summary. The strongest upward air motions of the IOP, however, occurred on 27-28 April (observations 130-140), where we see vertical pressure velocities of over -40 to -50 mb hr^{-1}, according to the radiosonde plot, from about 600 - 400 mb. This is coincidental with the outbreak of strong to severe thunderstorms with rain in excess of 2 inches at many locations on the CART site reported in the weather summary. This is good verification that the data gathered from the radiosondes is, in spite of the many difficulties encountered, quite valuable in evaluating the wind and thermodynamic tendencies of the atmospheric column, and that the many algorithms used along the way, from the ingest site to the final product, appear to be performing as intended.

Temperature Tendency due to Horizontal Advection

Unfortunately, the majority of information in the lowest levels of the boundary layers is missing from the radiosonde data (although this has been filled in where possible by linear interpolation in the heat and moisture budget calculations, as well as the GCAPE computation), so it is not possible to glean much information from these regions in the time series plot of temperature tendency due to horizontal advection (Fig. 7.7). Nevertheless, a few features from Fig. 7.7 corroborate the main synoptic events of this period. For example, the cold air advection in the mid- and lower-troposphere accompanying the passage of the second cold front of the period on 15 April (observation 40) is easily identifiable on both the radiosonde and MAPS plots, where maximum cooling rates are shown to be excess of -1.5 K hr^{-1}. The cold air advection associated with the first frontal passage on 16 April (observations 8-16) is hinted at in both the radiosonde and MAPS plots, on either side of the gaps in data. Additionally, the MAPS plot shows the cold air advection that followed in the wake of the frontal passage on 27 April (observation 136) that was on the order of -1 K hr^{-1}. Just prior to this, the warm air advection accompanying the advance of the dry line mentioned in the weather summary shows warming rates of about 1 K hr^{-1}. Both of these cold and warm air advection events are also evident in the radiosonde plot to a certain extent. What is interesting about this last cold air advection event following the frontal passage is that, on the morning of 29 April, the weather summary indicates freezing temperatures were noted in the northern sections of the CART site, and maximum daytime temperatures only reached the 4-8°C range across the entire site. This seems to be confirmed by the depth of the cold air advection in the MAPS plot, which shows that cooling took place almost the entire depth of the troposphere from 28-29 April (observations 140-142). One final note in passing, the lowest values of the temperature tendency due to horizontal advection have risen, on average, about a degree from their counter parts during the winter IOP. The maximum cooling rates during the

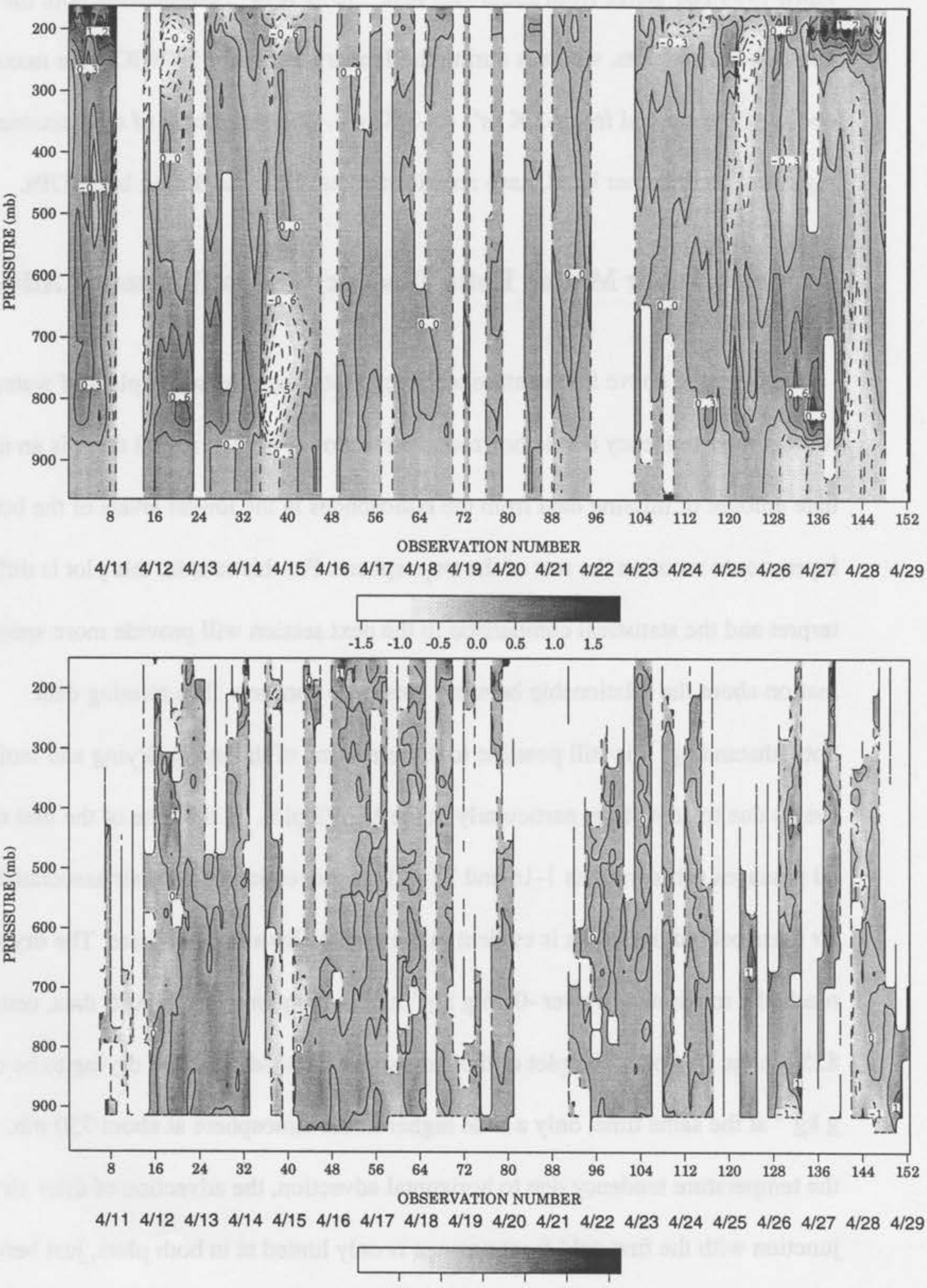

FIGURE 7.7: 19-day time series plots of horizontal temperature advective tendency from MAPS model (upper) and radiosonde (lower) data, starting at 00 UTC on 11 April 1994 through 21 UTC on 29 April 1994. Contours are in K hr^{-1} (dashed contours represent negative values), and numbers on the abscissa represent multiples of 8 observations spaced 3 hours apart (8 observations per day), with dates below.

April 1994 IOP range from about -1.5 K hr^{-1} to -2 K hr^{-1}, considering both the MAPS and radiosonde plots, whereas during the January-February 1994 IOP, the maximum cooling rates ranged from -2 K hr^{-1} to -3 K hr^{-1}. The magnitude of the maximum warming rates, on the other hand, have remained about the same during both IOPs.

Water Vapor Mixing Ratio Tendency due to Horizontal Advection

As with the above temperature tendency plots, the time series plots of water vapor mixing ratio tendency due to horizontal advection (Fig. 7.8) reveal there is an unfortunate amount of missing data from the radiosondes in the lowest levels of the boundary layer, not to mention the rest of the troposphere. For this reason, this plot is difficult to interpret and the statistical comparison in the next section will provide more specific information about the relationship between these two data sets. The missing data notwithstanding, it is still possible to discern some of the major drying and moistening events due to advection, particularly in the MAPS plot. At the time of the first two frontal passages (observations 1-16 and 32-40), the advection of drier air associated with the air mass behind the fronts is evident in the mid- to lower-troposphere. The drying reached a maximum of over -0.75 g kg^{-1} hr^{-1} in the plot of the MAPS data, centered at 825 mb on 15 April. The plot of the radiosonde data indicates the drying to be over -0.5 g kg^{-1} at the same time, only a little higher in the atmosphere at about 750 mb. As with the temperature tendency due to horizontal advection, the advection of drier air in conjunction with the first cold front passage is only hinted at in both plots, just before the gap of data between observations 8-16. The advance of the dry line across the CART site mentioned in the weather summary shows up clearly in the MAPS plot, starting at obser-

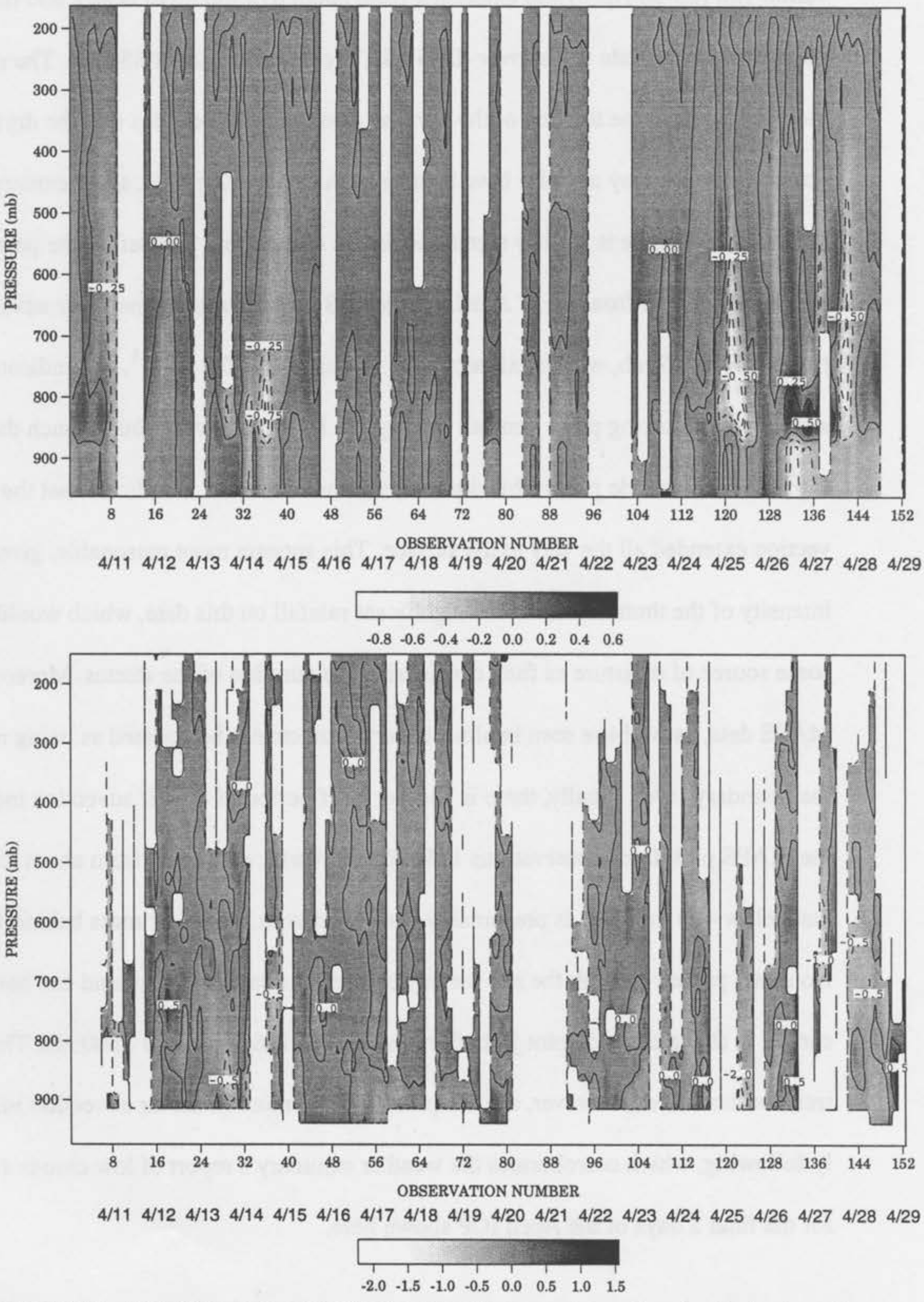

FIGURE 7.8: 19-day time series plots of horizontal water vapor mixing ratio advective tendency from MAPS model (upper) and radiosonde (lower) data, starting at 00 UTC on 11 April 1994 through 21 UTC on 29 April 1994. Contours are in g kg^{-1} hr^{-1} (dashed contours represent negative values), and numbers on the abscissa represent multiples of 8 observations spaced 3 hours apart (8 observations per day), with dates below.

vation 120 (25-26 April) and extending from about 875 mb up to nearly 500 mb. The maximum drying rate is just over -0.75 g kg^{-1}, centered at about 850 mb. The radiosonde plot just captures the tail end of the dry line passage, and indicates that the drying rate at observation 124 may actually have been as high as over -2 g kg^{-1}, again centered around 850 mb. Next, there is a fairly significant influx of moisture just before the passage of the last, stronger cold front on 27 April. The MAPS plot centers the moist air advection between 850 - 775 mb, with maximum rates reaching over 0.5 g kg^{-1}, and indicates dry air advection was taking place beneath this region. However, even though much data is missing in the radiosonde plot at this time, it nevertheless seems to indicate that the moist advection extended all the way to the surface. This appears more reasonable, given the intensity of the thunderstorms and significant rainfall on this date, which would require some source of moisture as fuel, considering the duration of the storms. Moreover, the MAPS data, as we have seen in almost every plot, cannot be counted as being reliable in the boundary layer. Finally, there is another brief period of dry air advection indicated in the MAPS plot, from observations 138-142 (28 April), extending from about 850 mb to just below 400 mb. This is presumably associated with a drier air mass behind the cold front that passed through the site the day before. The same drying trend can barely be discerned in the radiosonde plot just after observation 136, from 700 - 600 mb. This drying trend is short-lived, however, as both plots indicate more moist air advection immediately following, which corroborates the weather summary's report of low clouds and rain for the final 2 days of the April IOP shown here.

Apparent Heat Source Q_1

As discussed in Chapter 6, Q_1 is a diagnostic tool that gives us information about the heat budget of convectively active regions due to condensational heating/evaporative cooling, and the horizontal and vertical eddy heat flux convergence. The time series plots of Q_1 computed from the April 1994 IOP MAPS and radiosonde data are shown in (Fig. 7.9) Unfortunately, the radiosonde plot obviously suffers from the lack of usable data. However, the MAPS plot is relatively complete and reveals several interesting features, a few of which are verified by the sparse information in the radiosonde plot. First of all, a glance at the general pattern of the MAPS plot shows that maximum warming tends to be concentrated in the upper troposphere, from about 500 - 300 mb. This can be seen from observations 1-8 (11 April), 32-40 (15 April), 112-122 (24-25 April) and 136-144 (28 April). Thunderstorm activity, to a greater or lesser extent, was observed during each of these time intervals, as noted in the weather summary. Although the maximum warming rates during the periods of strong-severe thunderstorm outbreaks are not that impressive, relatively speaking (6 K hr^{-1} on 11 April and 4 K hr^{-1} on 28 April), they are nevertheless stronger than any of the heating rates shown in the MAPS Q_1 time series plot for the January/February 1994 IOP. Plus, the fact that the MAPS data are being averaged over a much larger area must be taken into consideration. However, the radiosonde plot does indicate that the maximum warming rate, given the amount of usable data there is, was more on the order of over 11 K hr^{-1} in the upper troposphere from observations 138-139, almost 3 times as strong as the local maximum warming rate of 4 K hr^{-1} shown for the corresponding observation interval in the MAPS plot. At this particular time, severe thunderstorms noted in the weather summary. In another instance where thunder-

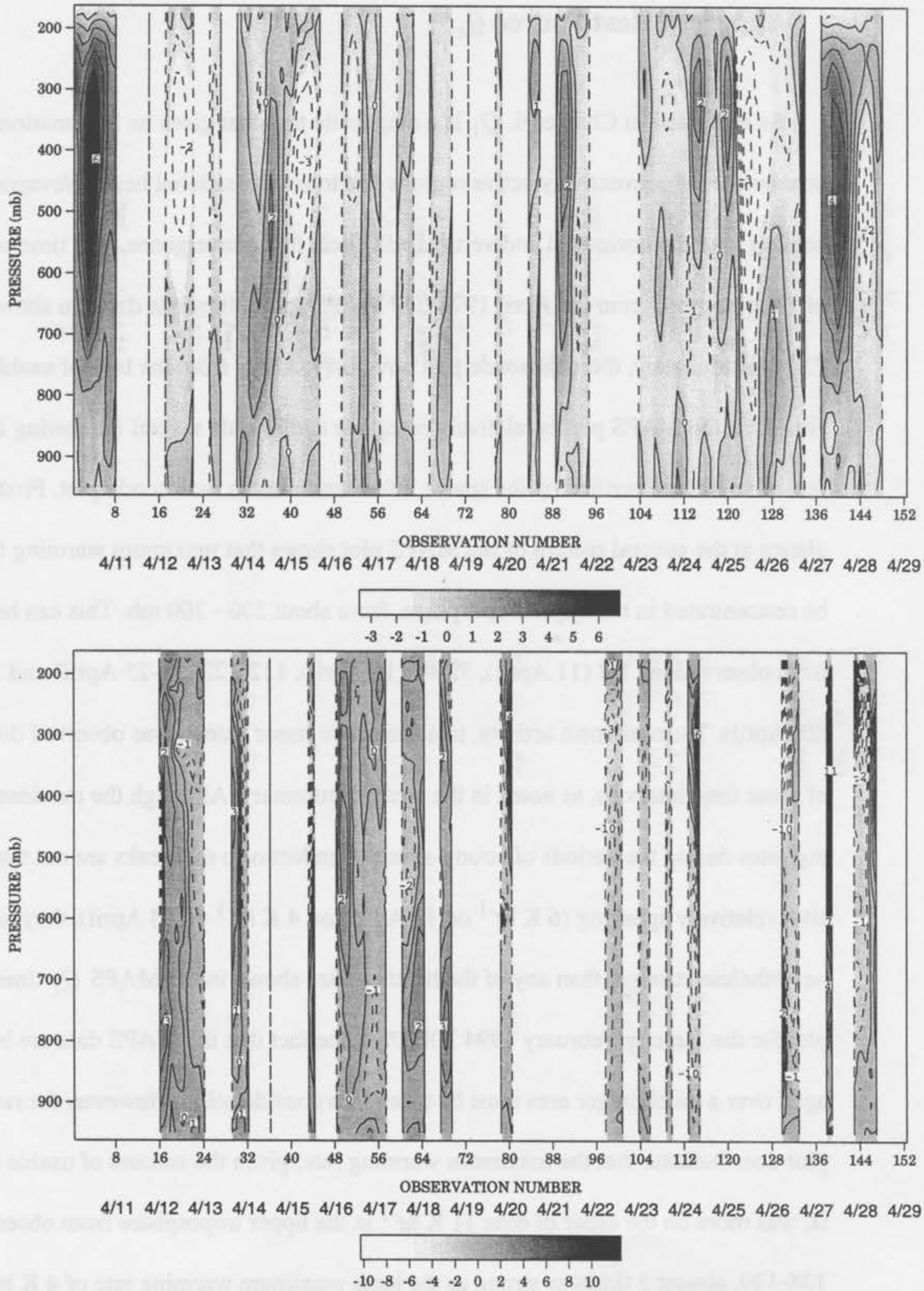

FIGURE 7.9: 19-day time series plots of the apparent heat source from MAPS model (upper) and radiosonde (lower) data, starting at 00 UTC on 11 April 1994 through 21 UTC on 29 April 1994. Contours are in K hr^{-1} (dashed contours represent negative values), and numbers on the abscissa represent multiples of 8 observations spaced 3 hours apart (8 observations per day), with dates below.

storms were observed, the radiosonde plot indicates that the local maximum warming rate in the upper troposphere was at least 6 K hr^{-1} (observations 113-114) at a time when the MAPS plot shows the local maximum heating rate to be only about 2 K hr^{-1}, a rate, again, 3 times smaller than that shown by the radiosonde plot. This leads us to conclude that the estimates of Q_1 derived from the MAPS data are strongly underestimated, for the variety of reasons already mentioned in Chapter 6. Moreover, the maximum warming rate of over 11 K hr^{-1} compares favorably with the maximum found by Gallus and Johnson (1991) of 13 K hr^{-1} in their analysis of the mature stage of an intense squall line in Oklahoma.

Another interesting feature that this time series figure brings out, especially in the MAPS plot, is the dipole nature of Q_1 values in the mid- and upper-troposphere. Each time there is a significant warming event, associated with thunderstorm activity, there immediately follows a cooling event covering roughly the same vertical depth as the preceding warming. This is most likely explained by the evaporation of cloud droplets as the thunderstorms reach the mature stage and then dissipate. Additionally, the dry-line passage mentioned in the weather summary on 25-26 April (observations 120-124) shows up distinctly throughout a good portion of the troposphere. The cooling rates associated with cloud evaporation at this time reaches a local maximum of over -3 K hr^{-1}. As with the maximum warming rates, we suspect that this value is underestimated, and indeed, the radiosonde plot indicates other regions where the maximum cooling rates were about -10 K hr^{-1} around 500 mb, at observations 100 (23 April) and 130 (early on 27 April). By comparison, Gallus and Johnson (1991) found maximum cooling rates in their squall line analysis to be on the order of -6 K hr^{-1}, also around the 500 mb region, in the rear inflow regions of the squall line dominated by downdrafts.

Another small point worth mentioning is that on at least two occasions, the MAPS plot shows weak warming was occurring in the lower levels of the atmosphere prior to the mid- and upper-tropospheric maxima associated with thunderstorm development. This can be seen from observations 30-32 (14 April) and more distinctly from 128-132 (27 April). These are probably indications of cloud formation and scattered shower activity that broke out prior to the thunderstorms, consistent with the weather summary reports.

As noted above, the general pattern of regions where the values of the apparent heat source are positive shows that maximum heating tends to take place in the mid- to upper-troposphere from about 600 - 300 mb. These maxima trends are similar to the ones reported in Cotton and Anthes (1989) in their survey of diagnostic studies regarding heat and moisture budget of extratropical convection. They found that, in general, Q_1 reaches a maximum in the upper troposphere, has a minimum in the mid troposphere, and a secondary maximum around 750 mb for vigorous squall lines and thunderstorm activity. The secondary maxima in the lower troposphere are not directly evident here, most likely due to the boundary layer problems we have seen in the MAPS data, as well as the averaging over a larger domain. We would expect this kind of information to be more readily represented in the data streams from the radiosondes, which, unfortunately, are not complete enough in the April IOP to allow us to detect the lower maxima.

By way of comparison with warming rates derived from tropical data, Fig. 7.10 shows the $Q_1 - Q_R$ profile evaluated by Wang (1994 Ph.D. dissertation) using GATE data. We see that the maximum warming rates are only 6-9 K day^{-1}, considerably less

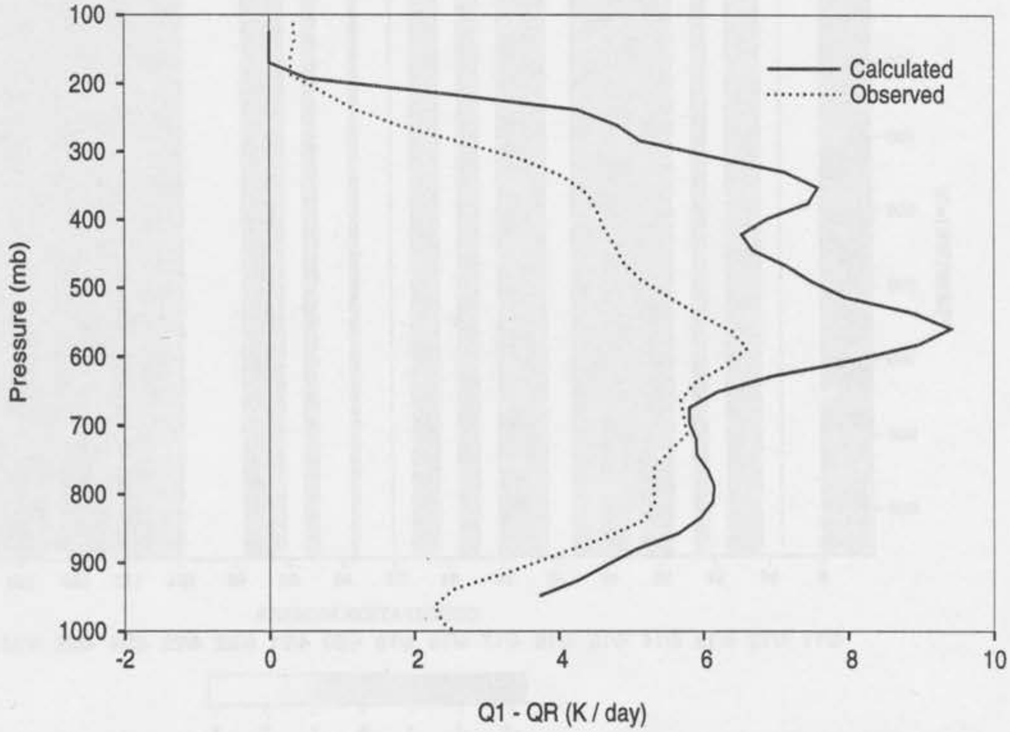

FIGURE 7.10: From Wang, P.h.D dissertation. Calculated versus observed profiles of Q_1-Q_R using GATE data.

than the values calculated here, and also smaller than those obtained by Gallus and Johnson. The much larger values of the apparent heat source verifies our expectation that midlatitude convection can be significantly more intense than its tropical counterpart, due to the stronger large-scale forcing.

Apparent Moisture Sink Q_2

As discussed in Chapter 6, the apparent moisture sink, Q_2, is another diagnostic tool that allows us to analyze moisture budgets by examining the warming rates from condensation (positive) and cooling rates from evaporation (negative) due to convective activity. Fig. 7.11 shows the time series plots of Q_2 derived from the April 1994 IOP MAPS and radiosonde data sets.

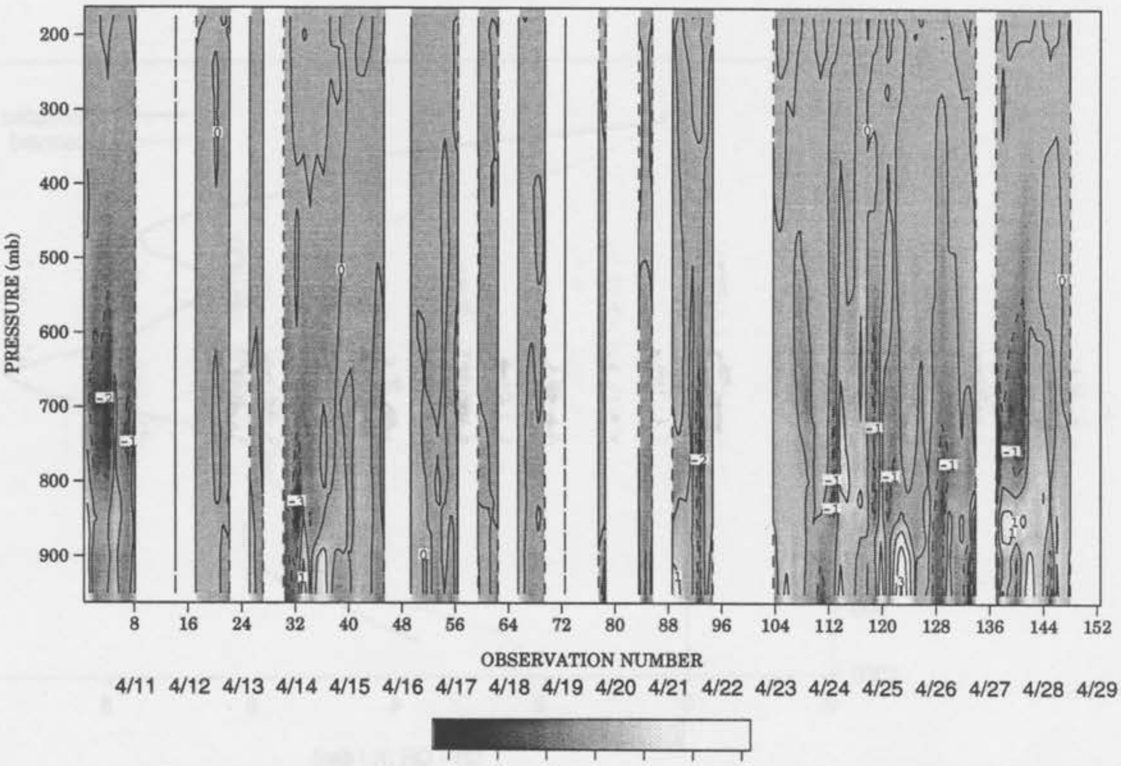

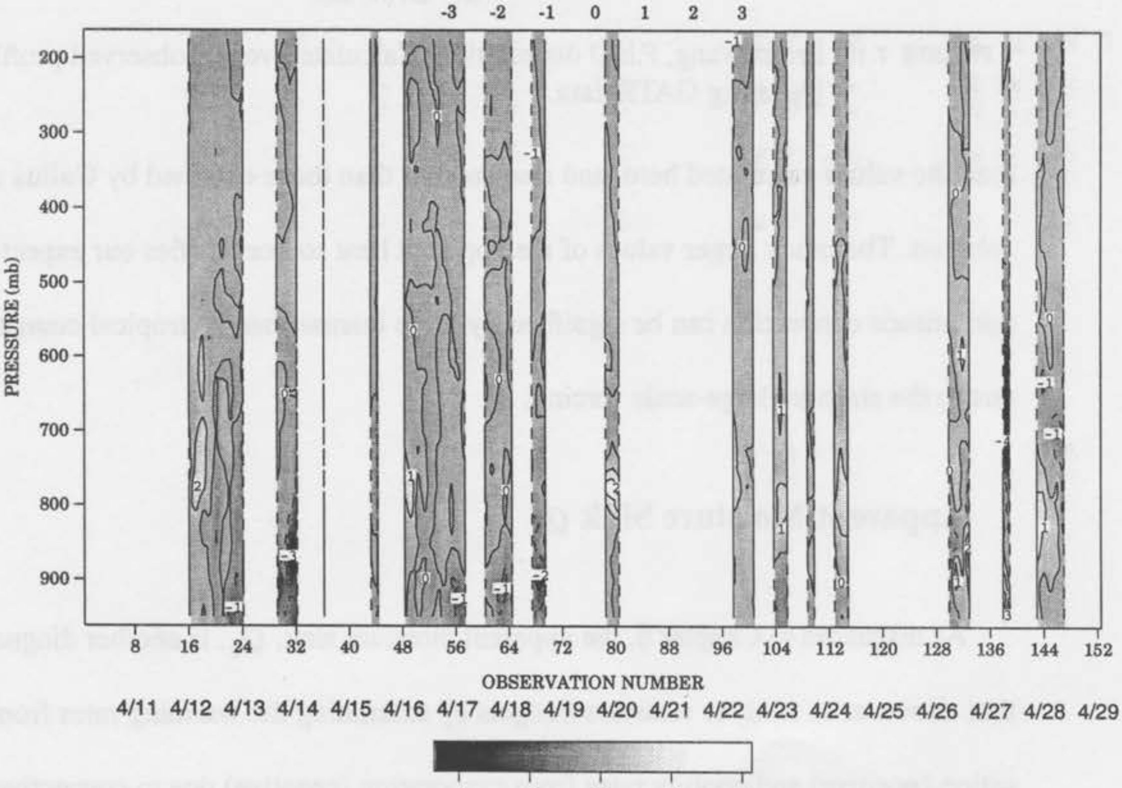

FIGURE 7.11: 19-day time series plots of the apparent moisture sink from MAPS model (upper) and radiosonde (lower) data, starting at 00 UTC on11 April 1994 through 21 UTC on 29 April 1994. Contours are in K hr^{-1} (dashed contours represent negative values), and numbers on the abscissa represent multiples of 8 observations spaced 3 hours apart (8 observations per day), with dates below.

The trend identified by Cotton and Anthes (1989) in the general pattern of Q_2 is reflected in the radiosonde time series plot of the apparent moisture sink. They noticed that the diagnostic studies of moisture budgets for extratropical convection all tend to show a maximum value of the apparent moisture sink in the lower troposphere, in the 800 - 700 mb region. Gallus and Johnson (1991) also reported this tendency, where cloud production by condensation was occurring at the fastest rates during the onset of thunderstorm development. The radiosonde plot verifies this feature at several instances where cloud formation was occurring, showing a maximum sink of over 2 K hr^{-1} in the 800 - 700 mb region from observations 16-20 (early on 12 April), over 1 K hr^{-1} at the same pressure levels near observation 48 (early on 17 April), over 2 K hr^{-1} between 800 - 700 mb around observation 80 (20 April) and from 1-2 K hr^{-1} in the observation interval 128-144 (26-28 April). These features are not as is easily detected in the MAPS plot, however, and presumably this is due to the model problems in the boundary layer. Gallus and Johnson (1991) found that the field of Q_2 is generally nosier than that of Q_1, which is also the case here, and explain this trait by pointing out that shallow dry layers are often present in sections of the radiosonde network, which may account for noise in the data collected.

The maximum moistening and drying rates shown in the time series plot are about +/- 4 K hr^{-1}. These are comparable to, if perhaps a bit weaker, the moistening/drying rates found by Gallus and Johnson (1991). They noted a double maximum sink (positive Q_2) feature that often was present in the formative stage of the storms along the squall line. We do not find that here; but this is likely due to the fact that Gallus and Johnson focussed their analysis more narrowly on specific thunderstorm events, whereas the data from the radiosondes used here are averaged over a larger domain, with the MAPS data being from a domain larger still.

A couple of interesting features are evident in the MAPS plot especially, and the first of these is that there are several pronounced regions of cooling (negative Q_2) in the mid-lower troposphere, which indicates evaporation of either precipitation or cloud droplets was taking place. These can be seen from about 600 mb down to 800 - 900 mb on 6 distinct occasions: observations 1-8 (11 April), 30-32 (14 April), 90-96 (22 April), 112-120 (24-25 April), 126-130 (26 April), and 136-142 (28 April). Each of these instances is closely associated with thunderstorm activity as observed in the weather report, and can are most likely explained by either precipitation evaporating as it fell through sub-saturated air beneath the cloud bases, or the entrainment of dry air as rear inflow jets under the trailing stratiform regions of the stronger thunderstorm complexes, as suggested by Gallus and Johnson (1991). On the other hand, cases where evaporation was strongest at and near the surface (observations 111, 128, 134, 138 and 144) are more probably associated with surface evaporation of precipitation that had fallen previously.

Drawing a comparison with the apparent moisture sink computed by Wang (1994 Ph.D. dissertation) using GATE data (Fig. 7.10), we see that the highest observed value of Q_2 is approximately 6 K day^{-1} in the lower troposphere. Once again, the overall magnitudes of the apparent moisture sink are considerably greater in the midlatitudes, which should not be surprising given the higher amounts of Q_1 we have already seen above as a result of the stronger moisture (and temperature) gradients, hence forcing, found in the midlatitudes.

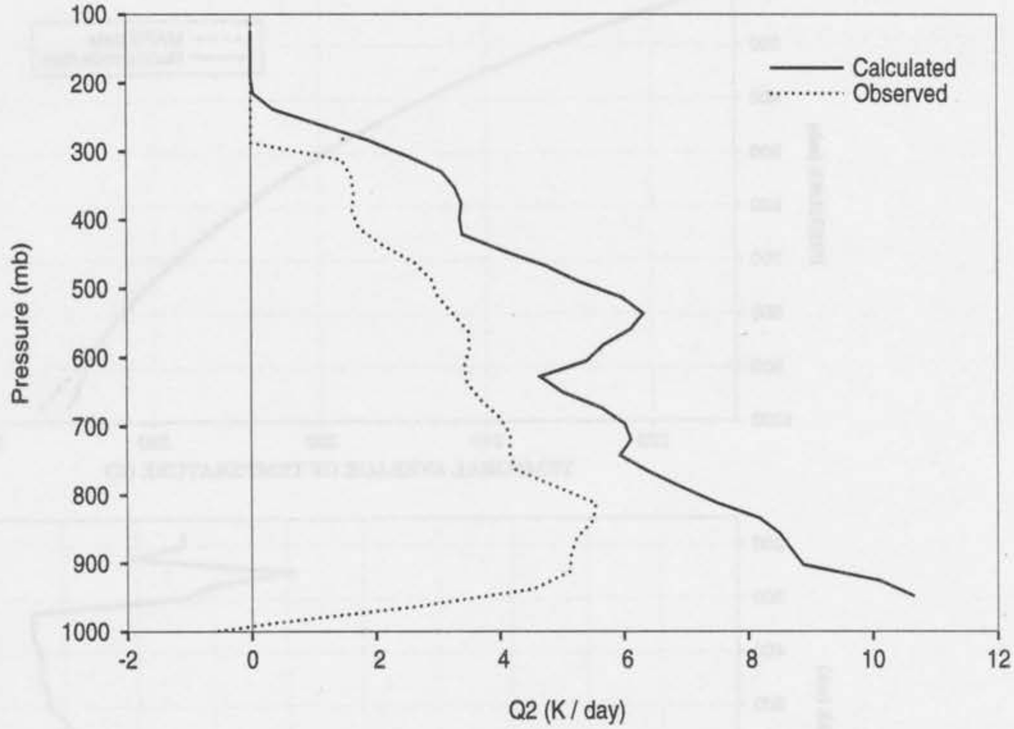

FIGURE 7.12: From Wang, P.h.D dissertation. Calculated versus observed profiles of Q_2 using GATE data.

7.2.2 Statistical Comparison

The plots of temporal averages, standard deviations and correlation shown here for the April 1994 IOP were produced following the same procedures used with the January-February 1994 data sets. For the most part, these plots echo the main trends seen in Chapter 6, with a few notable exceptions.

Temperature

The plot of the temporal average of temperature shown in Fig. 7.13 quite similar to the corresponding January-February 1994 IOP plot in that the averages are virtually identical between the 2 data sets throughout the troposphere. However, in the boundary layer,

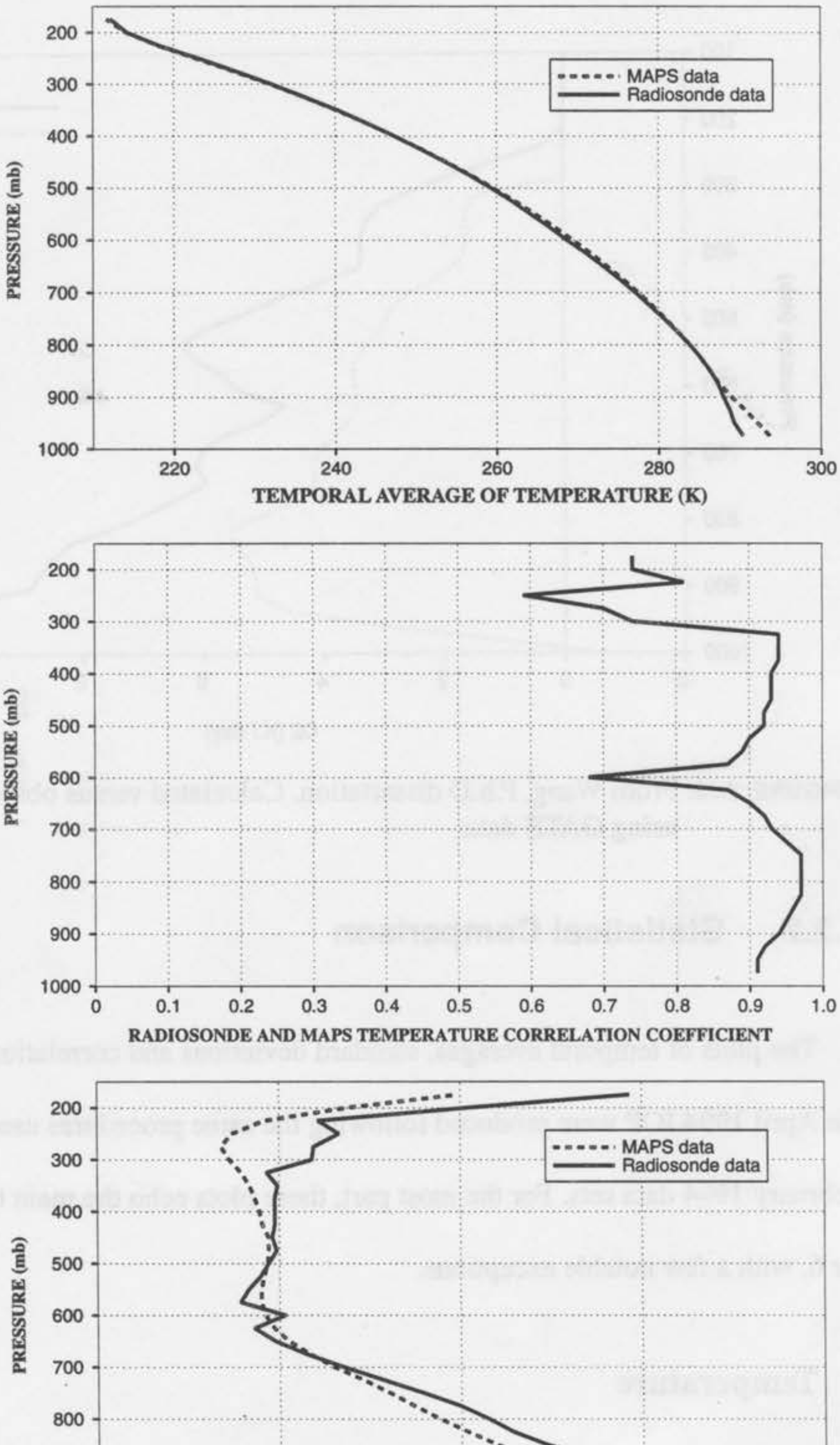

FIGURE 7.13: Temperature temporal averages, correlation and standard deviations of April 1994 IOP MAPS and Radiosonde data.

from just above 900 mb to the surface, we see the same discrepancy as before between the MAPS data and that of the radiosondes. The time average values from the MAPS data look as though they have been linearly extrapolated to the ground, whereas the radiosonde averages show some signs of mixing as would be expected in the boundary layer. Note the overall warmer profile during the April 1994 IOP versus the January-February 1994 IOP: the average temperature in the boundary layer is roughly 20 degrees higher in the spring than in the winter, and the average temperature at 500 mb has warmed from 250 K in the winter to 260 K in the spring. The correlation plot between the two data sets reveals mostly strong, positive coefficients, with couple of interesting dips in an otherwise fairly straight profile with height. At 600 mb, the correlation drops down from over 0.9 to under 0.7. A look at the time series plot for temperature (Fig. 7.1) shows that this corresponds to the temperature blip evident at observation time 76 in the radiosonde plot. Again, the correlation drops from over 0.9 to below 0.6, starting at just below the 300 mb level and extending to the tropopause. This can also be explained by the radiosonde temperature anomalies evident in the time series temperature plot at these pressure levels. Interestingly, the standard deviation profiles of temperature for both data sets indicate much lower deviation values than their winter counterparts, from above the boundary layer to the tropopause. This could be explained by warmer, more consistent average temperatures in the mid- and upper troposphere, not as subject to wide temperature fluctuations since waning frontal activity in late spring makes less of an impact on upper-atmospheric temperature profiles. By contrast, the standard deviations in the boundary layer are almost as high as those of the winter data sets. This would be consistent with the expectation that the diurnal temperature range close to the ground should remain fairly consistent over the span of a few months, since this profile is more consistently driven by radiational heating and cooling of the earth than by frontal passages. The radiosonde reported temperature anomalies make their presence known once again by the sharp increases noted in the radiosonde deviations at the 600 mb and 300 mb levels.

Water Vapor Mixing Ratio

The overall increase in atmospheric water vapor is confirmed by the average mixing ratio values shown in Fig. 7.14. At 500 mb, the average value has jumped from 0.5 g kg^{-1} during the winter IOP to almost 1.0 g kg^{-1} during the April 1994 IOP. Similarly, at 700 mb, the average value has doubled from 1.25 g kg^{-1} in the winter to over 2.5 g kg^{-1} in the spring. The increase in the boundary layer is even more dramatic: near the surface, the average water vapor mixing ratio has gone from under 2.5 g kg^{-1} in the January-February 1994 IOP to over 7 g kg^{-1} in the spring. As before, the two profiles follow each other very closely, but to a lesser extent in the boundary layer. In fact, the agreement is slightly better than in the winter IOP in the lower troposphere, between 900 mb and 700 mb. The high correlation between the two data sets reflects this overall agreement by high, positive coefficients from about 900 - 400 mb. The correlation coefficient drops off below 900 mb in the boundary layer, not surprisingly. However, it also shows a sharp drop above 300 mb. This can be explained by another blip in the radiosonde reported mixing ratio values, evident at 300 mb in the radiosonde time series plot (Fig. 7.2) at observation 120. Turning to the standard deviation profile plot, given the fact that the average mixing ratio values are roughly twice those of the winter data set, it is reasonable to expect that the standard deviations of the spring data set would likewise show values about twice as

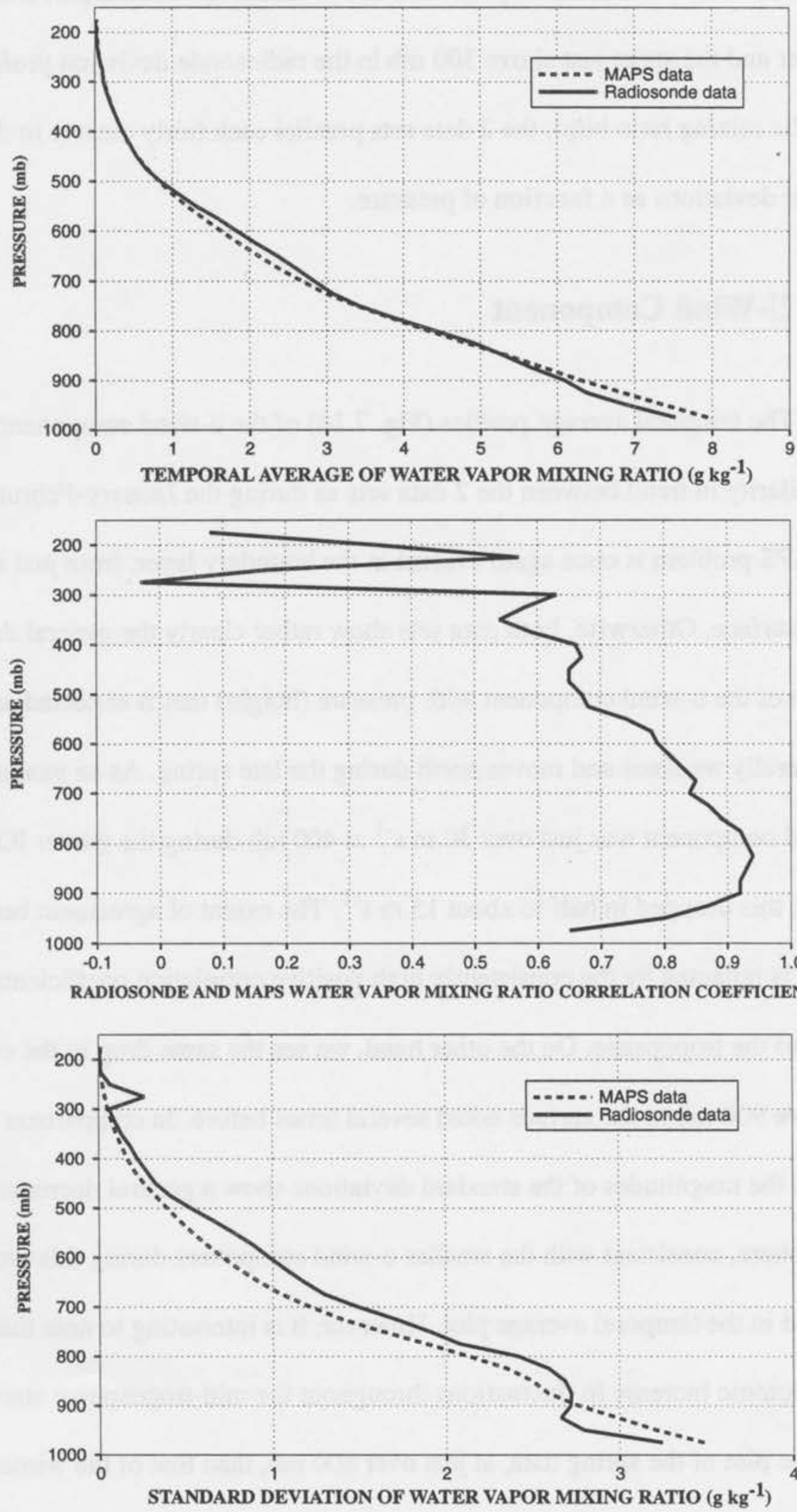

FIGURE 7.14: Water vapor mixing ratio temporal averages, correlation and standard deviations of April 1994 IOP MAPS and Radiosonde data.

high as their winter counterparts, and this is indeed the case. Apart from the boundary layer and the spike just above 300 mb in the radiosonde deviation profile (corresponding to the mixing ratio blip), the 2 data sets parallel each fairly closely in the magnitude of their deviations as a function of pressure.

U-Wind Component

The temporal average profiles (Fig. 7.14) of the u-wind component show the same similarity in trend between the 2 data sets as during the January-February 1994 IOP. The MAPS problem is once again evident in the boundary layer, from just above 900 mb to the surface. Otherwise, both data sets show rather clearly the general decrease in magnitude of the u-wind component with pressure (height) that is expected as the jet stream generally weakens and moves north during the late spring. As an example, the average u-wind component was just over 30 m s^{-1} at 400 mb during the winter IOP. In the spring IOP, this dropped in half to about 15 m s^{-1}. The extent of agreement between the 2 data sets is reflected by the consistently high positive correlation coefficients from above 900 mb to the tropopause. On the other hand, we see the same drop in the coefficient just above 900 mb to the surface noted several times before. In comparison with the winter IOP, the magnitudes of the standard deviations show a general decrease in the upper-troposphere, consistent with the smaller u-wind component during this time period as indicated in the temporal average plot. However, it is interesting to note that the generally monotonic increase in fluctuations throughout the mid-troposphere starts at a lower level in the plot of the spring data, at just over 800 mb, than that of the winter data where the increase commences at about 600 mb. Additionally, the standard deviations are higher in

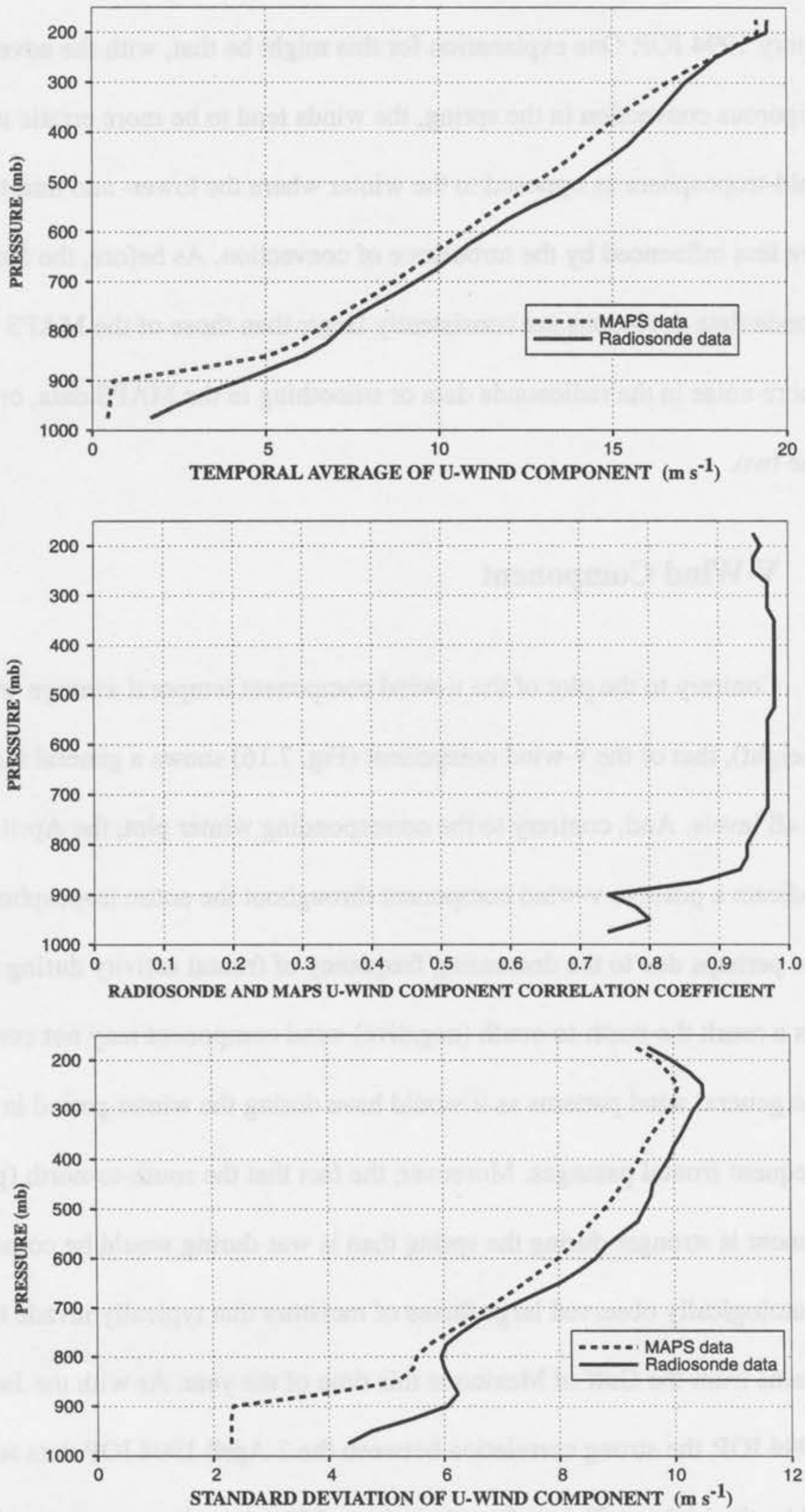

FIGURE 7.15: U-wind component temporal averages, correlation and standard deviations of April 1994 IOP MAPS and Radiosonde data.

the boundary layer during the April 1994 IOP than was the case during the January-February 1994 IOP. One explanation for this might be that, with the advent of more deep and vigorous convection in the spring, the winds tend to be more erratic in the lower- and mid-troposphere as opposed to the winter where the lower- and mid-tropospheric winds are less influenced by the turbulence of convection. As before, the fact that the radiosonde data deviations are consistently larger than those of the MAPS data points to either more noise in the radiosonde data or smoothing in the MAPS data, or a combination of the two.

V-Wind Component

Contrary to the plot of the u-wind component temporal average with pressure (height), that of the v-wind component (Fig. 7.16) shows a general increase in magnitude at all levels. And, contrary to the corresponding winter plot, the April 1994 time averages indicate a positive v-wind component throughout the entire troposphere. These results are perhaps due to the decreasing frequency of frontal activity during the spring period. As a result the north-to-south (negative) wind component may not contribute as much to the general wind patterns as it would have during the winter period in the wake of more frequent frontal passages. Moreover, the fact that the south-to-north (positive) wind component is stronger during the spring than is was during would be consistent with the climatologically observed large fluxes of moisture that typically invade the southern great plains from the Gulf of Mexico at this time of the year. As with the January-February 1994 IOP, the strong correlation between the 2 April 1994 IOP data sets is again illustrated by the high coefficient from just above 900 mb to the tropopause, the boundary layer

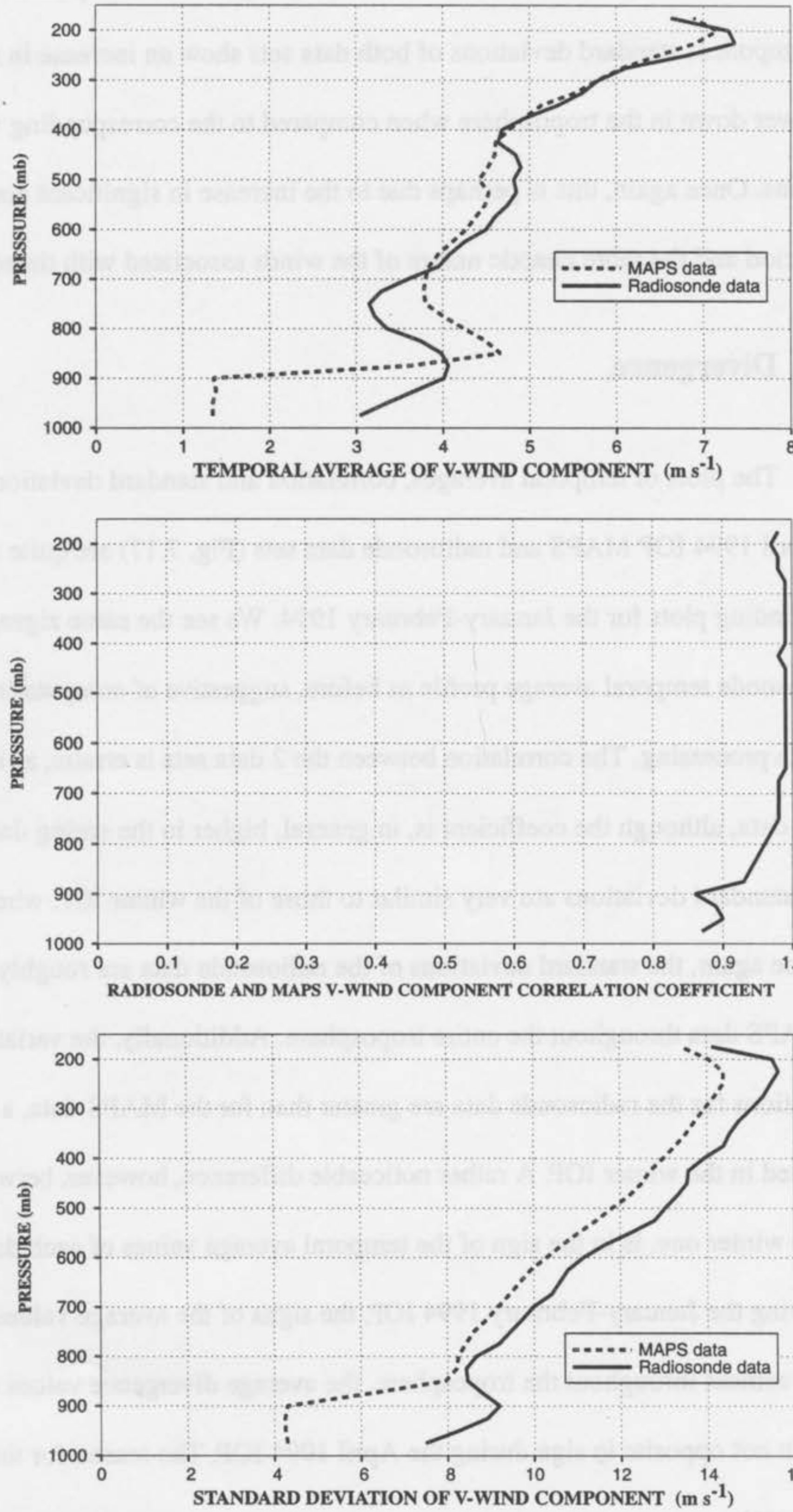

FIGURE 7.16: V-wind component temporal averages, correlation and standard deviations of April 1994 IOP MAPS and Radiosonde data.

notwithstanding. As was the case with the spring u-wind component above, the v-wind component standard deviations of both data sets show an increase in magnitude much lower down in the troposphere when compared to the corresponding winter plot of deviations. Once again, this is perhaps due to the increase in significant convection during this period and the more chaotic nature of the winds associated with thunderstorm activity.

Divergence

The plots of temporal averages, correlation and standard deviations based on the April 1994 IOP MAPS and radiosonde data sets (Fig. 7.17) are quite similar to the corresponding plots for the January-February 1994. We see the same zigzag pattern in the radiosonde temporal average profile as before, suggestive of computational noise in the data processing. The correlation between the 2 data sets is erratic, as it was with the winter data, although the coefficient is, in general, higher in the spring data set. The profiles of standard deviations are very similar to those of the winter IOP, where we see that, once again, the standard deviations of the radiosonde data are roughly twice those of the MAPS data throughout the entire troposphere. Additionally, the variations in standard deviations for the radiosonde data are greater than for the MAPS data, a trait that was also noted in the winter IOP. A rather noticeable difference, however, between this IOP and the winter one, is in the sign of the temporal average values of each data set. Whereas, during the January-February 1994 IOP, the signs of the average values were mostly in agreement throughout the troposphere, the average divergence values were more often than not opposite in sign during the April 1994 IOP. The reason for this is unclear at present.

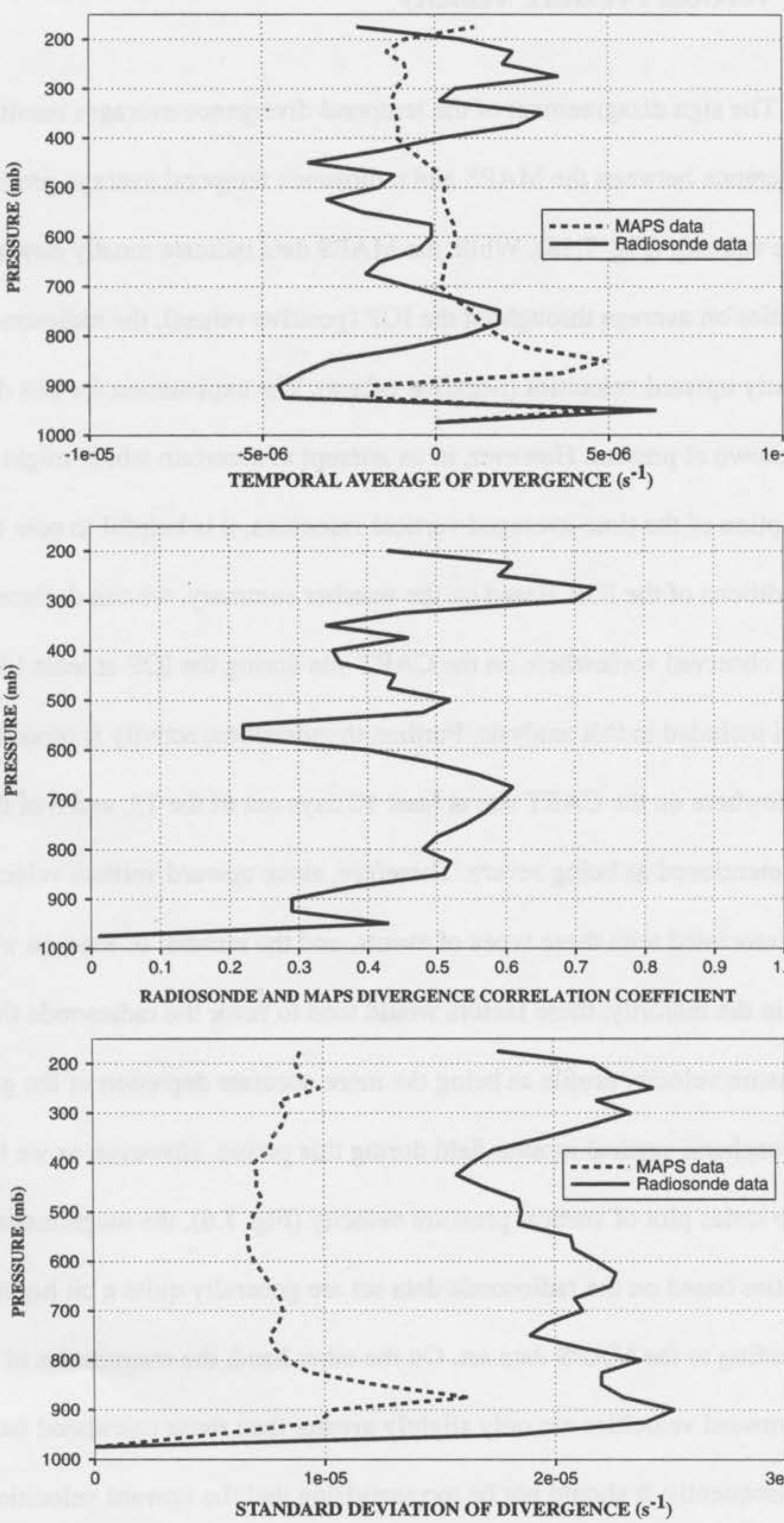

FIGURE 7.17: Divergence temporal averages, correlation and standard deviations of April 1994 IOP MAPS and Radiosonde data.

Vertical Pressure Velocity

The sign disagreement of the temporal divergence averages results in a a substantial difference between the MAPS and radiosonde temporal average profiles of vertical pressure velocity (Fig. 7.18). While the MAPS data indicate mostly downward pressure velocities on average throughout the IOP (positive values), the radiosonde data indicates mostly upward velocities (negative values). The explanation for this difference is, again, unknown at present. However, in an attempt to ascertain which might be the "correct" description of the time-averaged vertical velocities, it is helpful to note the general weather conditions of the IOP. Based on the weather summary, we can deduce that precipitation was observed somewhere on the CART site during the IOP at least 13 days out of the 19 total included in this analysis. Further, thunderstorm activity is reported to have occurred somewhere on the CART site at least 10 days out of the 19, and 5 of these occurrences are mentioned as being severe. Therefore, since upward vertical velocity would naturally be associated with these types of events, and the number of days on which they happened are in the majority, these factors would tend to favor the radiosonde time average vertical pressure velocity profile as being the more accurate depiction of the general state of the atmospheric vertical motion field during this period. However, as we have seen in the time series plot of vertical pressure velocity (Fig. 7.6), the magnitudes of the upward velocities based on the radiosonde data set are generally quite a bit higher than those corresponding to the MAPS data set. On the other hand, the magnitudes of the radiosonde downward velocities are only slightly greater than those calculated from the MAPS data. Consequently, it should not be too surprising that the upward velocities may tend to dominate the radiosonde time average, whereas the MAPS time average reflects the lack of

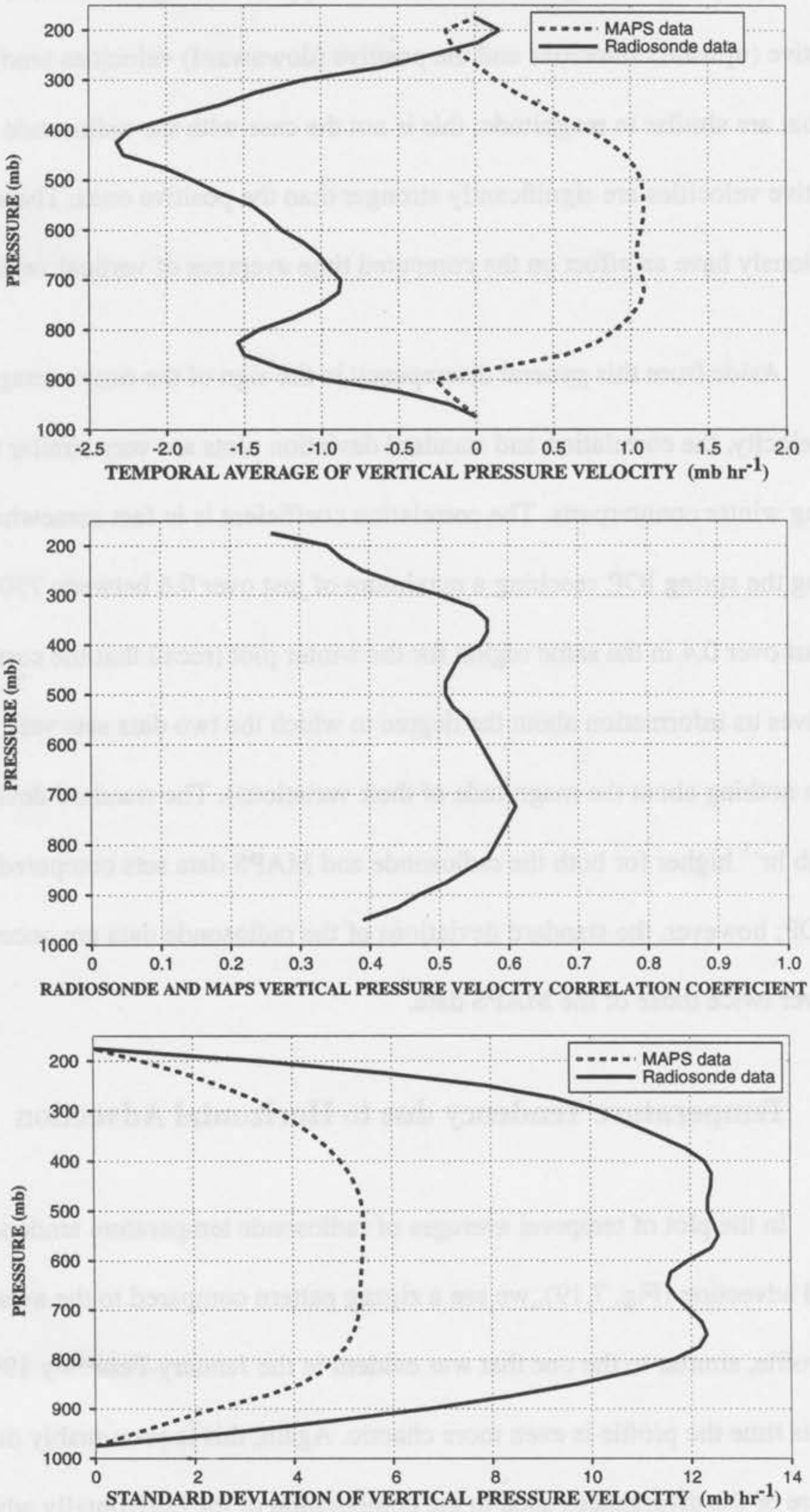

FIGURE 7.18: Vertical pressure velocity temporal averages, correlation and standard deviations of April 1994 IOP MAPS and Radiosonde data.

wide disparity in magnitude of velocities opposite in sign. In other words, the MAPS negative (upward) velocities and the positive (downward) velocities tend to have maximums that are similar in magnitude; this is not the case with the radiosonde data where the negative velocities are significantly stronger than the positive ones. These disparities will obviously have an effect on the computed time averages of vertical velocity.

Aside from this general discrepancy in the sign of the time averaged vertical pressure velocity, the correlation and standard deviation plots are very similar to their corresponding winter counterparts. The correlation coefficient is in fact somewhat more positive during the spring IOP, reaching a maximum of just over 0.6 between 750 - 700 mb versus just over 0.4 in the same region for the winter plot (recall that the correlation coefficient gives us information about the degree to which the two data sets vary together, yet tells us nothing about the magnitude of their variations). The standard deviations are about 1 mb hr^{-1} higher for both the radiosonde and MAPS data sets compared with the winter IOP; however, the standard deviations of the radiosonde data are once again, generally, over twice those of the MAPS data.

Temperature Tendency due to Horizontal Advection

In the plot of temporal averages of radiosonde temperature tendencies due to horizontal advection (Fig. 7.19), we see a zigzag pattern compared to the averages of the MAPS profile, similar to the one that was evident in the January-February 1994 IOP plot, only this time the profile is even more chaotic. Again, this is presumably due to the erratic nature of the divergences used in the computation of the horizontally advected thermody-

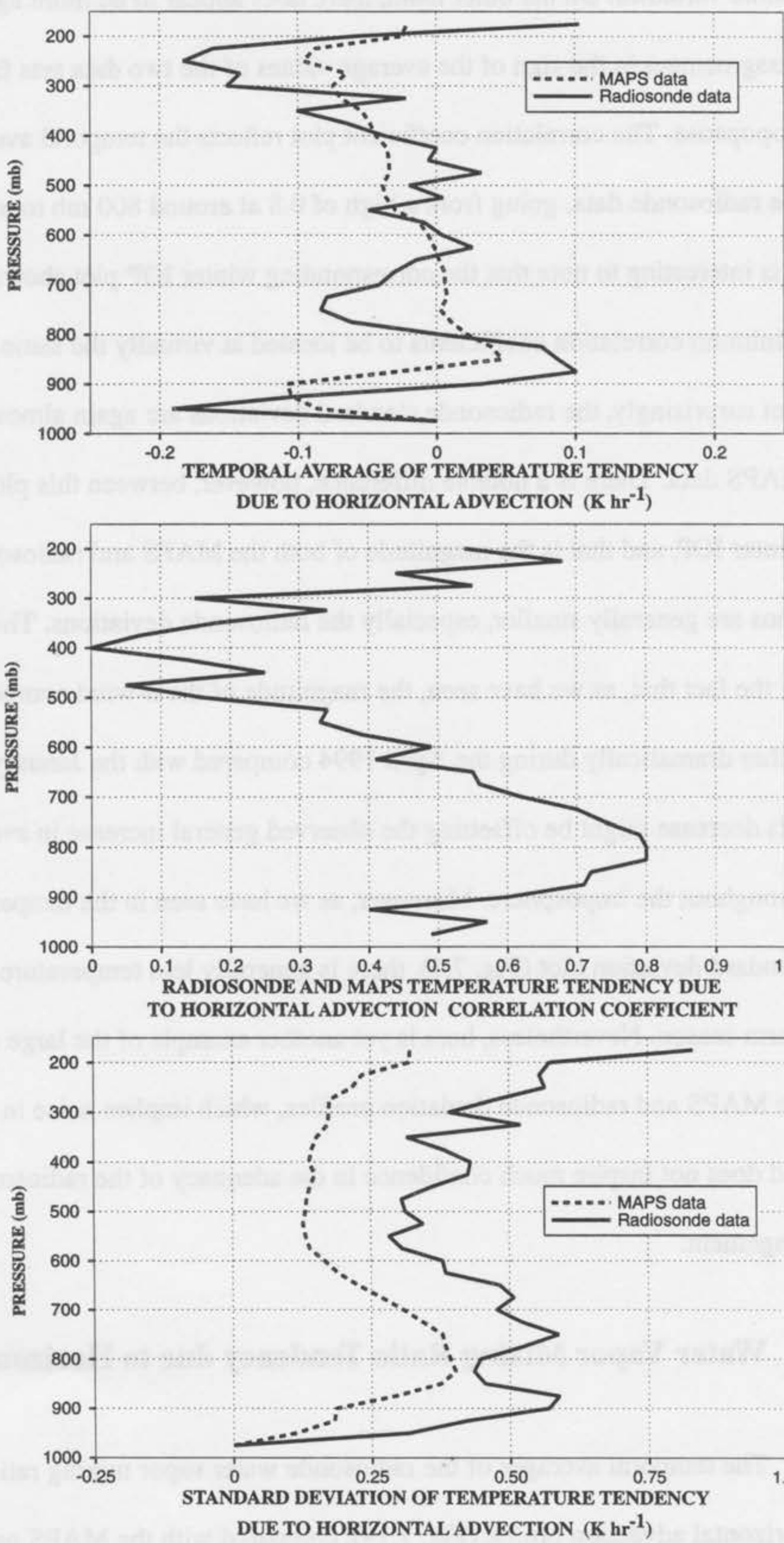

FIGURE 7.19: Temperature tendency due to horizontal advection temporal averages, correlation and standard deviations of April 1994 IOP MAPS and Radiosonde data.

namic variables. On the other hand, there does appear to be more agreement than disagreement in the sign of the average values of the two data sets from the surface to the tropopause. The correlation coefficient plot reflects the temporal average oscillations in the radiosonde data, going from a high of 0.8 at around 800 mb to a low of 0 at 400 mb. It is interesting to note that the corresponding winter IOP plot shows the maximum and minimum correlation coefficients to be located at virtually the same levels, respectively. Not surprisingly, the radiosonde standard deviations are again almost double those of the MAPS data. There is a notable difference, however, between this plot and the one for the winter IOP, and that is the magnitude of both the MAPS and radiosonde standard deviations are generally smaller, especially the radiosonde deviations. This might be explained by the fact that, as we have seen, the magnitude of the u-wind component has decreased rather dramatically during the April 1994 compared with the January-February IOP, and this decrease might be offsetting the observed general increase in average temperatures throughout the troposphere. Moreover, as we have seen in the temperature time series standard deviation plot (Fig. 7.1), there is generally less temperature variation in the warm season. Nevertheless, here is yet another example of the large difference between the MAPS and radiosonde deviation profiles, which implies noise in the radiosonde data and does not inspire much confidence in the adequacy of the radiosonde triangular arrangement.

Water Vapor Mixing Ratio Tendency due to Horizontal Advection

The temporal averages of the radiosonde water vapor mixing ratio tendency due to horizontal advection profile (Fig. 7.19), compared with the MAPS profile, is equally as

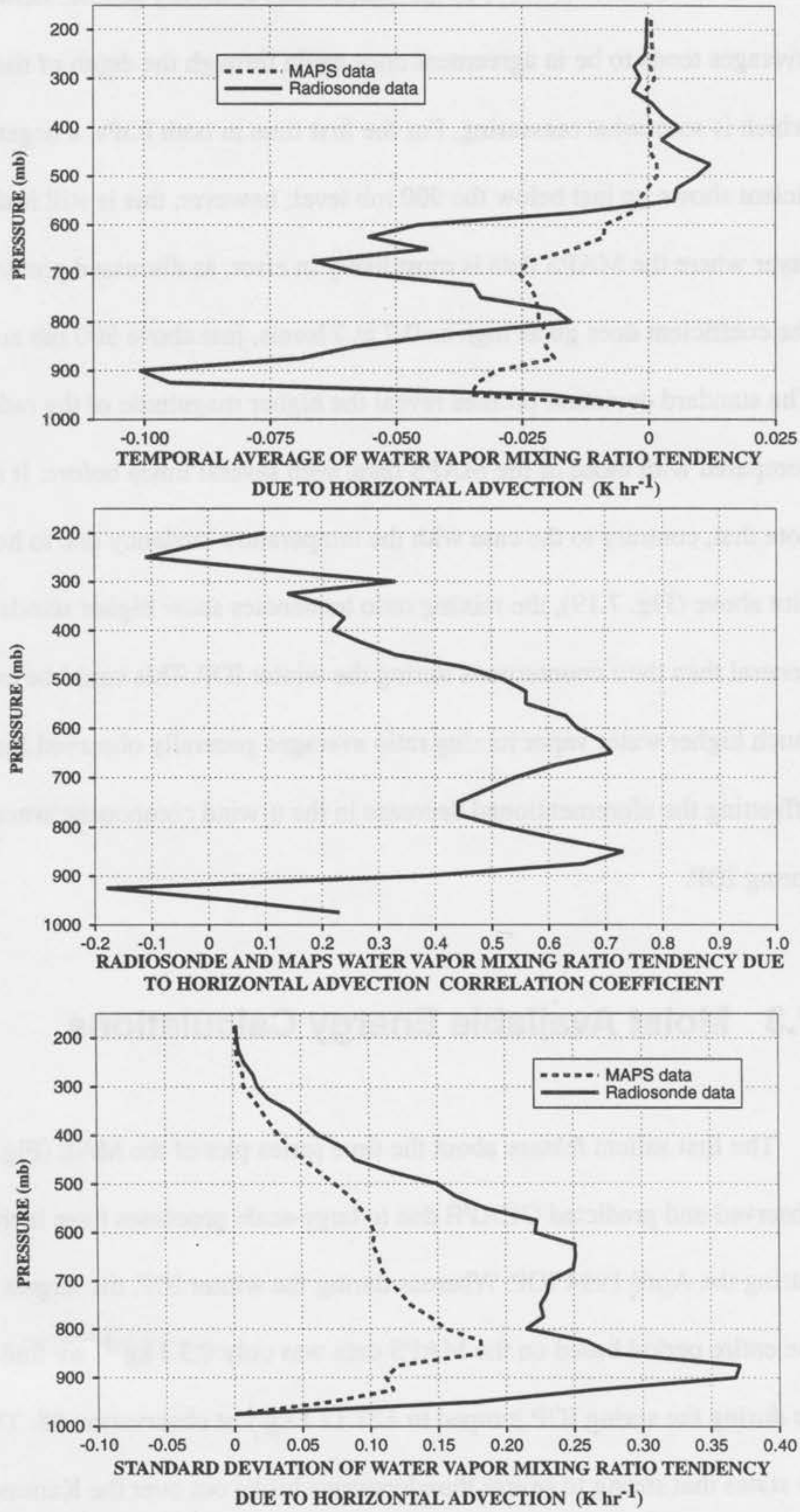

FIGURE 7.20: Water vapor mixing ratio tendency due to horizontal advection temporal averages, correlation and standard deviations of April 1994 IOP MAPS and Radiosonde data.

chaotic as that shown above in the temperature tendency profile. However, the sign of the averages tends to be in agreement once again through the depth of the troposphere, which is somewhat reassuring. For the first time in both IOPs, a negative correlation coefficient shows up just below the 900 mb level; however, this is still inside the boundary layer where the MAPS data is most likely in error, as discussed previously. Otherwise, the coefficient does go as high as 0.7 at 2 levels, just above 900 mb and around 650 mb. The standard deviation profiles reveal the higher magnitude of the radiosonde deviations compared with those of the MAPS data, seen several times before. It is interesting to note that, contrary to the case with the temperature tendency due to horizontal advection plot above (Fig. 7.19), the mixing ratio tendencies show higher standard deviations in general than their counterparts during the winter IOP. This could be explained by the much higher water vapor mixing ratio averages generally observed for the spring IOP, offsetting the aforementioned decrease in the u-wind component averages during the spring IOP.

7.3 Moist Available Energy Calculations

The first salient feature about the time series plot of the MAE (Fig. 7.21) is that both observed and predicted GCAPE due to large-scale processes have increased significantly during the April 1994 IOP. Whereas during the winter IOP, the largest observed MAE for the entire period based on the MAPS data was only 0.3 J kg^{-1}, we find that the largest value during the spring IOP jumped to 127.12 J kg^{-1} at observation 88. The weather summary states that strong to severe thunderstorms broke out over the Kansas-Oklahoma border

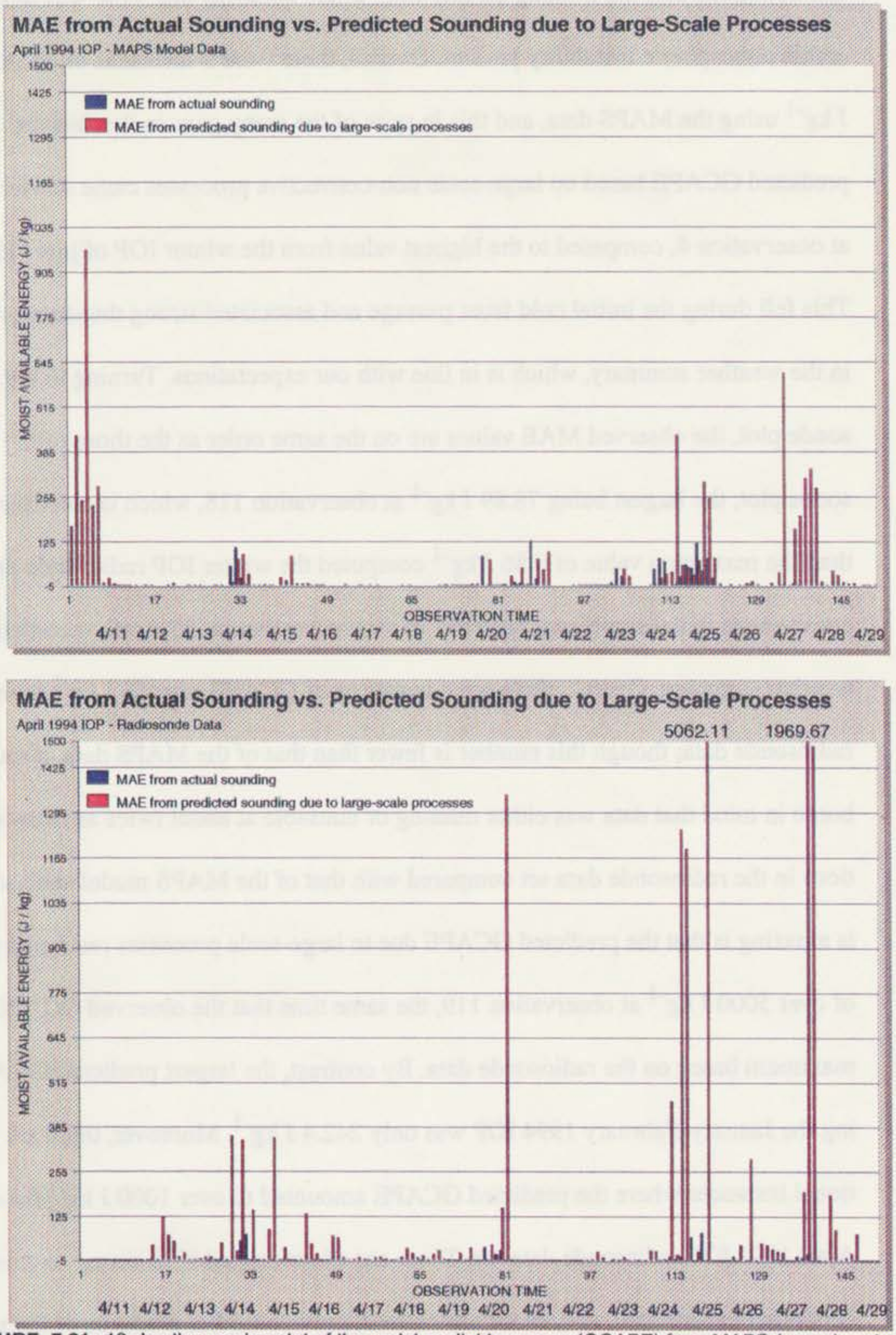

FIGURE 7.21: 19-day time series plot of the moist available energy (GCAPE) from MAPS (upper) and radiosonde (lower) data, starting at 00 UTC on 11 April 1994 through 21 UTC on 29 April1994. Units are J kg^{-1}, and numbers on the abscissa represent multiples of observations, with dates below. Negative values indicate data missing for that observation. To keep scaling consistent between plots, outlier data is identified at top of radiosonde plot.

and continued into the evening on this date, which confirms that there was indeed considerable atmospheric instability present. Overall, there were 9 instances of GCAPE over 50 J kg^{-1} using the MAPS data, and this in spite of the many gaps in the data set. The largest predicted GCAPE based on large-scale non-convective processes came to over 968 J kg^{-1} at observation 4, compared to the highest value from the winter IOP of just 115.7 J kg^{-1}. This fell during the initial cold front passage and associated strong thunderstorms noted in the weather summary, which is in line with our expectations. Turning to the radiosonde plot, the observed MAE values are on the same order as the those of the radiosonde plot, the largest being 78.89 J kg^{-1} at observation 118, which is considerably more than the maximum value of 0.86 J kg^{-1} computed the winter IOP radiosonde data. This corresponds to the significant outbreak of severe weather on 25 April, recorded in the weather summary. Overall, there are 4 instances of GCAPE over 50 J kg^{-1} based on the radiosonde data; though this number is fewer than that of the MAPS data, it must be borne in mind that data was either missing or unusable at about twice as many observations in the radiosonde data set compared with that of the MAPS model analyses. What is amazing is that the predicted GCAPE due to large-scale processes reaches a maximum of over 5000 J kg^{-1} at observation 119, the same time that the observed GCAPE was at a maximum based on the radiosonde data. By contrast, the largest predicted GCAPE during the January-February 1994 IOP was only 242.4 J kg^{-1}. Moreover, there are 5 additional instances where the predicted GCAPE amounted to over 1000 J kg^{-1} based on the April 1994 IOP radiosonde data set. These are all associated with strong-to-severe thunderstorm development, and, as we anticipated, provide further evidence of the much stronger large-scale forcing at work in the midlatitudes. As another example, the second highest MAE observed was almost 2000 J kg^{-1} at observation 138, which is again associated with the severe weather reported on 27-28 April. On the other hand, it is interesting to note that, apart from the one thunderstorm outbreak (observations 80-90, 20-21 April) in the middle of the quiescent period (observations 40-100), both the observed and predicted MAE are relatively small, as we would expect during stretches of large-scale subsidence. Finally, the instability of the first day (11 April) is well documented by the large consecutive values of predicted MAE shown in the MAPS plot (for which the radiosonde data is not usable, unfortunately). At the same time, the observed GCAPE is virtually zero, which seems to provide strong evidence of the efficiency with which cumulus convection was consuming the GCAPE as it was being produced by large-scale forcing. This naturally leads us to consider the scatter plot of the observed GCAPE change versus the production rate of GCAPE due to non-convective processes.

In Fig. 7.22, we see that the more frequent instances of positive GCAPE in the MAPS data accounts for a wider spread along the vertical axis than is the case in the radiosonde plot. However, both are significantly different when compared with the corresponding scatter plots from the winter IOP, which is entirely indicative of the higher degree of atmospheric instability during the April 1994 IOP.

For the most part, both plots show the majority of points lying scattered along the positive x-axis, and very close to zero in relation to the y-axis. These are the points that confirm the GCAPE quasi-equilibrium hypothesis. They show that, although there was considerable production of GCAPE by large-scale processes over the 3-hour time interval between observations, the observed GCAPE tendency was virtually unchanged. The

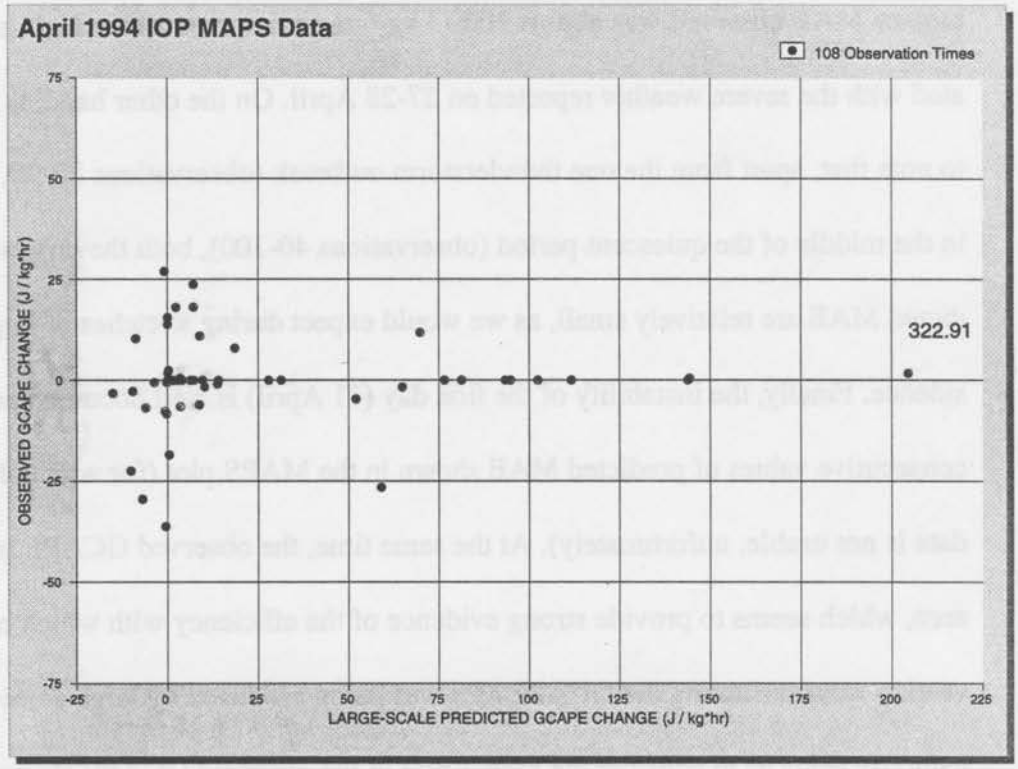

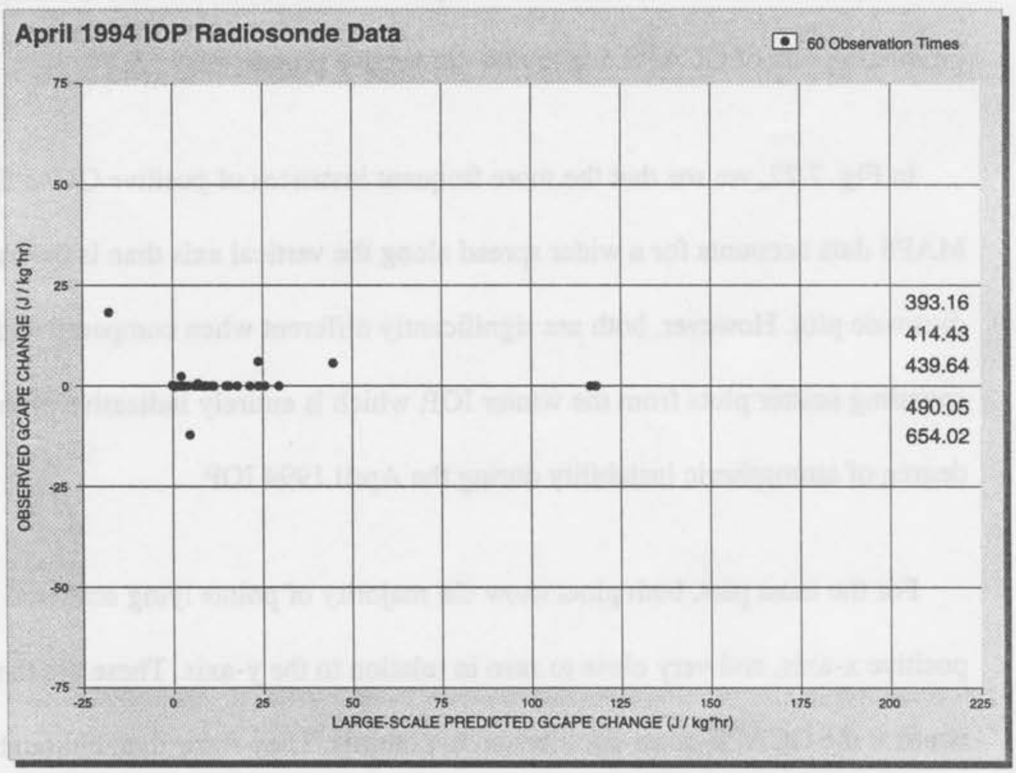

FIGURE 7.22: Scatter plot comparing the time rate of change of the observed GCAPE (ordinate) with the GCAPE rate of production by large-scale processes (abscissa) from MAPS (upper) and radiosonde (lower) data. Each of the points represents the GCAPE calculations corresponding to a pair of temporally adjacent observation times. To keep scaling consistent between plots, outlier data is listed on the right-hand margin of the radiosonde plot.

implication is, therefore, that strong cumulus convection was efficiently consuming the produced GCAPE practically as fast as it was being produced. If this were not the case, we would expect to see points lying along a 45° line in the first quadrant, indicating that the rate at which GCAPE was produced by large-scale processes and the observed GCAPE change were the same. This in turn would imply that cumulus convection was leaving the produced GCAPE untouched, and was instead drawing upon some other mechanism as a source of instability.

Not only do we see very strong GCAPE production rates due to large-scale forcing compared with the January-February 1994 IOP (consider the outlier points on the right-hand margin of both the MAPS and radiosonde plots which were very close to zero with respect to the y-axis), but in general, a significant number of these values are significantly higher than those found by WR94 using GATE data. The computations based on MAPS data in particular indicate that, on 16 occasions the production rate of GCAPE due to large-scale forcing was greater than 30 J kg^{-1} hr^{-1}, a number higher than the maximum production rate found by WR94. The maximum production rate based on MAPS data is computed to be over 322 J kg^{-1} hr^{-1}, compared with a maximum production rate of 38.6 J kg^{-1} hr^{-1}. The same figures based on the radiosonde data are 654 J kg^{-1} hr^{-1} for the April 1994 IOP and 74.5 J kg^{-1} hr^{-1} for the January-February 1994 IOP.

The few points that are positive in relation to the y-axis, and less than or equally positive in relation to the x-axis are a bit troublesome, as these would tend to disprove the GCAPE quasi-equilibrium hypothesis. The obvious explanation is that the large-scale production rate of GCAPE was less than or equal to the observed GCAPE time rate of change, implying that cumulus convection consumed little or none of the MAE produced. However, there are three alternative explanations for these points. The first is that perhaps the large-scale forcing in effect at the time of a given observation was in fact tending towards stabilizing the atmosphere. The assumption in calculating the production rate of GCAPE by large-scale forcing is that this forcing remains unchanged over the duration of the 3-hour time interval. However, it is possible that the large-scale forcing did not remain the same, but rather changed over the time interval such that instability was produced quickly as a consequence. Additionally, we have not explicitly taken into account the effects of surface evaporation and sensible heat flux, and these both tend to increase the MAE, sometimes rapidly. The last explanation is that the observational data itself is possibly in error, leading to either overestimates of the observed GCAPE time rate of change, or underestimates of the production rate of GCAPE by large-scale forces, or both.

The points that are negative with respect to the y-axis, and are zero or positive with respect to the x-axis indicate that the observed GCAPE declined from one observation to the next, while the large-scale production rate caused the GCAPE to increase during the same interval. This is entirely consistent with the GCAPE quasi-equilibrium hypothesis because the implication is that cumulus convection consumed the produced GCAPE very efficiently, leaving the atmosphere in a more stable state than it had been 3 hours previously. However, it could also be a result of changes in the large-scale forcing over the 3-hour interval between observations.

The few points that are negative relative to both axes imply that both the observed time rate of change of GCAPE and the large-scale production rate decreased between observations. This is not inconsistent with the GCAPE quasi-equilibrium hypothesis, because it is entirely plausible that non-convective processes were acting to suppress instability at the time, and the fact that they did so is confirmed by the drop in actual GCAPE at the subsequent observation.

Finally, those points that are negative with respect to the x-axis, yet positive relative to the y-axis indicate that the observed GCAPE increased from one observation to the next while the predicted GCAPE actually decreased between observations. The likely explanation for this is, as mentioned previously, we have not directly included the effects of surface fluxes of evaporation or sensible heat. Therefore, omitting them from the consideration of non-convective processes producing GCAPE may be equivalent to negative forcing. Likewise, radiational effects have not been explicitly taken into account here either, for the sake of simplicity. Thus, on a few occasions, the large-scale forcing may be tending towards stabilizing the atmosphere, whereas radiational cooling along cloud tops may be acting to decrease atmospheric stability, producing a net positive time rate of change of GCAPE.

Of course, while trying to explain these anomalous points, there is always the possibility that the observational data are subject to various kinds of errors and sampling deficiencies. Moreover, there is a considerable amount of important boundary layer information missing from the MAPS data set, which may explain in part why the MAPS scatter plot is less uniform than the radiosonde plot. Nevertheless, the important item to note here is that in both scatter plots, the majority of data points are strongly positive in regards to the GCAPE production rate by large-scale forcing, and at the same time either zero or weakly positive with respect to the observed time rate of change of GCAPE, which is evidence in favor of the GCAPE quasi-equilibrium hypothesis.

Fig. 7.23 shows the MAE (GCAPE) computed from the radiosonde data compared

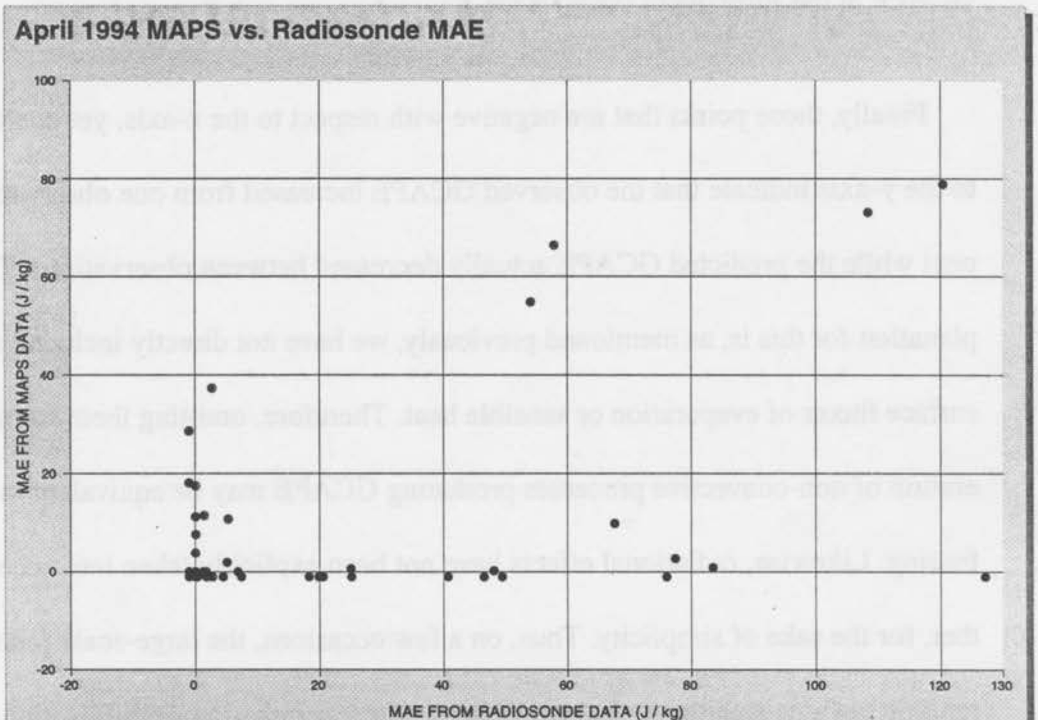

FIGURE 7.23: Scatter plot showing MAE (GCAPE) computed from radiosonde data (abscissa) versus MAPS data (ordinate). Units are J kg^{-1}.

with the MAE computed from the MAPS data. Ideally, all points would fall along a 45 degree line emanating from the origin, indicating that the GCAPE computed from both data sets was equivalent. We do in fact see a number of points that lie close to such a line. However, it appears for a majority of observations that the GCAPE was not able to be calculated from either one or the other of the data sets (indicated by positive values along one axis and negative values along the other). In other cases, the GCAPE was zero for one data set, and positive for the other. This is most likely due to errors in the data, especially considering how much important boundary layer information is missing from the MAPS data set.

CHAPTER 8

Conclusions

8.1 Summary

One of the objectives stated at the beginning of this study was to monitor the quality of the atmospheric radiosonde data being collected at the new SGP CART site under the auspices of the ARM program. The present study is in effect one of the first to make extensive use of this new source of data. Moreover, this goal was actually two-fold, since we wished to simultaneously check the quality of FSL analyses produced by the MAPS model. We accomplished our objective of quality control by examining time series plots of the wind and thermodynamic variable fields and performing a series of statistical comparisons between the data sets produced by both sources, for 2 IOPs. Our findings may be summed up as follows:

- The radiosonde data from the CART site appears promising. Once the errors in the algorithms designed to produce the derived fields were detected and corrected, we have been able to produce the results we were anticipating to a certain extent. However, there still remain a number of technical difficulties to be ironed out, especially in connection with telemetry interference due to the proximity of the wind profilers and the similar frequencies on which both of these instruments operate.

- Though the radiosonde data has proven to be useful, we have shown that there is cause for concern in regards to noise in the data due to undersampling of the atmospheric column with the present triangular radiosonde configuration. This was made especially clear in the statistical comparisons made between the MAPS and the radiosonde data sets, where it was found that the radiosonde standard deviations of time-averaged quantities involving wind measurements were consistently double those of the MAPS data. Indeed, Michael (1994) performed analyses of the CART site radiosonde set-up, and has determined that a great reduction in the noise factor would be effected by the addition of a fourth radiosonde at one of the boundary facilities, such that the disposition would be a square instead of a triangle (not counting the radiosonde launched at the central facility).

- There appears to be something seriously wrong in the MAPS model output for the boundary layer. We have contacted Stanley Benjamin at FSL and he is investigating the source of these problems at the time of this writing.

As a way of evaluating the radiosonde and MAPS data, as well as being an integral component in the evaluation of the MAE, several quantities were computed and compared with the synoptic conditions at the CART site in this study. Among these were omega (the vertical pressure velocity), Q_1 (the apparent heat source), and Q_2 (the apparent moisture sink). The latter two quantities provided an indication of the degree of convective activity during the IOPs. Moreover, the fact that the magnitudes of Q_1 and Q_2 we calculated here were similar to those calculated by Gallus and Johnson (1991) was encouraging, and lead us to believe that valid estimates of the MAE could be obtained from the data available to us. The former quantity, ω, necessary for the computation of vertical advective tendencies in the large-scale forcing, was eventually incorporated into the ARM data processing procedures, and made available as one of the derived fields for use by the scientific community. It is also anticipated that the ω algorithm, including the O'Brien adjustment scheme, will be used in further research involving the operation of an SCM.

The ultimate goal of this study was to evaluate the MAE in a midlatitude setting, and to thereby test the GCAPE quasi-equilibrium hypothesis. Even though evidence in favor of this hypothesis has been established by analyses of deep tropical convection (RW92, WR94), an even stronger case for it would be to examine the hypothesis in the midlatitudes, where large-scale processes, such as moisture and temperature advection, are significantly stronger compared to the tropics with its tendency towards relatively flat temperature and moisture gradients. The GCAPE quasi-equilibrium hypothesis maintains that the atmosphere stays close to a state of conditional neutrality as a result of efficient and fast GCAPE consumption by cumulus convection. Since large-scale, non-convective forcing is more vigorous in the midlatitudes than in the tropics, we anticipated these processes would lead to periods of greater atmospheric instability, which would be manifested by both higher amounts of observed GCAPE and larger GCAPE production rates by large-scale forcing. In spite of some setbacks due to missing data, this is what we discovered:

- The MAE is indeed several times larger under convectively active conditions in the midlatitudes than it is in the tropics.
- The rates of GCAPE production by large-scale forcing appear to be as much as an order of magnitude greater at times than the maximum production rates computed using tropical data. Further, the evidence in this study seems to indicate that large-scale production rates of GCAPE are significant even when there is a lack of strong convection, as was sometimes the case in the January-February IOP.
- The April 1994 IOP scatter plots of the time rate of change of observed GCAPE versus the production rate by large-scale forcing appear to suggest that cumulus convection does indeed rapidly and efficiently reduce the often very large amounts of MAE made available by non-convective processes. Thus, atmosphere, even in the midlatitudes, does appear to stay close to a state of conditional neutrality, or at least does not wander very far away from it and we conclude that the GCAPE quasi-equilibrium hypothesis is upheld by the tests performed here.

8.2 Future Work/Recommendations

The case for the GCAPE quasi-equilibrium hypothesis would perhaps be rendered even more rigorous than the one presented here if the effects of radiation, as well as surface fluxes of moisture and sensible heat, were included in the calculations. For without explicit knowledge of the destabilizing influence they may exert on the atmosphere, it could be argued that the hypothesis does not really hold under all circumstances as some of the data points in the April 1994 MAS scatter plots imply.

In terms of data quality improvement, not only would the introduction of a fourth radiosonde to the perimeter of the CART site provide a better signal-to-noise ratio in connection with evaluation of the wind fields, but also the eventual combination of the radiosonde data with that of the collocated wind profilers through some type of objective analysis scheme would provide a more robust determination of the divergence field. An accurate computation of this variable is critical, since it plays a pivotal role in the derivation of the vertical pressure velocity and the horizontal advective tendencies of temperature and moisture. Any errors in its estimation, as was almost certainly the case in this study with the limited radiosonde and MAPS data available at times, will have definite repercussions on these derived fields, which in turn will adversely affect the accurate assessment of the MAE and its production rate by large-scale processes.

Appendix A

A linear interpolation scheme was used in some instances as a means of reconstructing the vertical profile of a missing variable over gaps of 250 mb or less. As shown in the figure below, if, for example, the temperature T is known at pressure levels p_1 and p_2,

Known pressure levels and temperatures used to linearly interpolate a value for the unknown temperature T_n at some intermediate pressure level p_n.

and we wish to determine T_n at some intermediate pressure level p_n, then a ratio may be formed

$$\frac{T_1 - T_2}{T_n - T_2} = \frac{p_1 - p_2}{p_n - p_2}, \tag{A}$$

from which the unknown temperature can be calculated by

$$T_n = \frac{T_1 (p_n - p_2) + T_2 (p_1 - p_n)}{(p_1 - p_2)}. \tag{B}$$

Using (B) with the values shown in the figure above, we obtain

$$T_n = 277.0. \tag{C}$$

REFERENCES

Arakawa, A., and W. H. Schubert, 1974: Interaction of a cumulus cloud ensemble with the large-scale environment, Part I. *J. Atmos. Sci.*, **31,** 674-701.

Benjamin, S. G., K. A. Brewster, R. Brummer, B. F. Jewett, T. S. Schlatter, T. L. Smith, and P.A. Stamus, 1991a: An isentropic three-hourly data assimilation system using ACARS aircraft observations. *Mon. Wea. Rev.*, **119**, 888-906.

Benjamin, S. G., T. L. Smith, P. A. Miller, D. Kim, T. W. Schlatter, and R. Bleck, 1991a: Recent improvements in the MAPS isentropic-sigma data assimilation system. Preprints, *Ninth Conf. Numerical Weather Prediction*, Denver, Amer. Meteor. Soc., 118-122.

Bleck, R. and S. G. Benjamin, 1993: Regional weather prediction with a model combining terrain-following and isentropic coordinates. Part I: mode description. *Mon. Wea. Rev.*, **121**, 1770-1785.

Bluestein, H. B., 1993: *Synoptic-Dynamic Meteorology in Midlatitudes, Vol. 1.* Oxford University Press, Inc., New York.

Brown, R. A., 1991: *Fluid Mechanics of the Atmosphere*. Academic Press, Inc., San Diego.

CEES, 1990: Committee on Earth and Environmental Sciences. *Our Changing Planet: The FY 1991 Research Plan of the U.S. Global Change Research Program.* U.S. Geological Survey, Reston, VA, 250.

Cheng, M.-D., 1989: Effects of downdrafts and mesoscale convective organization on the heat and moisture budgets of tropical cloud clusters. Part II: Effects of convective-scale downdrafts. *J. Atmos. Sci.*, **46**, 1540-1564.

Cotton, W. R. and R. A. Anthes, 1989: *Storm and Cloud Dynamics*. Academic Press, Inc., San Diego.

Dudhia, J., and W. M. Moncrieff, 1987: A numerical simulation of quasistationary tropical convective bands. *Quart. J. Roy. Meteor. Soc.*, **113**, 929-967.

Fankhauser, J. C., 1974: The derivation of consistent fields of wind and geopotential height from mesoscale rawinsonde data. *Jour. Appl. Meteorol.*, **13**, 637-646.

Gallus, W. A., Jr., and R. H. Johnson, 1991: Heat and moisture budgets of an intense midlatitude squall line. *J. Atmos. Sci.*, **48,** 122-146.

Houze, R. A., Jr., and A. K. Betts, 1981: Convection in GATE. *Rev. Geophys. Space Phys.*, **19**, 541-576.

Krueger, S. K., 1988: Numerical simulation of tropical cumulus clouds and their interaction with the subcloud layer. *J. Atmos. Sci.*, **45**, 2221-2250.

Lord, S. J. and A. Arakawa, 1980: Interaction of a cumulus ensemble with the large-scale environment. Part II. *J. Atmos. Sci.*, **37**, 2677-2692.

Lorenz, E. N., 1955: Available potential energy and the maintenance of the general circulation. *Tellus*, **7**, 157-167.

Lorenz, E. N., 1978: Available energy and the maintenance of a moist circulation. *Tellus*, **30**, 15-31.

Lorenz, E. N., 1979: Numerical evaluation of moist available energy. *Tellus*, **31**, 230-235.

Michael, P., 1994: Estimating advective tendencies from field measurements. *Mon. Wea. Rev.*, **122**, 2203-2209.

Miller, P. and S. G. Benjamin, 1992: A system for the hourly assimilation of surface observations in mountainous and flat terrain. *Mon. Wea. Rev.*, **120**, 2342-2359.

O'Brien, J. J., 1970: Alternative solutions to the classical vertical velocity problem. *Jour. Appl. Meteorol.*, **9**, 197-203.

Ramanathan, V., R. D. Cess, E. F. Harrison, P. Minnis, B. R. Barkstrom, E. Ahmad, and D. Hartmann, 1989: Cloud-radiative forcing and climate: results from the earth radiation budget experiment. Science, **243**, 57-63.

Randall, D. A., and J. Wang, 1992: The moist available energy of a conditionally unstable atmosphere. *J. Atmos. Sci.*, **49**, 240-255.

Randall, D. A., and K.-M. Xu, 1991: *Use of ARM Data to Test an Improved Parameterization of Upper Tropospheric Clouds for Use in Climate Models*. Proposal to the D.O.E., Colorado State University, Ft. Collins, CO.

Soong, S.-T., and W.-K. Tao, 1980: Response of deep tropical cumulus clouds to mesoscale processes. *J. Atmos. Sci.*, **37**, 2016-2034.

Stokes, G. M. and S. E. Schwartz, 1994: *The Atmospheric Radiation Measurement (ARM) Program: Programmatic Background and Design of the Cloud and Radiation Testbed.* Prepared for the D.O.E., Pacific Northwest Laboratory, Richland, WA.

Thompson, R. M., S. W. Payne, E. E. Recker, and R. J. Reed, 1979: Structure and properties of synoptic scale wave disturbances in the intertropical convergence zone of the eastern Atlantic. *J. Atmos. Sci.*, **36**, 53-72.

Wang, J., and D. A. Randall, 1994: The moist available energy of a conditionally unstable atmosphere. Part II: further analysis of GATE data. *J. Atmos. Sci.*, **51**, 703-710.

Xu, K.-M., 1991: The coupling of cumulus convection with large-scale processes. Ph.D. thesis, University of California, Los Angeles.

Yanai, M., S. K. Esbensen, and J.-H. Chu, 1973: Determination of bulk properties of tropical cloud clusters from large-scale heat and moisture budgets. *J. Atmos. Sci.*, **30**, 611-627.